



University  
of Basel

Swiss Nanoscience Institute



# Annual Report 2021 Supplement Swiss Nanoscience Institute

[www.nanoscience.ch](http://www.nanoscience.ch)

Follow us:



# Contents

<b>SNI PhD School reports</b>		
P1304	Monitoring $\beta$ -barrel membrane protein folding	2
P1503	Filming biological factories	4
P1505	Electron phase modulation with five-layer Boersch phase shifter device	6
P1601	Optical enhancement in water-splitting photoelectrodes with nanoparticles	8
P1602	XMCD reveals magnetic frustration of spin and angular moments in Fe atom containing kagome networks	10
P1603	Mesoscale dynamics of the yeast nuclear pore complex transport channel	12
P1604	Hybrid biomimetic platforms based on amphiphilic block copolymers	14
P1606	Smart peptide nanoparticles for efficient and safe gene therapy	16
P1607	Understanding phonon propagation in nanodevices	18
P1701	Subgap quantum interference effects in monolayer semiconductors with superconducting contacts	20
P1702	A 3D nanofluidic device for rapid and multiplexed diagnosis: SARS-CoV-2 and Influenza antibody	22
P1704	Engineering mechanical properties of protein binders	24
P1705	Towards label-free HTS in enzyme engineering	26
P1706	Fiber-based cavity optomechanics	28
P1707	Capacitively-coupled and inductively-coupled excitations in bilayer MoS <sub>2</sub>	30
P1708	Freeform micro-optical structure	32
P1801	Plasma membrane vesicles as an alternative to exosomes	34
P1802	Deep learning enhanced direct evolution	36
P1803	Giant energy dissipation on twisted bilayer graphene at the magic angle twist	38
P1805	Quantifying bacterial responses to antibiotics at the single-cell level	40
P1806	Image the twist!	42
P1807	Interactions between a high-impedance resonator and semiconducting nanowires	44
P1808	Quantum control of a trapped ion coupled to a nanomechanical oscillator	46
P1901	Whole cell vitrification to study neurodegenerative disorders	48
P1902	Dual scale approach using conductive nanofibers towards enhanced cardiac tissue engineering	50
P1903	Magnetic nano-sensors for fuel cells	52
P1904	Development of fixed targets for protein-dynamic studies at SwissFEL	54
P1905	Applying nanowire MFM to 2D materials	56
P1906	Screening for heteromeric nm-sized self-assembled molecular containers	58
P1907	Coherent feedback cooling of a nano-mechanical membrane with atomic spins	60
P1908	How to tune molecular stacking towards functional nanowires	62
P2001	Synthesis of hafnium oxide nanocrystals and their contrast in Y-ray phase contrast CT	64
P2002	A death-dealing nanomachine	66
P2003	Towards all-optical single-spin scanning magnetometry	68
P2004	Surface preparation of multiferroic GeTe	70
P2005	Harnessing polymer compartments with bacterial toxins	72
P2006	Synthesis and surface chemistry studies of zirconium oxo clusters	74
P2007	Manipulation of small particles by acoustic radiation pressure	76
P2008	Integrating a nanowire quantum dot on a scanning probe tip	78
P2009	Hybrid Van der Waals heterostructures for organic electronics	80
<b>Argovia project reports</b>		
A15.01	Mechanoresponsive liposomes: formulation and process development	82
A15.08	Post-treatment of wear-resistant implant coatings	84
A15.11	Antibacterial titanium nanostructures by helium plasma irradiation	86
A16.01	An achromatic X-ray lens	88
A16.04	Detectors to look inside cells	90
A16.05	Peptide-hydrogel-patch for lesion coverage on oral mucosa	92
A16.06	Acoustic signal to control laser ablation processes	94
A16.07	Microstructured degradable hydrogel-based periodontal LIGament RE-Constitution device	96
A16.10	Nanocompass: Nanoscale magnetometer with nanotesla resolution	98
A16.11	Blue laser diode pumped Ti:Sapphire sub-100 fs laser amplifier for nanomachining	100
A16.12	Combinatorial nanoparticle design for therapeutic drug delivery across the blood brain barrier	102
A16.13	PEPS: Printed Electrochemical Protein Sensor	104
<b>Publication list</b>		

# Monitoring $\beta$ -barrel membrane protein folding

Project P1304: Folding mechanisms of  $\beta$ -barrel outer membrane proteins and their catalysis by natural holdases and foldases

Project Leader: S. Hiller and D. J. Müller

Collaborators: N. Ritzmann (SNI PhD Student), P. Rios Flores, T. Raschle, J. Thoma

$\beta$ -barrel membrane proteins are essential functional components of the outer membrane of Gram-negative bacteria, mitochondria and chloroplasts. Membrane proteins have highly interesting folding properties, since they fold in an external environment that comprises hydrophobic and hydrophilic phases. The biogenesis of these outer membrane proteins (Omps) poses a complex biophysical challenge to the pro- and eukaryotic cell, because the Omps are synthesized at locations distant from their target membrane. The overall essential biological function of Omp biogenesis is accomplished by molecular chaperones that pass the unfolded substrates from the ribosome to the destination membrane [1]. In the Gram-negative bacterium *E. coli*, the periplasmic chaperones SurA and Skp transport the substrate to the Bam complex, which folds and inserts them into the outer membrane [2]. The in vitro and the in vivo folding mechanisms of  $\beta$ -barrel Omps from mitochondria or Gram-negative bacteria are so far not understood at atomic resolution. The same polypeptide chains can refold in vitro in the absence of chaperones and other proteins, resulting in the same three-dimensional  $\beta$ -barrel structures. In this project, we employ structural biological and nanotechnological approaches to characterize the folding process of complex Omps at atomic resolution. In the following we report on recent papers, which we published since starting our project and thereafter provide an overview of the following challenges in this project.

## Monitoring Backbone Hydrogen Bond Formation

The three-dimensional structure of a  $\beta$ -barrel membrane protein is defined by backbone hydrogen bonds between adjacent strands. The biogenesis pathways of  $\beta$ -barrel membrane proteins are essential, but the underlying mechanism is still unclear. To obtain insight into this process, we characterized folding of the 8-stranded OmpX from *E. coli* as a model system and found that the residue-specific kinetics of interstrand hydrogen-bond formation are uniform in the entire  $\beta$ -barrel and synchronized to formation of the tertiary structure [3]. OmpX folding thus propagates via a long-lived conformational ensemble state in which all backbone amide protons engage in hydrogen bonds only transiently. Stable formation of the entire OmpX hydrogen bond network occurs downhill of the rate-limiting transition state and thus appears cooperative on the overall folding time scale.

## Chaperone Assisted Insertion and Folding

The correct insertion and folding of membrane proteins is essential to function in living cells. Whereas in living cells molecular chaperones increase the folding yields of soluble proteins by suppressing misfolding and aggregation, it is not understood how they modulate the insertion and folding of integral membrane proteins into membranes. To study this process, we used single-molecule force spectroscopy (SMFS)

and NMR spectroscopy to characterize how periplasmic holdase chaperones SurA and Skp shape the folding trajectory of the large  $\beta$ -barrel Omp FhuA from *E. coli* [4]. After having unfolded and extracted a single FhuA from the lipid membrane by SMFS, we thus monitored how the unfolded polypeptide inserts and folds back into the membrane. The presence of either of the two periplasmic chaperones SurA or Skp prevented misfolding of FhuA by stabilizing a dynamic, unfolded state. Thereby SurA allowed the unfolded substrate to stepwise insert and fold the unfolded FhuA polypeptide towards its native structure.

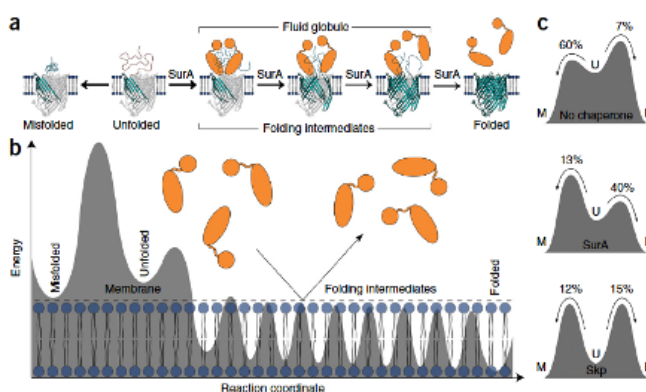


*Fig. 1* Folding pathways and free-energy landscape of FhuA receptors. *a)* Insertion and folding pathways of FhuA in the absence of chaperones and in the presence of SurA (orange). Without chaperones, the majority of unfolded FhuA receptors misfold. SurA stabilizes the unfolded state of FhuA and promotes stepwise insertion and folding of  $\beta$ -hairpins in the lipid membrane. This stepwise insertion of secondary structures proceeds until the receptor completed folding. *b)* Hypothetical folding free-energy landscape of FhuA in the presence of SurA. SurA (orange) is spatially excluded from the lipid membrane (blue). Each  $\beta$ -hairpin inserted into the lipid membrane is stabilized by a free-energy well. *c)* Modulation of the folding free-energy landscape by chaperones. The free-energy barriers separating the unfolded (U) from the misfolded (M) and folded (F) states, are determined from the observed folding probabilities. Image taken from ref [4].

## Directed Insertion of Membrane Proteins

To study whether we could apply the knowledge gained in this proposal and guide the insertion of membrane proteins, we engineered light-driven proton pumps having either a red (RFP) or green (GFP) fluorescent protein fused to its N- or C-terminus [5]. The hydrophilic fluorescent proteins allowed the directed insertion of proton pumps into liposomes and to select the liposomes depending on fluorescence. The

thus manufactured nanoreactors were used to generate proton gradients by light, which is a prerequisite to power a broad variety biomolecular processes [6]. In the future, this side project will enable to supply nanoscopic factories with energy and to translocate polypeptides or other molecules across membranes.

### Maltoporin Unfolding Pathways

The next challenge in this project was to study whether Omps generally unfold and fold similarly to FhuA. We hence first unfolded maltoporin LamB from *E. coli* by SMFS [7]. It was observed that also maltoporin stepwise unfolds  $\beta$ -hairpins until the  $\beta$ -barrel has been completely unfolded and extracted from the membrane. Thereby the folding probability of a  $\beta$ -hairpin was found to be correlated to its mechanical stability. The study was fundamental to characterize at later stage the insertion and folding of other Omps by BAM.

### BamA Unfolding Pathways

The next challenge in this project was to characterize the unfolding pathways of BamA. These unfolding pathways can then later be used as fingerprint to study the folding of BamA. To approach as native as possible conditions for the unfolding and later for the unfolding process we developed the utilization of outer membrane vesicles (OMVs) released from *E. coli* to study Omps in the native membrane environment [8]. Enriched in the native membrane of the OMV we characterize the assembly, folding, and structure of OmpG, FhuA, Txs, and BamA. Comparing Omps in OMVs to those reconstituted into artificial lipid membranes, we observe different unfolding pathways for some Omps. The observation highlights the importance of the native membrane environment to maintain the native structure and function relationship of Omps.

Next we studied the unfolding pathways of BamA in OMV in detail [9]. It was observed that the core component of BamA adopts several conformations, which are thought to facilitate the insertion and folding of  $\beta$  barrel proteins into the bacterial outer membrane. Which factors alter the stability of these conformations remains to be quantified. We thus applied SMFS to characterize the mechanical properties of BamA from *E. coli*. In contrast to the N-terminal periplasmic polypeptide-transport-associated (POTRA) domains, it was found that the C-terminal transmembrane  $\beta$ -barrel domain of BamA is mechanically much more stable. Exposed to mechanical stress this  $\beta$ -barrel stepwise unfolds  $\beta$ -hairpins until unfolding has been completed. Thereby, the mechanical stabilities of  $\beta$ -barrel and  $\beta$ -hairpins are modulated by the POTRA domains, the membrane composition and the extracellular lid closing the  $\beta$ -barrel. We anticipate that these differences in stability, which are caused by factors contributing to BAM function, promote conformations of the BamA  $\beta$ -barrel required to insert and fold outer membrane proteins.

In a concluding project, to better understand the structure-function relationship of BamA, we monitored how the natural antibiotic compound darobactin inhibits BamA by dynamic single-molecule force spectroscopy (SMFS) [10]. The data quantifies how the antibiotic darobactin modulates the mechanical, kinetic, and energetic properties of the POTRA domains, the linker domain, and the  $\beta$ -hairpins of the transmembrane  $\beta$ -barrel of BamA. The the insights gained in this project are helpful to better understanding the insertion and folding mechanism of BamA and how these activities can be inhibited by novel antibiotics.

### References

- [1] T. J. Knowles, A. Scott-Tucker, M. Overduin, I. R. Henderson, Membrane protein architects: the role of the BAM complex in outer membrane protein assembly, *Nat Rev Microbiol* 7, 206 (2009)
- [2] J. G. Sklar, T. Wu, D. Kahne, T. J. Silhavy, Defining the roles of the periplasmic chaperones SurA, Skp, and DegP in *Escherichia coli*, *Genes Dev* 21, 2473 (2007)
- [3] T. Raschle, P. Rios Flores, C. Opitz, D. J. Müller, S. Hiller, Monitoring backbone hydrogen bond formation in  $\beta$ -barrel membrane protein folding, *Angew Chem Int Ed* 55, 5952 (2016)
- [4] J. Thoma, B. M. Burmann, S. Hiller, D. J. Müller, Impact of holdase chaperones Skp and SurA on the folding of  $\beta$ -barrel outer membrane proteins, *Nat Struct Mol Biol* 22, 795 (2015)
- [5] N. Ritzmann, J. Thoma, S. Hirschi, D. Kalbermatter, D. Fotiadis, D. J. Müller, Fusion domains guide the oriented insertion of light-driven proton pumps into liposomes, *Biophys J* 113, 1181 (2017)
- [6] K. Jahnke, N. Ritzmann, et. al., Proton gradients from light-harvesting *E. coli* control DNA assemblies for synthetic cells, *Nat Commun* 12, 3967 (2021)
- [7] J. Thoma, N. Ritzmann, D. Wolf, E. Mulvihill, S. Hiller, D. J. Müller, Maltoporin LamB unfolds beta-hairpins along mechanical stress-dependent unfolding pathways, *Structure* 25, 1139 (2017)
- [8] J. Thoma, S. Manioglu, D. Kalbermatter, P. D. Bosshart, D. Fotiadis, D. J. Müller, Protein-enriched outer membrane vesicles as a native platform for outer membrane protein studies, *Communications Biology* 1, 23 (2018)
- [8] J. Thoma, Y. Sun, N. Ritzmann, D. J. Müller, POTRA-domains, extracellular lid and membrane composition modulate the conformational stability of the beta-barrel assembly factor BamA, *Structure* 26, 987 (2018)
- [9] N. Ritzmann, S. Manioglu, S. Hiller, D. J. Müller, Monitoring the antibiotic darobactin modulating the  $\beta$ -barrel assembly factor BamA, *Structure* 30, 1 (2021)

# Filming biological factories

Project P1503: Watching giant multienzymes at work using high-speed AFM

Project Leader: T. Maier and R. H. Y. Lim

Collaborators: S. Singh (SNI PhD Student), Y. Sakiyama, F. Benning

## Biological Factories are dynamic assemblies

Living organisms require numerous chemical reactions to transform nutrients into biological structures, and to maintain the dynamics of cells and organisms. Altogether these reactions build the metabolism of a cell. Most reactions require catalysis for efficient turnover and the principal catalysts of cells are proteins known as enzymes.

Simple enzymes carry a single active site. Freely diffusing substrates bind to the active site, are turned over, and released into the cellular environment. However, many metabolic pathways require more elaborate solution to prevent unwanted side reactions, to protect unstable or insoluble intermediates and to achieve the required specificity. Multienzymes address this problem by integrating two or more active sites into one enzyme combined with facilitated transfer of intermediates between the active sites. Bringing active sites into spatial proximity is a simple method for improving substrate transfer, however, it doesn't prevent substrates from diffusing away or from interacting with unwanted partners. Substrate tunneling through channels between two active sites fully abolishes such risks, but is not a versatile solution to connect several active sites and to transport diverse intermediates. Substrate shuttling via specific carrier proteins, which covalently tether substrates, is the most versatile option of protected substrate transfer. It is used in acetyl-CoA carboxylase [1] to transfer a carboxy-group linked to biotin between just two active sites, or in fatty acid synthase [2] to shuttle growing intermediates between six active sites. We are studying the functional architecture of multienzymes by obtaining high-resolution structural snapshots by X-ray crystallography and cryo electron microscopy single particle analysis. However, analyzing the dynamic behavior of individual multienzyme molecules in solution and in cells is essential for understanding their function. We have successfully employed high-speed atomic force microscopy to film individual molecules of fatty acid synthase with sub-second frame rate to spatially resolve large conformational re-arrangements. Still, for a comprehensive analysis of multienzyme function, we further require to measure faster and more subtle events. An ideal and well-established technique for this purpose is single-molecule fluorescence microscopy. The key prerequisite for application of this method is to attach fluorescent labels to a molecule of interest in defined positions and without interfering with function. Chemical methods of labeling are not suited for multienzymes, as they commonly interfere with function.

## Genetic code expansion for fluorescent labeling

Genetic code expansion (GCE) for translational incorporation of unnatural amino acids (UAA) into proteins circumvents issues observed in chemical labeling. This method has been well established in bacterial systems and major advances have recently been made for more complex label-

ing schemes or higher efficiency in eukaryotic cells [3]. Still, successful labeling of giant multienzymes in eukaryotic cells is a major challenge. In this project we aim to establish tools and methods for efficient single- and dual-site labeling of multienzymes in human cell lines.

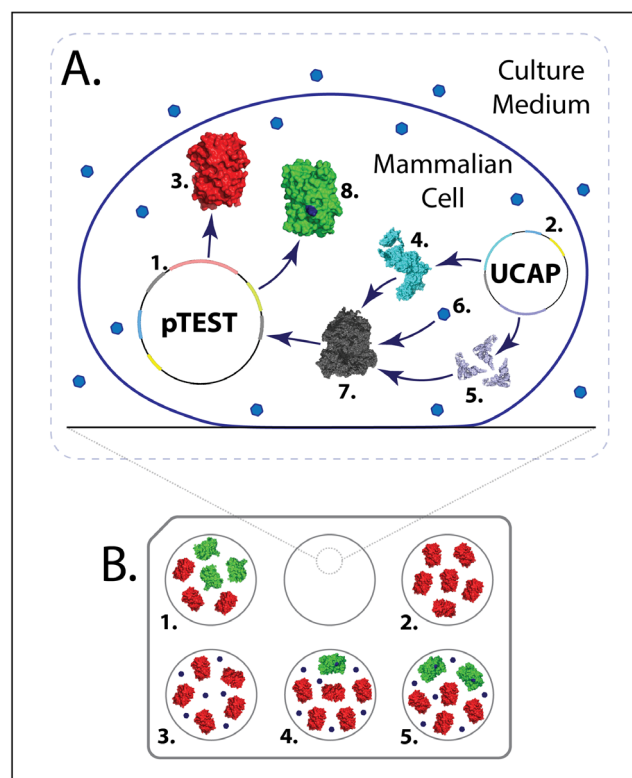


Fig. 1: Approach for screening unnatural amino acid (UAA) incorporation. A. Plasmids pTEST (1) and UCAP (2) are transiently transfected into cells. pTEST codes for red fluorescent protein (RFP) and for green FP (GFP) with an engineered stop codon (3), UCAP produces an orthogonal tRNA-synthetase (4) and the cognate tRNA suppressing a stop codon (5). After addition of UAA (6), the cellular machinery (7) incorporates the UAA in GFP (8), in response to the stop codon signal present on the GFP gene of pTEST. B. RFP & GFP genes are expressed from the same promoter, so when no stop codon is present in the GFP gene, equal amounts of RFP and wild-type GFP are produced (1). When a stop codon signal is present in the GFP gene, in absence of either UAA or UCAP, no intact GFP is produced (2). When both UAA and UCAP are present (3 to 5), the relative amount of GFP produced with respect to RFP provides a measure of the efficiency of any given UAA incorporation system.

Earlier in this project, we have established an approach to screen UAA incorporation based on a collection of genetic tools for different tRNA synthetase/tRNA and UAAs combinations (Fig. 1). We have implemented the screening procedure on an automated robotic setup to perform efficient screening to identify the best tRNA synthetase-tRNA-UAA combinations for labeling different individual single sites in a protein target (Fig. 2).

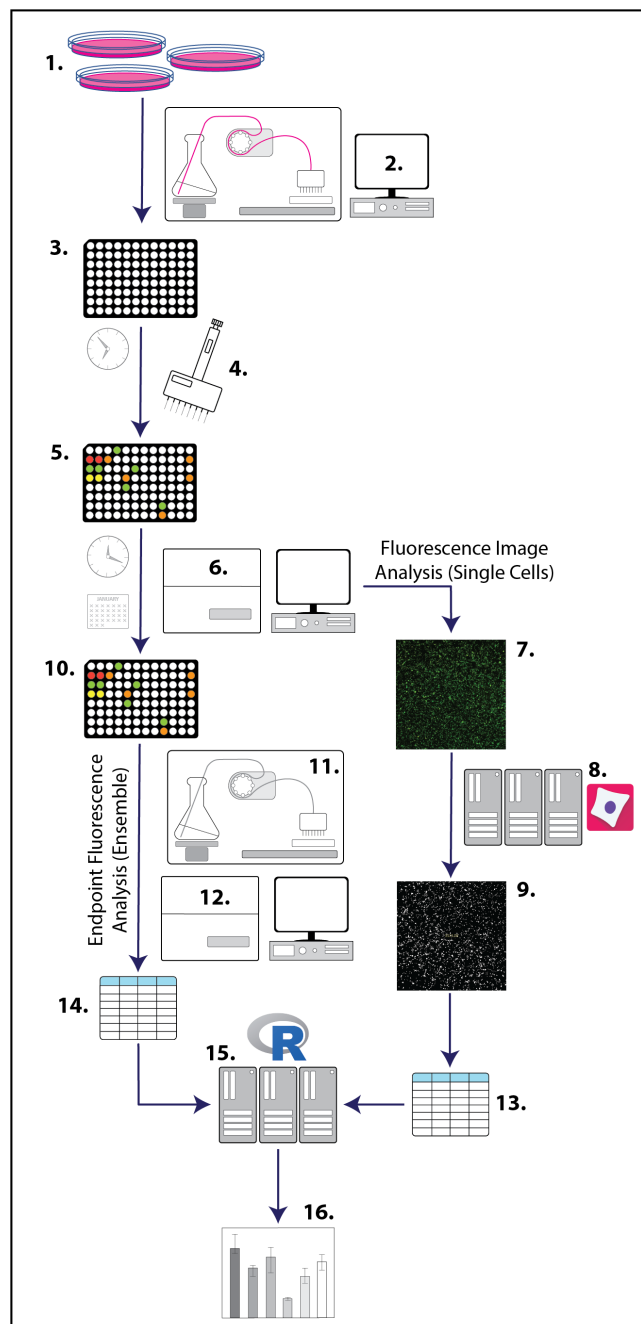


Fig. 2: Automated screening and data analysis pipeline. Cells are grown in adherent culture (1). Liquid handling robot (2) is used for cell seeding in multi-well plates (3), transient transfection is performed manually (4). When cells start expressing fluorescent proteins (5), cells are automatically imaged daily for 3-5 days (6). Acquired images (7) are analyzed computationally (8). Quality control is performed manually on a subset of images (9). After 3-5 days (10), cells are lysed using liquid handling robot (11) and endpoint fluorescence is measured (12). Data generated from single-cell analysis (13) and ensemble endpoint fluorescence (14) is statistically analyzed (15) with graphics generation (16).

### Towards dual-site labeling in eukaryotes

We have validated the approach by screening for optimal UAA incorporation in different sites of GFP. This screen yielded 15 conditions that provided more than 25% percent of the expression of wild-type (wt) GFP, while the baseline expectation was to obtain at least 10% of wt-GFP expression (Fig. 3).

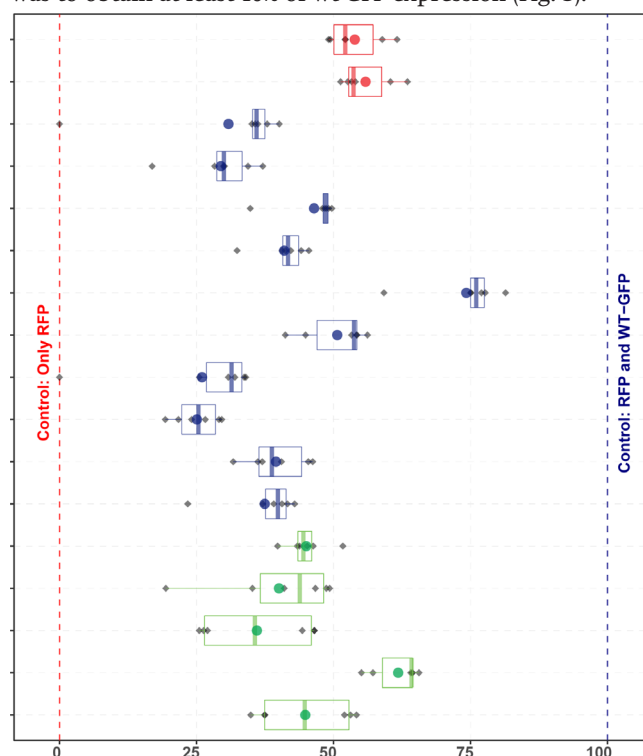


Fig. 3: Screening of unnatural amino acid incorporation efficiency of different genetic code expansion systems. 450 conditions were screened. 15 of those (on Y axis) provided higher than 25% incorporation efficiency. Colors represent different kinds of unnatural amino acids. Solid circles represent mean, boxplots the spread and median, and diamonds individual values.

Encouraged by this success, we entered the final stage of establishing this UAA-labelling system, the screening for dual-site incorporation. We have selected successful combinations of genetic code expansion systems and insertion sites from the single-site insertion screen. Based on these conditions we have set up and run a large scale screen using an expansion of the screening procedure for single site insertion. Substantial expression of dual-site labeled protein was observed, final data evaluation is currently ongoing. After completion of data evaluation and eventual validation experiments we expect to publish the results and to make the full collection of tools and protocols available for re-use and further development in the scientific community.

### References

- [1] M. Hunkeler, A. Hagmann, E. Stutfeld, M. Chami, Y. Guri, H. Stahlberg, T. Maier, Structural basis for regulation of human acetyl-CoA carboxylase, *Nature* 558, 470 (2018)
- [2] T. Maier, M. Leibundgut, N. Ban, The crystal structure of a mammalian fatty acid synthase, *Science* 321, 1315 (2008)
- [3] D. de la Torre, J. W. Chin, Reprogramming the genetic code, *Nat Rev Genet* 22, 169 (2021)

# Electron phase modulation with five-layer Boersch phase shifter device

Project P1505: A programmable e-beam shaper for diffractive imaging of biological structures at Å resolution  
Project Leader: S. Tsujino and J. P. Abrahams  
Collaborator: P. Thakkar (SNI PhD Student)

## Abstract

In our previous work, we reported on fabrication and demonstration of a three-layer Boersch phase shifter device in a transmission electron microscope. However, the analysis of experimental results showed parasitic crosstalk between neighboring phase shifting elements due to exposed contact wires. To minimize such effects, we further developed an improved device design and fabrication protocol, and after careful optimization, we successfully fabricated a Boersch device with top and bottom shielding electrodes – a five-layer Boersch phase shifter device on a suspended thin silicon nitride membrane. With the voltage-controlled electron-beam interference experiment performed in a transmission electron microscope, we demonstrate that our device is scalable for multiple such elements and is programmable for a sophisticated synthesis of electron waves in two- and three-dimensions for various applications in the field of electron microscopy.

## Introduction

A Boersch phase shifter device can alter the phase of electron wavefront proportional to the applied voltage to the device. A hexagonal interference pattern is obtained in far-field with three-element Boersch phase shifter device when incident with a coherent electron wavefront. A bright central spot is formed by the constructive interference of three in-phase electron beams. When a voltage corresponding to the  $\pi$  phase shift is applied to one of the phase shifter elements, the central spot of the interference pattern becomes dark due to destructive interference. We demonstrated the voltage-controlled three-electron-beam interference with three-layer Boersch phase shifter device in our previous work [1]. In this work, we report on the upgrade on the fabrication of five-layer Boersch phase shifter device. We also discuss the experimental confirmation of significant suppression of electron beam deflection compared to the previously reported results.

## Fabrication of five-layer Boersch Phase Shifter Device

We fabricated the five-layer device in continuation to the three-layer Boersch device on a suspended low-stress 200-nm-thin silicon nitride membrane. First, we fabricate the three-layer Boersch device with a bottom shielding metal layer, silicon nitride insulating layer and the central ring electrodes-metal layer [1] (Fig. 1a). After fabricating the three-central ring electrodes, the sample is cleaned in oxygen plasma at about 100 W for about 10 min to remove solvent residues before further processing. In the following step, we spin-coat ~220-nm-thin negative tone resist (HSQ). We pattern the HSQ resist with electron beam lithography. The exposed regions attain insulating properties like silicon dioxide and after development, the unexposed resist is washed away. After few cycles of rinsing the sample in isopropanol and wa-

ter, the sample is ready for the last lithography step for the top shielding electrode. The top metal electrode is patterned in PMMA that covers the insulator layer and which is electrically insulated from the central ring electrodes (Fig. 2c). The gold metal is evaporated on the developed PMMA resist. During the resist removal process in acetone, the unexposed PMMA is removed along with the metal on top of it, leaving with the desired metal electrodes and we finally achieve the five-layer Boersch device with three-elements (see Fig. 1b (schematic) and Fig. 2b (fabricated device)).

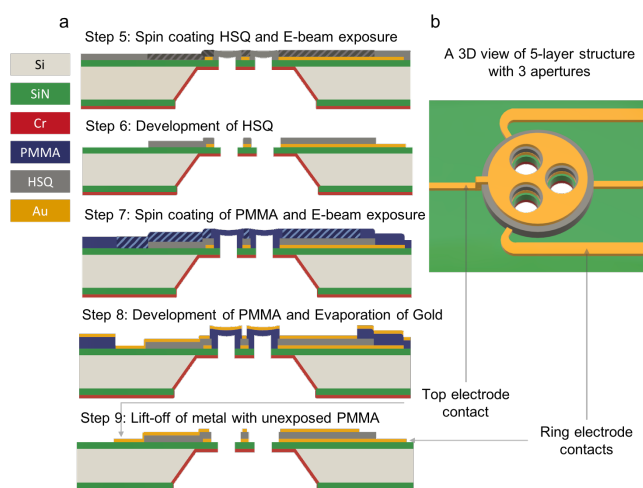


Fig. 1: Schematic explaining the fabrication process steps for a five-layer Boersch phase shifter device. The omitted steps 1-4 are for the fabrication of three-layer device that are explained in the published article [1]. a) shows the process steps to further fabricate two more layers on top of the MIM device structure: Steps - 5. A 200-nm-thin negative e-beam resist HSQ is spin-coated on top of the three-layer device. The hatched region is exposed in an e-beam tool, 6. The exposed device is then developed removing the unexposed areas, 7. PMMA is spin-coated on top surface and the hatched areas are exposed in an e-beam tool, 8. The sample is developed removing the exposed resist. Gold metal layer is the evaporated on the developed resist, 9. The resist layer is then stripped off leaving the metal layer on the developed areas and removing elsewhere. b) A perspective view of the five-layer Boersch phase shifter device with three elements along with contact wires and a contact wire for grounding the top metal layer is shown.

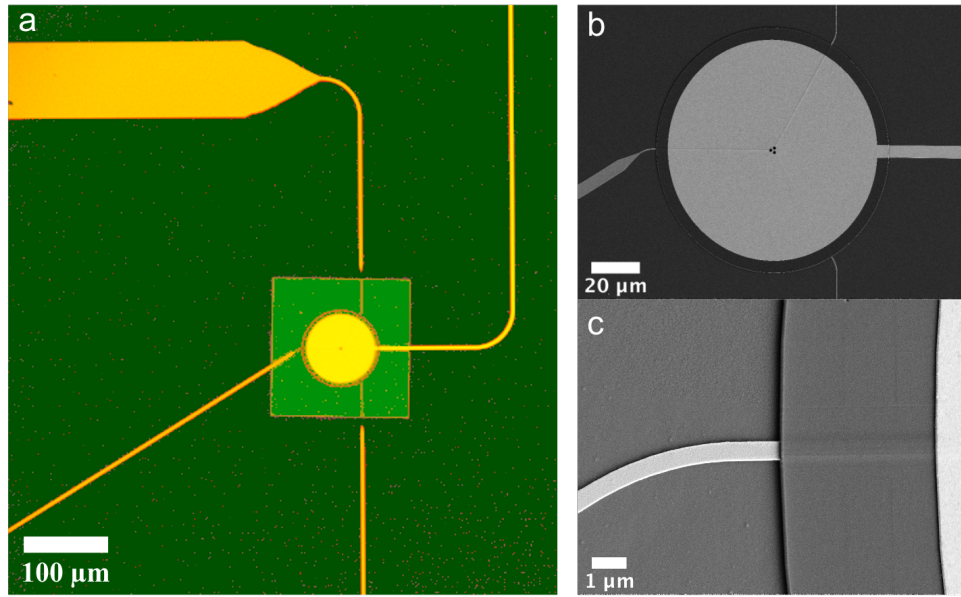


Fig. 2: a) A false-colored optical image of the five-layer device. The square in the center is the silicon nitride membrane. b) SEM image of the central part of the membrane showing top metal electrode layer ( $\sim 80 \mu\text{m}$  big circle in bright gray). c) SEM image showing the contact wire in the central metal layer is insulated from the top metal layer.

### Voltage-controlled three-beam Interference

The fabricated five-layer device is tested in a transmission electron microscope at an energy of 200 keV. We collect the far-field interference pattern of our device kept at sample position in the microscope. First, initial offset voltages are applied to each element to compensate for the probable intrinsic charging and achieve the reference constructive interference pattern with the central bright spot (Fig. 3a). We then increase the voltage to only one phase shifting element to observe the destructive interference pattern corresponding to  $\pi$  phase shift (Fig. 3b). For the five-layer device, we applied  $\sim 1.5$  V voltage bias for  $\pi$  phase shift of the electron wave. The comparison of the relative position of the two cases (black circle in Fig. 3a and b) demonstrates that the beam deflection caused by the voltage bias to the phase shifting element for  $\pi$  phase shift is suppressed in the five-layer device. This deflection was significant for the previously reported three-layer device. We also compared the experimental results with the finite-element simulation model and found that both the results agree within 20% margin.

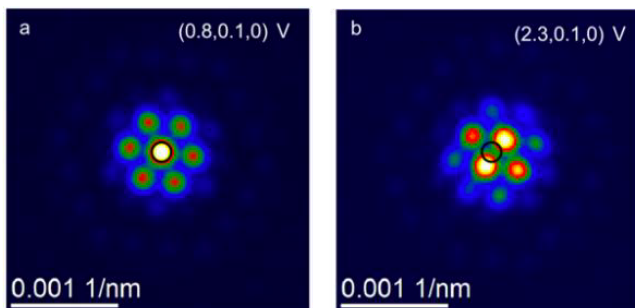


Fig. 3: Voltage-controlled three-beam interference of electrons for five-layer Boersch phase shifter elements. The voltages applied to the three-phase shifting elements are shown on the top-right corner of the images. a) shows the reference constructive interference pattern with (0.8 V, 0 V, 1.0 V) voltage bias to the three elements and b) shows the destructive interference pattern with +1.5 V additional voltage bias to the phase shifting element 1 relative to the case a). The circle in the center is used as a reference to evaluate the beam deflection.

### Conclusion

Multi-element Boersch phase shifter device with the five-layer structure fabricated with scalable methods is demonstrated. With the proposed MIMIM structure, the crosstalk between elements by parasitic beam deflection is minimized. This is an important step forward to realize an array of programmable phase shifter with many elements to arbitrarily manipulate electron wavefront for aberration correction, massively parallel electron beam lithography, and novel imaging applications.

### Reference

- [1] P. Thakkar, V. A. Guzenko, P.-H. Lu, R. E. Dunin-Borkowski, J. P. Abrahams, S. Tsujino, Fabrication of low aspect ratio three-element Boersch phase shifters for voltage-controlled three electron beam interference, *J. Appl. Phys.*, 128(13), 134502, (2020)

# Optical enhancement in water-splitting photoelectrodes with nanoparticles

Project P1601: Optical plasmonic nanostructures for enhanced photochemistry

Project Leader: E. C. Constable and S. Fricke

Collaborators: L. Driencourt (SNI PhD Student), B. Gallinet, C. E. Housecroft

The increased energy demand related to the economic growth and demographic explosion, and the current ecological crisis poses a massive challenge. In addition to emitting  $\text{CO}_2$ , fossil resources are not unlimited, and their extraction peak has already been or is soon to be reached. Therefore, they need progressively to be replaced. Sustainable, low carbon technologies for electricity production such as solar cells and wind turbines have significantly improved over the last years, but large-scale storage remains problematic with the current battery technologies, because of the increased system cost and large amounts of materials needed. Nuclear energy is carbon free but not sustainable, and a significant proportion of the waste remains radioactive for extremely long periods of time; appropriate storage is also essential. Hydrogen has a high potential as a solar fuel, in industries such as agriculture and metallurgy. Most hydrogen is currently generated with steam reforming of methane (gray hydrogen) which emits  $\text{CO}_2$ . For this reason hydrogen cars have a similar carbon footprint as gasoline cars. This is because green hydrogen technologies (water electrolysis) are not yet competitive, because they suffer from high complexity and require significant amounts of noble metal catalysts. Realistic scenarios for the future of the world involve energetic efficiency, sustainability, and reduced consumption. Therefore, we have investigated an approach to produce hydrogen from sunlight called photo-electrochemical water splitting that involves a simple, integrated system immersed in water and we choose to use mostly earth abundant materials, cheap and not energy demanding to extract and transport. Some metal oxide semiconductors such as hematite ( $\alpha\text{-Fe}_2\text{O}_3$ ) can be used to harvest the energy from sunlight and they are meeting the above criteria. The main challenge is their poor charge transport properties, making the light-to-electricity conversion extremely inefficient. This is also the reason those materials are not massively used in the semiconductor industry. Only charge carriers that are transported over very short distances can be extracted. On the other hand, a very thin layer absorbs light poorly limiting the efficiency. Thus, electrode morphologies which extremely small feature sizes (nm) and high surface to volume ratio have shown the highest performances. However, this is still limited to about 50% of the theoretical maximum (considering perfect below bandgap absorption and 100% internal quantum efficiency). For this reason, we developed a multi-physics theoretical approach that models the performances of a single photoelectrode and can be used to optimize the geometry [1]. We showed that this method can quantitatively be compared to experimental results. It can also be used to study other strategies to enhance the absorption in the active material, such as thin film effects (e.g using reflective films). Several reported nanostructuring techniques rely on expensive and/or non-scalable fabrication procedure. Therefore, we have investigated deposition of nanoparticles on metal oxide photo-

electrodes as an alternative or complementary approach to enhance light absorption in the active material, which can be achieved with cheap and up-scalable processes. It has been mostly reported for plasmonic nanoparticles, which are made of noble metals containing a lot of free electrons (Au, Ag, Cu). These free electrons can be resonantly coupled to incident light, at a wavelength much larger compared to the nanoparticle dimension in contrast to a classical antenna. Plasmonic nanoparticles can confine high light intensities at the nanoscale and are therefore interesting to study as an enhancement strategy. Noble metals are of course rare and expensive, however this is not the limiting factor if they are used in very small quantities. We investigated plasmonic nanoparticles for photoelectrode performances enhancement by first validating the model experimentally and then unveiling the factor affecting the performances such as the choice of plasmonic material for a given active material, the illumination direction, position of nanoparticles with respect to the active material, etc [1, 2].

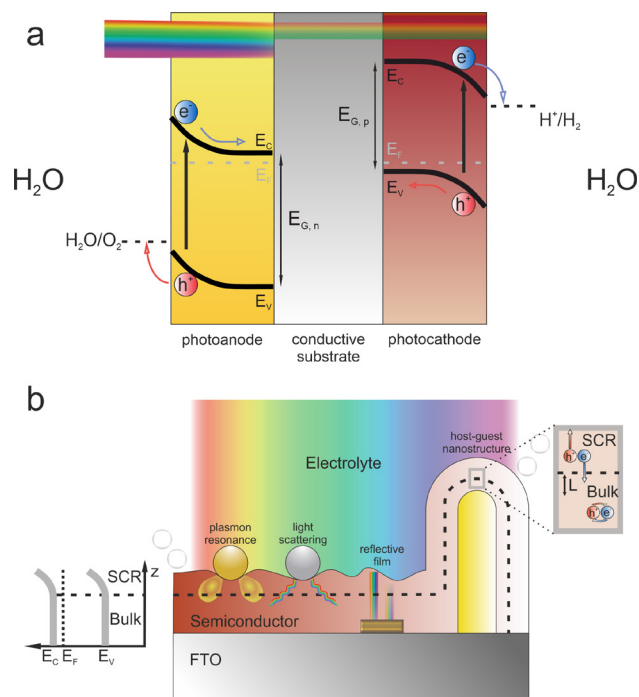


Fig. 1: a) Scheme of a PEC tandem cell with a n-type and a p-type semiconductor and  $E_{G,n} > E_{G,p}$ . b) Some reported strategies to enhance the absorption in the active material.

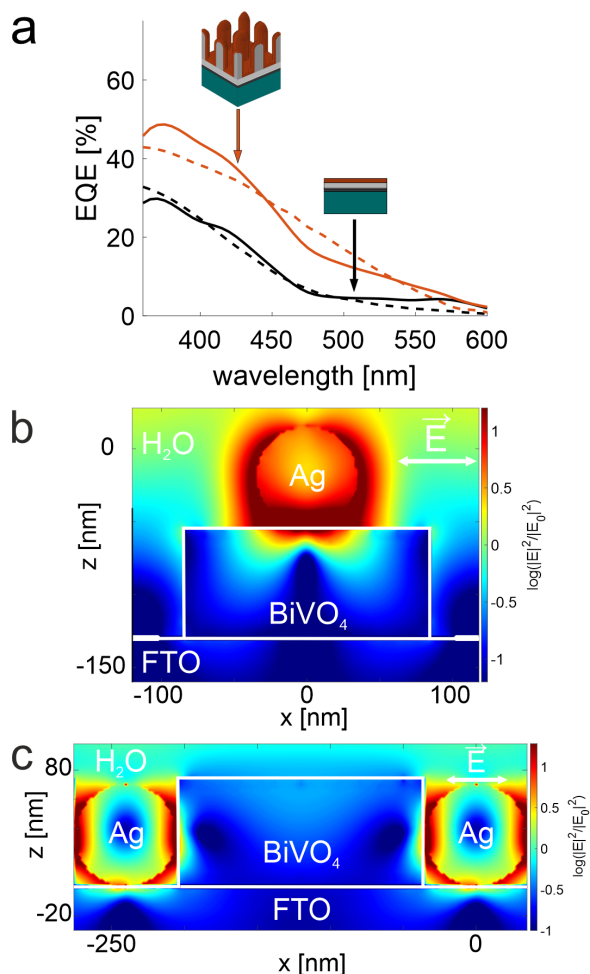


Fig. 2: a) Simulations with our model (plain curves) are compared to experimental results (dashed curves) for the analysis of performance enhancement by nanostructuring. Electric field distribution for a photoelectrode where plasmonic nanoparticles are deposited b) on active material grains ( $\text{BiVO}_4$ ) and c) inside the grooves.

We concluded that gold is poorly efficient for optical enhancement compared to silver, in combination with hematite or bismuth vanadate. However, silver nanoparticles need to be protected from contact with water otherwise they rapidly oxidize in typical operating conditions. Core-shell silver nanoparticles cannot achieve comparable near field enhancements than nanoparticles without shell but can still enhance the active material absorption via interference effects from the light scattered by the nanoparticles.

We have finally investigated the effect of high refractive index nanoparticles deposited on metal oxide electrodes [3]. High refractive index materials such as  $\text{TiO}_2$  and  $\text{ZrO}_2$  have the advantage of being much cheaper/chemically resistant than gold/silver. We showed experimentally that metal oxide photoelectrodes decorated with  $\text{TiO}_2$  nanoparticles show enhanced performances under front illumination compared to bare photoelectrodes. It was suggested that high refractive index nanoparticles function as anti-reflective nanostructures, increasing the amount of light reaching the active material. In particular, the performance enhancement correlates strongly with the decrease in reflectance. The effect was experimentally demonstrated for hematite and bismuth vanadate ( $\text{BiVO}_4$ ) photoelectrodes, and simulation suggested that a constant enhancement, correlated with the decrease in reflectance, can be expected irrespective of the charge transport and electricity to fuel conversion properties of the bare electrode.

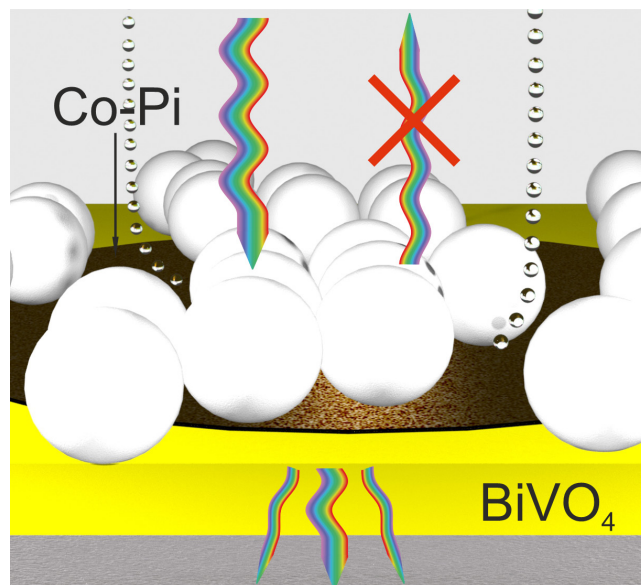


Fig. 3:  $\text{TiO}_2$  nanoparticles deposited on a photoanode (here  $\text{BiVO}_4/\text{Co-Pi}$ ) can enhance the performances under front illumination by reducing the reflection losses.

The tools developed in this project are expected to improve the design of photoelectrodes based on nanostructuring and optical nanoparticles, with the goal of decreasing the cost of hydrogen produced.

## References

- [1] L. Driencourt, B. Gallinet, C. E. Housecroft, S. Fricke, E. C. Constable, Modeling Enhanced Performances by Optical Nanostructures in Water-Splitting Photoelectrodes. *J. Phys. Chem. C* 125, 7010–7021 (2021)
- [2] L. Driencourt and B. Gallinet, Design Guidelines for Enhanced Activity of Water Splitting Photoelectrodes with Plasmonic Nanoparticles, *J. Phys. Chem. C* 126 (4), 1701–1710 (2022)
- [3] L. Driencourt, B. Gallinet, C. E. Housecroft, S. Fricke, E. C. Constable, High refractive index dielectric nanoparticles for optically enhanced activity of water-splitting photoanodes. *ChemPhotoChem* n/a, (2021)

# XMCD reveals magnetic frustration of spin and angular moments in Fe atom containing kagome networks

Project P1602: Self-assembly and magnetic order of 2D spin lattices on surfaces

Project Leader: T. A. Jung and J. Dreiser

Collaborators: M. Heydari (SNI PhD Student), M. Hua, N. Lin

Geometrically frustrated magnets have been intensely studied in both theoretical and experimental efforts for the past decades [1,2]. Among different magnetic systems which show geometrical frustration, kagome antiferromagnets are known as promising systems to study magnetic frustration due to their smaller coordination number compared to e.g. triangular systems [3]. The small number of natural materials with kagome antiferromagnetic configurations has limited experimental studies of these system [4]. 2D-metal organic frameworks (2D-MOFs) offer a rich platform to engineer kagome structure and have been shown to exhibit exotic magnetic phases. In this work we synthesize an iron based two dimensional metal organic network on Au(111). After characterizing the sample by scanning tunneling microscopy, we investigated its magnetic properties by means of X-ray absorption spectroscopy and X-ray magnetic circular dichroism.

Two-component networks were prepared on Au(111) substrates at room temperature under UHV conditions ( $p = 10$ - $10$  mbar). Subsequent to deposition of benzenehexol and Fe, samples were annealed at  $T = 160^\circ\text{C}$  for 10 min and characterized by room temperature scanning tunneling microscopy (Fig. 1a). In the specific example given, the coordination network covered approximately 30% of the surface area.

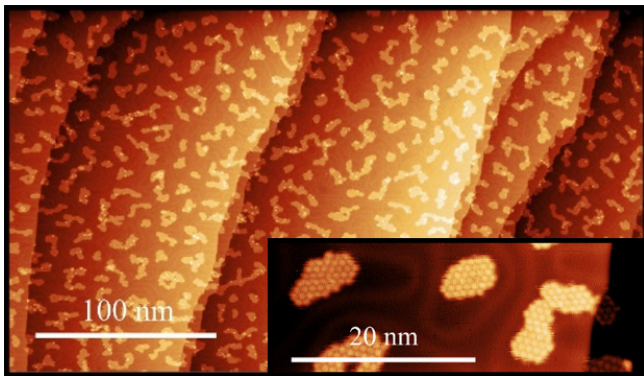


Fig. 1: Morphology of the Fe-benzenehexol containing Kagome network. STM micrograph ( $T = 300$  K) of the coordination network. ( $U = 1$  V,  $I = 100$  pA)

Figure 2a shows the normalized X-ray absorption spectra (XAS) taken with circularly (+/-) polarized light at  $T = 2.5$  K and  $B = 6.8$  T at the Fe  $L_{2,3}$  edges. All spectra were recorded in total electron yield mode, and they were normalized to the difference between edge and pre-edge in the sum of the spectra with the two circular polarizations at the  $L_3$  edge.

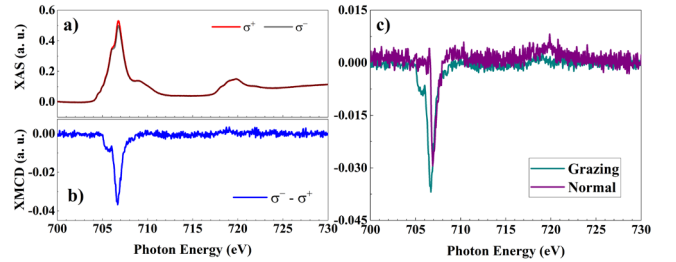


Fig. 2: XAS/XMCD spectra recorded at the Fe  $L_{2,3}$  edges with  $T = 2.5$  K and  $B = 6.8$  T. a) Circularly polarized X-ray absorption spectra, b) X-ray magnetic circular dichroism spectra all recorded in grazing angle and c) angle dependent X-ray magnetic circular dichroism spectra for the two incident angles of  $\theta = 0^\circ$  and  $60^\circ$ .

Both Fe absorption spectra as shown in figure 2a exhibit two absorption peaks at the Fe  $L_3$  edge with an energy difference of about 0.7 eV at 706.1 and 706.8 eV. Assigning the peaks to the specific transitions/oxidation states of the ions is not easily possible without proper simulations, because XAS spectra are highly dependent on changes in the ligand field. It is that spin-orbit and electron-electron interactions are of the same order of magnitude with ligand field effects for Fe and most of the transition metal ions. In the present case, earlier DFT work evidences the presence of Fe(II) in high spin ( $S=2$ ) state [4].

X-ray magnetic circular dichroism (XMCD) for both normal and grazing incidence of the x-rays is shown in figure 2c. The very similar absorption spectra for the two different circular polarizations corresponds to a weak XMCD signal. This indicates a weak magnetic response of the system, which, according to the sum rule analysis (Table 1), suggests a small value for the total magnetic moment of the Fe atoms in the coordinated network of a fraction of a Bohr magneton for both normal and grazing incident angles.

Table 1. Expectation values of orbital ( $Lz$ ) and spin ( $Sz$ ) angular momentum operators obtained from sum rule analysis of XMCD data at  $T = 2.5$  K and  $H = 6.8$  T.

	$\theta = 0^\circ$	$\theta = 60^\circ$
$\langle S_{z_{\text{eff}}} \rangle$ [ $\hbar$ ]	0.06 (0.1)	0.06 (0.1)
$\langle Lz \rangle$ [ $\hbar$ ]	0.02 (0.2)	0.05 (0.2)
$\langle Lz/S_{z_{\text{eff}}} \rangle$	0.33	0.83
$\langle M \rangle$ [ $\mu\text{B}$ ]	0.11 (0.3)	0.18 (0.3)

The weak magnetic response of the Fe atoms on the surface can be explained by antiferromagnetic (AFM) coupling of the Fe atoms in the network and implies the frustration of a significant share of the magnetic moments in the kagome lattice. Another possibility is that the magnetic moments of the Fe atoms have slightly deviated from their staggered, AFM coupled configuration in favor of aligning with the magnetic field. This would be expected for a Fe-Fe exchange coupling of moderate strength, which is still largely dominating the Zeeman interaction.

XMCD recorded at grazing incidence angle ( $\Theta = 60^\circ$ ) plotted in (Fig. 2d) shows a considerable change in the peak shape compared to the one taken at normal incidence ( $\Theta = 0^\circ$ ). For grazing incidence, the spectra show a broadened peak with a shoulder at lower energy. The difference between normal and grazing incidence spectra is a manifestation of linear dichroism, which in turn can have a magnetic origin as well as a structural origin.

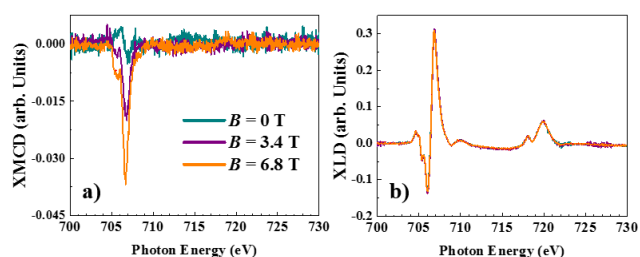


Fig. 3. XMCD/XLD spectra recorded at grazing incidence at the Fe  $L_{2,3}$  edges and at  $T = 2.5$  K. Field dependent a) XMCD signal and b) XLD signal.

Figure 3b shows x-ray linear dichroism spectra at the Fe  $L_{2,3}$  edges, calculated by subtracting intensities of linear horizontal and vertical polarized lights. The observation of the linear dichroism recorded at grazing incidence of the x-rays at the Fe  $L_{2,3}$  edges indicates an anisotropic charge distribution around the Fe atoms caused by the interaction of the Fe atoms with the benzenehexol ligands and the Au surface. The field-dependent XMCD and XLD signals for three different magnetic fields  $B = 0, 3.4$  and  $6.8$  T has been shown in figure 3a and b respectively. The XMCD signal is increasing by applying a higher magnetic field, which is in agreement with expectation. At zero magnetic field ( $B = 0$  T), there is virtually no dichroism, indicating that the net Fe magnetic moment along the magnetic field direction is zero within the detection limit and there is no remanence. The XLD signal is independent of the magnetic field for all three B-values. This reflects the fact that the linear dichroism is originating from charge distribution anisotropy and does not have a magnetic origin.

In summary, we have synthesized an Fe-based 2D metal-organic framework with high spin configuration of Fe(II) atoms and characterized it using scanning tunneling microscopy. We have investigated its magnetic properties by means of XMCD and XLD show that even at a temperature of 2.5 K, the system has a very weak magnetic response, much weaker than what is expected for free Fe(II) ions. We have also evaluated quantitatively the total magnetic moment in fractional value of a Bohr magneton per Fe atom using sum rule analysis. The low magnetic moment is assigned to the geometric frustration occurring in the kagome antiferromagnetic spin system.

## References

- [1] R. Moessner, A. P. Ramirez, Geometrical frustration. *Physics Today* 59, 24 (2007)
- [2] L. Anghinolfi, H. Luetkens, J. Perron, M. G. Flokstra, O. Sendetskyi, A. Suter, T. Prokscha, P. M. Derlet, S. L. Lee, L. J. Heyderman, Thermodynamic phase transitions in a frustrated magnetic metamaterial. *Nat Commun* 6, 8278 (2015)
- [3] D. J. J. Farnell, Emergence of magnetic order in kagomé antiferromagnets. *Front. Phys.* 14, 23302 (2019)
- [4] M. Hua et al. Highly Degenerate Ground States in a Frustrated Antiferromagnetic Kagome Lattice in a Two-Dimensional Metal–Organic Framework. *J. Phys. Chem. Lett.* 12, 3733–3739 (2021)

# Mesoscale dynamics of the nuclear pore complex transport channel

Project P1603: A mechano-optical microscope for studying force transduction in living cells

Project Leader: R. H. Y. Lim and E. Meyer

Collaborator: T. Kozai (SNI PhD Student)

## Introduction

The nuclear pore complex (NPC) is the sole gateway between the cytoplasm and nucleus in eukaryotic cells. Each NPC possesses numerous intrinsically disordered proteins that contain Phe-Gly repeats (also termed FG nucleoporins or FG Nups) that regulate biomolecular exchange. Collectively, the FG Nups function as a permeability barrier within the central channel of the NPC. However, structural characterization of the NPC interior has remained challenging. Here, we have resolved the dynamic behavior of the permeability barrier inside the central channel of isolated *S. cerevisiae* NPCs at millisecond timescales by high-speed atomic force microscopy (HS-AFM). Importantly, HS-AFM serves to capture dynamic FG Nup behavior with 2-3 nm lateral and 0.15 nm vertical spatial resolution [1].

## Structural characterization of isolated yeast NPCs

The entire structure of the isolated yeast *S. cerevisiae* NPC has been determined at sub-nanometre precision [2]. However, the dynamic behavior of FG Nups within the NPC channel remains elusive. In collaboration with Prof. Mike Rout (Rockefeller University), we have now visualized FG Nup dynamics inside isolated yeast NPCs for the first time. HS-AFM reveals isolated NPCs without and with cargoes “caught” in transit (known as central plugs, or CP) [3] (Fig. 1a-d), as also verified by cryo-electron microscopy (cryo-EM). Corresponding cross-sectional profiles reveal 8 protrusions that correspond eight distinct sub-complexes (or “spokes”) that enclose the central channel. Further analysis (Fig. 1e) shows that pore depths corresponds to the absence or presence of CPs (Fig. 1g). However, the diameter of the isolated NPC does not vary significantly between NPCs with and without CPs (Fig. 1f).

## Resolving FG Nup dynamic behavior within NPCs

We next focused on resolving FG Nup behavior within the NPC central channel. In vacant NPCs, the FG Nups were observed to dynamically and repeatedly extend into and retract from the pore interior (Fig. 2a). Nevertheless, the FG Nups occasionally bound to each other and formed transient entanglements. In order to quantify the dynamics of the FG Nups within the NPC, we first generated kymographs of HS-AFM data orientated radially around the central axis of the image (Fig. 2b). The kymographs were taken at intervals of one pixel from the radius of 0 nm (Fig. 2c). Second, autocorrelation functions (ACF) were computed from the kymographs (Fig. 2d), averaged and assembled into a single plot (Fig. 2e).

Short or a lack of correlation suggest fast/random movements, whereas long correlations suggest slow movements. Averaged ACF plots were fitted with exponential linear decay functions to estimate the average decay rates for all NPCs. The result of this analysis carried out over 17 NPCs is

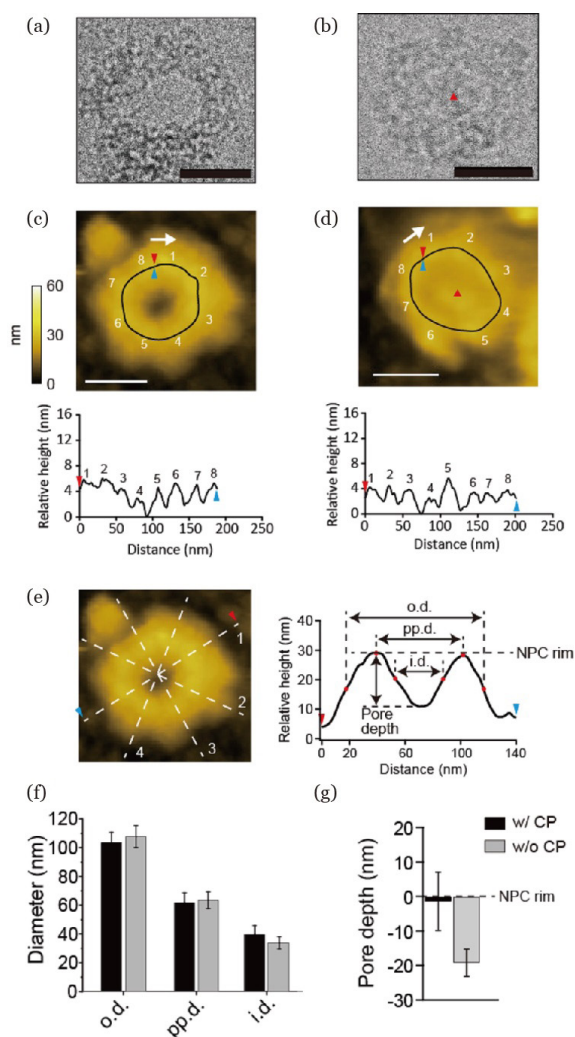


*Fig. 1: Representative Cryo-EM (a-b) and HS-AFM (c-d) images of isolated NPCs without (a and c) and with (b and d) CPs (red triangles). Eight spokes (numbered) can be resolved from the corresponding cross-sectional profiles (black lines). Scale bars, 50 nm. (e) NPC diameter was calculated by averaging over 4 different rotations (dashed-lines). Outer, peak-to-peak and inner diameters are given by o.d., pp.d. and i.d., respectively. Pore depth was measured from the NPC rim. These parameters correspond to the cross-sectional profile shown on the right panel. (f and g) Dimensional analysis summary.*

shown in figure 2f. This so-called onion map indicates that FG Nups dynamics is most rapid within the central region of the pore and slower near the periphery.

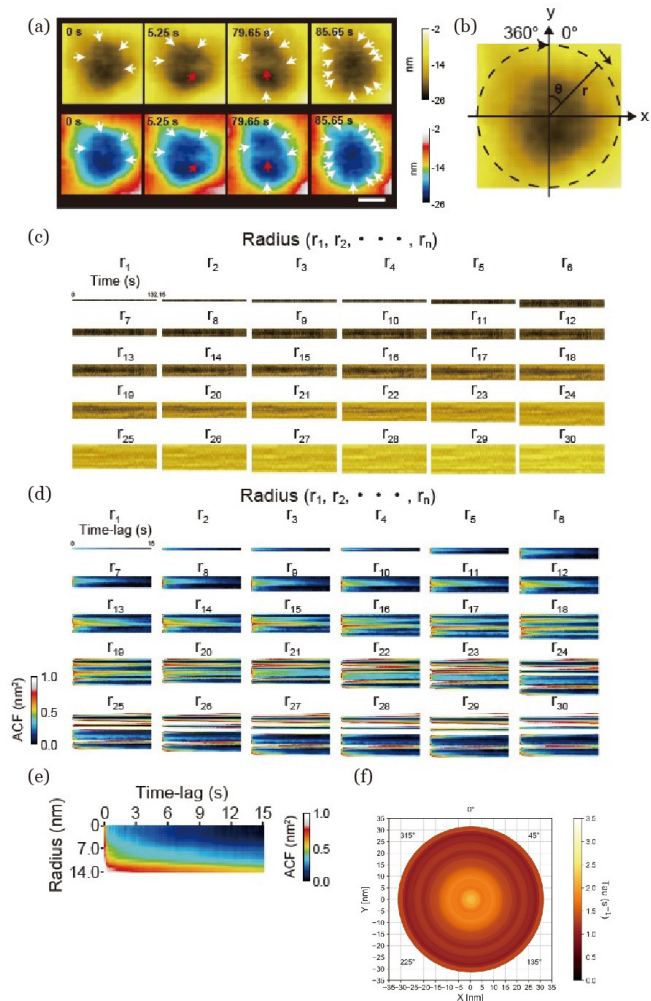


**Fig. 2:** a) FG Nup dynamics within vacant NPCs. The white and red arrows point to individual FG Nups and entanglement, respectively. Scale bar, 10 nm. b) Euclidean  $xy$  coordinate is assigned to each pixel placing the origin at the exact center of the image and the kymograph is taken along a circle with the center of the image. The circle has radius  $r$  and angle  $\theta$ . c) Kymographs taken at different radii at intervals of 1 pixel. The  $x$ - and  $y$ - axis represent time and radial angle, respectively. d) Autocorrelation function (ACF) maps computed from the kymographs. e) Reassembled ACF map after averaging over all ACF maps along the column. f) Averaged onion map of the decay rates estimated from all the reassembled ACF maps ( $n = 17$ ).

### Dynamic behavior of the central plug

Furthermore, we explored the dynamic behaviors of the CP and FG Nups within NPCs. FG Nups can be resolved in the non-obscured gaps between the CP and the NPC walls (Fig. 3a). Interestingly, the FG Nups show to interact with the CP dynamically and intermittently. The averaged ACF plots show long correlations in the gaps between the center of the CP and the inner walls (Fig. 3b). As in figure 2f, the onion map represents the decay rates averaged over the 9 NPC pores and indicates that the dynamics is faster in the central region and slower at the periphery (Fig. 3c).

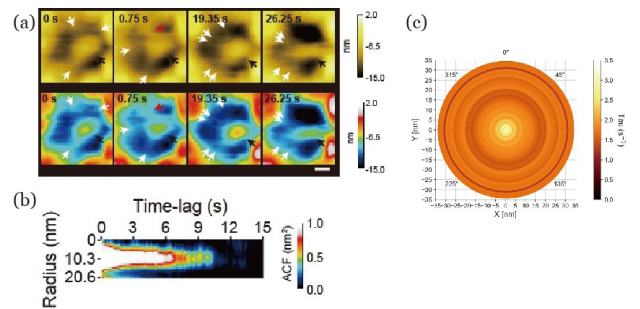


**Fig. 3** a) Dynamic behavior of CP and FG Nups. The white, red and black arrows point to FG Nups, entanglement and central plug, respectively. Scale bar, 10 nm. b) Reassembled ACF map after averaging over all ACF maps. c) Averaged onion map of the decay rates estimated from all the reassembled ACF maps ( $n = 9$ ).

### Summary

We have used HS-AFM to investigate the dynamic behavior of FG Nups within isolated yeast NPCs to reveal the molecular basis of the NPC permeability barrier. These findings have been further substantiated by HS-AFM analysis of NPCs isolated from  $\Delta$ FG mutant strains and Brownian dynamics (BD) simulations of the FG Nup dynamics in collaboration with Prof. Andrej Sali (UCSF) (data not shown).

### References

- [1] Y. Sakiyama, A. Mazur, L. E. Kapinos, R. Y. H. Lim, Spatiotemporal dynamics of the nuclear pore complex transport barrier resolved by high-speed atomic force microscopy, *Nature Nano.* 11, 719-724 (2016)
- [2] S. J. Kim, et al., Integrative structure and functional anatomy of a nuclear pore complex. *Nature* 555, 475-482 (2018)
- [3] D. Stoffer, K. N. Goldie, B. Feja, U. Aebi, Calcium-mediated structural changes of native nuclear pore complexes monitored by time-lapse atomic force microscopy. *J. Mol. Biol.* 287, 741-752 (1999)

# Hybrid biomimetic platforms based on amphiphilic block copolymers

Project P1604: Selective reconstitution of biomolecules in polymer-lipid membranes

Project Leader: W. Meier and U. Pielec

Collaborator: S. Di Leone (SNI PhD Student)

## Introduction

Artificial membranes, as materials with biomimetic properties, can be applied in various fields, such as DNA sequencing, screening and bio-sensing [1]. The solvent-assisted method (SA) represents a straightforward method to prepare lipid solid-supported membranes [2]. The SA method involves three basic steps: i) the deposition of amphiphilic molecules dissolved in a water-miscible organic solvent (e.g. ethanol, isopropanol) onto a solid surface, ii) the exchange of the organic phase into aqueous phase, which triggers the self-assembly process and iii) the planar membrane formation once the system reaches equilibrium. SA is versatile, rapid and allows for real-time monitoring. However, it has not yet been applied to create artificial membranes based on amphiphilic block-copolymers, which possess enhanced mechanical stability and chemical versatility compared to lipid-based membranes and bio-compatible properties.

In the first part of this project, we applied the SA method for the first time on different amphiphilic di- and triblock poly(dimethylsiloxane)-block-poly(2-methyl-2-oxazoline) (PDMS-b-PMOXA) copolymers (Fig. 1).

lo-enzyme (ADAse) and a DNA strand were parallel combined with the polymer membranes to create a bio-active platform. To prove the accessibility of the ADAse after the anchoring, its catalytic activity was monitored over time [3].

The second part of the project focuses on the application of SA method on hybrid mixture for preparing hybrid supported membranes. The term hybrid in this case refers to the blending of PDMS-b-PMOXA copolymers and phospholipids commonly found in cell membranes (e.g. 1,2-hexadecanoyl-sn-glycero-3-phosphocholine (DPPC), 1-palmitoyl-2-oleoyl-sn-glycero-3-phosphoethanolamine (POPE), Sphingomyelin (SM), and 1,2-dioleoyl-sn-glycero-3-phosphoethanolamine-N-(glutaryl) (NGPE)). Poly(butylene oxide)-block-poly(glycidol) (PBO-b-PG) was also employed for the preparation of polymer-lipid hybrid membranes, due to its higher hydrophilicity compared to PDMS-b-PMOXA. With this study we wanted to evaluate the determining factors for the formation of a hybrid membrane onto a solid support and then optimize the conditions for various polymer-lipid hybrid mixtures.

## Materials and Methods

Quartz crystal microbalance with dissipation (QCM-D) was utilized to monitor the real-time kinetics of membrane formation depending on concentration and polymer composition and then to estimate the membrane quality via BSA adsorption. Atomic force microscopy (AFM) and force spectroscopy (FS) were employed to characterize the morphology and viscoelastic properties of polymer and hybrid membranes. Fluorimetry was used to evaluate the activity of the enzymes after the combination with the membrane.

## Result and discussion

QCM-D measurements showed that the SA method was able to form membranes when polymer of different PDMS block length were employed, and those membrane presented a thickness in accordance with the results reported in literature [4]. AFM and FS were crucial for determining the membranes morphology and mechanical properties. It was found that the membranes had high roughness due to the presence of island structures on the adlayer. Those islands represent inverted micelles and worm-like assembly embedded in the polymer membrane matrix and characterized by a higher softness and dimension dependent from the PDMS block length. The anchoring of ADAse with the membrane was quantified with QCM-D and optimized in order to obtain the maximum amount of enzyme. Then, we evaluated the catalytic activity of the enzyme after the combination, by observing the conversion of a coumarine substrate into a fluorescent species. In this specific case, we evaluated and compared the activity of two different ADAses: the wild type (WT) and the mutant (YR). The fluorescence that was detected for either WT or YR, anchored on the polymer mem-

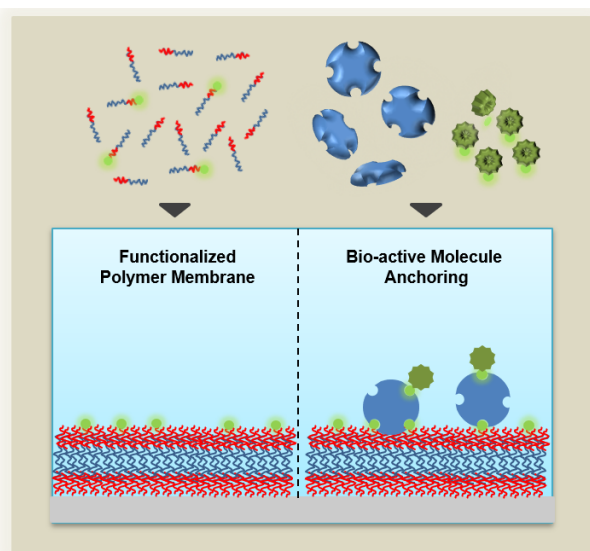


Fig. 1: Schematic representation of polymer membrane formation through SA method and selective combination with biomolecules for the development of bio-active surfaces.

We optimized the conditions to prepare polymer membranes on a solid support. Then, we inserted into the polymer membrane a biotin end-group functionalization to improve the chemical versatility of the system. More specifically, the membrane is amenable to anchor biomolecules by the specific biotin/streptavidin interactions. An artificial metal-

brane, correlated well with the trends observed in solution. YR displayed a higher catalytic activity compared to wild type both in solution and when attached to the membrane. The values of the converted substrate after 48 hours for the experiments reported was estimated at 5 and 7 ng for the YR mutant (for the membrane- and in solution-ADase respectively) compared to 2 and 4 ng for the wild type ADase (Fig. 2).

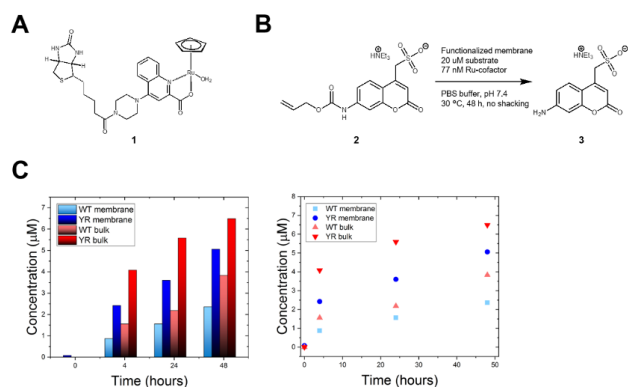


Fig. 2: Schematic representation of the ruthenium-cofactor (A) and deallylation reaction (B); bar chart of the substrate converted with the catalysis performed by the ADase. Wild type (WT) and mutant (YR) ADase over time comparison in bulk or attached onto functional membrane (C).

For the second part of the project, AFM characterization provided information on the hybrid membrane formation by SA method (Fig. 3). A comparison between a good quality membrane (high membrane coverage and clear phase separation) and a poor-quality (defective-containing membrane) indicated significant differences in the morphological characteristics and assembly for the two polymer-lipid mixtures. In PMOXA89-PDMS10:NGPE hybrid membranes a clear phase separation was visible, with darker areas representing clusters of lipids entrapped within a polymer matrix. On the contrary, when POPE was mixed with PDMS-PMOXA or PBO-PG block copolymers we observed defects and big protrusions membrane components which in our case are the copolymer parts. We observed incomplete membrane formation and presence of several islands or “fused vesicles” with height values between 15 and 30 nm. Thus, POPE is an insufficient candidate for the preparation of biomimetic membrane platforms via SA method.

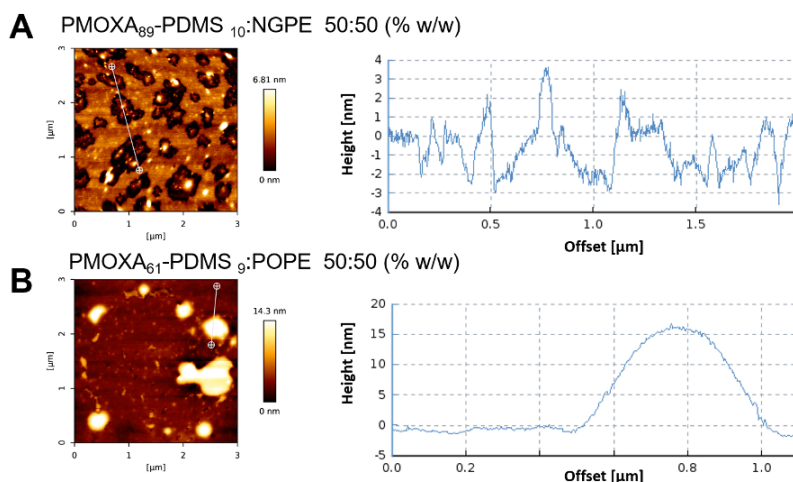


Fig. 3: AFM height image comparisons between membranes with good quality in terms of coverage and phase separation (A) and defected membranes (B) obtained with SA method.

## Conclusions

The combination of artificial membranes with biomolecules has high potential for the development of bio-interfaces with desired properties, given by the specificity of the biomolecules. We applied for the first time the solvent-assisted method to PDMS-b-PMOXA diblock and triblock copolymers to form polymer porous membranes highly reproducible, regardless of the hydrophobic block length or the structure of the polymer used. Polymer membranes obtained in this way present biocompatibility and good mechanical resistance, and can be employed as biomimetic platforms in different fields of application. In the first specific case, the biotin functionalization of the polymer increased the versatility of the system. Then we extended the SA method on the preparation of solid-supported hybrid membranes composed of polymer and lipids. Particularly, we looked at lipid-polymer domain separation, average thickness and characteristic assemblies of the hybrid membrane. This takes us one-step further towards the understanding of the molecular parameters and the appropriate conditions for the fabrication of advanced hybrid membranes with dual functionality with specificity for the lipidic and the polymeric domains.

## References

- [1] A. Krywko-Cendrowska, S. di Leone, M. Bina, S. Yorulmaz-Avsar, C. G. Palivan, W. Meier, Recent Advances in Hybrid Biomimetic Polymer-Based Films: from Assembly to Applications. *Polymers*, 12(5), 1003 (2020)
- [2] S. R. Tabaei, J.-H. Choi, G. H. Zan, V. P. Zhdanov, N.-J. Cho, Solvent-Assisted Lipid Bilayer Formation on Silicon Dioxide and Gold. *Langmuir*, 30, 34, 10363–10373 (2014)
- [3] S. Di Leone, J. Vallapurackal, S. Yorulmaz-Avsar, M. Kyropoulou, T. R. Ward, C. G. Palivan, W. Meier, Expanding the Potential of the Solvent-Assisted Method to Create Bio-Interfaces from Amphiphilic Block Copolymers, *Biomacromolecules*, 22, 7, 3005–3016 (2021)
- [4] F. Itel, A. Najer, C. G. Palivan, W. Meier, Dynamics of Membrane Proteins within Synthetic Polymer Membranes with Large Hydrophobic Mismatch, *Nano Lett.*, 15, 6, 3871–3878 (2015)

# Smart peptide nanoparticles for efficient and safe gene therapy

Project P1606: Smart peptide nanoparticles for efficient and safe gene therapy

Project Leader: C. G. Palivan and J. Benenson

Collaborator: S. Tarvirdipour (SNI PhD Student)

## Introduction

Gene delivery systems encounter several membrane barriers on their way to successful gene therapy. Hence, non-specific uptake, insufficient targeting, inability to escape endosomes, and inefficient nuclear delivery of non-viral delivery systems hinder their application [1,2]. As the nucleus is a key target in diseases derived from gene mutations, crossing the nuclear membrane is vital non-viral vectors need for delivering DNA to the final destination [1].

Nuclear localization signals (NLS) allow nuclear targeting of non-viral delivery systems and facilitate translocation of cargo through the nuclear pore complex (NPC). This mechanism involves complex formation of NLS with karyopherins (kaps), predominantly  $\text{kap}\beta$  and  $\text{kap}\alpha$  which acts as import receptor for NLS and lead to multivalent binding interactions with phenylalanine-glycine-rich nucleoporins (FG-Nups). Once the ternary import complex importin  $\beta/\alpha$ /NLS interact with the FG-repeats of Nups, nuclear transport occurs in a RanGTP-regulated manner [3].

To overcome cellular barriers and translocate therapeutic DNA to the nucleus, we developed a novel nuclear targeting platform based on the self-assembly of an amphiphilic peptide comprising an NLS. The NLS-peptide (Fig. 1) was produced by introducing KRKR residues at the amino-terminus of HR)3gT, a recently reported nonNLS-peptide [4]. To achieve self-assembled multicompartiment micelles (MCMs) similar to those observed for nonNLS-peptide, we preserved the hydrophilic to hydrophobic weight ratio in the NLS-peptide.

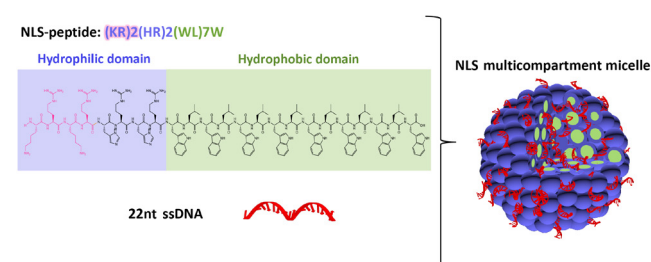


Fig. 1: Sequences of the amphiphilic NLS-peptide and schematic representation of DNA entrapped in NLS multicompartiment micelles (NLS-MCMs).

## Material and methods

NLS-peptide comprising 23 amino acids was synthesized on a rink amide resin, purified, and analysed by time-of-flight mass spectrometer (MALDI-TOF-MS) in the positive mode. The self-assembly of DNA loaded NLS-MCMs was achieved via the solvent exchange method [4].

To study nuclear translocation mechanism of NLS-MCMs, we measured the binding of  $\text{Kap}\beta 1 \bullet \text{Kap}\alpha \bullet \text{NLS-MCM}$  complexes to a phenylalanine-glycine-rich nucleoporin (FG-Nup) layer on a sensor chip by surface plasmon resonance (SPR). To reveal the fate of MCMs inside the cell at the ultra-structural level, ultra-thin serial sections of cell pellets were examined by transmission electron microscopy. Moreover, cells treated with NLS-MCMs were examined by confocal microscopy and the intracellular fate of the platform statistically analyzed by Imaris software.

## Results

SPR sensograms (Fig. 2) and consecutive langmuir isotherm analyses using a two-component fit demonstrated that  $\text{Kap}\alpha \bullet \text{Kap}\beta 1 \bullet \text{NLS-MCMs}$  increased the maximal binding responses to Nup214 (Rmax1 and Rmax2) compared to standalone  $\text{Kap}\alpha \bullet \text{Kap}\beta 1$  (Table 1). Notably, the binding of  $\text{Kap}\alpha \bullet \text{Kap}\beta 1 \bullet \text{NLS-MCMs}$  to Nup62 led to a much bigger increase in the maximal binding responses.

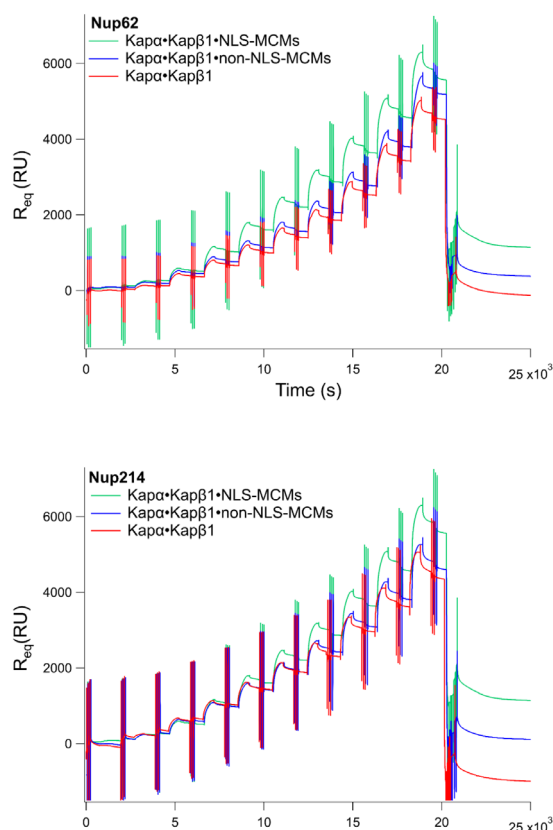


Fig. 2: SPR sensograms resolve the binding interactions of  $\text{Kap}\alpha \bullet \text{Kap}\beta 1 \bullet \text{NLS-MCMs}$ ,  $\text{Kap}\alpha \bullet \text{Kap}\beta 1 \bullet \text{nonNLS-MCMs}$ , and standalone  $\text{Kap}\alpha \bullet \text{Kap}\beta 1$  to Nup214 and Nup62.

Table 1. Maximal SPR response signals and equilibrium dissociation constants of nanocarrier/karyopherin complexes binding to Nups.

		R <sub>max1</sub> (RU)	R <sub>max2</sub> (RU)	K <sub>d1</sub> (nM)	K <sub>d2</sub> (nM)
Kapa-Kapβ1-NLS-MCMs	Nup214	3352.3+373	7599.7+1840	28.2+4.7	1183.5+652
	Nup62	2967.6+399	16295+1470	36.7+7.4	3387.6+4190
Kapa-Kapβ1-non-NLS-MCMs	Nup214	2723.3+415	5711.8+1480	23.2+5.5	954.8+647
	Nup62	2057.2+140	10201+1260	20.8+2.4	1423+332
Kapa-Kapβ1	Nup214	2672+387	5711.4+1850	19.4+4.8	1028.1+779
	Nup62	1895+229	7495.2+1420	22.4+5.7	1077.3+477

To reveal the fate of NLS-MCMs inside the cell, ultra-thin serial sections of cell pellets were prepared from HeLa-GFP treated with NLS-MCMs, and investigated by electron microscopy (Fig 3). NLS-MCMs accumulated at the cytoplasmic face of the nuclear envelope, often in association with NPCs and localized inside the nucleus.

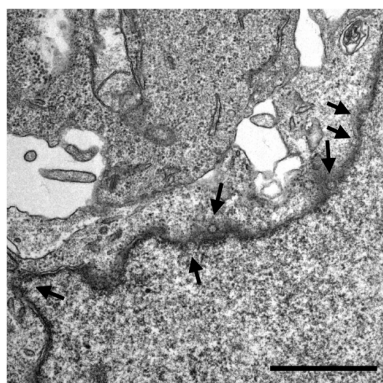


Fig. 3: Ultra-structural localization of DNA-loaded NLS-MCMs in cells. Electron micrographs reveal NLS-MCM accumulation at the nuclear envelope, associated with NPCs, and inside the nucleus. Scale bars, 1μm.

This data confirmed that KRKR residues function as NLS sequence and trigger the passage of NLS-MCMs through the nuclear pore complex into the nucleus.

Next, we statistically evaluated the nuclear accumulation of NLS-MCMs by treating HeLa-GFP cells with fluorescently labeled 22nt ssDNA-loaded NLS-MCMs. After 24 h of incubation, multiple z-stacks of cells were recorded by confocal microscopy and used for 3D reconstruction (Fig. 4A).

Subsequently, the number of NLS-MCMs associated with the nuclear membrane and inside the nuclei were determined (Fig. 4B). Statistical analysis revealed that there is a significant difference in nuclear localization of DNA-loaded NLS-MCMs compared to non-NLS-MCMs. The average number of DNA-loaded NLS-MCMs at the nuclear envelope and more importantly inside the nucleus was double the number of non-NLS-MCMs. Statistical analysis of MCMs in individual cell nuclei confirmed that NLS-MCMs move inside the nucleus over time. Our data suggest that NLS-MCMs are a promising platform for ferrying oligonucleotides to the nucleus.

### Conclusion

We developed DNA-loaded peptidic nano assemblies to direct DNA delivery to the cell nucleus. To this end, we integrated KRKR amino acid residues as NLS targeting moieties in the design of the amphiphilic (KR)<sub>2</sub>(HR)<sub>2</sub>gT peptide. Our SPR results confirmed that Kapa•Kapβ1 authenticates and binds NLS-MCMs and thereby enables binding of the resulting complex to specific FG Nups in order to efficiently transport particles through the NPC. Moreover, cellular studies demonstrated that KRKR residues are vital for trafficking multimicellar particles to the nucleus. The ease of producing peptide-based vectors through one-step self-assembly

besides the propensity for nuclear translocation of cargo, makes our platform an attractive candidate for delivering diverse genetic payloads.

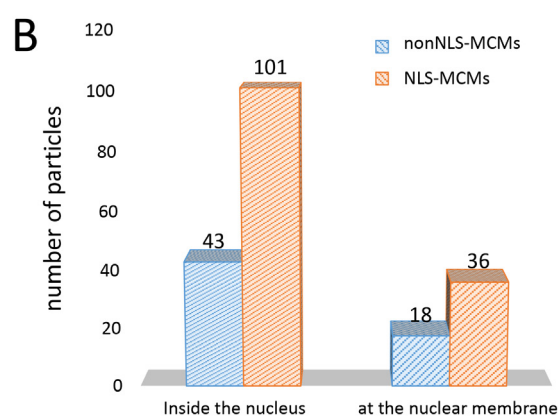
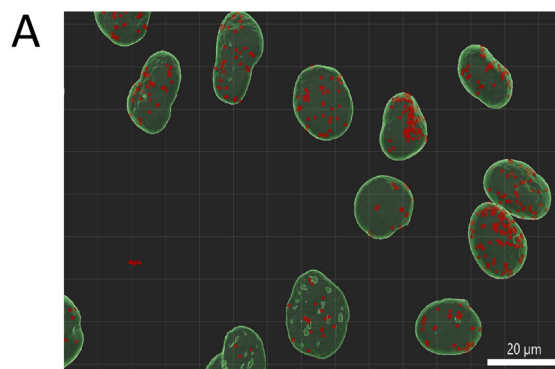


Fig. 4: A) Imaris 3D reconstructions from multiple confocal sections of HeLa-GFP cells treated for 24 h with DNA-loaded NLS-MCMs. NLS-MCMs are represented by red dots and the nuclear boundaries as green 'surfaces', based upon the fluorescence of the corresponding dyes. B) Statistical evaluation of NLS- compared to non-NLS-MCMs localized inside the nucleus and at the nuclear membrane after 24h by Imaris. Bars represent number of MCMs per nucleus.

### References

- [1] S. Tarvirdipour, V. Mihali, C-A. Schoenenberger, C. G. Palivan, Peptide-Assisted Nucleic Acid Delivery Systems on the Rise, *Int. J. of Mol. Sci.*, 22(16), 9092 (2021)
- [2] S. Tarvirdipour, X. Huang, V. Mihali, C-A. Schoenenberger, C. G. Palivan, Peptide-Based Nano-assemblies in Gene Therapy and Diagnosis: Paving the Way for Clinical application, *Molecules* 25, 3482 (2020)
- [3] C. Zelmer, L. P. Zweifel, L. E. Kapinos, I. Craciun, Z. P. Güven, C. G. Palivan, R. H. Y. Lim, Organelle-specific targeting of polymersomes into the cell nucleus, *PNAS* 117, 2770-2778 (2020)
- [4] S. Tarvirdipour, C-A. Schoenenberger, Y. Benenson, C. G. Palivan, A self-assembling amphiphilic peptide nanoparticle for the efficient entrapment of DNA cargoes up to 100 nucleotides in length, *Soft Matter* 16, 1678-1691(2020)

# Understanding phonon propagation in nanodevices

Project P1607: Understanding and engineering of phonon propagation in nanodevices by employing energy resolved phonon emission and adsorption spectroscopy

Project Leader: I. Zardo and C. Schönenberger

Collaborators: L. Gubser (SNI PhD Student)

## Introduction

During the last few decades, research has improved our knowledge and control over electrons and photons, enabling impressive advances for electronic and optoelectronic applications. The same degree of control is still lacking for phonons. The ability to manipulate phonons and phonon transport on a quantum level would lead to full control over heat flow in nanodevices. This could be used in the form of phonon transistors [1] or is also proposed as a building block for logic gates [2]. The main issue so far is that no phonon detectors exist that are comparably efficient to those for electrons. This is mostly due to the discrepancy between thermal and electrical insulators. The effectiveness of charge detection is based on low loss capacitors, where current can be accumulated to a measurable amount. The availability of very good electrical conductors as well as insulators makes this possible. For heat transport (i.e. phonons) this is very different. The range of thermal conductivity is much narrower, providing no good thermal insulators.

The goal of the project is twofold. First, efficient phonon emitters and detectors have to be developed. Those can then be used to investigate and engineer phonon band structure. To realize this, the tunneling through a double quantum dot will be modulated using bottom gates or inbuilt barriers.

## DQD phonon emitter/detector

The aim of this project is the realization of local phonon spectroscopy on the nanometer scale, using inelastic tunneling through the discrete energy levels of double quantum dots (DQD), converting electrons to phonons, or vice-versa, to investigate and thereby enable the engineering of phonon dispersions (Fig. 1). Inelastic tunneling takes place if the energy levels are detuned ( $\epsilon_1 \neq \epsilon_2$ ). The electron will then tunnel through the DQD emitting/absorbing a particle (a photon or a phonon) able to account for the energy difference. When  $\epsilon_1 > \epsilon_2$ , tunneling from QD1 to QD2 can only take place if such a particle is emitted. Hence, the device acts as a photon or phonon emitter (Fig. 1a). Analogously, when  $\epsilon_2 > \epsilon_1$ , tunneling from QD1 to QD2 can only take place if a particle is simultaneously absorbed. The device now acts as a detector (Fig. 1b).

Within the scope of this project we focus on a single DQD, configured as a phonon detector. The upper detection limit for phonon energies is given by the charging energy of each QD.

To move as close as possible to an ideal 1D system the diameter of the NWs should be as small as possible, as long as they can still be used for low temperature measurements. For this reason, the group of Lucia Sorba (NCR Nano, Pisa) provided InAs NWs with a diameter of 40 nm.

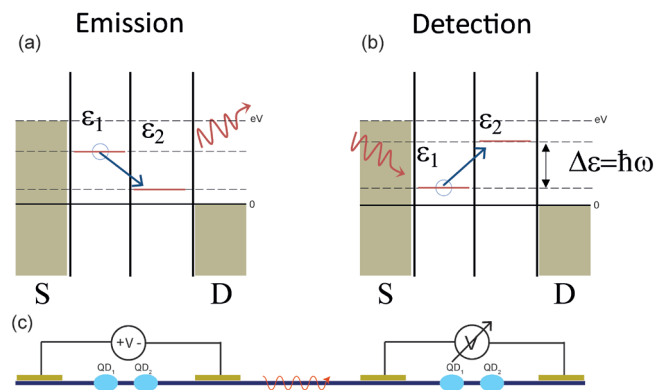


Fig. 1: a) Schematic illustration of a phonon emitter and detector b) using a double quantum dot system. Driven by a finite applied bias inelastic tunneling between the dots is used to either generate or detect phonons. c) Schematic of the aimed at final device. Inside the semiconducting nanowire (blue) two double quantum dots (light blue) are defined by local bottom gates (red). Phonons are then generated by an applied bias through source drain contacts (brown) in one DQD system, and detected by measuring the voltage in the second DQD system.

## Results

In order to perform phonon assisted transport experiments in a DQD, we have fabricated devices with implemented Joule heaters (Fig. 2). The heterostructure NW is electrically contacted by two Ti/Au electrodes (S/D), in order to enable electrical measurements of the DQD system. In addition to the S/D contacts, two side gates (SG1, SG2) and a Joule heater line are placed on opposite sides of the NW. Furthermore, we also fabricated devices covered by a  $\text{HfO}_2$  layer, employed to improve the thermal conductance between the Joule heater and DQD.

With these devices we could investigate the transport characteristics of a DQD formed in InAs/InP heterostructure NWs. Due to the large confinement provided by the in-situ grown InP barrier segments, the DQD confinement is preserved up to  $\approx 10$  K.

Figure 3a displays a DQD charge stability diagram at the  $(N, M) \rightarrow (N+1, M+1)$  transition, where  $N(M)$  describes the number of electrons occupying the left (right) QD,  $\epsilon$  the charge transfer axis, and  $\Delta$  the detuning axis. Coloured areas indicate regions, where a net current may be driven by an external heat source. Here the system is heated using a Joule heater electrode, driving an electrical current through the NW through either phonon assisted transport (PAT) or the thermoelectric effect (TE).

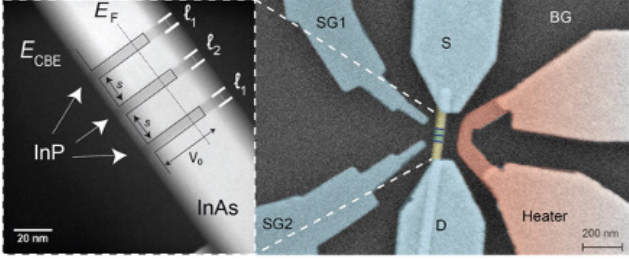


Fig. 2: False coloured SEM micrograph of a characteristic DQD device consisting of an InAs NW with three in-situ grown InP barriers that are connected to metallic contacts (S/D). Two side gates (SG<sub>1</sub>/SG<sub>2</sub>) in combination with the global back gate (BG) are employed to tune the QD energy levels. A constricted metal line is used as a Joule heater in an effort to locally heat the DQD. The inset shows a TEM image of such a three barrier heterostructure NW. Two QDs form in the InAs segments (length  $s \approx 17.5$  nm) which are encapsulated by the InP barrier segments (length  $l_1 \approx 5.5$  nm and  $l_2 \approx 6.8$  nm), due to a conduction band offset between the materials of  $V_0 \approx 400$  meV, as schematically overlaid on the TEM micrograph.

In an effort to isolate inelastic transport across the DQD, all measurements were executed at zero bias across the device. Measurements of ISD for different Joule heating powers are displayed in figure 3d and e using a device covered by an ALD HfO<sub>2</sub> layer. With the increased thermal conductance, a higher local phonon temperature (at the DQD region) is expected for similar heating powers. For the investigated triple point, as denoted by  $\epsilon$  and  $\Delta$ , signatures of TE transport are almost absent. The PAT signal for the indicated triple point in figure 3e shows almost a discontinuity along  $\Delta$ , with significant current only at large detuning values. This supports the importance of the excited state spectrum, modulating the PAT current, as the onset of PAT agrees well with excited state resonance, seen in bias spectroscopy measurement.

We compared these measurements with those obtained with devices without HfO<sub>2</sub> layer. By increasing the thermal conductance between the heater and the NW, thereby increasing the local phonon bath temperature  $T_{ph}$ , the heating power necessary to allow inelastic transport at  $\Delta \approx 1$  meV reduces by more than one order of magnitude. This clear dependence on  $T_{ph}$  within the NW DQD region clearly indicates phonon absorption as the dominant inelastic process. To further investigate the dependence of PAT on the applied heating power, an additional device (without oxide layer) is measured for a larger range of heating powers. In the detected  $I_{SD}$  we observe a sharp increase for a specific heating power. We attributed this increase to a sort of resonance with the flattening of the dispersion of the acoustic phonon modes, related also to the decrease of the sound velocity for these modes.

## Outlook

Progressing the project to its next stage would include the departure from a broad phonon source. While a second DQD within the same NW would perform well as phonon emitter, operating it would require two metal electrodes in contact to the NW, within the path of any emitted phonon. Using a superlattice excited by a pulsed laser as phonon transducer seems the more convenient approach.

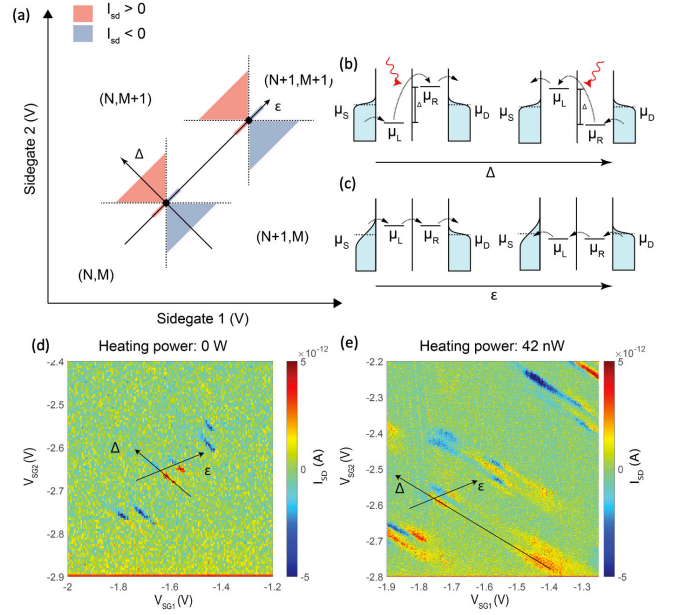


Fig. 3: Heat induced transport processes. a) Schematic illustrating heat induced current through the DQD system in absence of an external bias voltage, illustrated on a schematic of the DQD charge stability diagram at  $V_{SD} = 0$ . The charge on the left (right) QD are denoted by  $N(M)$  within each charge domain. Current may be induced through inelastic tunneling processes presenting themselves along the detuning axis  $\Delta$  or through thermoelectric transport which presents itself along the DQD charging axis  $\epsilon$ . b) Schematic illustration of inelastic transport along  $\Delta$ , where the QD energy levels are symmetrically detuned from the electrochemical potential in source (drain) ( $\mu_{S(D)}$ ). Electron transport from the occupied lower level to the unoccupied higher level is facilitated by absorption of either a phonon or a photon with the energy  $\Delta$ . Passing the triple point along  $\Delta$  inverts the QD level detuning and the current direction. c) Schematic illustration of thermoelectric transport through the DQD due to a temperature gradient between S and D. Charge polarity reverses as the QD energy levels pass  $\mu_{S(D)}$  along  $\epsilon$ . d) PAT in a DQD device covered with HfO<sub>2</sub>,  $I_{SD}$  as a function of the two side gates voltages ( $V_{SG1}$ ,  $V_{SG2}$ ) at a constant BG voltage of 0 V,  $T_{Bath} = 1.7$  K, and  $V_{SD} = 0$  for different Joule heating powers: d) no applied heating power and e) PH = 42 nW.

## References

- [1] B. Li, L. Wang, G. Casati, Negative differential thermal resistance and thermal transistor, Appl. Phys. Lett. 88, 143501 (2006)
- [2] L. Wang and B. Li, Thermal Logic Gates: Computation with Phonons, Phys. Rev. Lett. 99, 177208 (2007)

# Subgap quantum interference effects in mono-layer semiconductors with superconducting contacts

Project P1701: Van der Waals 2D semiconductor nanostructures with superconducting contacts

Project Leader: A. Baumgartner and C. Schönenberger

Collaborators: M. Ramezani (SNI PhD Student), I. Correa Sampaio, K. Watanabe, T. Taniguchi

## Introduction

The aim of this project is to establish two-dimensional layered semiconductors with superconducting contacts as a platform to investigate various new phenomena based on the interplay of superconducting electron pairing, electrically tunable electron densities, large spin-orbit and electron-electron interactions, or unique bandstructures and band topologies. In addition, one might gain more control over phenomena like Cooper pair splitting for entanglement generation, coherent transport in quantum dots, or Majorana bound states. Currently, one of the most promising examples of such layered semiconductors is molybdenum di-sulfide ( $\text{MoS}_2$ ) [1], for which we have recently developed superconducting MoRe vertical interconnect access (VIA) contacts with clear evidence of a superconducting energy gap and a weak to intermediate coupling strength between the superconductor and the semiconductor, which we extensively characterised at cryogenic temperatures and in large magnetic fields [2].

In this reporting period, we have developed superconducting contacts to InSe, another layered semiconductor, and have performed first optical experiments on single layer  $\text{MoS}_2$  (both not shown here). In addition, we have significantly improved the contact quality and yield in  $\text{MoS}_2$  electronic devices, which now allows us to investigate more interesting effects. In this report we focus on quantum interference effects specific to such superconductor hybrid structures.

## Materials and Methods

Figure 1a shows an optical microscopy image of an investigated device. The basic fabrication technique is described in Ref. [2] and results in a single layer  $\text{MoS}_2$  flake, sandwiched between two hexagonal boron nitride (hBN) layers, with a multilayer graphene below serving as a backgate. In addition to the recipe given in Ref. [2], we take special care to avoid, and in the worst case remove metal residues from the lift-off procedure, which results in a significantly improved reproducibility and a larger yield in the VIA contacts.

We have characterized this and similar devices in a dilution refrigerator with a base temperature of 60 mK, and in magnetic fields up to 8 T applied perpendicular to the sample plane.

## Results and discussion

Figure 1b shows the differential conductance  $G_{12}$  measured between contacts 1 and 2 as a function of the bias voltage  $V_{SD}$ , at the backgate voltage  $V_{BG} = 8$  V, while figure 1c shows the conductance in a colorscale plot as a function of  $V_{BG}$  and  $V_{SD}$ . Both figures show a strong increase in  $G$  for  $e|V_{SD}| > 2.3$  meV, which corresponds well to twice the superconducting energy gap  $\Delta$  of MoRe [2]. In contrast to earlier experiments [2], this finding suggests quasi-particle tunneling across two very

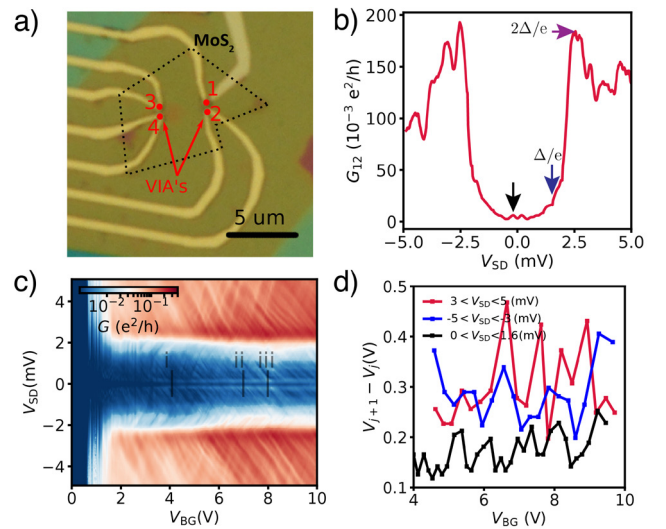


Fig. 1: a) Optical microscopy image of a  $\text{MoS}_2$  monolayer flake (shape outlined by the dotted black lines), fully encapsulated by two hBN layers and contacted by MoRe vertical interconnect access (VIA) contacts. b) Differential conductance  $G$ , measured in a two-terminal configuration between two contacts, plotted vs the bias voltage  $V_{SD}$  at a backgate voltage  $V_{BG} = 8$  V (position iii in Fig. 1c). Clearly visible is an increase in  $G$  for  $|V_{SD}| > 2\Delta/e$ . c)  $G$  vs  $V_{SD}$  and  $V_{BG}$  at  $B=0$ . The roman numerals indicate the gate voltages where the data in figure 2 were recorded. d) The spacing in bias between sequential resonances visible in Fig. 1c, plotted as a function of  $V_{BG}$  as extracted in the indicated bias voltage ranges. The black symbols correspond to subgap resonances, the blue and red to biases larger than the superconducting energy gap.

similar normal metal / superconductor (N/S) interfaces, illustrating a much better reproducibility of the individual VIA contact characteristics. Most importantly, in contrast to the previous report, we do not find Coulomb blockade characteristics anymore. Here, we now focus on quantum interference phenomena between two contacts at a distance of  $\sim 300$  nm. In figure 1c, we find a regular pattern of narrow resonances with an enhanced conductance. For biases much larger than  $2\Delta/e$ , these resonances can be well understood as constructive interference of the electron wave function propagating in opposite directions in a cavity, similar to Fabry-Pérot resonances in optics, with a slope (not shown) consistent with an effective mass of  $m^* \sim 0.6 m_{\text{free}}$ , only slightly smaller than reported before [1]. The spacing in bias between the resonances is plotted in figure 1d as a function of  $V_{BG}$ , extracted in three bias ranges, two for  $|V_{SD}| > 2\Delta/e$  (red and blue), and one for the resonances around zero bias (black), well in the subgap regime  $|V_{SD}| < \Delta/e$ . In spite of large variations, we find that the average spacing at low bias is roughly half of the spacing at large biases. In a single particle picture, this would suggest

a doubling of the cavity length for low biases. This finding is easily understood if we assume that this cavity is coupled directly to one superconducting contact and that the incoming electrons are reflected as holes in an Andreev reflection (AR) process. The hole needs to traverse the cavity, too, and to undergo another Andreev reflection into an electron, before constructive interference can occur with the original electron wave function. This process can be seen as doubling of the effective cavity length, or better as the formation of (non-interacting) Andreev bound states due to constructive interference of the electron and hole wave functions in the same cavity [3].

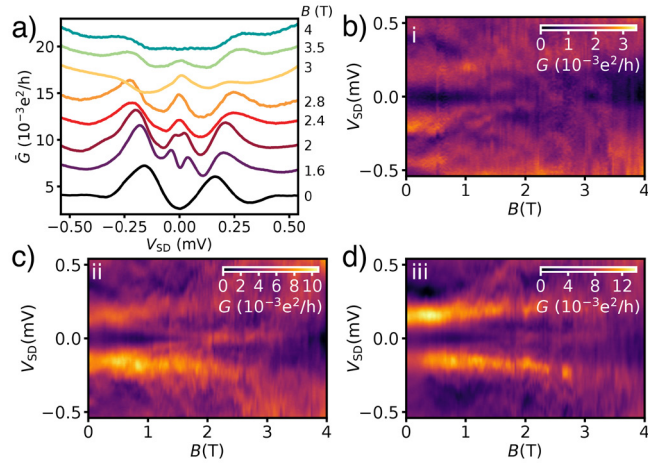


Fig. 2: a) Differential conductance  $\bar{G}$  averaged over a backgate voltage range of 0.4 V around  $V_{BG}=7$  V, plotted vs the bias  $V_{SD}$  for a series of magnetic fields between zero and 4T. b)-d)  $G$  (not averaged) vs  $V_{BG}$  and  $B$  at the gate voltages indicated in figure 1c.

In figure 2, we zoom into the low-bias regimes and find that at zero magnetic field, the conductance shows peaks around  $|eV_{SD}| \sim 140 \mu\text{eV}$ , clearly not related to the energy gap of bulk MoRe. With increasing magnetic fields, these peaks seem to split in energy, with two peaks merging at zero bias around  $B \sim 2$  T to form a single maximum that “sticks” to  $V_{SD} \approx 0$  for an extended magnetic field range. As shown in figure 2b-c, the overall field dependence is relatively independent of the gate voltage, reminiscent of the strongly debated Majorana bound states [4]. In our case, however, we can resolve a large number of resonances that are modulated in amplitude, constituting the observed broad peaks. The individual resonances are clearly not the same for different gate voltages. Similar zero-bias peaks were found before at zero magnetic field, and later interpreted as “reflectionless tunneling” [5], in which constructive interference of a multitude of potential Andreev processes due to backscattering at disorder near the superconducting contact results in a large total probability for AR. The process can be thought of as an electron/hole analogon of weak localization, which enhances the Andreev reflection at the end of the cavity near the superconductor. This constructive interference is lost when a bias or an external magnetic field are applied [5], which we indeed find in InSe devices (not shown). In contrast, in MoS<sub>2</sub>, we find the maximum conductance at finite biases for  $B=0$ , and zero-bias peaks only at large fields. This finding we tentatively attribute to the spin-orbit split bandstructure in MoS<sub>2</sub>, in analogy to weak anti-localization, in which a strong spin-orbit coupling results in the destructive interference of the single electron spin wave function at zero magnetic fields, lifted with increasing fields.

In conclusion, we have further improved the quality of the superconducting contacts to MoS<sub>2</sub>, which allows us to investigate non-interacting Andreev bound states due to Andreev reflection, and a series of subgap features, most prominently zero bias peaks that occur around magnetic fields of 2T, reminiscent of Majorana bound states - which, however, we attribute to reflectionless tunneling [5] and a strong spin-orbit interaction.

## References

- [1] R. Pisoni, et al. Interactions and magnetotransport through spin-valley coupled Landau levels in monolayer MoS<sub>2</sub>. Phys. Rev. Lett. 121, 247701 (2018)
- [2] M. Ramezani, I. Correa Sampaio, K. Watanabe, T. Taniguchi, C. Schönenberger, A. Baumgartner, Superconducting contacts to a monolayer semiconductor, Nano Lett. 21, 5614 (2021)
- [3] C. Jünger, A. Baumgartner, R. Delagrè, D. Chevalier, S. Lehmann, M. Nilsson, K. A. Dick, C. Thelander, C. Schönenberger, Spectroscopy of the superconducting proximity effect in nanowires using integrated quantum dots, Commun. Physics 2, 76 (2019)
- [4] V. Mourik, K. Zuo, S. M. Frolov, S. R. Plissard, E. P. A. M. Bakkers, L. P. Kouwenhoven, Signatures of Majorana Fermions in Hybrid Superconductor-Semiconductor Nanowire Devices, Science 336, 1003 (2012)
- [5] B. J. van Wees, P. de Vries, P. Magnée, T. M. Klapwijk, Excess conductance of superconductor-semiconductor interfaces due to phase conjugation between electrons and holes, PRL 69, 510 (1992)

# A 3D nanofluidic device for rapid and multiplexed diagnosis: SARS-CoV-2 and Influenza antibody detection

Project P1702: Single organelle size sorting by a nanofluidic device

Project Leader: Y. Ekinici and R. H. Y. Lim

Collaborators: T. Mortelmans (SNI PhD Student), X. Li, T. Braun

## Research context

In 2019, a previously unknown pathogen, SARS-CoV2, infected numerous people in Wuhan, China, giving rise to the severe respiratory syndrome COVID-19 and sending the world into a medical and economic crisis [1,2]. In various fields, research developments went ahead at an unprecedented rate and scale to develop scientific solutions to fight the pandemic.

Currently, accurate diagnostic testing is primarily performed in a clinical setting, where either a nasal swab or blood sample is taken by a clinician and sent for further testing in a biosafety level 2 facility. Here, trained medical personnel characterizes the biospecimen mostly with respect to either COVID-19 related genetic material or COVID-19 associated antibodies with a PCR or ELISA-test, respectively [3]. In light of this cumbersome procedure, there are clear benefits to the development of a device that can provide this information rapidly and cost-effectively without the need for specialized laboratories. The proposed sensor uses fluorescence as a readout mechanism, rendering it highly sensitive and, because of advances in mobile microscopy, could in the future be compatible with smartphone-based read-out systems [4]. This makes it applicable in resource-limited environments. Innovative testing solutions are even more needed taking into account that 30.8% of all COVID-19 infections are asymptomatic [5] and previously commercialized lateral flow-based rapid tests have limited sensitivity and only provide binary information (yes/no) on a possible previous infection [6,7].

## Results and discussion

To address the aforementioned shortcomings of alternative antibody tests, we introduce a three-dimensional (3D) nanofluidic sensor that can size-dependently immobilize nanoparticles at predefined locations enabling pre-concentration and multiplexed detection of antibodies. The fabricated nanofluidic device was designed to contain only passive capillary microfluidic components to control the fluid flow without the need for external loading mechanisms, such as syringe or pressure pumps. This makes the device easy in operation and versatile in applications. As a proof-of-principle experiment to demonstrate the trapping capabilities of the device, a particle mixture consisting out of five different fluorescent polystyrene calibration grade particles was loaded into the device solely through capillary forces. Due to the 3D wedge profile in the device, particles are immobilized at different positions along the wedge depending on their size, giving rise to distinct trapping lines (Fig. 1). We show that it's possible to trap particles down to sub-micron size ranges.

As a next step, we have used the immobilization properties of our nanofluidic device to trap particles which were functionalized with the receptor binding domain of the spike-protein of SARS-CoV-2. Prior to device loading, these

particles were firstly mixed with varying concentrations of anti-spike antibodies. These will bind to the spike protein on the bio-functionalized particles. To visualize this binding, we have added fluorescent detection antibodies. As such, the larger the bead's fluorescence, the larger the concentration of SARS-CoV-2 antibodies on top of the beads' surface. Hereafter, the particles were loaded into the 3D device and imaged with fluorescence microscopy (Fig. 2). It was seen that the fluorescence of the particles correlated very well with the concentration of anti-spike antibodies. It was estimated that the limit-of-detection (LOD) of the developed assay is 0.8 nM. As a comparison, recent literature has shown that the average COVID-19 patient will produce between 9.6 – 28 880 nM of this specific antibody, showing that the developed sensor operates within the relevant physiological concentrations [8].

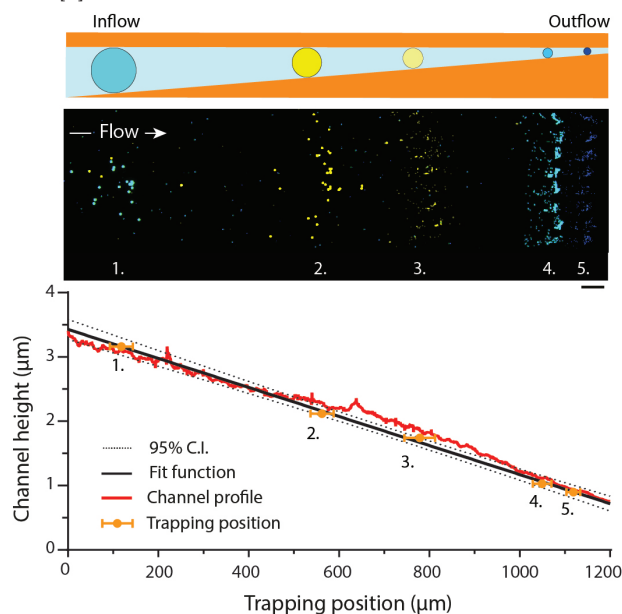


Fig. 1: Size-dependent particle trapping of fluorescent polystyrene calibration beads in a capillary-driven 3D nanofluidic device.

It should be mentioned that the LOD experiments were performed with immunoglobulin G-antibodies, which are representative of the late-stage immune responses upon disease infection. However, during the early stages, the immune response is primarily dominated by antibodies of the immunoglobulin M sub-type. Therefore, it is of importance to perform concurrent detection of both antibody types. To do so, we have developed color-based multiplexed detection to enable detection of both antibody types on a single particle, while simultaneously evaluating device function with calibration bead particles (Fig. 3).

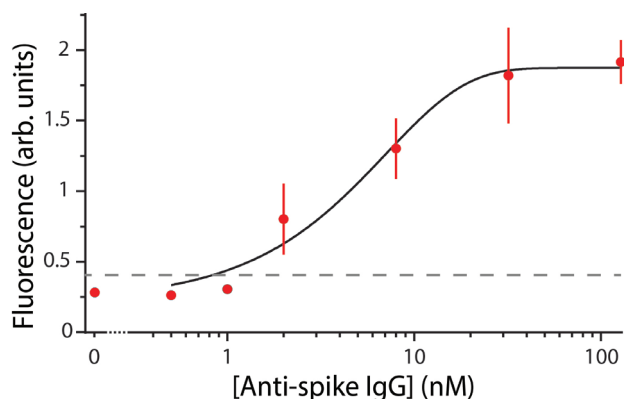


Fig. 2: Limit-of-detection of COVID-19 IgG antibodies in the nano-fluidic device.

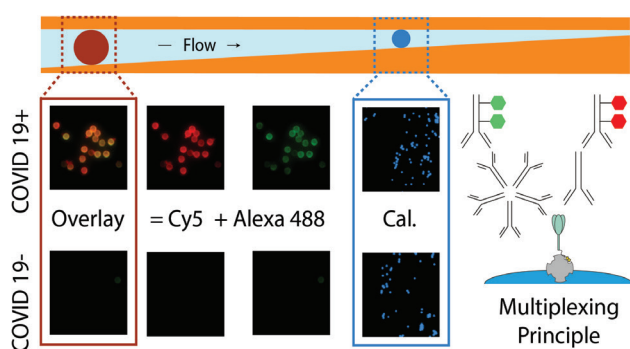


Fig. 3: On-bead color multiplexed detection of different COVID-19 antibody subtypes. The scale bar represents a length of 10  $\mu\text{m}$ .

In addition to on-particle multiplexed detection of different antibody subtypes against the same disease, we have leveraged the size-sorting properties of the device to perform disease-specific antibody detection on different particle sizes (results not shown). To do so, we have used smaller nanoparticles which were functionalized with an Influenza A surface protein. This disease is symptomatically very similar to COVID-19 but requires different treatment. It is therefore of importance to rapidly make the correct disease diagnosis to ensure proper patient care [9]. We have used these smaller particles in conjunction with the larger SARS-CoV-2 functionalized particles to rapidly distinguish between antibody types in a proof-of-principle setting.

In conclusion, we have introduced a novel and innovative approach towards multiplexed antibody and disease testing by using a unique 3D PMMA-based nanofluidic device. The presented results pave the way for the device to be applied in the point-of-care diagnostics setting, but also in the research lab setting where in-depth qualitative immunological characterization of human serum is needed. For future research, we aim to make the device compatible with more complex bio-fluids, such as whole blood, to further increase its versatility and applicability. Moreover, we aim to adapt the device operation principle to decrease the time needed for signal readout, while maintaining the same degree of specificity and sensitivity. Also, we plan to perform device fabrication in a foundry facility to increase its cost-effectiveness and scalability, enabling possible commercialization of the developed technology.

## References

- [1] P. Zhou et al. A pneumonia outbreak associated with a new coronavirus of probable bat origin. *Nature* 579, 270–273 (2020)
- [2] A. E. Gorbalenya et al. The species Severe acute respiratory syndrome-related coronavirus: classifying 2019-nCoV and naming it SARS-CoV-2. *Nat. Microbiol.* 5, 536–544 (2020)
- [3] M. Lipsitch, R. Kahn, M. J. Mina, Antibody testing will enhance the power and accuracy of COVID-19-prevention trials. *Nat. Med.* 26, 814–817 (2020)
- [4] Y. Sung, F. Campa, W.-C. Shih, Open-source do-it-yourself multi-color fluorescence smartphone microscopy. *Biomed. Opt. Express* 8, 236–247 (2017)
- [5] H. Nishiura et al. Estimation of the asymptomatic ratio of novel coronavirus infections (COVID-19). *Int. J. Infect. Dis.* 94, 154–155 (2020)
- [6] G. Guglielmi, Rapid coronavirus tests: a guide for the perplexed. *Nature* 590, 202–205 (2021)
- [7] R. Rubin, The Challenges of Expanding Rapid Tests to Curb COVID-19. *JAMA - J. Am. Med. Assoc.* 324, 1813–1815 (2020)
- [8] X. Tan et al. Rapid and quantitative detection of SARS-CoV-2 specific IgG for convalescent serum evaluation. *Biosens. Bioelectron.* 169, (2020)
- [9] B. Alhalaili, I. N. Popescu, O. Kamoun, F. Alzubi, Coronavirus 2019-nCoV and Other. *Sensors* 20, 1–45 (2020)

# Engineering mechanical properties of protein binders

Project P1704: Evolving protease enzymes with new sequence specificity using peptide-hydrogel cell encapsulation

Project Leader: M. Nash and S. Reddy

Collaborator: J. López Morales (SNI PhD Student)

Rational design of proteins coupled to artificial directed evolution can adjust the course of natural evolution to obtain the desired properties in a protein. Binding to targets of clinical interest is one of the most needed properties. In this project, we selected a cell receptor called programmed death ligand 1 (PDL1 or CD274) as the bait to the engineered binder. This receptor is overexpressed in cells from different types of cancer and helps them to evade the immune system from eliminating spreading cancer cells [1]. PDL1 is an essential target for immunotherapy against aggressive cancers. The most important binders to PDL1 in such therapy are anti PDL1 antibodies. These, however, can suffer from induced dissociation from metastatic cancer cells if subjected to mechanical stresses in the bloodstream. Currently, there is no antibody or scaffold that can alleviate this need.

Therefore, we are studying the evolvability of an alternative scaffold to develop mechanostable antibody mimics that bind to PDL1 under shear stress. These antibody mimics are based on a bacterial cohesin domain (Coh7) that is highly resistant to chemical, thermal and mechanical denaturing forces. We are rationally engineering the scaffold by a bioinformatic- and biophysics-guided approach to select and engineer a pair of loops in Coh7 that is amenable to random mutagenesis for a synthetic library of scaffolds with potential binding to PDL1. As a first step, a Solvent Accessible Surface Area (SASA) scan was carried out through the crystal structure of Coh7 (PDB ID: 1AOH) using a model sphere of water with a solvent radius = 1.4 Å on the ProtSA server [2]. The SASA of every residue was ranked across the whole protein sequence and focused on the loops across the protein structure (Fig. 1a). Four loops were selected and underwent structural analysis. Two opposing loops in the same region of Coh7 were selected based on proximity. The loops are at least 6 AAs long and contain at least 5 highly SASA ranked residues. The residues 86GTGAY90 in Loop 6-7 and 126NNDLV130 in Loop 8-9 create a cavity amenable to mutagenesis and form overall a clamp-like surface that seems suitable for conferring binding ability (Fig. 1b).

Once the loops were selected and target residues were identified, a deeper analysis of the residues was applied to determine the mutational tolerance of the scaffold. The analysis was run on the PredictSNP server, which is a consensus classifier of computational tools for predicting the effects of amino acid substitution. It predicts whether a particular substitution is neutral or deleterious for protein function based on various parameters derived from the evolutionary, physicochemical, or structural characteristics [3].

The amino acid sequence of Coh7 WT was fed to the server, the 10 positions of interest in the identified loops were selected and *in silico* mutated into all 20 available amino ac-

ids. A mutational tolerance scan was run on the consensus classifier PredictSNP server on the target residues in loops 1 and 2. The mutational scanning heatmap shows deleterious mutations in red and neutral mutations in blue. In loop1, 4/5 positions tolerate mutations well (except G88). Loop 2 is more sensitive to mutations, especially to hydrophobic residues. 3 /5 positions tolerate mutations in Loop 2 (N126 and L129 are restrictive) (Fig. 1c).

The second step of the construction of an AntiPDL1 binder is to analyze the effect of mutations on the desired properties of the scaffold. To do so, ten positions in Loops 1 and 2 from Coh7 were mutated to Ala to scan the biophysical effects of mutations. Point mutants were cloned, expressed, and purified from *E. coli*. The purity and functionality of the Coh7 point mutants were observed and validated by SDS PAGE analysis (Fig. 1d). The influence of point mutations on the thermal stability was analyzed by nano-differential scanning fluorimetry, with a melting range of temperature from 20 to 95°C. Overall, the selected single mutations do not affect the thermal stability (Fig. 1e). Particularly, G88 sensitivity correlates with the predicted thermal instability; L129 sensitivity does not correlate with the prediction. Mutations in D128 affects the thermal stability more than L129. Finally, G88 is the most sensitive position to temperature. Besides, the effect of mechanical unfolding forces was assessed by single molecule force spectroscopy using a pulling speed of 800 nm/s and previously reported chemistry [4]. The general observed effect was that single mutations do not affect the mechanical stability. Mutations in G88 have no impact. Interestingly, Y90 and N126 sensitivities correlate with the prediction. While single mutations in L129 do not affect the mechanical stability, the opposite occurred for mutations in Y90, which had the largest effect (Fig. 1f).

The next stage involves the library design of the scaffold to be engineered, considering the simulation and the experimental data. To preserve the mechanical properties of the scaffold, only six positions were considered allowing consensus for randomization. Degenerated codons were employed to create four libraries with different amino acid content and to contain bias towards residues that play a role in binding interactions.

We envision that the outcome of this project will ease the development of diagnostic and therapeutic solutions for cancer malignancies, and an efficient platform for directed evolution of proteins within the rising field of mechanobiology.

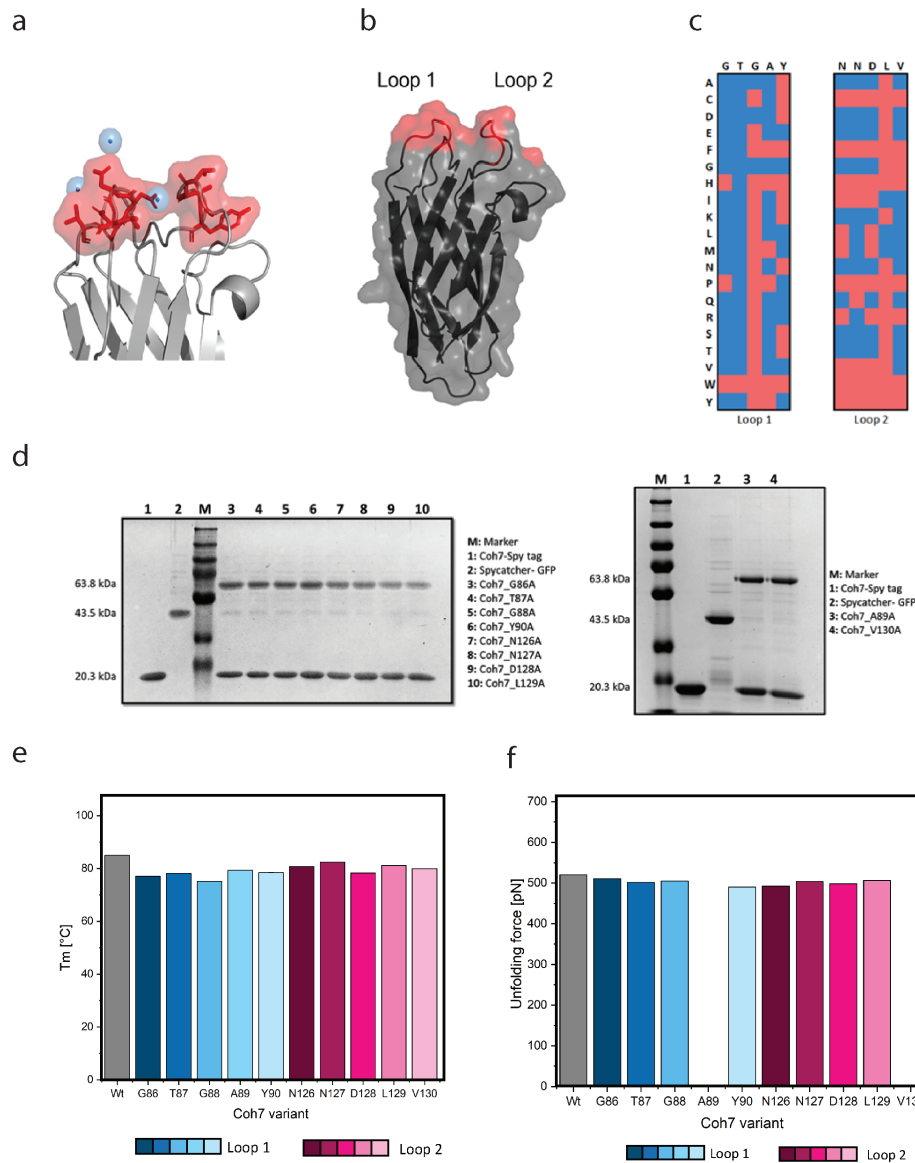


**Fig. 1: Strategy for engineering mechanical properties of scaffold domains.** *a)* Solvent Accessible Surface Area (SASA) scan showing loops of interest using a model sphere of water with a solvent radius = 1.4 Å on the ProtSA server. *b)* Structural correlation and identification of target loops 1 and 2. *c)* Mutational tolerance scan using the consensus classifier PredictSNP server on the target residues in loops 1 and 2. The mutational scanning heatmap shows deleterious mutations in red and neutral mutations in blue. *d)* SDS PAGE analysis of the identified Coh7 single mutants. Bioconjugation was performed using the Spy system to validate the functionality. PDDL1-Spytag (27 kDa); GFP-Spycatcher (43 kDa); conjugated PDDL1-GFP (70 kDa). *e)* Thermal stability analysis of point mutants by differential scanning fluorimetry. *f)* Single molecule force spectroscopy analysis of point mutants by AFM. Mutations are well tolerated in the selected loops. \*(empty columns were not determined).

## References

- [1] J. M. Chemnitz, R. V. Parry, K. E. Nichols, C. H. June, J. L. Riley, SHP-1 and SHP-2 associate with immunoreceptor tyrosine-based switch motif of programmed death 1 upon primary human T cell stimulation, but only receptor ligation prevents T cell activation. *J. Immunol.*, 173. 945–54(2004)
- [2] J. Estrada, P. Bernadó, M. Blackledge, J. Sancho, ProtSA: a web application for calculating sequence specific protein solvent accessibilities in the unfolded ensemble. *BMC Bioinformatics*, 10, (2009)
- [3] J. Bendl, J. Stourac, O. Salanda, A. Pavelka, E. D. Wieben, J. Zendulka, J. Brezovsky, J. Damborsky, PredictSNP: robust and accurate consensus classifier for prediction of disease-related mutations. *PLoS Computational Biology*, 10(1), (2014)
- [4] Z. Liu, H. Liu, A. M. Vera, R. C. Bernardi, P. Tinnefeld, M. A. Nash, High Force Catch Bond Mechanism of Bacterial Adhesion in the Human Gut. *Nat. Comm.* 11, (2020)

# Towards label-free HTS in enzyme engineering

Project P1705: Genetic selection of nanocatalysts

Project Leader: S. Panke, P. S. Dittrich, and T. R. Ward

Collaborator: E. Rousounelou (SNI PhD Student)

## Introduction

Homogeneous catalysis plays a crucial role in the production of chemicals but designing and optimizing catalysts with high activity and selectivity rank among the most challenging tasks in synthetic chemistry [1]. In this respect, the catalytic proficiency of enzymes acting on native substrates has inspired a range of approaches to engineer enzymes for chemical synthesis, whilst expanding their reaction scope [2]. Although proteins can be engineered via rational design [3], this is tricky when there is only limited biochemical and/or structural data available, as it is often the case. In that context, protein engineering often mimics natural evolution and creates large variant libraries which are then screened to identify those with desired properties [4]. Consequently, there is a need for genotype-to-phenotype linkage which is often respected by compartmentalization to spatially separate the library members, while miniaturizing the compartments and accelerating the screening [5]. Moreover, screening efforts require an assay where the enzymatic activity of the variants is coupled to a readout, which is often a change in optical properties (e.g., fluorescence or absorbance), usually via either substrate depletion or product formation [6]. Hence, it is typically required to either label the analyte or use an indicator reaction. However, an indicator reaction is usually of no industrial importance, as few biotechnologically relevant substrates carry fluorophores or chromophores, while, an optical readout is not always or easily related to a chemical reaction, thus making quantification of the reaction challenging [5]. This problem could be tackled by using label-free analysis methods, such as mass spectrometry (MS). MS reports the mass of the molecule and can observe each of the species present in a reaction, including the enzyme's substrate, the intended products, and the unintended side-products. Although, that leads to a more complete assessment of an enzyme's activity, the throughput of MS methods is currently low when compared to label-dependent methods. Furthermore, owing to the destructive process of mass determination, it is associated with loss of the genetic information [7].

To overcome these fundamental problems, we are developing a novel high-throughput screening (HTS) methods that [i] addresses the speed issue by coupling microfluidics with MALDI MS and [ii] compensates the de-

structiveness of MS analysis by co-analyzing the product or side-products of the reaction with unique peptide barcodes that maintain the genotype-phenotype linkage. In figure 1, an overview of the method is illustrated. Firstly, a library of unique DNA and peptide barcode combinations is generated, which is identified via next generation sequencing. The enzyme variant library is then cloned into the barcoded vectors so that every variant is associated with a unique combination of a DNA and a peptide barcode. The barcoded enzyme library is transformed into *E. coli* competent cells, followed by single cell spotting onto a picolitre array and cell lysis (Fig. 1.1). After enzyme/peptide barcode expression, each sample is incubated with candidate substrate(s) and co-factor(s) (Fig. 1.1) and the reaction is analyzed by MALDI-TOF MS. The mass spectrum of each sample delivers information about the product amount or distribution, but also its unique identity via the peptide barcode (Fig. 1.2). The latter is uniquely linked to the variant, but also to a DNA barcode and thus, after designing DNA primers specific to the DNA barcode, the desired variant can be retrieved by PCR, from a large pool of variants, and the genotype can be determined by sequencing (Fig. 1.3).

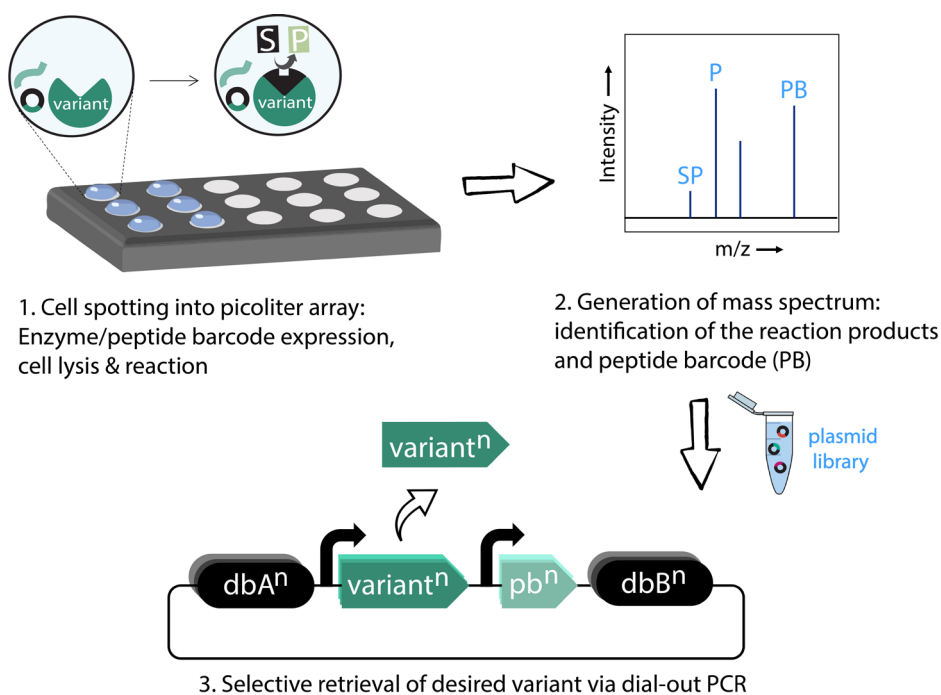


Fig. 1: Simplified overview of the proposed HTS method. For further information, refer to text. SP: side-product; P: product; PB: peptide barcode; db: DNA barcode; pb: peptide barcode gene template.

### Co-expression of peptide barcode & enzyme

The proposed method depends on the detection of the peptide barcode and the reaction product(s) during MALDI-MS analysis. Consequently, we need to ensure that both the peptide barcode and the enzyme variant are expressed sufficiently.

For that reason, each clone is transformed with two plasmids. The first plasmid, which is the “barcoded” plasmid, carries an enzyme variant fused at the N-terminal with the SpyTag. Moreover, each variant is under the control of an inducible promoter (PT7) and is flanked with a unique set of DNA barcodes and a unique peptide barcode.

The second plasmid, which is called the “lysis” plasmid, carries the gene template of protein E under the influence of synthetic promoter that depends on the alternative sigma factor  $\sigma$ S. This protein is a coliphage protein that forms pores perforating the cell membrane and wall of *E. coli* leading to a release of cytosolic proteins and eventually complete cell lysis in the late exponential to stationary growth phases.

In autoinduction medium the two plasmids lead to an autonomous protein production and release system. The autoinduction medium that is used is ZYM-5052. The principle behind that medium is based on carbon sources present in the medium that are metabolized differentially to promote high density cell growth and automatically induce protein expression driven by lac promoters.

### Peptide barcode library for unique MS identification of the enzyme variant

As discussed above, the peptide barcodes are encoded on the same plasmid that encodes the enzyme variant and they serve as the unique identifiers of the variant they are associated with during MALDI-MS analysis. For that reason, each barcode is composed of genetically encoded peptide sequences designed to produce a unique and detectable MS signal.

The peptide barcode library was initially designed in silico using a python script. Subsequently, 50 peptides from the library were randomly selected, synthesized and analyzed in MALDI-MS. All the peptides showed high ionization efficiency and were detectable even at low concentrations (0.006  $\mu$ M). The peptides are now being tested for their ability to be expressed efficiently in *E. coli* cells and analyzed in a more complex background (lysate).

Although recombinant protein synthesis in *E. coli* is a standard method of genetic engineering, the synthesis of short peptides is not. One of the central reasons for that might be that short peptides are an important nutrient source in *E. coli* and therefore might be difficult to accumulate in the cytoplasm. This problem will be tackled by ensuring that peptide production is as efficient as possible and by combining three peptides through protease recognition sites that together will compose one bigger peptide barcode. Each peptide barcode will be enzymatically digested right before MS analysis, producing a characteristic peptide fingerprint during MALDI-MS.

### DNA barcode library for selective retrieval of desired variants

Although we can uniquely identify each clone during MALDI-MS analysis based on the MS signal of each peptide barcode, the sample and with it the enzyme variant is still destroyed in the process due to the destructive nature of ionization. To keep the genotype-phenotype linkage and retrieve the sequence of the enzyme, we need to map the

peptide barcode information back to the specific plasmid from which it originated, and which is still available from a duplicate of the plasmid library. This mapping is achieved via barcoded plasmids that are “tagged” with a unique peptide barcode sequence and a unique set of DNA barcode sequences that flank each enzyme variant present in the pool (see Fig. 1.3). The unique set of DNA barcodes can then be used to design PCR primers and selectively retrieve the gene in question from the duplicate library.

### Picoliter well array for bacterial growth, protein production and reaction analysis

To address the speed issue, a picoliter (pl) well array was designed and manufactured by Dr Todd Duncombe, from the Dittrich lab. Each well has a 50  $\mu$ m diameter and a volume of 29 pl.

The picoliter wells of the array are coated with SpyCatcher protein before single cells are trapped inside the wells and let grown to a high-density culture. During cell growth, enzyme expression is induced via the autoinduction medium ZYM-5052. When enough target enzyme variants and peptide barcodes are produced and nutrients become scarce, protein E is expressed leading to cell lysis. Next, the enzyme variant and the peptide barcode are released into the extracellular space and are immobilized at the surface of the picoliter well array via the SpyCatcher/Spytag system.

The next step will be to develop a system for bulk reagent exchange and addition of the substrate to perform the enzymatic reaction inside the picoliter wells of the array.

### References

- [1] T. R. Ward, Artificial Metalloenzymes Based on the Biotin-Avidin Technology : Enantioselective Catalysis and Beyond. *Acc. Chem. Res.* 44, 47–57 (2011)
- [2] U. T. Bornscheuer, G. W. Huisman, R. J. Kazlauskas, S. Lutz, J. C. Moore, K. Robins, Engineering the third wave of biocatalysis. *Nature* (2012)
- [3] P. S. Huang, S. E. Boyken, D. Baker, The coming of age of de novo protein design. *Nature* (2016)
- [4] M. Jeschek, S. Panke, T. R. Ward, Artificial Metalloenzymes on the Verge of New-to-Nature Metabolism. *Trends Biotechnol.* 36, 60–72 (2018)
- [5] C. Zeymer, D. Hilvert, Directed Evolution of Protein Catalysts. *Annu. Rev. Biochem.* 87, annurev-biochem-062917-012034 (2018)
- [6] M. Wójcik, A. Telzerow, W. J. Quax, Y. L. Boersma, High-throughput screening in protein engineering: Recent advances and future perspectives. *Int. J. Mol. Sci.* 16, 24918–24945 (2015)
- [7] P. Liigand, K. Kaupmees, A. Kruve, Influence of the amino acid composition on the ionization efficiencies of small peptides. *J. Mass Spectrom.* (2019)

# Fiber-based cavity optomechanics

Project P1706: Ultrasensitive force microscopy and cavity optomechanics using nanowire cantilevers

Project Leader: M. Poggio and F. Braakman

Collaborator: D. Jäger (SNI PhD Student)

## Introduction

Nanoscale mechanical resonators such as thin membranes or nanowire crystals have the potential to uniquely enrich the capabilities of force microscopy. Currently, force microscopy techniques rely heavily on micron-sized cantilevers as force transducing elements, such as silicon beams or quartz tuning forks. In recent years, a new direction has emerged that replaces these conventional cantilevers with bottom-up grown nanoscale structures, such as carbon nanotubes or nanowires. Their small size and nearly defect-free crystal structures leads to potentially record force sensitivities, low mechanical losses and high operation frequencies. Several experiments have recently demonstrated the potential and versatility of this approach. In our own lab, we have demonstrated a new type of force microscopy using nanowires, in which we have shown sensitivity not only to the magnitude of forces, but also their direction [1].

Furthermore, nanomechanical resonators enable fundamental studies into the hybridization of different physical quantities, such as light and mechanical motion. Such hybrid systems form a promising platform to implement measurements operating at the limits imposed by quantum uncertainty and quantum non-demolition measurements. They may also allow investigation of quantum decoherence mechanisms, entanglement, and ultimately the transition from quantum to classical physics. We focus on two types of hybrid structures: nanowire heterostructures and 2D membranes with defects. Both systems combine excellent mechanical properties with the possibility of hosting optically active qubits in the form of embedded quantum dots or crystal defects. These qubits themselves already form interesting objects of study, as they can be used to sensitively measure electric and strain fields [2]. Moreover, when coupled to a mechanical degree of freedom, qubits can – through their nonlinear character – generate a large enhancement of the radiation pressure interaction between light and matter, as well as boost optical cooling of the mechanical resonator [3]. Our aim is to enable operation of such hybrid systems in regimes dominated by quantum effects, by improving optical excitation and detection of the mechanical resonator and embedded quantum emitters. To reach this goal, we will:

1: Integrate such hybrid systems into high-finesse optical cavities. Read-out of both the mechanical motion and of the photons emitted by embedded quantum emitters can be much improved by placing the system inside an optical cavity. Moreover, such a cavity allows to strongly couple the motion as well as quantum emitters to the cavity light field. In particular, this provides a straightforward path to the realization of a tri-partite hybrid system [3]. Such a tri-partite system allows to significantly enhance optical cooling and will allow the observation and utilization of quantum states of motion.

2: Implement resonant excitation of quantum emitters in a force microscopy setup. This will significantly reduce the optical linewidth of the qubits and should allow for mechanical displacement sensitivity reaching the Heisenberg uncertainty limit.

## Optical Setup and Cavity

We have constructed a table top optical setup that serves as the basic platform for our experiments. The setup allows to insert two beams of light with tunable frequency difference into an optical Fiber Fabry-Perot cavity (FFPC). The cavity can be measured through reflection or transmission and can be stabilized using a Pound-Drever-Hall scheme. This will enable optomechanical experiments, such as optical cooling of a mechanical oscillator, as well as cavity QED experiments, allowing the measurement of a tri-partite hybrid system.

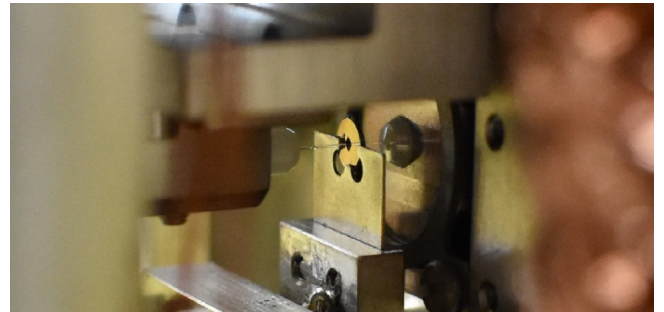


Fig. 1: Photograph of fiber Fabry-Perot cavity mounted in a probe operating in vacuum and low temperature (4K).

Previously, we have adapted this setup to work in a cryostat at 4K (Fig. 1). We have constructed a probe that allows us to control the alignment and length of our cavity in situ using piezoelectric actuators, while also improving its stability. Using this new probe, we were able to cool down the cavity and retain its optical properties that we measured with our table top setup. We achieved a stable lock of the cavity length within a few percent of the cavity linewidth (Fig. 2) both at room temperature and at 4K. Until now this was only possible with FFPC's that were severely limited in finesse or tunability. We are currently preparing a manuscript regarding this stabilization setup.

In addition, we have implemented a white light spectroscopy technique to characterize the mode spectrum of our cavity in a single shot, giving us information about the cavity length and sample position even while inside the cryostat.

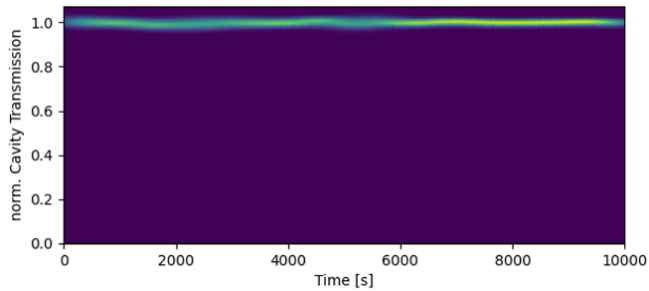


Fig. 2: Normalized cavity transmission signal as a function of time, showing long term stability.

### hBN drum resonators

As a first step towards creating a tri-partite system, we focus on drums of hexagonal boron nitride (hBN), which has been shown to contain crystal defects that can serve as quantum emitters. These emitters are ultra-bright, highly stable and can be observed at room temperature [4]. In addition, hBN drums are mechanical oscillators with favorable frequencies (MHz regime), low mass, and small mode volume.

We have successfully used high temperature annealing recipes to create emitters located at edges of hBN flakes, and we were able to observe several such emitters in spectroscopy measurements.

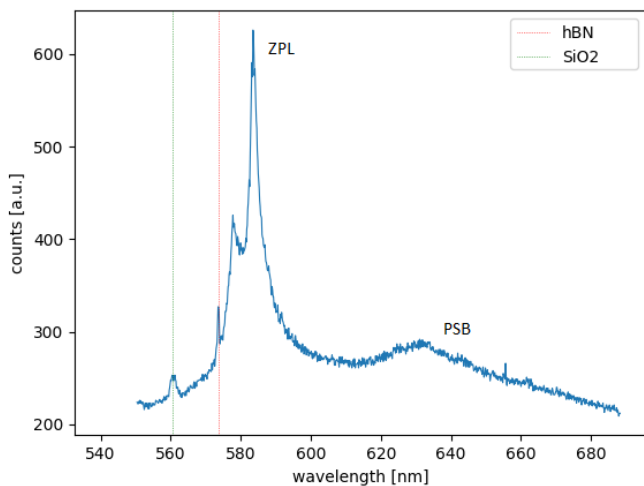


Fig. 3: Spectrum of an emitter found in an exfoliated and subsequently annealed hBN flake.

To use these flakes as mechanical resonators that can be positioned inside our cavity, we have developed a wet transfer technique that allows us to place them on top of a silicon nitride (SiN) hole grid membrane, resulting in hBN drum resonators (Fig. 4). To optimize the properties of our drums and to ensure sufficient separation between the resonance frequencies of the hBN drums and the silicon nitride membrane, we designed custom SiN membranes (manufactured by Norcada) as basis for our devices.



Fig. 4: Optical microscope image of an hBN drum resonator on a custom Norcada SiN membrane. More recently, we have integrated these devices into our cavity to characterize their mechanical properties and the resulting optomechanical interaction. As a first step, we have

measured the dispersive and dissipative optomechanical coupling by displacing the hBN drum in the cavity field.

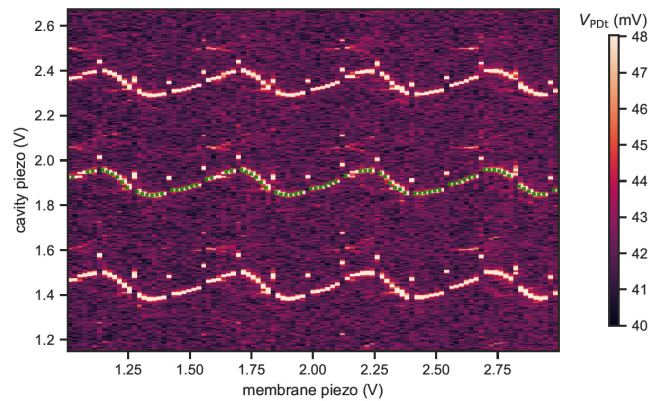


Fig. 5: Cavity resonance length modulated by the position of the hBN drum along the cavity axis.

The observed dispersive coupling of 5.9 GHz/nm in our experiment compares favorably to state of the art systems [5] and underlines the potential of our setup.

### Outlook

In the immediate future, we will finalize the characterization of the mechanical properties of our hBN drums. We plan to further explore the optomechanical interaction by performing optomechanically induced transparency experiments. In parallel, we are working on a way to deterministically position quantum emitters within hBN flakes, paving the way towards a fully coupled tripartite system. Moreover, we want to use our highly versatile experimental platform to investigate the interaction of other samples with our cavity, such as nanowires, carbon nanotubes or 2D magnets.

### References

- [1] N. Rossi, F. R. Braakman, D. Cadeddu, D. Vasyukov, G. Tütüncüoğlu, A. Fontcuberta i Morral, M. Poggio, Vectorial scanning force microscopy using a nanowire sensor, *Nat. Nanotechnol.* **12**, 150 (2017)
- [2] M. Montinaro, G. Wüst, M. Munsch, Y. Fontana, E. Russo-Averchi, M. Heiss, A. Fontcuberta i Morral, R. J. Warburton, M. Poggio, Quantum dot opto-mechanics in a fully self-assembled nanowire, *Nano Lett.* **14**, 4454 (2014)
- [3] J. Restrepo, C. Ciuti, and I. Favero, Single-Polariton Optomechanics, *Phys. Rev. Lett.* **112**, 013601 (2014)
- [4] T. Tran, K. Bray, M. Fordet al., Quantum emission from hexagonal boron nitride, *Nat. Nanotechnol.* **11**, 37–41 (2016)
- [5] F. Rochau, I. Sanchez Arribas, A. Brioussel, S. Tapfner, D. Hunger, E. M. Weig, Dynamical Backaction in an Ultrahigh-Finesse Fiber-Based Microcavity, *Phys. Rev. Applied* **16**, 014013 (2021)

# Capacitively-coupled and inductively-coupled excitons in bilayer MoS<sub>2</sub>

Project P1707: Nano-photonics with van der Waals heterostructures  
 Project Leader: R. J. Warburton and I. Zardo  
 Collaborators: L. Sponfeldner (SNI PhD Student) and N. Leisgang

Exciton-exciton interactions in semiconductors lead to a plethora of phenomena such as nonlinear optical effects and quantum condensation. These effects have been studied using quantum wells. Two-dimensional (2D) semiconductors provide fresh impetus and new possibilities. On the one hand, excitons are very robust in these materials – they are stable even at room temperature. On the other hand, the interactions can be engineered in a rich way by exploiting the spin, valley and layer quantum numbers.

We focus on bilayer MoS<sub>2</sub>, a material in the transition-metal dichalcogenide (TMD) family. Each layer hosts the so-called A- and B-excitons. In addition, an interlayer exciton (IE) was very recently discovered. The IE lies energetically between the A- and B-excitons and couples strongly to light [1]. The energy of the IE can be tuned into resonance with both A- and B-excitons via an applied electric field [2]. Here, we probe the IE-A and IE-B couplings. We present an experiment which is sensitive to the sign of the coupling, not just its magnitude.

Our main result is that the IE-A and IE-B couplings have opposite signs [3].

The structure of our sample is shown in figure 1a. An electrically grounded homobilayer MoS<sub>2</sub> is encapsulated in h-BN. The electric field  $F_z$  across the device is controlled by applying voltages to the top and bottom few-layer graphene (FLG) gates.

The excitonic transitions are probed optically with absorption spectroscopy. Figure 2a shows the measured absorption of bilayer MoS<sub>2</sub> as a function of the applied electric field  $F_z$ . At  $F_z = 0$ , the absorption shows three peaks: the intralayer A- and B-excitons at 1.93 eV and 2.10 eV, respectively, and in between, the interlayer exciton IE. Increasing the electric field leads to a splitting of the IE into two resonances that shift in opposite directions. At high  $F_z$ , the IE is tuned into resonance with the A- and B-excitons. There is a clear avoided crossing between the upper IE branch and the B-exciton, while interaction of the lower IE branch and the A-exciton shows a weak avoided crossing [2,3]. In both cases, excitons are coupling to each other. However, the intensity evolution is quite different for the IE-B and IE-A interactions. Our goal is to understand the different coupling behaviors.

The excitonic interaction is well described by a classical model as sketched in figure 1b. Each exciton is modeled as an optical dipole driven by an external field  $E$  with a certain coupling strength  $F_{1,2}$ . The dipoles are coupled to each other through the coupling constant  $\kappa$ . Solving the equations of motion of the system yields analytic equations for the eigenenergy and the absorption strength for each excitonic resonance.

Applying the model to the measured data reveals not just the magnitude but also the sign of the excitonic coupling. The coupling constant of the IE-B (IE-A) interaction is  $\kappa = +35.8$  meV ( $\kappa = -3.5$  meV). The full  $F_z$ -dependence of the absorption spectra of bilayer MoS<sub>2</sub> is calculated and plotted in figure 2b. The classical model reproduces very closely the experiments (Fig. 2a). This model unearths a crucial result: the IE-A coupling constant is of opposite sign to the IE-B coupling constant.

By making an analogy to coupled electrical circuits, we describe these couplings as capacitive (positive  $\kappa$ ) in one case, inductive (negative  $\kappa$ ) in the other. Capacitive coupling is well known – microscopically, it arises via hole tunneling from one layer to the other (red arrow in Fig. 3a). In contrast, inductive coupling is new – it has a different origin. With the help of microscopic calculations (taking into account the complex band structure and the Coulomb interaction within the excitons) we show that the inductive coupling arises via

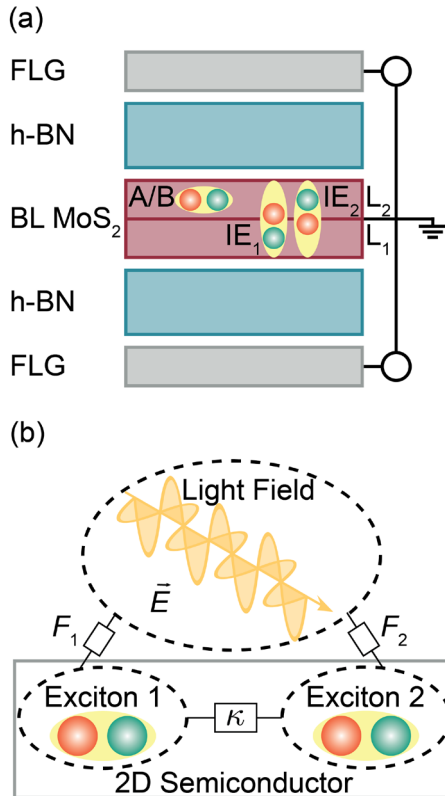


Fig. 1: a) Schematic of the van der Waals heterostructure consisting of homobilayer MoS<sub>2</sub> embedded in h-BN. b) Sketch of two coupled excitons in a 2D semiconductor both driven by an external light field.

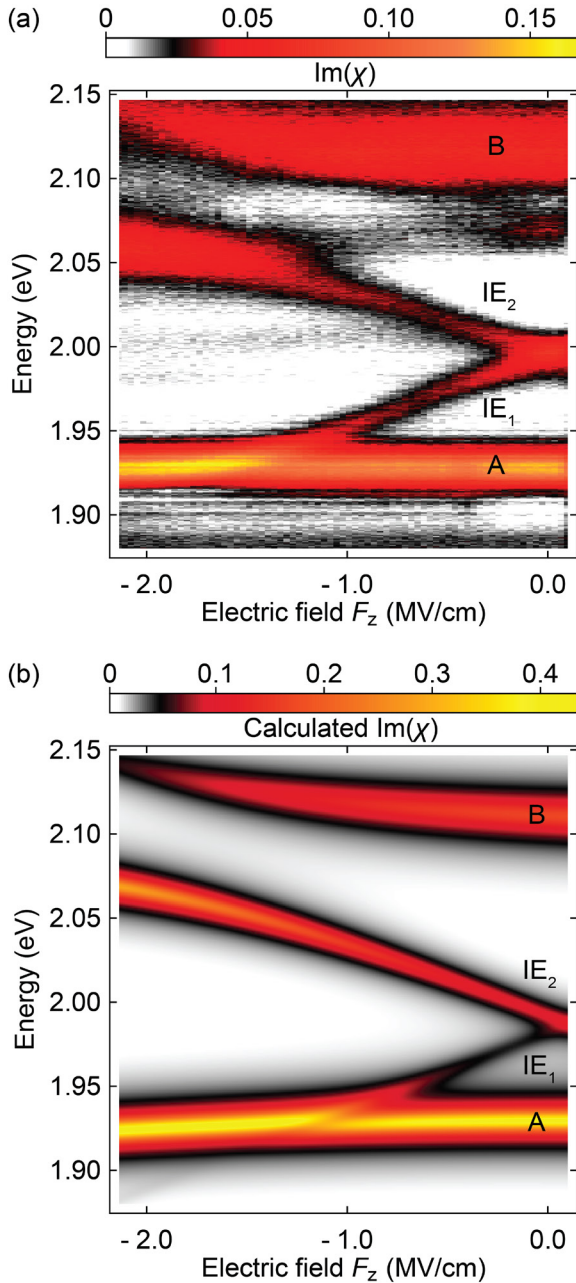


Fig. 2: a) Measured absorption of gated bilayer  $\text{MoS}_2$  as a function of applied electric field  $F_z$ . b) Calculated absorption  $\text{Im}(\chi)$  with parameters extracted from model fits to the measured data.

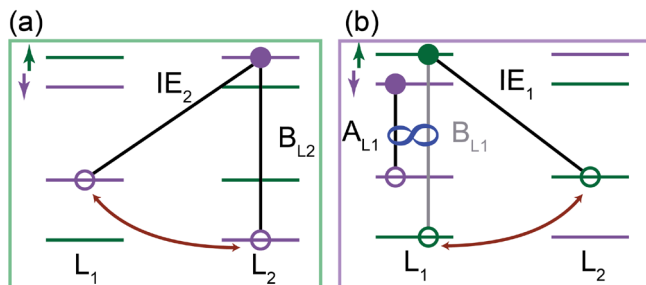


Fig. 3: Sketch of the microscopic origin of the a) IE-B and b) IE-A interaction. Hole tunneling is sketched as the red arrow. A and B are coupled through intralayer and intravalley exchange interaction (blue  $\infty$ -symbol).

spin, specifically an A-B exchange interaction (blue  $\infty$ -symbol in Fig. 3b). As a consequence, our results show that the A- and B-excitons, nominally with opposite spin, are coupled.

We state two main conclusions. First, our work uncovers the importance of exciton-exciton interactions not just in a TMD bilayer but also in the constituent TMD monolayers. We find that spin is an imperfect quantum number even for the lowest energy excitons. This conclusion is reached using the IE as a tunable probe to quantify the A-B intravalley exchange coupling. We find -16.6 meV. Second, a measurement of the optical susceptibility enables not just the magnitude but also the sign of the exciton-exciton couplings to be determined.

## References

- [1] Gerber, I. C. et al. Interlayer excitons in bilayer  $\text{MoS}_2$  with strong oscillator strength up to room temperature. *Phys. Rev. B* 99, 035443 (2019)
- [2] N. Leisgang et al. Giant Stark splitting of an exciton in bilayer  $\text{MoS}_2$ . *Nature Nanotechnology* 15, 901-907 (2020)
- [3] L. Sponfeldner et al. Capacitively-coupled and inductively-coupled excitons in bilayer  $\text{MoS}_2$ . arXiv:2108.04248 (2021)

# Free-form micro-optical arrays

Project P1708: Non-visual effects of LED lighting on humans

Project Leader: E. Meyer and R. Ferrini

Collaborator: T. Aderneuer (Associate SNI PhD Student)

The potential for free-form micro-optical arrays (FMOAs) has been demonstrated in applications such as automotive lighting, aerospace, augmented reality, and precision engineering. As a result of their asymmetric shapes, FMOAs can overcome several limitations of the more standard spherical and aspherical (symmetrical) microlenses [1]. For example, they can reduce optical aberrations more effectively and can produce asymmetric light distributions. Oftentimes these performance improvements come together with a system simplification by reduction in the number of required optical components.

Recent advances in precision manufacturing have enabled the realization of complex microstructuring at industrially relevant volumes triggering industrial interest in FMOAs [2]. Prominent precision microstructuring technologies are for example, ultra-fast laser ablation, grayscale laser photolithography, two-photon polymerization and ultra-precision micromachining.

As a flip side, the more complex surface topography of FMOAs poses challenging demands on surface representation and sample characterization [3]. The lack of efficient and reliable inspection processes will hinder further progress in manufacturing, discourage optical designers from using them and ultimately make the future of the FMOAs uncertain.

## Reverse engineering of free-form surfaces

Manufacturing deviations with respect to the nominal designs, often translate in performance degradation. The ability to quantify is fundamental to identify which deviations need to be corrected and which ones have only a negligible (or at least acceptable) impact. In contrast to the more standard symmetric microlenses, characterized by relatively few and well-understood parameters (sag, radius of curvature, etc.), the description of free-form surfaces typically requires a much larger parameter space or even non-parametric representations.

The experimental testing of the (typically) small area FMOA prototypes is difficult or often simply unfeasible. The quality is commonly assessed by measurement of the surface form of FMOAs which is compared to the nominal design. This information of manufacturing deviation provides though little or no insight into their impact on optical performance.

We have demonstrated a method to accurately predict the optical functionality from experimentally measured surface topography [4].

Firstly, the measured profile, given in the form of point clouds, is fitted to a NURBS surface (Fig. 1). This representation has the following advantages:

- It can represent complex surfaces using a manageable low amount of data

- it is widely implemented in CAD and optical simulation software tools
- it enables (contrary to e.g., analytical expressions) the representation of local deformations (i.e., manufacturing deviations).

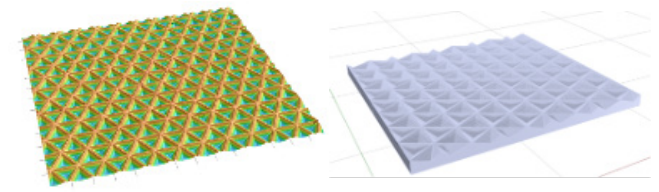


Fig. 1: Left: Form characterization of a free-form micro-optical array with confocal laser microscope. Right: NURBS surface representation based on measured metrology data.

In a second step, the NURBS surface is used to build a 3D ray-traceable CAD model whose performance can therefore be predicted through optical simulations (Fig. 2).

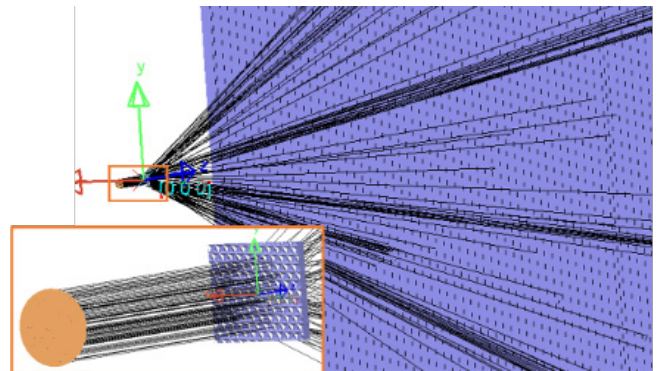


Fig. 2: Raytracing of the 3D CAD-model. The simulations were performed using LightTools. The rays are shown in black. The inset shows the collimated light source.

This approach to convert measured surface topography into a 3D CAD model, widely applied in the field of mechanical engineering (reverse engineering), is however, much less exploited for optical applications.

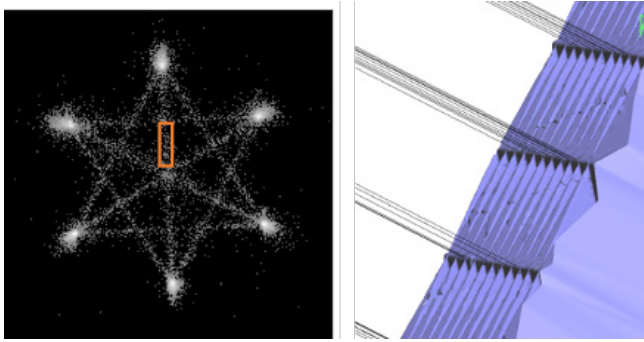


Fig. 3: The selected area (orange rectangle) on the observation plane is linked to the responsible geometry of the free-form surface. It shows that the edges of the surface redirect the light to the selected part on the observation plane.

As mentioned earlier, the ultimate objective is to identify, and subsequently correct, the problematic deviations; in our example, those responsible for the light between the (hexagonally distributed) hotspots (orange rectangle in Fig. 3). Simulations indicate that the edges of the micropyramids are responsible for the light redirection to the selected area. This is a valuable information to improve manufacturing if the observed broadening needs to be minimized.

#### Design for manufacturing CAD-tools

A further challenge for FMOAs is to analyze designs upon their manufacturability. The fabrication process of FMOAs is complex and typically includes multiple steps such as design, mastering, tooling, up-scaling, and replication; all with certain (different) limits. It is often underestimated how challenging is to design FMOAs compatible with all the steps involved in their manufacturing.

We implemented design for manufacturing tools that enable optical designers to implement these limitations at the design phase in order to avoid costly and time-consuming trial and error steps. Tools for evaluating local surface slope (angle between the vertical direction and the surface normal) and height (the distance between the upper and lower z-coordinates) were developed to identify critical areas [5]. Figure 4 which shows a script programmed to automatically visualize areas of a FMOA which don't fulfill the maximum surface slope constraint.

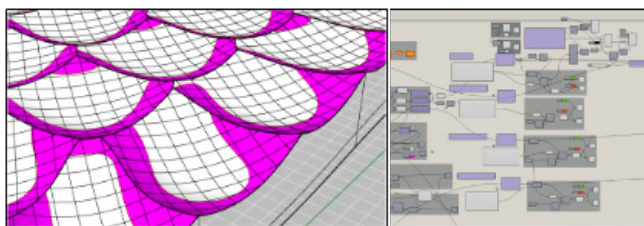


Fig. 4: Left: Optical design with user specified surface slope analysis. Right: Interface of implemented algorithm in visual programming language Grasshopper.

#### Conclusion

We have presented and validated an effective method that exploits the recent advances in surface topography to rapidly identify problematic manufacturing deviations of fabricated prototypes and therefore allow speeding-up the manufacturing of FMOAs. The described method can accurately simulate and successfully predict the optical performance of manufactured free-form microstructures without confronting the limitations of experimental optical setups. Furthermore CAD tools were implemented that automatically check designs for limitations of different manufactur-

ing technologies. The results can help designers to compare different manufacturing technologies and the potentially critical parameters, thus facilitating the mastering technology selection and reduce risk.

#### Outlook

The reverse engineering approach to create a virtual 3D model of a measured surface (in point cloud representation) using the NURBS surface representation has also the potential to be used in other fields. CAD modeling for simulation is used in many other fields, such as microfluidics, where smooth models are required for flow simulations.

Further geometric manufacturing constraints need to be described mathematically and implemented in the CAD-based algorithms. There is a great potential in general for using CAD tools to speed up processes through automation and to develop more custom solutions for specific FMOA designs that are not possible with general commercial software.

#### References

- [1] F. Z. Fang, X. D. Zhang, A. Weckenmann, G. X. Zhang, C. Evans, Manufacturing and measurement of freeform optics. *CIRP Annals* 62, 823–846 (2013)
- [2] T. Gissibl, S. Thiele, A. Herkommer, H. Giessen, Sub-micrometre accurate free-form optics by three-dimensional printing on single-mode fibres. *Nature Communications* 7, 11763 (2016)
- [3] X. Jane Jiang, P. Scott, *Advanced Metrology: Freeform surfaces*, (Academic Press, Oxford, 2020)
- [4] T. Aderneuer, O. Fernández, A. Karpik, J. Werder, M. Marhöfer, P. M. Kristiansen, R. Ferrini, Surface topology and functionality of freeform microlens arrays, *Optics Express* 29, 5033-5042 (2021)
- [5] T. Aderneuer, O. Fernández, J. Chaves, R. Mohedano, R. Ferrini, Fabrication of free-form micro-optics: design assessment for manufacturability, *Proc. SPIE 11873, Optical Fabrication, Testing, and Metrology VII*, 1187304 (2021)

# Plasma membrane vesicles as an alternative to exosomes

Project P1801: Bioinspired nanoscale drug delivery systems for efficient targeting and safe in vivo application

Project Leader: J. Huwyler and C. Palivan

Collaborator: C. Alter (SNI PhD Student)

## Introduction

Extracellular vesicles (EV) can be used for therapeutic applications [1]. EVs, which are secreted by eukaryotic cells, are hollow sphere lipid vesicles which can carry cell specific lipids, proteins such as enzymes, cell adhesion molecules, or cluster of differentiation proteins, nucleic acids (i.e., RNA and DNA), metabolites, and even organelles [2]. EVs are classified into three main categories: exosomes, microvesicles, and apoptotic bodies. Therapeutic nucleic acids, proteins or small molecular weight drugs were loaded into EVs and successfully delivered to cells in vitro and in vivo, but only few EV technologies have progressed into clinical trials. One of the major drawbacks for clinical translation is the EV production [3]. Typical EV secretion rates range between 60–170 exosomes/cell/hour, depending on the cell line [4].

To overcome this hurdle, we have developed an efficient and scalable EV production protocol, which can be applied to cell lines as well as primary cells. It is based on chemical stimulation of donor cells to generate giant plasma membrane vesicles (GPMVs). They are harvested and processed by homogenization into nano-sized plasma membrane vesicles (nPMVs). It was the aim of the present work to study the cellular interaction of nPMVs with Huh7 cells.

## Material and methods

Chemical vesiculation agents (paraformaldehyde and dithiothreitol) were used to induce cellular injury and membrane blebbing in Huh7 cells. The vesiculation started few minutes after incubation (37°C and 5% CO<sub>2</sub>) and the produced GPMVs (red arrows) were harvested from donor cells after 6 hours (Fig. 1A).

GPMVs were stained with a lipophilic dye (DiI) and homogenized by filter extrusion in order to produce nPMVs (Fig. 1B). DiI labeled DOPC and DOPC:PS liposomal formulations, serving as negative and positive controls, were produced by thin-film hydration method [5].

## Results and discussion

DiI labeled Huh7 nPMVs and control liposomes (DOPC and DOPC:PS) were incubated with Huh7 cells for 15 minutes, 1, 4, and 24 hours. Uptake was analyzed by flow cytometry. We observed a time-dependent strong uptake (relative fluorescence unit (RFU)) in Huh7 cells for all particles containing phosphatidylserine (PS) (Fig. 2A). Uptake was fast in the first 4 hours, then started to saturate and reached the highest value after 24 hours. Huh7 nPMVs had a 5-fold higher uptake compared to DOPC:PS liposomes. Uptake of control-DOPC liposomes was negligible. Additionally, we visualized cellular uptake of Huh7 nPMVs in Huh7 cells by confocal laser scanning microscopy (Fig. 2B). These results indicate, that nPMVs are rapidly internalized by Huh7 cells, presumably by endocytosis. In a next series of experiments, we measured

the EV production rate. Huh7 cells produce 1500 nPMVs/cell/hour. This exceeds the natural production rate of exosomes by more than an order of magnitude.

## Conclusion

We were able to produce with high yield nPMVs. They were obtained from Huh7 cells using an optimized EV production protocol. We observed a fast and efficient uptake of nPMVs by cultured cells. These results will be used as a starting point for the design of novel EV based therapeutic systems.

## References

- [1] D. E. Murphy, O. G. de Jong, M. Brouwer, M. J. Wood, G. Lavie, R. M. Schiffelers, P. Vader, Extracellular vesicle-based therapeutics: natural versus engineered targeting and trafficking. *Exp. Mol. Med.* 51, 1–12 (2019)
- [2] G. van Niel, G. D'Angelo, G. Raposo, Shedding light on the cell biology of extracellular vesicles. *Nat. Rev. Mol. Cell Biol.* 19, 213–228 (2018)
- [3] S. G. Antimisiaris, S. Mourtas, A. Marazioti, Exosomes and Exosome-Inspired Vesicles for Targeted Drug Delivery. *Pharmaceutics* 10, 218 (2018)
- [4] Y.-J. Chiu, W. Cai, Y.-R. V. Shih, I. Lian, Y.-H. Lo, A Single-Cell Assay for Time Lapse Studies of Exosome Secretion and Cell Behaviors. *Small* 12, 3658–3666 (2016)
- [5] H. Zhang, Thin-Film Hydration Followed by Extrusion Method for Liposome Preparation. in *Liposomes* 17–22 (Humana Press, New York, NY, 2017)

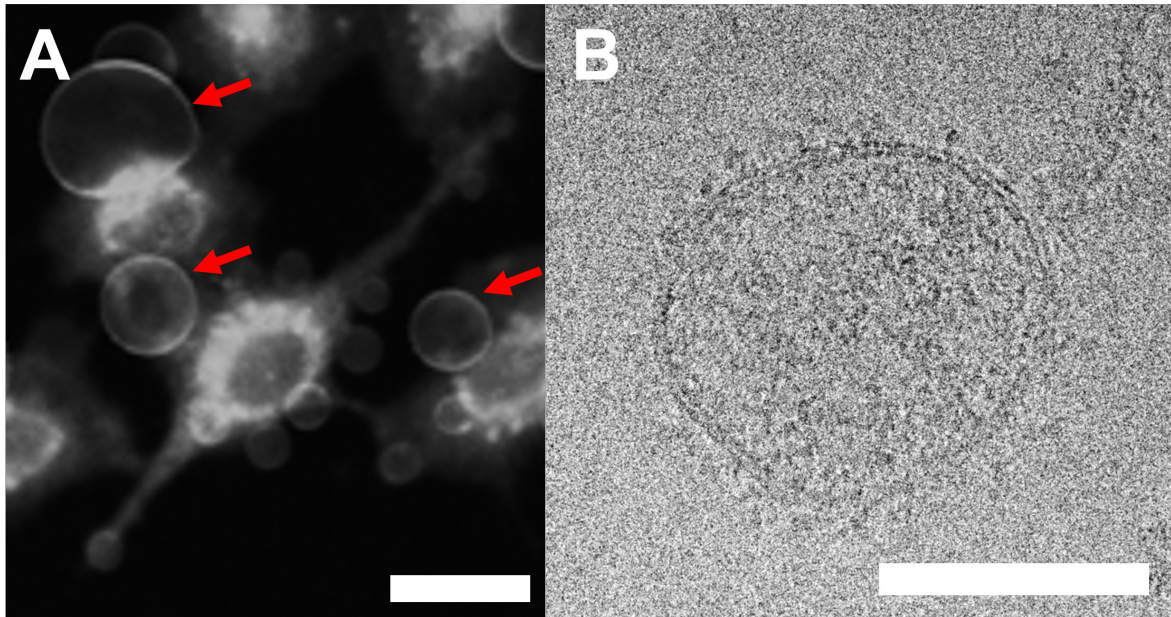


Fig. 1: A) Induced blebbing of Huh7 cells is used to produce giant Plasma Membrane Vesicles (giant PMVs; red arrows). Scale bar: 10  $\mu\text{m}$ . B) Cryo-TEM image of a Huh7 derived nano-sized PMV. These nPMVs are decorated with proteins. Scale bar: 100 nm.

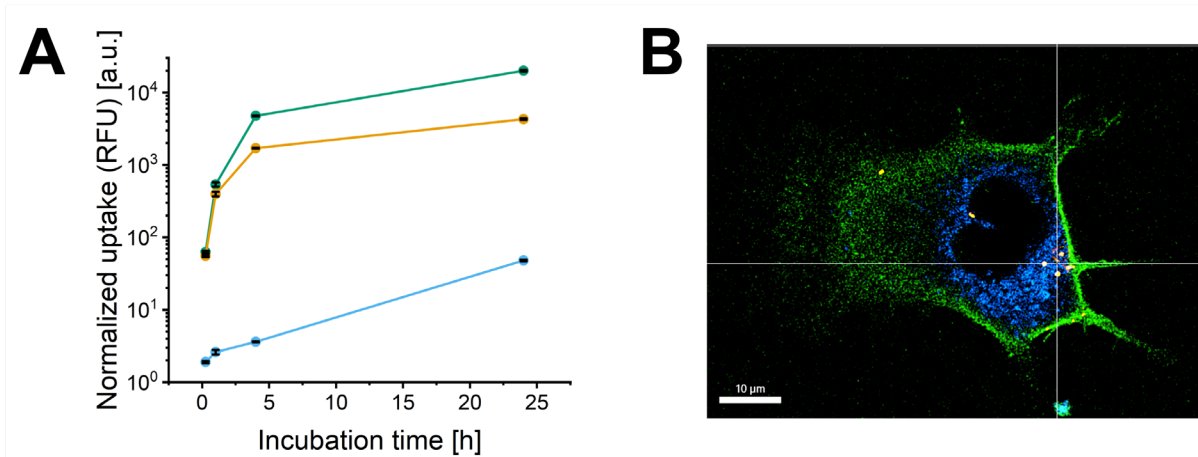


Fig. 2: Interaction of DiI labeled particles with Huh7 cells. A) Time-dependent uptake of Huh7 nPMVs (green), DOPC:PS (yellow), and DOPC (blue) liposomes. B) Uptake of Huh7 nPMVs (red) by Huh7 cells (blue: cytosol, green: plasma membrane) as imaged using confocal laser scanning microscopy. Scale bar: 10  $\mu\text{m}$ .

# Deep learning enhanced direct evolution

Project P1802: From Schrödinger's equation to biology: Unsupervised quantum machine learning for directed evolution of anti-adhesive peptides

Project Leader: M. Nash and A. von Lilienfeld

Collaborator: V. Doffini (SNI PhD Student)

## Introduction

The Covid-19 pandemic showed us that our deeply interconnected world is extremely vulnerable to highly contagious pathogens. In this context, viruses are not the only threat we might face in future epidemic scenarios. Specifically, bacteria that show antibiotic resistance characteristics are an enormous hazard to humanity, and this topic has garnered increased interest from across the biomedical research community in recent years. It is crucial to explore new strategies to fight against antibiotic resistant pathogens and develop new pharmacological treatments.

In our project, we focus on a specific class of microbes which use specialized surface proteins called adhesins to bind human tissue and spread the infection inside the host. The detailed structure and mechanism behind many such bacterial binding adhesin domains are known, while for others no structural information is available. Such adhesins typically bind short peptide sequences located on abundant blood or cell-surface proteins of the intended host (Fig. 1). The goal of our project is to identify novel peptide candidates which bind strongly to the bacterial adhesin of the pathogen agent, inhibiting it from attaching to the host's cells.

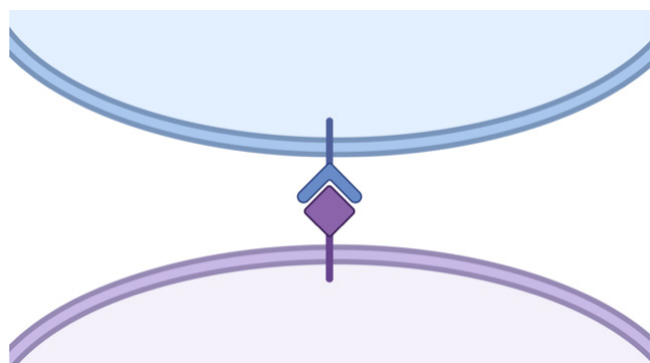


Fig. 1: Schematic representation of the binding between the pathogen (in blue) and the human cell (violet). The binding protein of the microorganism is shown in blue as well, while the attach site of the human cell is the violet square.

By using state of the art technologies like deep mutational scanning and next generation sequencing, it is already possible to generate data for hundreds of thousand different peptide variants in a relative short amount of time. Despite the fact that this might sound like a lot of data, they cover just a minimal fraction of the enormous space of possible amino acid combinations, even for small chains. For example, even for a peptide of a couple dozen amino acids, the number of total possible combinations are many orders of magnitude greater than the stars in the whole universe. Practically, this problem usually leads to a repetitive approach, called di-

rected evolution, where mutations are screened and ranked based on a fitness function. In our case, the fitness function would be a measure of the binding strength between the adhesin protein and the peptide. After this first screening, the best mutations are selected, fixed and millions of new variants are produced changing the amino acids on the other positions. Afterwards, the new variants are screened and ranked again and the procedure is repeated for many iterations until an optimum is reached. Unfortunately, such protocol is not exempt from criticism; firstly, by exploring just single point mutations it is likely to get stuck on a local optimum instead of finding the global one; and secondly, since the presented protocol needs to be repeated multiple times, the burden of experiments needed is still high and it impacts negatively the time, resources and costs involved.

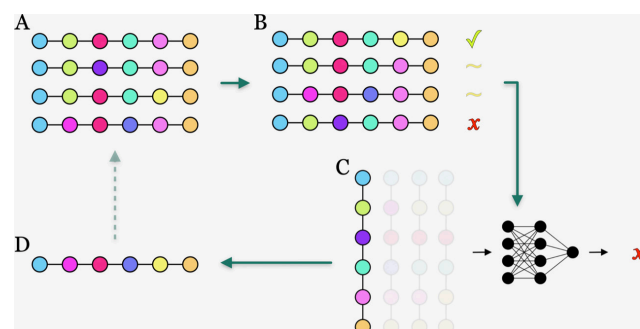


Fig. 2: Schematic representation of deep learning enhanced direct evolution. Starting from upper left, a library containing many mutants is synthesized (A). Then, the different variants are sequenced and sorted by a chosen output (B). After that, a neural network is trained in order to connect the specific sequences to the fitness variable (C). Finally, the model is used to perform in-silico screening of new variants. The best candidates are synthesized in the lab (D) and, eventually, added to the library for a new iteration.

In order to increase the efficiency as well as the accuracy of directed evolution, we propose a deep learning assisted approach (see Fig. 2). Such a methodology is still based on screening and ranking peptides, but in this case a deep neural network is fitted to connect the specific amino acid residues to the corresponding fitness function value. If successful, the deep neural network can be used to screen in-silico many more variants than are available experimentally, giving the possibility to efficiently find a new maximum of the fitness function without the need of many iterations as in the "classical" directed evolution approach. Moreover, since we are not anymore constrained by fixing the single best mutations found in the previous screening, the fitness maximum we reach using metaheuristic techniques will be theoretically better than the previous one.

## Material and methods

In the first part of the project, we focused on the synthesis and fluorescent labeling of one of the binding proteins of a pathogenic organism as well as the production of an *E. Coli* library. This library contains millions of bacteria, where each of the individual cells displays on its surface a specific peptide of defined length with up to four different mutations. Such library was obtained via multiple polymerase chain reactions using various tailed primers. This library was then screened using the bacterial adhesin labeled with a fluorescent dye molecule (see Fig. 3). Peptides that strongly bind the adhesin will keep the fluorescent label after washing. The fluorescent intensity is detected by flow cytometry analysis and the cells are sorted, isolated and enriched for positive binders.

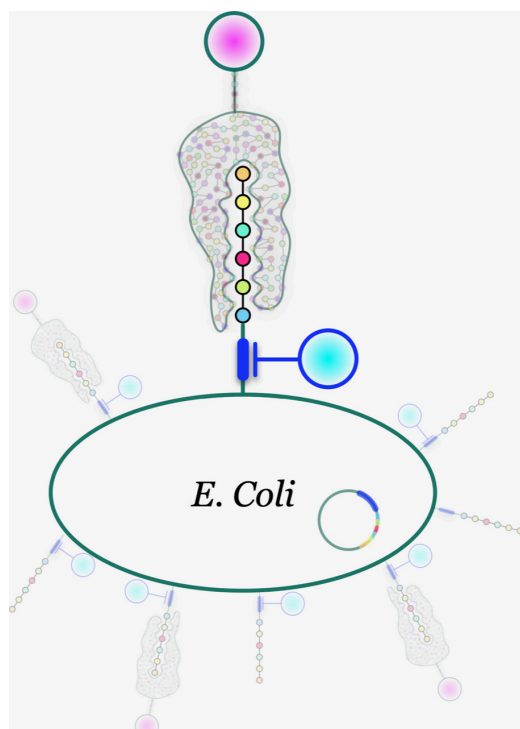


Fig. 3: Schematic representation of the binding between the protein of the pathogenic organism and one of the randomized peptides displayed on the cell surface of an *E. Coli*. The fluorescent label is shown in pink.

## Results and discussion

Here we present one of the preliminary screens of our library. Flowcytometry analysis clearly shows a good binding of a consistent part of the peptides (Fig. 4, right upper quadrant). One additional sign of the binding activity is the correlation trend shown in the plot. In fact, if the expression level of a surface displayed peptide variant that binds to the label protein increases, one should expect a higher signal coming from the adhesin.

Another interesting aspect coming from the analysis of figure 4 is the presence of binders in the upper left quadrant. In an ideal scenario, the peptides should not be present at the cells surface in that region, since the expression level measured is low. This phenomenon could be explained by the existence of unspecific binders between the labeled adhesin and the bacterial cell itself. To back up this hypothesis, one can notice as well the events apparently randomly distributed in the upper quartile of the plot. Such behavior is a valuable advice regarding the need of screening different washing protocols before carrying out any sorting experiment.

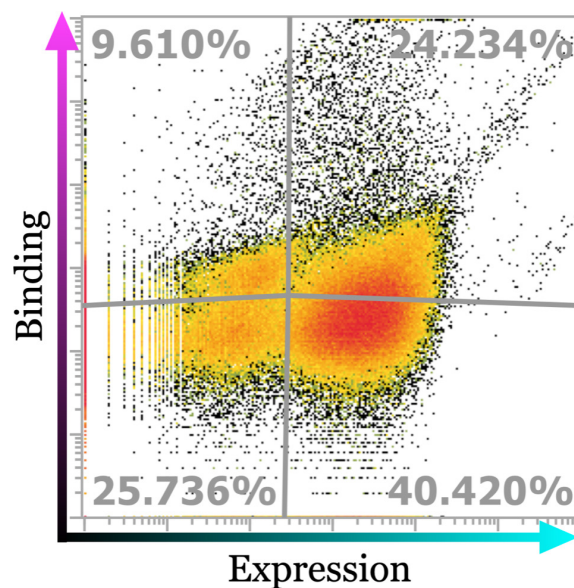


Fig. 4: Screening plot of the binding between the peptide library and the labeled protein of the pathogenic organism. Each point corresponds to one distinct peptide. On the abscissa is shown the binding strength while on the ordinate is the expression level or, in other words, how many peptides are displayed on the cell surface of the *E. Coli*.

## Outlook

The following part of this project has to be divided in two parallel studies. On one hand, it will be necessary to optimize the experimental protocol, to minimize any variability in the flowcytometry analysis, and to synthesize a reliable peptide library. On the other hand, we will focus our resources in the study of the application of different machine learning techniques to predict in-silico simulated properties of biological systems. We believe this controlled step will be crucial to develop solid insights on the topic before switching on experimental, and noisier, data.

## References

- [1] R. Vanella, D. Tien Ta, M. A. Nash, Enzyme-mediated hydrogel encapsulation of single cells for high-throughput screening and directed evolution of oxidoreductases, *Biotechnol. Bioeng.*, 116(8), 1878–1886 (2019)
- [2] K. Yang, Z. Wu, F. Arnold, Machine-learning-guided directed evolution for protein engineering, *Nat. Methods* 16(8), 687-694 (2019)
- [3] Z. Wu et al., Machine learning-assisted directed protein evolution with combinatorial libraries, *PNAS*, 116 (18), 8852-8858 (2019)

# Giant energy dissipation on twisted bilayer graphene at the magic angle twist

Project P1803: Nanoscale mechanical energy dissipation in quantum systems and 2D-materials  
 Project Leader: E. Meyer and M. Poggio  
 Collaborator: A. Ollier (SNI PhD Student)

## Introduction

Twisted bilayer graphene (TBG) at the magic angle twist ( $\theta = 1.08^\circ$ ) has gained a lot of interest due to the presence of flat bands at the Fermi energy and strongly correlated insulating phases [1]. Here, we report on energy dissipation measurements on the TBG sample with a twist angle of  $1.1^\circ$ . The sample is composed of a silicon substrate with 300 nm thick silicon oxide layer followed by the TBG which is capped on top by 10 nm thick hexagonal boron nitride layer (Fig. 1a). The measured dissipation over the sample exhibits a series of peaks that can be attributed to the different filling factors. Our measurement confirmed that the presence of twist angle between the two sheets of graphene creates a superlattice structure that modulates the electronic properties by inducing a mini-Brillouin zone [1]. The mini-Brillouin zone is fully filled with four electrons and experiment demonstrates that the peaks on the dissipation are corresponding to every electron entering the mini-Brillouin zone, which leads to appearance of different filling factors. This effect is detectable using an Atomic Force Microscope where the tip is oscillating like a tiny pendulum over the sample surface (p-AFM). This geometry avoids the snapping of the tip into contact with the sample and enables to use very soft cantilevers making it more sensitive than conventional AFM sensor [2].

## Single electron charging and quantum capacitance model

The detection of single electron charging using AFM is a well-established phenomenon [3]. The system is described using a two-capacitance model (Fig. 1b), where  $C_{tip}$  is referring to the tip-sample capacitance and  $C_{sub}$  to the substrate. The first term is a geometric capacitance of a sphere and a plane. The second term is more complex, it can be described as follow:

$$C_{sub}^{-1} = C_{par}^{-1} + C_Q^{-1} \quad (1)$$

where  $C_{par}$  is a ‘parasitic’ capacitance that represents the tip coupled to anything different than TBG (back gate, gold contact electrodes, etc.). The later capacitance  $C_Q$  is the so-called quantum capacitance and it is proportional to the electronic density of states as follow [4]:

$$C_Q \propto q^2 \rho(\eta) \quad (2)$$

where  $q$  is the electron charge,  $\rho(\eta)$  is the density of state. The reduced energy  $\eta = E_F/kT$ , where  $E_F$  is the Fermi energy,  $k$  is the Boltzmann constant and  $T = 5K$  is the temperature.

The capacitance model is used to simulate the force. The measured frequency shift versus voltage ( $\Delta f(V)$ ) exhibits frequency drops characteristic for single electron charging and is related to the dissipation peaks. Figure 1d shows the typical  $\Delta f$  curve (blue curve) recorded over the sample surface. The spectrum is characterized by a double parabolic shape due to capacitive forces between the tip and the sample. The double parabola shape is presumably related to the presence of two capacitance  $C_{par}$  and  $C_Q$ . In addition to that, several jumps are visible at various biases and get attributed to single electron charging (see inset on Fig. 1d). The jumps in the  $\Delta f$  are followed by peaks in the dissipation curve (black curve) characteristic for single electron charging of TBG.

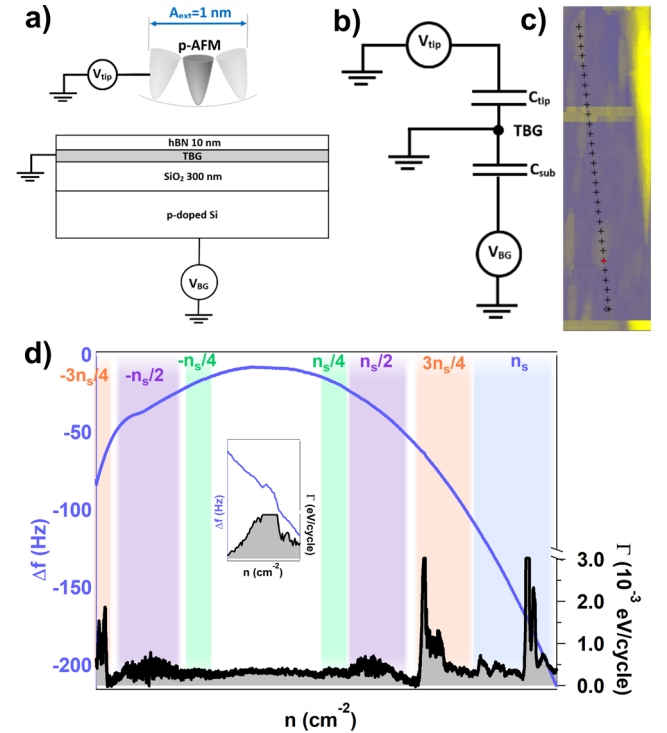


Fig. 1: a) Schematic of the side view of the TBG device with the tip in the pendulum geometry. b) Capacitance model. c) p-AFM topographic image with in yellow the high features and blue the low features. The cross line is referring to the different measurement places. The dimensions are  $200 \text{ nm} \times 1.2 \mu\text{m}$  d) is the characteristic dissipation and  $\Delta f$  spectrum that were recorded. The backgate voltage was changed into doping and the colors sections indicates the different filling factors. The inset indicate a zoom on the frequency drops that appears for every dissipation peaks.

### Angle detection

The experiment was performed by applying a backgate voltage ( $V_{BG}$ ) sweep from -40 V to 65 V to the silicon backgate and simultaneously recorded the dissipation and the  $\Delta f$ . The data were analyzed by converting the backgate voltage into doping ( $n$ ) using this formula [1]:

$$n = \frac{C_{ox} \cdot V_{BG}}{q} \quad (3)$$

where  $C_{ox} = \epsilon_0 \epsilon / t_{SiO_2}$  is the capacitance of the oxide layer. The position of the peaks with respect to the doping allows to resolve the angle and identify filling factor of every peak (see Fig. 1d) [1]:

$$n \approx n_s = \frac{8\theta^2}{\sqrt{3}a^2} \quad (4)$$

where  $n_s$  is the density needs to fully fill the mini-Brillouin zone,  $a = 0.246$  nm is the graphene lattice constant and  $\theta$  is the twist angle. The identification of every peak is noted on figure 1d.

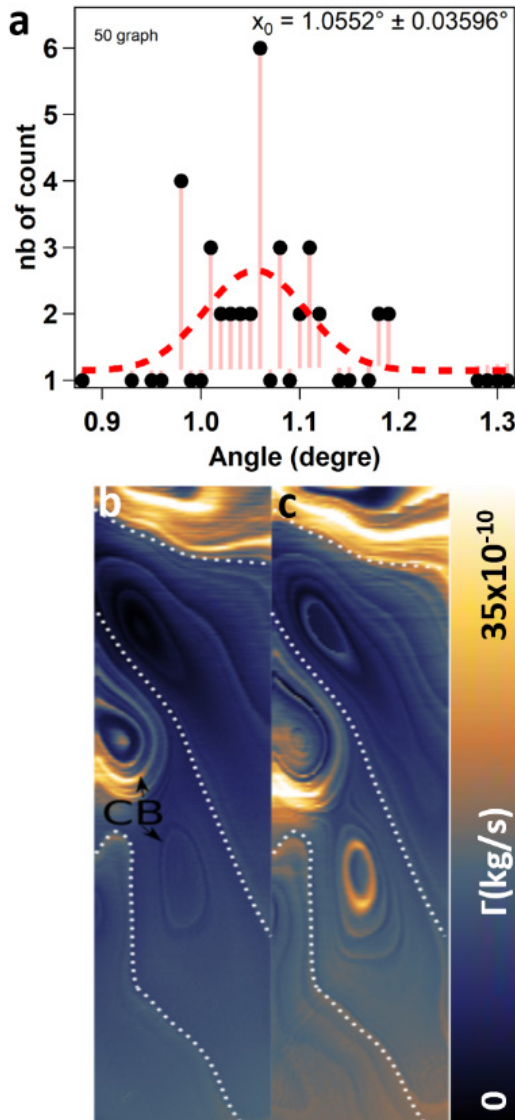


Fig. 2: Angle distribution a) is the number of counts versus the different angles. 50 graphs are taken in consideration. The red dash line is the Gaussian fit. b) and c) are excitation images over the sample surface at  $1/4$  and  $2/4$  fillings respectively. The images dimensions are  $200 \text{ nm} \times 1 \mu\text{m}$ . The dashed lines are delimitations the different angle domains.

### Angle distribution

p-AFM has the advantage to be a local probe and thus probe electronic properties at arbitrary surface spot. Figure 1c shows an AFM topographic image where the crosses on the line represent a different measurement place. A dissipation measurement at the different tip locations allows to determine the angle distribution over the sample surface. The corresponding distribution is presented on figure 2a, where a Gaussian fitting was made and revealed an average angle of  $1.06^\circ$  with a distribution of 4% over the sample surface. A complementary method to investigate the angle distribution is the recording of excitation image at a specific filling factor. Figures 2b and c show the dissipation maps for  $1/4$  and  $2/4$  fillings, respectively. Clearly visible concentric lines stand for Coulomb rings that are related to some defects in TBG [3]. Another feature that can be noted is the presence of non-concentric lines (marked by dashed lines) that suggest the existence of domains of slightly different tilt angle. The maps are validating the presence of different angles over the sample surface due to slight twist angle relaxation.

### Conclusion

In conclusion, our measurements on TBG exhibit dissipation peaks. They can be attributed to the different filling factors of the mini-Brillouin zone. In addition to that, we were able to perform angle distribution measurements that are showing a rather homogeneous angle distribution centered around  $1.06^\circ$ . The excitation maps revealed the presence of twist angle domains as well as Coulomb rings.

### References

- [1] Y. Cao, V. Fatemi, S. Fang, K. Watanabe, T. Tanaguchi, E. Kaxiras, P. Jarillo-Herrero, Unconventional superconductivity in magic-angle graphene superlattices, *Nature* 556, 43-50 (2018)
- [2] U. Gysin, S. Rast, M. Kisiel, C. Werle, E. Meyer, Low temperature ultrahigh vacuum noncontact atomic force microscope in the pendulum geometry, *Rev. Sci. Instrum.* 82, 023705 (2011)
- [3] L. Cockins, Y. Miyahara, S. D. Bennett, A. A. Clerk, S. Studenikin, P. Poole, A. Sachradja, P. Grutter, Energy levels of few electron quantum dots imaged and characterized by atomic force, *PNAS USA* 107, 9496-9501 (2010)
- [4] S. L. Tomarken, Y. Cao, A. Demir, K. Watanabe, T. Tanaguchi, P. Jarillo-Herrero, R. C. Ashoori, Electronic compressibility of magic-angle graphene superlattices, *Phys. Rev. Lett.* 123, 046601 (2019)

# Quantifying bacterial responses to antibiotics at the single-cell level

Project P1805: High-throughput multiplexed microfluidics for antimicrobial drug discovery

Project Leader: E. van Nimwegen and V. Guzenko

Collaborator: M.-E. Alaball Pujol (SNI PhD Student)

## Introduction

Without effective antimicrobials, the success of modern medicine would be at risk, for treating infections including during major surgery and cancer chemotherapy. Misuse and overuse of antimicrobials are the main drivers in the development of resistant pathogens; however, it has also become clear in the last decades that the sensitivity to treatment varies from cell to cell, even in an isogenic population. In particular, some cells are in physiological states that allow them to survive antibiotic treatment without any resistance mutations [1]. Slow growing cells have been reported to be more tolerant to antibiotics, and this increased tolerance can facilitate the subsequent fixation of resistance mutations [2]. Yet, in vitro assays used to discover antimicrobial compounds are based on liquid cultures in which bacterial cells grow exponentially so that slow-growing bacteria are outcompeted, making it impossible to assess the effects of the compounds on slow growing cells. Moreover, the determinants of sensitivity to antibiotics are only poorly understood at the single-cell level due to the lack of quantitative data.

In recent years, powerful methods have been developed to quantitatively measure behavior and responses in single bacterial cells. By combining microfluidics with time-lapse microscopy, it is possible to track growth, gene expression, division, and death within lineages of single cells. An especially attractive microfluidic design is the so-called Mother Machine, where bacteria grow within narrow growth channels that are perpendicularly connected to a main flow channel, which supplies nutrients and washes away cells growing out of the growth channels. In this field, our lab has developed an integrated microfluidic and computational setup to study the response of single bacteria to controlled environmental changes [3]: the dual-input Mother Machine (DIMM) allows arbitrary time-varying mixtures of two input media, such that cells can be exposed to a precisely controlled set of varying external conditions. The companion image analysis software MoMA segments and tracks cell lineages from phase-contrast images with high-throughput and high accuracy.

In the present project we use this integrated setup to quantify how the response of individual bacteria to treatment with antibiotics depends on their physiological state before the treatment. For this, we focus on treating *Escherichia coli* (*E. coli*) with a variety of clinically relevant antibiotics at clinically relevant concentrations. Moreover, we aim to develop new microfluidic designs that enable the study of multiple antibiotics and strains in parallel. On the long-term, this should allow us to identify compounds that specifically target non-growing subpopulations of pathogenic bacteria.

## Designing microfluidic devices to study bacterial responses to complex treatments at the single-cell level

Designing microfluidic chips that enable to multiplex the

testing of different strains and media requires improving two aspects: the loading of the cells into the device and the multiplexing of the media reservoirs. For the former, we want to design a modified version of the standard Mother Machine where the closed end of growth channels is replaced by filters. This allows to inoculate growth channels by simply “filtering” a diluted bacterial culture through the chip. In addition, with these filters, there is no nutrient gradient inside the chip and the addition or the removal of chemicals of interest is immediate. Last, the flow through the growth channels can help retaining motile cells by mechanically pushing them toward the filter end. These “filtering” channels have already been produced using a lateral constriction [4]. Given the size of these structures, it is very challenging to manufacture, and they require e-beam lithography which is not widely available.

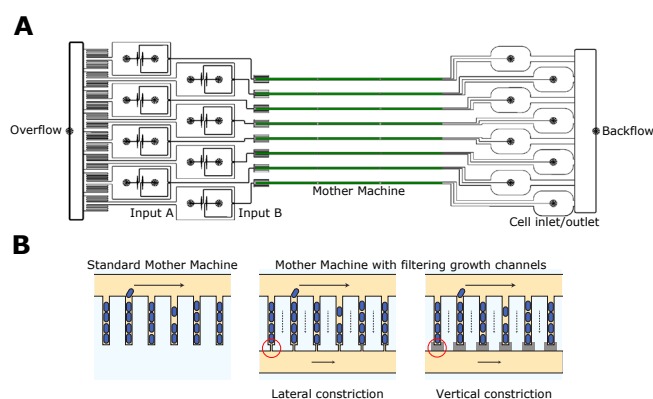


Fig. 1: Design of the microfluidic chips. A) Multiplexed DIMM. B) Different constriction designs.

The multiplexed design has eight inlets and outlets (Fig. 1A) and to establish the production of the filtering channels we have pursued two strategies (Fig. 1B). On the one hand, together with Dr. Vitaly Guzenko at PSI using different direct writing lithography techniques to microfabricate lateral constrictions. The strategy consists of two layers of different thicknesses, one for the main flow channels (20  $\mu\text{m}$  wide and 10  $\mu\text{m}$  deep), connected to the narrow (<1  $\mu\text{m}$ ) and shallow (900 nm deep) growth channels. This lateral constriction reduces the width of the channels to 250 nm. Fabrication of the growth channels and testing various constriction designs was initially done using the direct laser writer Heidelberg DWL66+. However, after several design and process parameters iterations, we concluded that the resolution of the laser writer is not sufficient to reliably define 250-300 nm wide features in the 900 nm thick resist layer. We then decided to start using e-beam lithography system Raith EBPG

5000Plus. The alternative strategy evaluated and validated by Dr. Thomas Julou is based on a 3-layer design, where the third layer is shallow enough to produce a vertical constriction, reducing the channel height by 250 nm.

### Using deep-learning to analyze Mother Machine experiments with antibiotic treatments

In our lab, the postdoc Dr. Michael Mell has developed DeepMoMA, a new version of the MoMA software, that integrates the U-Net convolutional neural network. In the beginning of the project, DeepMoMA was only capable to track cells with standard morphologies, but cells that were treated with antibiotic, which generally exhibit perturbed morphologies. Therefore, we were initially unable to analyse the experiments with antibiotic treatment. To get DeepMoMA to analyze treated cells, we have produced curated training data for U-Net from the different antibiotic treatments. We added new cell morphologies to the training data such as filamenting cells, lysing cells, and contrast-fading cells. We also introduced a new lysis assignment in the DeepMoMA software, to allow manually terminating lineages for dying cells whose remains stay in the channel. This enables tracking of cells regrowing after the treatment, while labeling dead cells at the time of death. All in all, we are now able to quantitatively analyze datasets in which *E. coli* is exposed to different antibiotics and different treatment protocols, although further improvements to increase throughput are needed.

### Mother Machine experiments to characterize bacterial responses to antibiotic treatment

We chose five antibiotics from different classes that are on the list of essential medicines: Ciprofloxacin (CIP), Ceftriaxone (CEF), Gentamicin (GEN), Trimethoprim (TMP) and Sulfamethoxazole (SMX). The experiments consist of treating repeatedly bacteria with clinically relevant concentrations of each antibiotic. We first performed a Minimum Inhibitory Concentration (MIC) study to ensure that the concentrations used in the media were consistent with peak serum concentrations. We performed Mother Machine experiments under two regimens: the first treatment lasts either 6 min or 2 hours, and the second treatment 2 hours. After each treatment, survival is assessed by exposing bacteria to fresh media for at least 10 hours. While all cells stop growing during the treatment, we find a small percentage of regrowing cells for every antibiotic treatment. The fact that we observe both death and regrowth indicate that the chosen concentrations are appropriate to study how the fate of individual bacteria during treatment depends on their physiological state before the treatment.

We obtained preliminary quantitative data from the analysis with DeepMoMA (Fig. 2) which support direct observations from the microscopy images. For the 6 min treatment in CEF the lysis rate is low and there are a small number of cells filamenting, while in the 2 hours treatment most cells lyse, and some can regrow. In CIP we see filamentation and death in both treatments, but in the 2 hours regime, cells exhibit a higher concentration of the expression of a GFP reporter of a constitutive promoter when they are exposed to the antibiotic. From the observations of the experiments, we know that cells in CIP treatment must go through filamentation to regrow while for CEF they do not have to. In GEN cells stop growing and start decreasing in contrast for both treatments. Finally, in TMP, cells stop growing during the time of the treatment but virtually all cells regrow right after it stops.

In future work, we plan to adapt our conditions to the study of UPEC strains in urine, together with testing how growth rate and gene expression are related to cell viability after treatment.

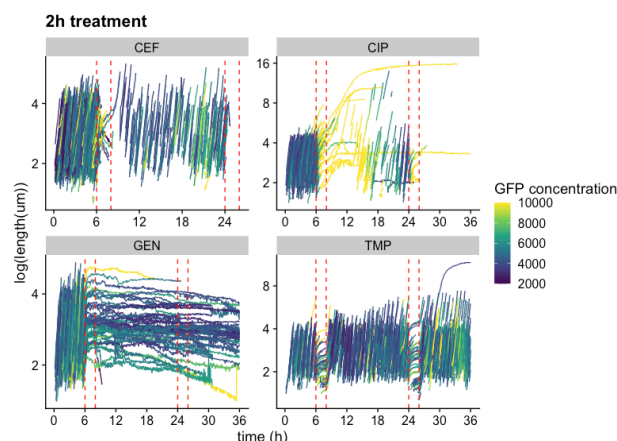


Fig. 2: Time series for cell length during the 2 h treatment. The red lines indicate the duration of the treatment. Traces are colored by concentration of GFP (GFP number of molecules divided by the length of the cell).

### References

- [1] D. Hughes and D. I. Andersson, Environmental and genetic modulation of the phenotypic expression of antibiotic resistance, *FEMS microbiology reviews* 41 (2017)
- [2] E. Rotem, A. Loinger, I. Ronin, I. Levin-Reisman, C. Gabay, N. Shoshitaishvili, O. Biham, N. Q. Balaban, Regulation of phenotypic variability by a threshold-based mechanism underlies bacterial persistence, *PNAS* 107 (2010)
- [3] M. Kaiser, F. Jug, T. Julou, S. Deshpande, T. Pfohl, O. K. Silander, G. Myers, E. van Nimwegen, Monitoring single-cell gene regulation under dynamically controllable conditions with integrated microfluidics and software, *Nat. Commun.* 9 (2018)
- [4] Ö. Baltekin, A. Boucharin, E. Tano, D. I. Andersson, J. Elf, Antibiotic susceptibility testing in less than 30 min using direct single-cell imaging, *PNAS* 114 (2017)

# Image the twist!

Project P1806: Image the twist!

Project Leader: V. Scagnoli and P. Maletinsky

Collaborators: S. Treves (SNI PhD Student), J. White, V. Ukleev

## Introduction and motivation

Recent discoveries of topological magnetic textures in centrosymmetric, rare-earth based materials have opened new perspectives for technological applications. Proposed from transport measurements and Lorentz transmission electron microscopy (LTEM), it is thought that  $\text{NdMn}_2\text{Ge}_2$  is a new room-temperature skyrmion host [1, 2]. A shortfall of LTEM is that it is only sensitive to the in-plane component of magnetization, which can be misleading for identification of the true topological charge [3]. Using x-rays to probe such a system should allow for a clear distinction between two skyrmionic structures (Fig. 1) to be visible. This is due to its sensitivity to the out-of-plane component of the magnetization. This sensitivity could allow us to observe the switching of the skyrmion lattice polarity using applied external magnetic field. Another potential investigation is the difference in response of the lattice to a field parallel or antiparallel to the skyrmion cores. Such observations were recently simulated for infinitely thin films with and without defects [4]. X-rays experiments are based on a modified tomographic setup, the so-called laminography geometry. This setup combines a scanning transmission x-ray microscopy (STXM) and a rotating sample stage, which is tilted at a predetermined angle (usually 30 degrees from the sample axis). X-ray magnetic circular dichroism (XMCD) projections are taken at angular intervals until at least one full sample rotation has been accomplished. Datasets such as these are passed through a reconstruction algorithm and result in a three-dimensional magnetic reconstruction [5]. These could provide further information on the skyrmion lattice and formation/annihilation events. Such information is critical if these topological structures are to be used for future magnetic memory storage devices [6]

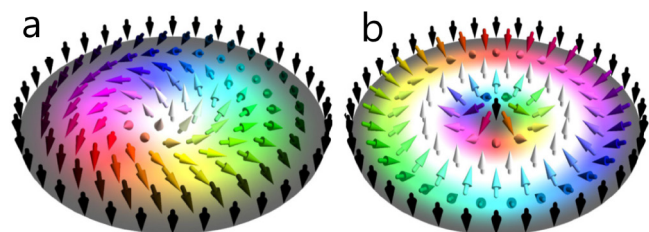


Fig. 1: Magnetic moment configuration for a) Skyrmion and b) Skyrmionium. The coloured arrows represent magnetic moment orientation. Black and white represents the negative and positive out-of-plane orientations respectively. Figure adapted from Ref. [7].

In the second year of this project, we have successfully established and imaged a metastable skyrmion lattice in two dimensions in a  $\text{NdMn}_2\text{Ge}_2$  sample. This material is interesting as our bulk measurements suggest the presence of different metastable magnetic textures stabilized by the high- and low-

field cooling protocols. Moreover, by taking advantage of the possibility to chemical substituting Nd by the non-magnetic La ion we would like to explore the role of the rare-earth element in determining the magnetic configuration in this family of compounds. Specifically, we expect that skyrmion/bubble lattice parameter in  $\text{LaMn}_2\text{Ge}_2$  will differ compared to  $\text{NdMn}_2\text{Ge}_2$  due to the interplay between d and f orbitals. Our preliminary measurements, supporting the presence of a skyrmion lattice, provide us with the basis to conduct laminography experiments at room temperature with zero field, in order to obtain a 3D magnetic dataset. Simulations of this material are being conducted with a similar approach as found in [4]. This will allow us to know whether to expect the switching behavior in our material that was seen in the simulations. These simulations can also provide stray field information which can be used to see if Nitrogen-vacancy (NV) magnetometry measurements of the system are possible. This could then be used to reconstruct the magnetic components quantitatively

## Key experimental results:

During the second year of this project, new opportunities presented themselves. One exciting development was the successful beamtime using scanning transmission x-ray microscopy at the Pollux beamline of the Swiss Light Source. This experiment used a lamella of  $\text{NdMn}_2\text{Ge}_2$  cut from a single crystal.

The initial milestone accomplished was to obtain the skyrmion phase from the as grown helical magnetic state of the sample (Fig. 2). This was achieved using a field cooling method, a small magnetic field (50 mT) is applied to the sample whilst cooling from above the  $T_c$  (330 K) temperature. The resulting skyrmion lattice remained unchanged once the field was removed at room temperature (RT). This metastable property is vital if laminography experiments are to be conducted as the sample will have to be imaged over a period of several days, without a magnetic field.

A further observation made involved increasing the system's temperature from 300 K (RT) to 330 K. Loss of the skyrmion lattice occurred around 325 K, where a helical phase was recovered. The skyrmion lattice remained unchanged in size and shape up until this point.

In order to fully characterize the phase diagram of the lamella (which could differ from the bulk crystal one due to magnetostatic effect) we have imaged the magnetic configuration of the sample as a function of applied magnetic field. Increasing the magnetic field from 50 mT to 200 mT caused a gradual breakup of the skyrmion lattice into individual skyrmions and the final state was a fully ferromagnetic (FM) state. When decreasing from 50 mT to -200 mT, skyrmions expand in size, gradually enveloping neighbouring skyrmions. This continues until large bubble domains eventually develop into a negative FM state.

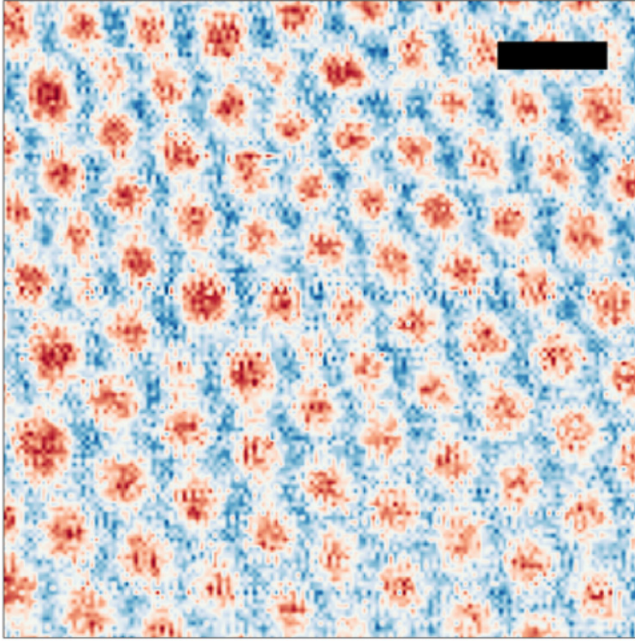


Fig. 2: Skyrmion lattice imaged in a thin lamella of  $\text{NdMn}_2\text{Ge}_2$  using STXM at room temperature with no magnetic field applied. The black scale bar represents 500 nm.

An interesting topological change occurs if the field is swept from 50 mT to -140 mT and then back to 200 mT (Fig. 3). Here we observe the skyrmion lattice expand in size initially, the magnetic structures then begin to elongate. These elongations then become thinner until we recover skyrmions closer to 200 mT. However, there are fewer skyrmions in this final configuration with greater spacing than the initial skyrmion lattice.

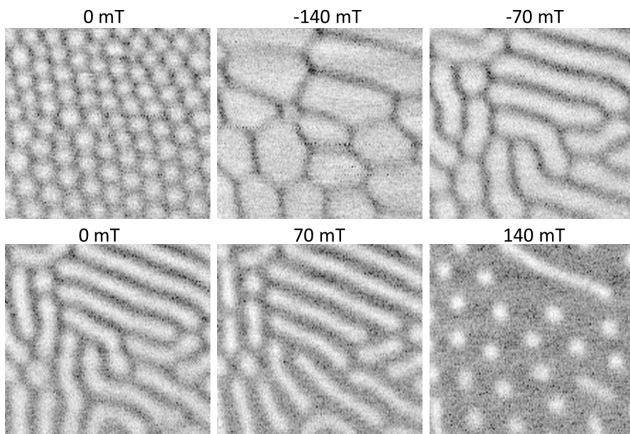


Fig. 3: Top row, left to right: Starting directly after the field cooling from 330 K to 300 K with a 50 mT field. The skyrmions in the lattice then expand in size as the field is taken from 0 to -140 mT. They then elongate as the field is stepped to -70 mT. Bottom row, left to right: The elongation and shrinking of the skyrmions continues as the field passes through 0 mT and reaches 70 mT. The long structures then start to break apart and a skyrmion lattice is regained as the field reaches 140 mT. The skyrmion number in this final lattice is reduced when compared with the starting state. The field of view of each image is  $3 \times 3 \mu\text{m}^2$ .

Our observations have a different outcome to the predictions of Pierobon et al [4]. Here it is predicted that the skyrmions will expand in size to form a hexagonal lattice as the applied magnetic fields direction is reversed. Then this state will undergo a first order phase transition to either a fully

FM state or a skyrmion lattice with a polarity that has the reverse polarity of the starting skyrmion lattice. This metamagnetic-like transition is characterized by a discontinuous change in the total magnetization and skyrmion radius. To understand why our measurements differ from these predictions simulations of our system will need to be conducted.

### Outlook

The results obtained from this beamtime demonstrate the highly interesting nature of the  $\text{NdMn}_2\text{Ge}_2$  system. The capability of hosting a metastable skyrmion lattice at room temperature, without application of external magnetic field make it an ideal candidate for future laminography experiments and NV experiments. Simulations will also assist in the understanding of this system's behavior with changing external stimuli.

### References

- [1] S. Wang, et al., Giant Topological Hall Effect and Superstable Spontaneous Skyrmions below 330 K in a Centrosymmetric Complex Noncollinear Ferromagnet  $\text{NdMn}_2\text{Ge}_2$ . *ACS Applied Materials and Interfaces*, 12(21), 24125–24132 (2020)
- [2] Z. Hou, L. Li, C. Liu, X. Gao, Z. Ma, G. Zhou, Y. Peng, M. Yan, X.-x. Zhang, J. Liu, Emergence of room temperature stable skyrmionic bubbles in the rare earth based  $\text{REMn}_2\text{Ge}_2$  (RE = Ce, Pr, and Nd) magnets. *Materials Today Physics*, 17, 100341 (2021)
- [3] J. C. Loudon et al., Do Images of Biskyrmions Show Type-II Bubbles? *Advanced Materials*, 31(16) (2019)
- [4] L. Pierobon, C. Moutafis, Y. Li, J. F. Löffler, M. Charilaou, Collective antiskyrmion-mediated phase transition and defect-induced melting in chiral magnetic films. *Scientific Reports*, 8(1), 1–9 (2018)
- [5] C. Donnelly, M. Guizar-Sicairos, V. Scagnoli, S. Gliga, M. Holler, J. Raabe, L. J. Heyderman, Three-dimensional magnetization structures revealed with X-ray vector nanotomography. *Nature*, 547(7663), 328–331 (2017)
- [6] S. S. P. Parkin, H. Masamitsu, L. Thomas, Magnetic Domain-Wall Racetrack Memory. *Science*, 320(5873), 190–194 (2008)
- [7] B. Göbel, I. Mertig, O. A. Tretiakov, Beyond skyrmions: Review and perspectives of alternative magnetic quasiparticles. *Physics Reports*, 895, 1–28 (2021)

# Interactions between a high-impedance resonator and semiconducting nanowires

Project P1807: Andreev Spin Qubit (ASQ) in Ge/Si Nanowires

Project Leader: C. Schönenberger, F. Braakman, I. Zardo, and D. Zumbühl

Collaborators: J. H. Ungerer (SNI PhD Student), A. Pally, L. Y. Cheung, P. Chevallier-Kwon, J. Ridderbos, T. Patlatiuk, R. Haller, A. Kononov, D. Sarmah, S. Lehmann, E. Bakkers, V. F. Maisi, C. Thelander, K. A. Dick, A. Baumgartner, D. Zumbühl, C. Schönenberger

## High-impedance resonators for investigation of semiconducting nanowires

The realization of quantum computers promises an enormous impact on many crucial parts of society [1]. Working prototypes of quantum computers that host a few qubits have been demonstrated, but in order to be able to perform useful calculations on, it is necessary to increase the number of qubits. However, scaling these system turns out to be very challenging. Currently, among the most promising contenders for the realization of scalable quantum computers are Josephson-junction based superconducting qubits and spins of confined particles in semiconductors and superconducting circuits. In both cases superconducting resonators can be used for qubit manipulation and readout.

Here we explore a hybrid approach by coupling a superconducting resonator to a semiconducting nanowire (NW). NWs are of particular interest, because of their large, intrinsic spin-orbit interaction (SOI). NWs can act as hosts of spin qubits or in combination with superconducting leads as hosts of Andreev levels or Majorana bound states.

## Coupling a high-impedance resonator to a double-quantum dot formed in a NW

For our project, we have realized high-quality, high-impedance, magnetic-field resilient superconducting resonators based on thin NbTiN films (see previous report). We have coupled these resonators to both, a gate-defined double-quantum dot (DQD) in a Ge/Si core/shell NW [2] and to a DQD formed by crystal-phase defined barriers in an InAs NW [3]. For the sake of brevity, we focus in this report on the implementation of an InAs DQD as a model system for a spin qubit. Although III-V semiconductors carry nuclear spins that can decohere the spin qubit, we use InAs NWs, because in this system the three barriers defining the DQD can be realized “in-situ” during growth. This has two advantages: i) one obtains a stronger and engineer-able barrier down to the atomic scale, and ii) potentially a more robust confinement that is less prone to charge-noise compared to gate-controlled DQDs.

In the InAs NWs, each QD is formed by a zincblende InAs segment of length  $\sim 300$  nm. Zincblende InAs NWs are of particular interest, because of their large Dresselhaus SOI. The SOI combined with the large length of the QDs maximize the spin-photon coupling when coupled to a high-impedance resonator.

A large interaction is furthermore ensured by galvanically connecting the resonator to the source contact of the NW (see inset of figure 1 as this contact has a large lever arm to one of the two QDs). In the false-colored scanning electron micrograph shown in the inset of figure 1, one can identify the two QDs which are separated by an InAs wurzite segment of  $\sim 30$  nm length acting as tunnel barrier. Two further tunnel barriers separate each QD from its respective lead

contact and the gate electrodes with voltages  $V_L$  and  $V_R$  are used for tuning the electro-chemical potential in either QD.

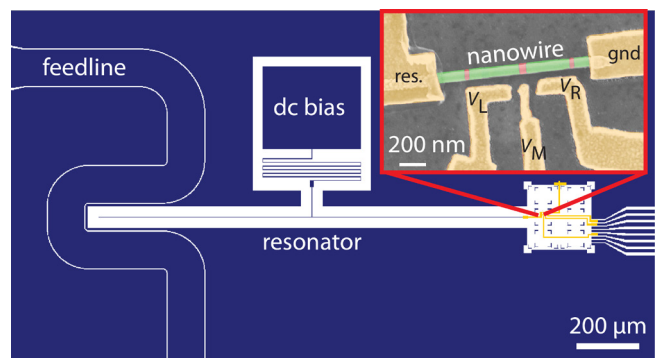


Fig. 1: Schematic of the circuit-QED architecture. NbTiN is shown in blue, Si in white, gold in yellow. Inset: False-colored scanning electron micrograph of the InAs homoepitaxial structure. Zincblende InAs is shown green, wurzite red. The gold contacts are yellow. The contact that is labeled ‘res.’ is galvanically connected to the center conductor of the resonator.

We identify the half-wave mode of the resonator at a frequency of  $f_0 \approx 3.543$  GHz and extract its coupling Q factor  $Q_c \approx 2'600$  and loss Q factor,  $Q_{\text{loss}} \approx 2'400$  by performing a circular fit [4] (see red data in Fig. 2).

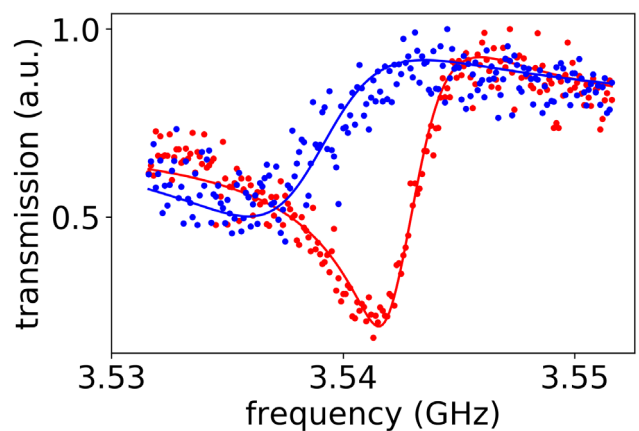


Fig. 2: Feedline transmission as function of probe frequency. Red data reflects the bare resonance. The blue data is acquired at a dot-dot detuning of  $\epsilon/2\pi = 17$  GHz. Solid lines are the amplitudes of circular fits.

We then perform continuous resonator spectroscopy at a frequency close to the resonance frequency and tune the electrostatic potential of the two QDs by changing the gate voltages (Fig. 3a). Whenever one of the QDs' electro-chemical potentials is degenerate with the electro-chemical potential of the lead or, if the potentials of both QDs are degenerate with each other, the microwave admittance of the DQD changes. As a consequence, the resonator responds by a change in magnitude and phase. In figure 3a, we recover the characteristic honeycomb pattern outlining the charge-stability diagram of the DQD.

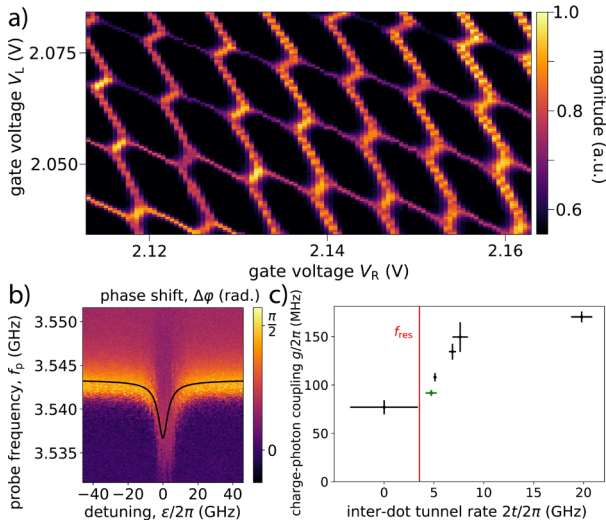


Fig. 3: a) Spectroscopy signal of the resonator as a function of gate voltages. One can clearly identify the characteristic honeycomb-pattern of the DQD charge-stability diagram. b) Resonator spectroscopy (phase shift) as a function of probe-frequency and electrostatic detuning from inter-dot degeneracy exhibiting a dispersive shift of the resonator due to a finite charge-photon coupling. The black line is a fit to the Hamiltonian model. c) Extracted charge-photon coupling strengths vs. inter-dot tunnel rate for different inter-dot configurations. The data point corresponding to b) is highlighted in green and the bare resonance frequency of the resonator is indicated by a red line.

Because of the tunnel coupling between the two QDs, a charge qubit forms which is interacting with the resonator. Figure 3b shows the resonator spectroscopy as a function of electro-static detuning between the two dots. As the detuning decreases, the charge-qubit transition frequency approaches the resonator, and the latter is dispersively shifted. To extract the resonance frequency, we perform a circular fit to the resonance for each detuning value. An exemplary line trace for a detuning is shown as blue curve in figure 2, where the shift with respect to the bare resonance is visible. Then, we fit a Jaynes-Cummings Hamiltonian model (solid, black line in Fig. 3b) and extract the tunnel rate  $2t/2\pi \approx 5$  GHz and the charge-photon coupling strength  $g \approx 170$  MHz. We note that the large charge-photon coupling strength, due to the large resonator impedance and large dipole moment of this DQD system, is the current world record for a NW DQD. We perform similar analyses at several DQD configurations and plot all tunnel rates and charge-photon coupling strengths against each other in figure 3c. The large spread of tunnel rates for different configurations allows to ‘tune’ the charge-qubit transition frequency and eventually bring it in resonance with the resonator. In the shown experiments, the charge qubit line width was large,  $\gamma > 1$  GHz and inhibited the observation of an avoided crossing between qubit

and resonator. We hope to reduce the qubit line width in future experiments by reducing the coupling with the leads.

### Nanowire Josephson Junctions

Besides the focus on DQDs in NWs, we have also worked on InAs NW Josephson junctions. These junctions host Andreev qubits [5]. In our project, we have used a new type of material where the Al/InAs/Al Josephson junctions are in-situ defined by means of shadow epitaxy [6]. We have coupled these junctions to microwave resonators with the goal to investigate the dynamics of the junction.

### References

- [1] T. D. Ladd, F. Jelezko, R. Laflamme, Y. Nakamura, C. Monroe, J. L. O’Brien, Quantum computers, *Nature* 464, 45 (2010)
- [2] F. N. M. Froning, M. K. Rehmann, J. Ridderbos, M. Brauns, F. A. Zwanenburg, A. Li, E. P. A. M. Bakkers, D. M. Zumbühl, F. R. Braakman, Single, double, and triple quantum dots in Ge/Si core/shell nanowires *Appl. Phys. Lett.* 113, 073102 (2018)
- [3] S. Lehmann, J. Wallentin, D. Jacobsson, K. Deppert, K. A. Dick, A general approach for sharp crystal phase switching in InAs, *Nano Lett.* 13, 4099 (2013)
- [4] S. Probst, F. B. Song, P. A. Bushev, A. V. Ustinov, M. Weides, Efficient and robust analysis of complex scattering data under noise in microwave resonators, *Rev. Sci. Instrum.* 86, 024706 (2015)
- [5] L. Tosi, C. Metzger, M. F. Goffman, C. Urbina, H. Pothier, Sunghun Park, A. Levy Yeyati, J. Nygård, P. Krogstrup, Spin-orbit splitting of Andreev states revealed by microwave spectroscopy, *Phy. Rev. X* 9, 011010 (2019)
- [6] D. J. Carrad, M. Bjergfelt, T. Kanne, M. Aagesen, F. Krizek, E. M. Fiordaliso, E. Johnson, J. Nygård, T. Sand Jespersen, Shadow epitaxy for in situ growth of generic semiconductor/ superconductor hybrids, *Adv. Mat.* 32 1908411 (2020)

# Quantum control of a trapped ion coupled to a nanomechanical oscillator

Project P1808: Quantum dynamics of an ultracold ion coupled to a nanomechanical oscillator  
Project Leader: S. Willitsch and M. Poggio  
Collaborator: M. Weegen (SNI PhD Student)

## Introduction

Ions stored in linear radio frequency traps are well-established quantum systems in which a high degree of control over their quantum states and dynamics can be obtained paving the way for many applications in the fields of physics and chemistry, e.g., mass spectrometry, precision measurements and quantum computing and technologies [1]. Nanomechanical oscillators, on the other hand, can be used as highly sensitive sensors interfaced with different quantum devices and hybrid systems [2]. One famous application is atomic force microscopy. Their nanoscopic size allows for their implementation in miniaturized devices.

The goal of the present project is to combine both platforms in an ion-nanowire hybrid system offering new ways for the control and manipulation of the motional quantum state of the ion. Coupling of the two systems is achieved via the Coulomb interaction by putting an effective charge on the nanowire. By driving oscillations of the nanowire, the ion's motional state is mechanically excited and manipulated [3]. The mechanical manipulation of the ion's motional quantum state is dependent on several parameters, such as the relative ion-nanowire position, the effective charge and the detuning between the ion's oscillation frequency and the nanowire's resonance frequency. The ion-nanowire interaction may also be used to manipulate the quantum state of the nanowire provided it can be cooled to the quantum regime of its motion [3, 4].

Because the conducting nanowire acts as an additional electrode in the ion trap, it will contribute to the total effective trapping potential. As such, we view the nanowire as a flexible addition to the trap that can be used for fine-tuning the trapping parameters and shaping trap potentials, e.g., by introducing anharmonicities and generating different potential topologies like double wells.

Here, we report progress on the experimental implementation of the ion-nanowire hybrid system consisting of a  $^{40}\text{Ca}^+$  ion and a metallic  $\text{Ag}_2\text{Ga}$  nanowire, showing the trapping of single ions as well as a characterization of the setup and the nanowire's impact on the trapping potentials.

## Experimental Setup

The heart of the experimental setup is a miniaturized, gold-coated-alumina-wafer radio frequency ion trap combined with a metallic  $\text{Ag}_2\text{Ga}$  nanowire. The nanowire is situated below the trap center and can flexibly be positioned in all three dimensions with nanopositioners. The setup is shown in figure 1.

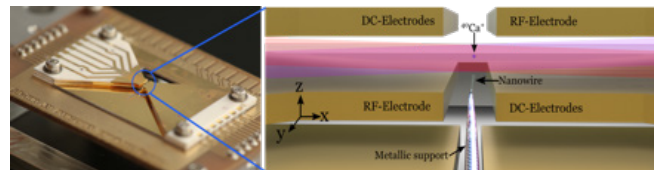


Fig. 1: Left: Photograph of the gold-coated alumina-wafer ion trap. Right: Schematic of the trap center with the nanowire [3].

Single  $^{40}\text{Ca}$  atoms are introduced into the trap via an evaporative calcium source and ionized in two steps using a combination of 423 nm and 375 nm lasers. The resulting  $^{40}\text{Ca}^+$  ions are Doppler cooled with a 397 nm cooling and 866 nm repumping laser and confined in the trap by a combination of static and dynamic electric fields. Single ions as well as large Coulomb crystals consisting of several ions can be stored in the trap. Their trapping frequency can be adjusted by varying the static and dynamic voltages of the trap. The ions can be observed by collecting the scattered 397 nm light on a CCD camera (Fig. 2).

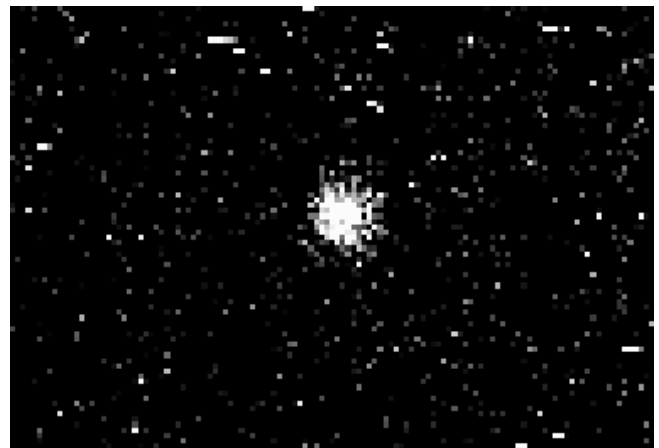


Fig. 2: CCD camera image of a single ion obtained by collecting the light scattering during Doppler laser cooling.

## Trapping Potential Characterization

The metallic nanowire in the trap acts as an additional electrode, changing the effective trapping potential of the ions. Since we aim for a full control over the ions' trap frequency to match it with the resonance frequency of the nanowire, we characterized the impact of the nanowire on the trapping potential.

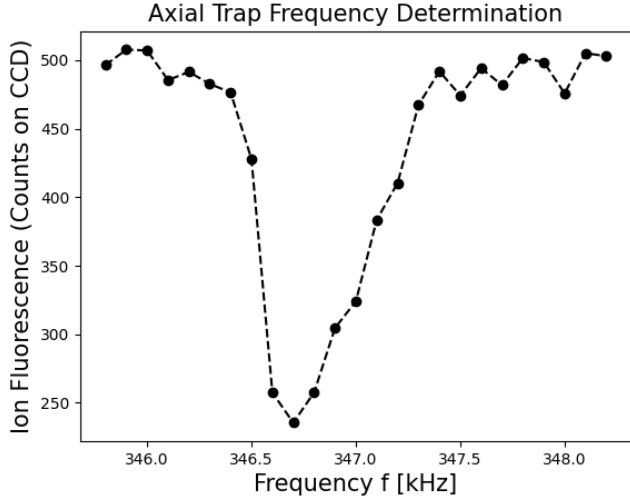


Fig. 3: Example for the determination of the motional frequencies of the ions in the trap. By applying an AC voltage to one of the trap electrodes and sweeping its frequency, the motion of the trapped ions is resonantly excited. The position of the minimum of the fluorescence yield indicates the motional frequency of the ion (here of the axial mode of motion).

The motional frequencies of the ion in the trap potential were determined by applying a small AC voltage on one of the trap electrodes. A decrease in the ion fluorescence signal can be observed due to motional heating when the frequency of the applied voltage matches the motional frequency of the ion, see figure 3.

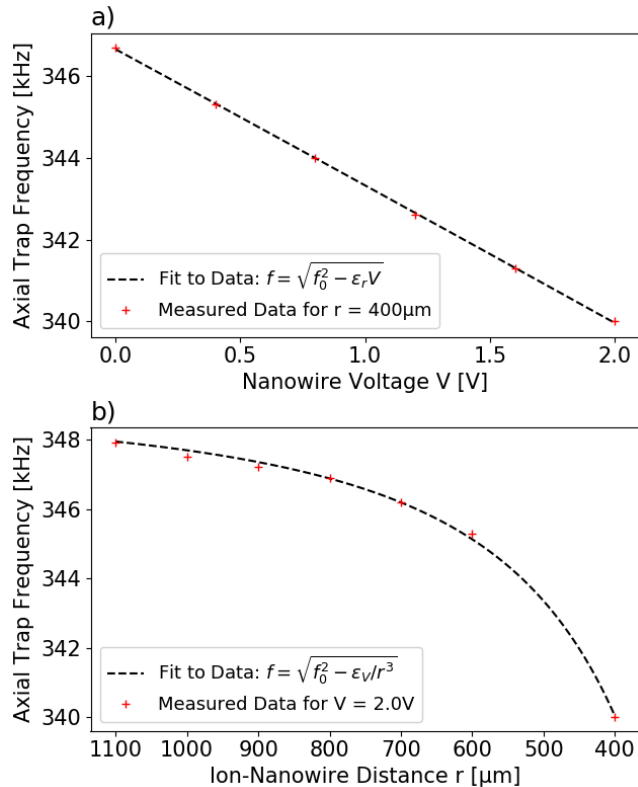


Fig. 4: Dependence of the axial motional frequency of the ions on the nanowire applied voltages (a) and position (b). The fit functions are a direct result from our theoretical model [3].  $f_0$  is the initial (unperturbed) axial ion frequency. The parameters  $\epsilon_r$  and  $\epsilon_v$  describe the strength of the ion-nanowire interaction as a function of  $r$  and  $V$ , respectively.

The ion-nanowire interaction is mainly dictated by two parameters: the effective charge (or voltage) on the nanowire and the relative ion-nanowire position. In a recently developed theoretical model, the interaction is described in terms of a Coulomb interaction between two-point charges [3]. Figure 4 shows the change in trap frequencies for different nanowire voltages and positions relative to the ion. Those results show the impact of a static voltage applied to the nanowire, but do not yet include any dynamic mechanical drive.

The experimental data are well described by our theoretical model [3] for relatively large ion-nanowire distances. For very small distances in the range of a few 10 micrometers, the nanowire's presence leads to stronger distortions of the electric fields, leading to an increase of anharmonic terms and, potentially, the generation of double well potentials.

### Summary & Outlook

During the reporting period, the experimental setup was completed and successfully commissioned. Ions were successfully trapped and laser cooled. The effect of the nanowire on the trapping fields and thus on the motional frequencies of the ion could be characterized and analyzed in terms of a recently developed theoretical model for the interaction. As a next step, we will explore the ion-nanowire interaction in the classical regime by exciting the ion motion with the mechanical drive and studying the resulting classical motional dynamics. This will be the basis for an investigation of the ion motion in the quantum regime under the action of the mechanical drive. For this purpose, resolved sideband cooling of the ions to their motional ground state of the trap will be implemented.

### References

- [1] S. Willitsch, Coulomb-crystallised molecular ions in traps: methods, applications, prospects, *Int. Rev. Phys. Chem.* 31(2), 175 (2012)
- [2] J. M. Pirkkalainen, S. Cho, F. Massel, J. Tuorila, T. Heikkilä, P. Hakonen, M. A. Sillanpää, Hybrid circuit cavity quantum electrodynamics with a micromechanical resonator, *Nat. Commun.* 6, 6981 (2015)
- [3] P. N. Fountas, M. Poggio, S. Willitsch, Classical and quantum dynamics of a trapped ion coupled to a charged nanowire, *New J. Phys.* 21(1), 013030 (2019)
- [4] F. Pistolesi, A. N. Cleland, A. Bachtold, Proposal for a Nanomechanical Qubit, *Phys. Rev. X* 11, 031027 (2021)

# Whole cell vitrification to study neurodegenerative disorders

Project P1901: Microfluidics to Study Huntington's Disease by Visual Proteomics

Project Leader: T. Braun, E. Pecho-Vrieseling, and H. Stahlberg

Collaborator: A. Fränkl (SNI PhD Student) and A. Almoudi

## Introduction

Developing and understanding of high-resolution structural information is essential to elucidate the protein's working mechanisms. In recent years, cryogenic electron microscopy (cryo-EM) has become a convincing method to determine macromolecules' architecture at atomic resolution. However, cryo-EM is still rapidly developing; a particular research focus is the development of new sample preparation methods and expanding the application of EM as an analytical tool.

During recent years, we have developed a system of microfluidic modules for cryo-EM sample preparation. The different modules can be combined specifically for an experiment. Typical examples are (i) the microfluidic isolation, cryo-EM preparation, high-resolution cryo-EM, and building of an atomic model from less than 1  $\mu\text{L}$  cell lysate [1, 2, 3], or (ii) the single-cell analysis by visual proteomics by combining microfluidic cell-lysis and EM sample preparation [3, 4]. The latter allows the proteome-wide detection of the structural rearrangement of protein complexes of single cells by a method we called "differential visual proteomics". Unfortunately, this method does not allow investigating the social context of proteins in the cell. However, new work-flows were developed, allowing us to "mill" a lamella into the cell, which is thin enough to investigate the proteins at high resolution by cryo-EM tomography. This allows the in situ investigation of the proteins in a small part of the cell. Unfortunately, classical preparation methods for whole-cell vitrification use extensive filter paper blotting or are extremely slow, disturbing thin cellular structures and exhibiting significant intra-cellular stress.

Here we aim at developing a new preparation protocol for the vitrification of adherent eukaryotic cells. The method avoids filter-paper blotting entirely and can be performed in less than half a minute. Furthermore, the cell's environment is controlled throughout the preparation, and the workflow should allow monitoring of the cellular structures by light microscopy immediately before vitrification. This whole-cell cryogenic module will provide (i) correlative light and electron microscopy information, (ii) full integration with the current cryoWriter toolchain, and (iii) the microfluidic aspiration and withdrawal of solution for controlled fluid dynamics. This new cryoWriter module will be combined with microfluidic chips in the future, controlling the geometrical rearrangement of neurons.

## Whole cell vitrification module integration with the cryoWriter setup

The cryoWriter keeps the EM-sample carrier ("grid") horizontally until the final vitrification step (Fig. 1), allowing the semi-automation of all actions and keeping the cells in a physiological state. However, the grid must be accessible for grid-gripping tweezers [4]. Therefore, a new grid holder

(Fig. 2A) was designed (i) allowing in situ cell culturing for several days to grow eukaryotic cells directly on EM grids, (ii) enabling light microscopy during the culturing and immediately before plunge-freezing, and (iii) efficient microfluidic introduction and removal of fluids for vitrification. We designed a 10 mm by 10 mm by 6 mm device that contains a small sealed chamber to allow for temperature control (Fig. 1A). The top allows for integrating a 100  $\mu\text{m}$  thick polydimethylsiloxane (PDMS) membrane enabling the non-permanent binding of gold EM grids to the surface.

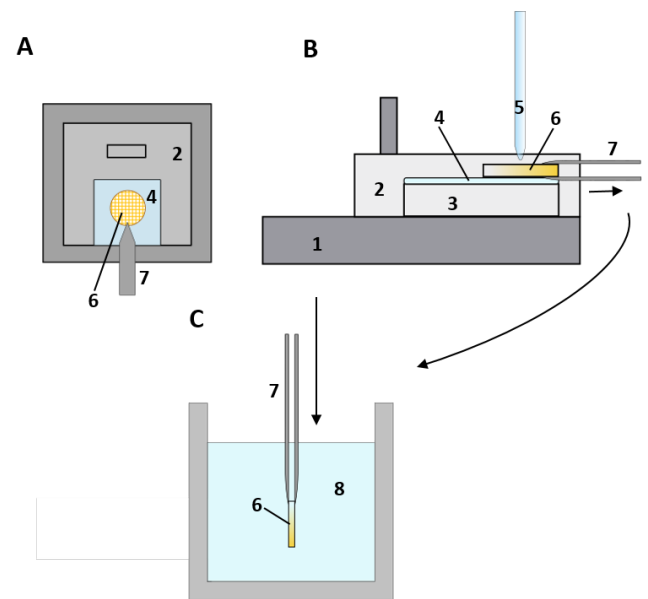
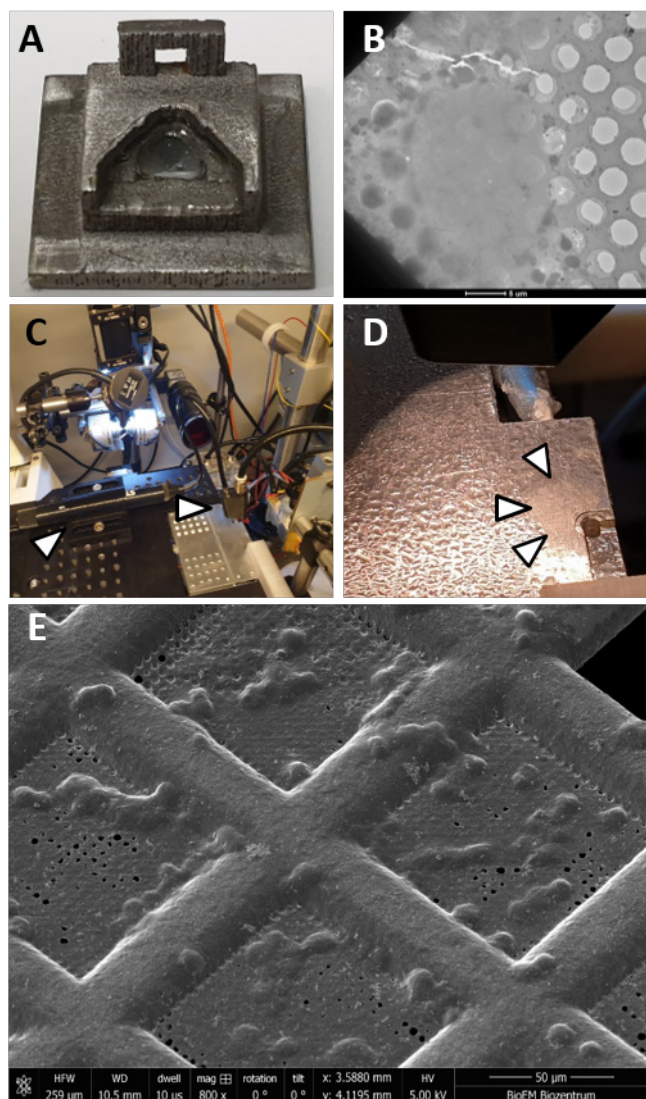


Fig. 1: A) A schematic top overview representation of a correlative light and electron compatible growth platform. B) A schematic side overview representation of a correlative light and electron compatible growth platform. Neuronal cells are grown on a functionalized gold EM grid (6) which is placed on thin PDMS membrane (4) that allows for correlative light electron microscopy. The growth device (2) contains a chamber that allows for heat retention (3) and a tweezers grip placed at the top for easy handling. This device is placed on a temperature-controlled platform (1). The gold grid is gripped by a temperature-cooled tweezers (8) before being plunge frozen in liquid nitrogen (8) after flipping the grid in a vertical position. Fluid dynamics are controlled via a microfluidic capillary (5).

Preliminary tests showed that eukaryotic cells grow homogeneously on functionalized cryo-EM grids when mounted in our device (Fig. 2E). Furthermore, the new device allows direct vitrification using the cryoWriter setup with good preservation of the overall cell structures (Fig. 2B). However, when withdrawn only via microfluidic capillaries, the

removal of the remaining buffer fluid left a thick ~20  $\mu\text{m}$  layer of liquid behind. This obscured any neurons for the Focused ion beam (FIB) milling of a lamella. Therefore, we developed a directed climate-control device to reduce the amount of remaining fluids alongside microfluidic withdrawal (Fig. 2C and D). These developments now enable a two-step whole-cell preparation: Firstly, most of the excess fluid is removed via the microfluidic capillary, and secondly, a directed “climate-jet” to remove the remaining liquid on the EM grid (Fig. 2E). The preparation platform is now ready for the vitrification of adherent eukaryotic cells and subsequent FIB-milling of a lamella for cryo-EM tomography.



*Fig. 2: A) Stainless steel 3D printed correlative light and electron compatible growth platform with PDMS membrane. B) Whole vitrified neuroblastoma cells on a gold EM grid. C) Directed climate-controlled device to deliver humidified temperature controlled gas stream to A) growth device. D) Excess fluid removed in a controlled fashion by the climate control device. E) Whole vitrified neuroblastoma cells on a gold EM grid.*

## Outlook

We will now aim to integrate the whole-cell vitrification device with microfluidic chips containing multi-chamber interfaces to observe geometrically controlled axon and dendrite outgrowth. We will use this new method to study the stereotypical spreading of prion-like seeds through the nervous system, which is a hallmark of many neurodegenerative disorders like Huntington’s disease.

## References

- [1] S. Kemmerling, S. A. Arnold, B. A. Bircher, N. Sauter, C. Escobedo, G. Dernick, A. Hierlemann, H. Stahlberg, T. Braun, Single-cell lysis for visual analysis in electron microscopy. *J. Struct. Biol.* 183, 467–73 (2013)
- [2] S. A. Arnold, S. Albiez, N. Opara, M. Chami, C. Schmidli, A. Bieri, C. Padeste, H. Stahlberg, T. Braun, Total sample conditioning and preparation of nanoliter volumes for electron microscopy. *ACS Nano*, 10, 4981–4988 (2016)
- [3] S. A. Arnold, S. A. Müller, C. Schmidli, A. Syntychaki, L. Rima, M. Chami, H. Stahlberg, K. N. Goldie, T. Braun, Miniaturizing EM Sample Preparation: Opportunities, Challenges and “Visual Proteomics”. *Proteomics*, 18, 1700176 (2018)
- [4] C. Schmidli, S. Albiez, L. Rima, R. Righetto, I. Mohammed, P. Oliva, L. Kovacik, H. Stahlberg, T. Braun, Microfluidic protein isolation and sample preparation for high-resolution cryo-EM, *PNAS* 16.30, 15007–15012 (2019)

# Dual scale approach using conductive nanofibers towards enhanced cardiac tissue engineering

Project P1902: Directional 3D nanofiber network to mimic in-vivo myocardial syncytium towards guiding contraction patterns in in-vitro heart models

Project Leader: M. Gullo, M. Poggio, and A. Marsano

Collaborator: F. Züger (SNI PhD Student)

## Introduction

Cardiovascular diseases are one of the most common causes of hospitalization or death in the industrialized world and are becoming a leading global threat of the 21st century. An impairment of heart functionality, after a myocardial infarction combined with a low intrinsic regenerative capability of cardiomyocytes (CMs) leads to a loss of cardiac tissue. Replacing affected tissue urges the need for novel biofabrication methods to counter this challenge [1, 2].

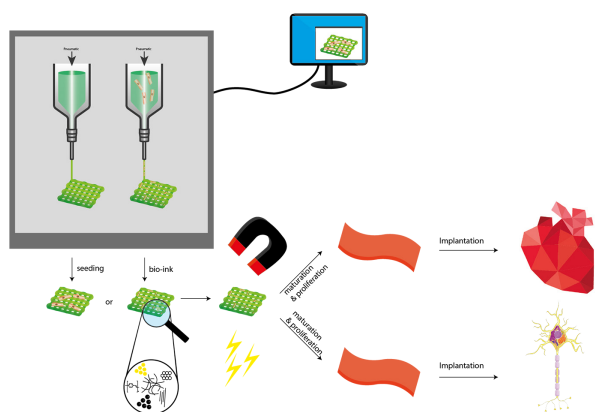


*Fig. 1: Schematic representation of a typical workflow of a biofabrication process to produce cardiac or neural constructs. Custom architecture is designed with a specific software and sent to the 3D-printing machine. The nanocomposite doped printed hydrogel, either already including cells or seeded on it after the printing process, is matured using electrical or magnetic cues and can be implanted into damaged or diseased cardiac or neural tissue.*

Using biofabrication techniques to mimic and replicate natural tissue as well as cell environment is a very capable way to achieve physiologically relevant conditions. Especially in electrophysiological human tissue like cardiac tissue, proper signal transduction is of paramount importance for appropriate function and cell maturation as well as differentiation. Precisely, these conductive properties are challenging to engineer. In human cardiac tissue the conductance within the whole myocardium is provided by specialized cells (Purkinje fibers) with a high conductivity, capable to propagate timely the electrical signal. These cells forming the so called syncytium [3]. To rebuilt this natural properties current research tries to exploit the intrinsic characteristics of conductive nanocomposites, like metal nanocomposites (NPs), carbon nanotube (CNTs) or graphene and integrate them into non-conductive hydrogels. In our project conductive nanofibers are being biofabricated to mimic this conductive system and make electrical stimulation possible. Together with our dual

scale approach in which 3D-printed micrometer scale and electrospun nanometer scale structures are combined, electrophysiological conditions should be possible to achieve. This approach to mimic the cardiac conductive system by means of conductive nanofibers has the potential to be a promising implementation in 3D-biofabricated human tissue substitutes and regenerative medical applications.

## Dual scale scaffolds

Increasing the resemblance of our biofabricated construct to extracellular matrix (ECM), in which the cardiac cells are embedded, is a key factor in tissue engineering. Therefore, by successful combination of 3D-bioprinting and electrospinning (ES) first dual scale constructs could be fabricated, mimicking the different length scales of ECM more closely. As shown in figure 2, a microscale construct is fabricated, layered with (conductive) nanoscale fibers on top of it. The microscale construct is fabricated out of a PCL ES solution. PCL is extruded using a RegenHU bioprinting apparatus with optimized sets of parameters for optimal 3D-printing. The parameters in question among others, are feeding rate (8 mm/s), applied pressure (550 kPa) and extrusion temperature (90°C). After the construct was produced, nanofibers were spun on top of it using a lab-built ES apparatus. Continuous and reproducible spinning was achieved through optimization of several important parameters including voltage (11.4 kV), feeding rate (1.1 mL/h), polymer concentration (35% w/v) and working distance (110 mm). The used ES solution was 35% (w/v) polycaprolactone (PCL) dissolved in an acetic acid/acetone mixture. First trials of nonconductive NF were followed by the development of conductive NF electrospinning. To induce conductivity in the solution, CNTs were added and dispersed.

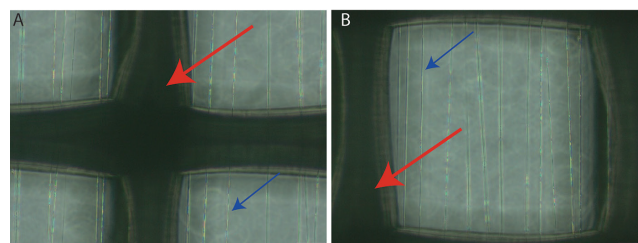


*Fig. 2: A) and B) Image of a 3D-printed dual scale construct. Red arrow indicates the 3D printed micro scale construct, while the blue arrow indicates the electrospun biocompatible, nanofibers in an aligned fashion; Scale bar = 100 μm.*

## Cell experiments

To study the influence of the aforementioned construct neonatal rat fibroblasts (NRFBs) were seeded and cultured on it (Fig. 3). The NRFBs as well as the cardiomyocytes (NRCMs) were obtained in collaboration with Dr. Anna Marsano's lab

(DBM, University of Basel) by a lab own isolation protocol. The cells were isolated from two to three days old rat pups in a two-step process over two days. NRFBs were first seeded into a culture dish layered with electrospun non-conductive nanofibers and cultured for three days. Subsequent fluorescence microscopy of the cultured cells grown on nanofibers indicate an alignment of the fibers along the given topography, compared to the control, where the fibers spread out into every direction (Fig. 3a/3b). After optimization, successful seeding of cells on the non-conductive dual scale construct was achieved showing an alignment as well of NRFBs along the given directionality of the fibers (Fig. 3c).

### Next steps

Since proper myogenesis of the isolated NRCMs is an important key for engineering mature and implantable cardiac substitutes, conductive materials are of paramount importance. Not only do they facilitate the propagation of electrical signals, they as well make electrical stimulation possible, which is a major factor for enhancing functional assembly of cardiac cells into synchronously contracting patches, i.e., become mature tissue [4]. Hence, currently the conductivity of the nanofibers, their biocompatibility, and their use in cell experiments is being assessed. The stability and quality of CNTs dispersion will be investigated using a different dispersion approach and quantified by Dynamic Light Scattering. Furthermore, cardiac cells will be seeded on conductive PCL-CNT nanofiber meshes and dual scale constructs. Their proliferation as well as maturation will be investigated. Additionally, further optimization of these dual scale construct will be studied by embedding them into optimized hydrogels to ensure proper physiological cell environment. Specialized hydrogels must be developed and studied.

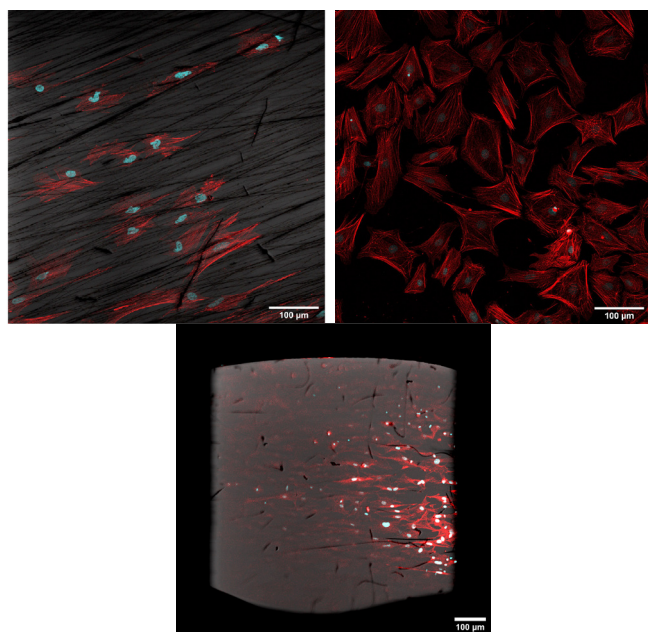


Fig. 3: Top left: NRFBs on aligned CNT-PCL NF after 3 days in culture appear to align along the given NF direction; top right: NRFBs without any topological cues after 3 days in culture spread out without any preferred direction; bottom: 'free standing' NRFBs on dual scale construct after 3 days in culture. Scale bar = 100  $\mu$ m.

### Review

While consolidating the acquired knowledge and overview over the 3D-biofabrication field, a review on nanocomposites and their use in physiological mimicking electro-conductive hydrogels for 3D-printing was published in December 2021 in the Advanced NanoBiomed Research Journal.

### References

- [1] N. Freemantle, J. Cleland, P. Young, J. Mason, J. Harrison, Beta Blockade after myocardial infarction: systematic review and meta regression analysis. *BMJ* 318, 1730–1737 (1999)
- [2] F. Züger, A. Marsano, M. Poggio, M. R. Gullo, Nanocomposites in 3D Bioprinting for Engineering Conductive and Stimuli-Responsive Constructs Mimicking Electrically Sensitive Tissue. *Adv. NanoBiomed Res.* n/a, 2100108 (2021)
- [3] R. E. Ideker, W. Kong, S. Pogwizd, Purkinje Fibers and Arrhythmias. *PACE* 32, 283–285 (2009)
- [4] G. Vunjak-Novakovic, K. O. Lui, N. Tandon, K. R. Chien, Bioengineering Heart Muscle: A Paradigm for Regenerative Medicine. *Annu. Rev. Biomed. Eng.* 13, 245–267 (2011)

# Magnetic nano-sensors for fuel cells

Project P1903: Neutron nanomediators for non-invasive temperature mapping of fuel cells

Project Leader: M. Kenzelmann and P. Boillat

Collaborator: A. Ruffo (SNI PhD Student)

## Introduction

A precise temperature measurement at the very heart of fuel cells constitutes valuable information for understanding performance and durability limitations, as well as for the validation of modeling studies. In this project, a novel approach using magnetic nano-sensors in combination with depolarization neutron imaging is developed. The proposed concept uses the temperature dependence of the neutron beam depolarization by magnetic materials integrated into the fuel cell structure – allowing a contactless and fully non-invasive measurement.

## Neutron depolarization characteristics of bulk and nanometric materials

One of the key reasons for using nanometric size materials is the known effect of the particle size on the Curie temperature [1]. To this purpose, the depolarization of the neutron beam by Nickel and Iron powders was measured. Besides coarse powders considered as being representative of the bulk material, two commercial nanoparticle powders (Ni and Fe) and one in house synthesized nanopowder (Ni) were analyzed. Additionally, commercial Neodymium-Iron-Boron (NdFeB, Newland Magnetics) alloys were measured, as coarse powders only. The commercial Ni powder has a specified size in the order of magnitude of 100 nm while the powder synthesized in house using the polyol method [2] has an estimated size of 22 nm (measured by XRD using the Debye-Scherrer relation). The commercial Fe powder has a specified size of 25 nm and is coated with carbon. All samples were mixed with PTFE powder, the weight fraction of the magnetic particles being 10%, except for the particles synthesized in house where the weight fraction was set to 50% due to their low contrast.

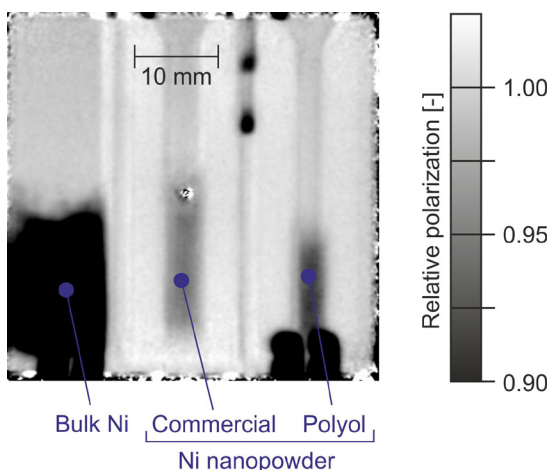


Fig. 1: Neutron depolarization image of three cuvettes containing bulk and nanometric Ni powders.

In figure 1, a neutron depolarization image of the three Ni samples is shown. As can be observed, all three samples result in a partial depolarization of the beam, though with different intensities. To analyze this depolarization quantitatively, a depolarization coefficient is introduced, which is computed as follows:

$$\Sigma_D = \frac{-\ln\left(\frac{p}{p_0}\right)}{\delta}$$

where  $p$  and  $p_0$  are the polarization of the beam with and without the sample, respectively, and  $\delta$  is the effective thickness of the magnetic powder, taking into account the mixing with PTFE and assuming a packing density of 50%.

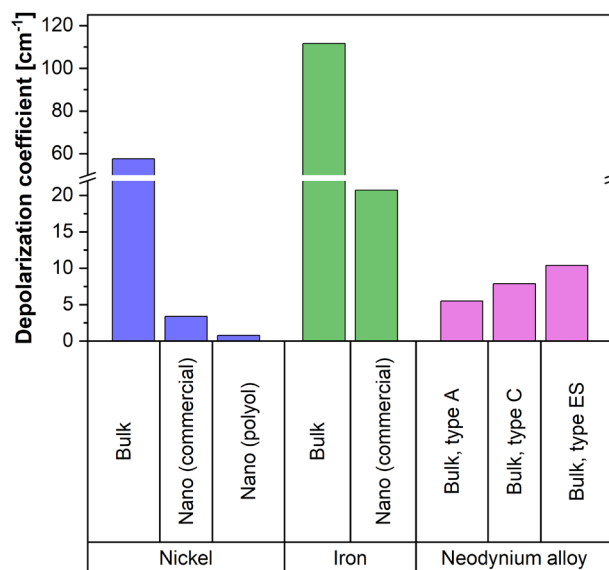


Fig. 2: Depolarization coefficient measured for different materials.

As summarized in figure 2, the particle size has an important impact on the depolarization coefficient, with the nanometric materials resulting in a significantly lower depolarization and thus requiring more material for obtaining a measurable signal. This has important practical implications, because the non-invasive integration into a fuel cell structure requires occupying as little volume as possible.

## Impact of temperature on the depolarization coefficient

In figure 3, the evolution of the depolarization coefficient as a function of temperature is shown. Due to its high Curie temperature, the depolarization by bulk Iron samples does not show any dependence, while the bulk Ni (Curie temperature of 354°C) already shows a temperature dependence in the measurement range of 30°C – 100°C. An impact of the

particle size on the temperature dependence is clearly visible, with the smallest particles being the most sensitive to temperature. However, it must be reminded that the temperature dependence alone is not sufficient to make a good nano-sensor, as a sufficient depolarization coefficient is also required.

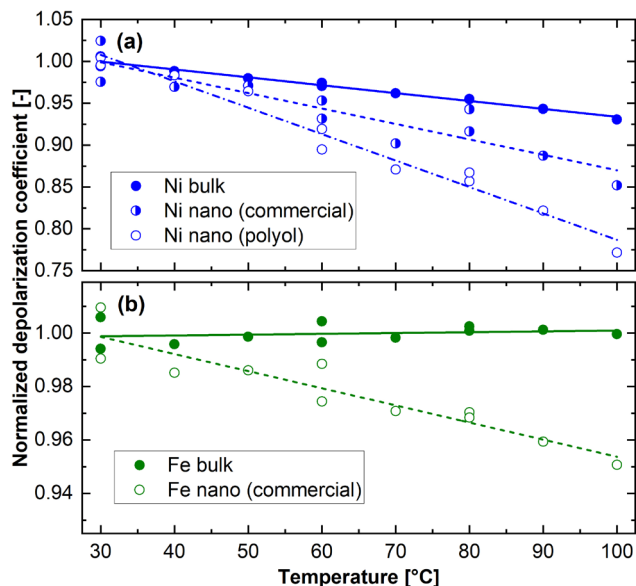


Fig. 3: Depolarization coefficient of a) Ni and b) Fe materials normalized to their value at 30°C.

Three types of commercial Neodymium based alloys were measured. While the precise composition is not specified by the manufacturer, the three types differ by their maximum rated temperature (type A: 120°C, type C: 150°C, type ES: 100°C) and by their Curie temperature (type A: 310°C, type C: 470°C, type ES: 400°C).

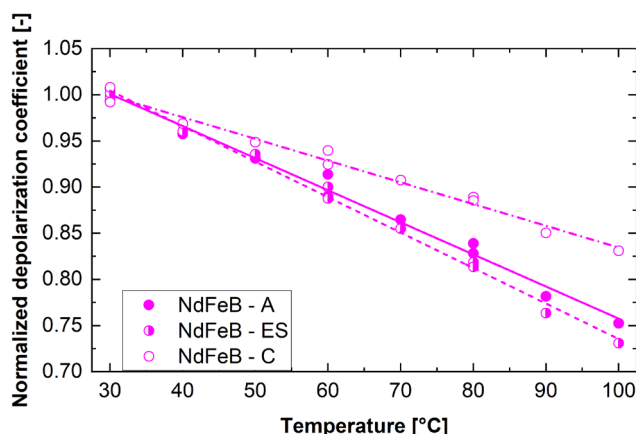


Fig. 4: Depolarization coefficient of Neodymium alloy materials normalized to their value at 30°C.

As shown in figure 4, all measured Neodymium based materials show an important temperature dependence of their depolarization coefficient. The combination of this strong dependence with a sufficiently high depolarization coefficient make these materials a very interesting candidate for our application, even with their bulk characteristics. However, it is still required to synthesize such materials in nanometric sizes in order to integrate them non-invasively into fuel cell structures.

### Towards integration in fuel cells

The use of the characterized nanoparticles as temperature sensors require them to be integrated in fuel cell materials in the least invasive way. First trials were realized where Ni and Fe nanoparticles were dispersed into the fluoropolymer coating commonly used in fuel cell gas diffusion layer materials (a porous carbon based material used for the fine distribution of the reactants) to help them repel water.

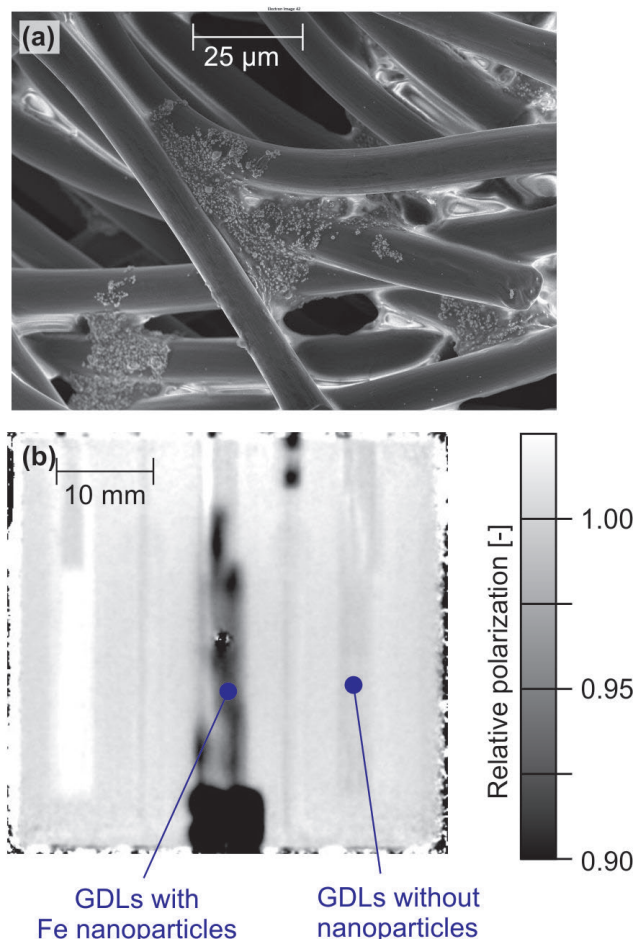


Fig. 5: a) SEM image of a fuel cell gas diffusion layer (Freudenberg H23) with Ni nanoparticles. b) Neutron depolarization image of GDLs (stack of 10 layers) with and without Fe nanoparticles.

As illustrated in figure 5, the integration of nanoparticles in the GDL materials result in a clearly observable beam depolarization, in comparison to the blank GDL without nanoparticles. Although the homogeneity of the nanoparticles distribution still needs to be improved, this constitutes a promising step towards in situ measurements in operating fuel cells.

### References

- [1] J. Chatterjee, M. Bettge, Y. Haik, C. J. Chen, Synthesis and characterization of polymer encapsulated Cu–Ni magnetic nanoparticles for hyperthermia applications. *J. Magn. Magn. Mater.*, 293, 303-309 (2005)
- [2] F. Fievet, J. P. Lagier, B. Blin, B. Beaudoin, M. Figlarz, Homogeneous and heterogeneous nucleations in the polyol process for the preparation of micron and submicron size metal particles. *Solid State Ion.* 32-3, 198-205 (1989)

# Development of fixed targets for protein-dynamic studies at SwissFEL

Project P1904: Revealing protein binding dynamics using time-resolved diffraction experiments at SwissFEL

Project Leader: C. Padeste and T. Ward

Collaborators: M. Carrillo (SNI PhD Student), T. Weinert, J. H. Beale

X-ray Free Electron Lasers (XFELs) such as SwissFEL, the new large-scale facility at the Paul Scherrer Institute (PSI), allow for the creation of molecular movies of biomolecules “in action” based on time-resolved diffraction experiments. The goal of this project is the development of a fixed-target sample delivery system for XFELs. The binding of a photo-cleavable biotin derivatives to streptavidin will be used as a model system to demonstrate the utility of these fixed-targets and to study the streptavidin-biotin binding dynamics.

## Background

XFELs are a new generation of light sources that provide novel experimental capabilities to study structure and dynamics in biology, chemistry and material sciences based on their ultra-brilliant, highly coherent, femtosecond X-ray pulses [1]. They allow high-resolution structure-determination at room temperature using crystals of smaller sizes than used in conventional diffraction studies. The special feature of the ultra-high pulse intensity, i.e. is the complete destruction of the probed crystal sample by X-ray laser pulse. This feature has led to the development of serial femtosecond crystallography (SFX) providing the ability of collecting many thousands of diffraction patterns from individual protein micro-crystals prior to radiation damage and at near physiological temperatures. The serial approach has also opened the door for time resolved measurements (TR-SFX) at femtosecond temporal resolutions, in order to study protein dynamics, in particular for proteins that react on light stimulation resulting in a conformational change. Important examples include proteins of the rhodopsin family, where triggering conformational changes by lasers followed by probing with X-rays at different time-points has been demonstrated [2].

Various design aspects have contributed to the advancement of TR-SFX. Developments such as X-ray light sources, X-ray detectors, sample delivery methods and data evaluation procedures have played a strong role in the success of these experiments. Ideal sample delivery systems allow for fast data collection, low consumption of crystalline sample, low background noise and short data collection time [3]. To deliver the protein crystals at high frequency to the probing X-ray beam, liquid jet and viscous media injection technologies, as well as the so-called fixed target technologies have been developed [4]. When using fixed targets, the crystalline samples are deposited on a chip prior to data collection. Fixed-target SFX sample delivery methods have mostly focused on chips microfabricated from silicon wafers that offer an inert support for the immobilized crystals and a precise aperture array for rapid alignment strategies [5, 6]. These chips are reusable but brittle and they can give strong Bragg reflections along the Si(111) axis when misaligned; potentially damaging x-ray detectors.

The main objective of this project is to design and fabricate polymer-based fixed-targets for SwissMX, the new end station dedicated to fixed-target SFX at SwissFEL (Fig. 1). The polymer-based film will provide a low x-ray absorption and scattering background, high design flexibility and the potential for mass-fabrication at low cost.

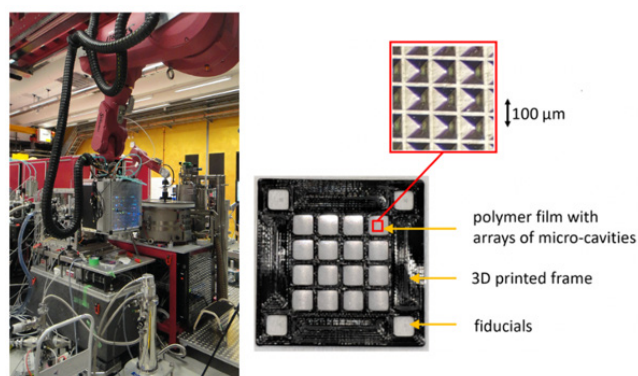


Fig. 1: Left: SwissMX, the fixed target endstation at SwissFEL. Right: First-generation polymer-based fixed target for serial protein crystallography at room temperature currently being developed at PSI. The inverted pyramidal wells serve for single crystals to funnel into predefined positions, optimizing the hit-rate of the probing X-ray beam. It also allows for reduction of preferential orientation of crystals and efficient blotting of the mother liquor of the deposited protein crystal suspension in order to minimize X-ray scattering background.

## Fixed Target Development

After establishing polymer-based fixed targets for application at cryo-conditions [7, 8] we are now focusing on room-temperature versions suitable for TR measurements. Here, we use hot embossing to imprint arrays of cavities into polymer films. Openings at the bottom of the cavities allow blotting of the solution containing micro-crystals. This produces a draft that should eventually drag individual crystals to the center of the cavities. Currently, various polymer film types and thicknesses, ranging from 25 μm to 55 μm, are being tested in order to optimize the chip parameters (Fig. 2). The relationship between the pyramid heights, film thicknesses and resulting sizes of the funnel openings will be accessed experimentally and will be further optimized for loading efficiency for crystals of different proteins such as lysozyme, rubisco and streptavidin. Furthermore, we expect minimized preferential orientation of the deposited crystals compared to flat substrates.

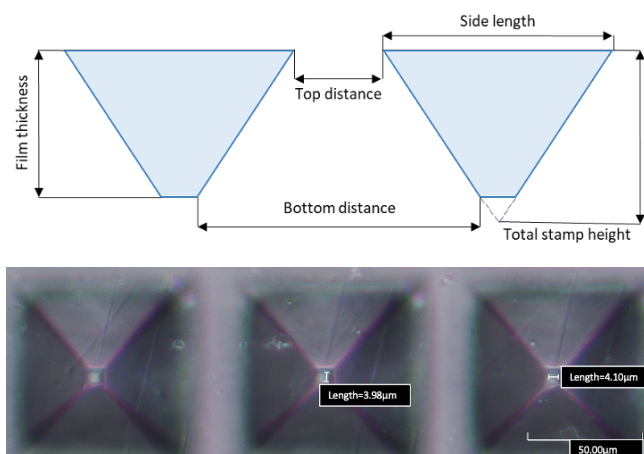


Fig. 2: Well cavities are being designed as inverted pyramids where optimization of side length, film thickness, top distance and total stamp height is currently being optimized. Bottom openings and film thickness are adjusted for appropriate crystal sizes.

For the current project, the holders need to be optimized in the dimensions and arrangements of the cavities to yield optimum crystal distribution. Furthermore, the in coupling of an optical laser beam triggering the photo-reaction has to be foreseen and planned in a way to guarantee activation of crystals exclusively in the probed cavity. Finally, a simple form of fixed-target enclosure will be created by sandwiching the chip between two polymer films, in order to preserve the loaded sample from dehydration.

### The streptavidin model system

Streptavidin is a highly symmetrical tetrameric  $\beta$ -barrel protein with a wide range of biotechnological applications. The most prominent feature is its very high affinity for biotin, which is among the highest known for small molecule-protein interactions. By enzymatic or chemical means, biotin can be easily linked to a very diverse array of targets including protein surfaces, fluorogenic probes, drug molecules or catalytically competent metal complexes, resulting in a wealth diverse of accessible properties and functionalities. More recently, evolved variants of streptavidin have been shown to bind peptides with high affinity (up to nanomolar dissociation constant). Strep-tag II, as used in this project as an alternative binder to biotin, consists of eight amino-acids (Trp-Ser-His-Pro-Gln-Phe-Glu-Lys). Photocaged derivatives of both, biotin and Strep-tag II, will be employed in this study. Exposure of streptavidin co-crystallized with these caged compounds with 250-350 nm photons induces uncaging and binding to streptavidin at a defined time point. Optimization of streptavidin crystallization is ongoing. The aim is to obtain various crystal morphologies and sizes suitable for serial experiments and fitting to the dimensions of our fixed targets.

### References

- [1] S. Boutet et al. High-resolution protein structure determination by serial femtosecond crystallography. *Science* 337, 362–364 (2012)
- [2] P. Nogly et al. Retinal isomerization in bacteriorhodopsin captured by a femtosecond x-ray laser. *Science* 361, (2018)

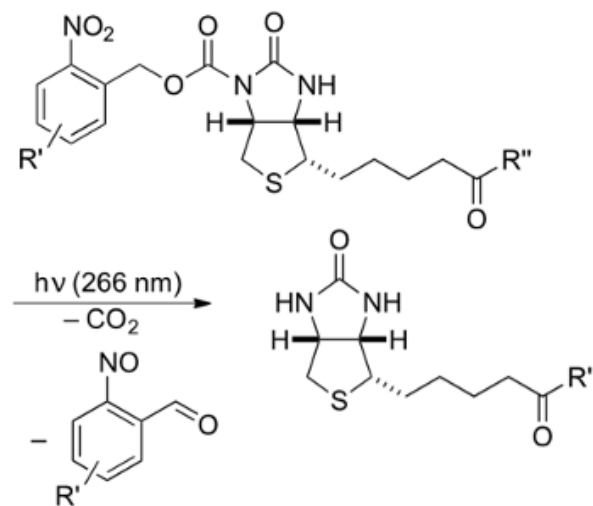


Fig. 3: One of the proposed systems to investigate protein-binding dynamics: The photo-caged biotin is not binding to streptavidin. Exposure with 266 nm photons induces uncaging and binding of this derivative co-crystallized with streptavidin.

- [3] F.-Z. Zhao, B. Zhang, E.-K. Yan, B. Sun, Z.-J. Wang, J.-H. He, D.-Ch. Yin, A guide to sample delivery systems for serial crystallography. *FEBS J.* 286, 4402–4417 (2019)
- [4] M. S. Hunter et al. Fixed-target protein serial microcrystallography with an x-ray free electron laser. *Sci. Rep.* 4, 6026 (2014)
- [5] P. Roedig et al. High-speed fixed-target serial virus crystallography. *Nat. Methods* 14, 805–810 (2017)
- [6] A. Tolstikova et al. 1 kHz fixed-target serial crystallography using a multilayer monochromator and an integrating pixel detector. *IUCrJ* 6, 927–937 (2019)
- [7] A. Karpik, I. Martiel, P. M. Kristiansen, C. Padeste, Fabrication of ultrathin suspended polymer membranes as supports for serial protein crystallography. *Nanoscale Microscale Thermophys. Eng.* 7, 100053 (2020)
- [8] I. Martiel et al. Versatile microporous polymer-based supports for serial macromolecular crystallography. *Acta Crystallogr D Struct Biol* 77, 1153–1167 (2021)

# Applying nanowire MFM to 2D materials

Project P1905: Magnetic force microscopy with nanowire transducers

Project Leader: M. Poggio and E. Meyer

Collaborator: L. Schneider (SNI PhD Student)

## Introduction

Recent years have seen rapid progress in nanometer-scale magnetic imaging technology, with scanning probe microscopy driving remarkable improvements in both sensitivity and resolution. Among the most successful tools are magnetic force microscopy (MFM), spin-polarized scanning tunneling microscopy, as well as scanning magnetometers based on nitrogen-vacancy centers in diamond, Hall-bars, and superconducting quantum interference devices. Over the past two years, we have been using nanowire (NW) force sensors as ultra-sensitive MFM probes. Using NWs functionalized with magnetic tips, we strive to map magnetic fields and dissipation with enhanced sensitivity and resolution compared to the state of the art. With these new capabilities, we intend to study magnetization in 2D materials.

The key component in any force microscope is the force sensor, which consists of a mechanical transducer, used to convert force into displacement, and an optical or electrical displacement detector. In MFM, “top-down” Si cantilevers with sharp tips coated by a magnetic material have been the standard transducer for years. Under ideal conditions, state-of-the-art MFM can reach spatial resolutions down to 10 nm, although more typically around 100 nm. These cantilevers are well-suited for the measurement of the large forces and force gradients produced by strongly magnetized samples. The advent of NWs and carbon nanotubes grown by “bottom-up” techniques now gives researchers access to much smaller force transducers than ever before. This reduction in size implies both a better force sensitivity and potentially a finer spatial resolution. Sensitivity to small forces provides the ability to detect weak magnetic fields and therefore to image subtle magnetic patterns; tiny concentrated magnetic tips have the potential to achieve nanometer-scale spatial resolution, while also reducing the invasiveness of the tip on the sample under investigation. Such improvements are crucial for imaging nanometer-scale magnetization textures in 2D systems.

Recent research efforts have demonstrated the use of single NWs as sensitive scanning force sensors [1]. When clamped on one end and arranged in the pendulum geometry, i.e. with their long axes perpendicular to the sample surface to prevent snapping into contact, they probe both the size and direction of weak tip-sample interactions. NWs have been demonstrated to maintain excellent force sensitivities around  $1 \text{ nN/Hz}^{1/2}$  near sample surfaces ( $< 100 \text{ nm}$ ), due to extremely low noncontact friction. As a result, NW sensors have been used as transducers in force-detected nanometer-scale magnetic resonance imaging and in the measurement of tiny optical and electrical forces. In a proof-of-principle microscopy experiment in the Poggio lab, we showed that a magnet-tipped NW can be sensitive to magnetic field gradients of just a few  $\text{mT}/(\text{m Hz}^{1/2})$ , equivalent to the gradient produced by a few tens of Bohr magnetons or a few nA

of flowing current at a distance of a few hundred nanometers [2]. Such sensitivity compares favorably to that of other magnetic microscopies, including scanning Hall microscopy, scanning SQUID microscopy, and scanning nitrogen-vacancy magnetometry [3].

## Goals

Despite these promising features, until now, only proof-of-principle NW MFM experiments have been carried out on the well-known magnetic field profile of a current-carrying wire [2, 4]. We intend to move past this demonstration stage by:

1. optimizing the magnet-tipped NW transducers to achieve the highest possible sensitivity and resolution;
2. using the new scanning probes to image magnetism in 2D vdW systems.

## Results

In the second year of work, we can report progress on two fronts.

First, because we are convinced that our unique nanometer-scale magnetic field imaging technique has much to reveal about the behavior of newly discovered 2D magnets, we are working on producing 2D magnets that we can image with our NW MFM. This effort consists mostly of exfoliating few or single layer 2D magnetic materials near the edge of a Si chip, where the flakes are accessible to our scanning NW microscope (the microscope works only within  $\sim 100$  of micrometers from an edge due to the constraints imposed by the optical detection of the NW motion). As a first sample, we are starting with layered  $\text{PtSe}_2$ , which can be purchased from HQ Graphene and is stable in air [5]. This material is particularly interesting to study, since it displays a layer-dependent magnetism, which – unlike previously studied 2D magnets – is induced by defects. Once we are able to produce mono- and few-layer samples of sufficient lateral size (several micrometers on a side) outside an inert atmosphere and without encapsulation, we will move to more demanding samples, which require greater care due to their tendency to corrode. The list of possible samples includes some which have already been studied by other techniques:  $\text{Fe}_3\text{GeTe}_2$ ,  $\text{Cr}_2\text{Ge}_2\text{Te}_6$ ,  $\text{MnPS}_3$ ,  $\text{CrI}_3$ ,  $\text{CrB}_3$ ,  $\text{CrCl}_3$ , and  $\text{VI}_3$ . Crystals of these samples are commercially available. Particularly intriguing samples, which have not yet been studied in few-layer form are non-collinear magnetic structures such as the helimagnets  $\text{MnCl}_2$  and  $\text{FeCl}_3$ , and multiferroic  $\text{MnI}_2$ ,  $\text{CoI}_2$ ,  $\text{NiI}_2$ , and  $\text{NiBr}_2$ .

In studying all of these samples, we aim to first characterize their static magnetism, i.e. to determine the magnetic state and its dependence on the number of layers, anisotropy, as

well as the presence of spatially modulated states, domains, defects, and inhomogeneities. Thereafter, we will move to study phase transitions and magnetic reversal: measuring the stability of magnetic phases, the nature of phase transitions, the process of magnetic reversal, and the role of domains and inhomogeneity therein.

Second, our collaborators from the De Teresa Group at the University of Zaragoza have functionalized GaAs NWs with nanometer-scale Co magnetic tips deposited via focused-electron-beam-induced deposition (FEBID). These highly sensitive NW MFM transducers, shown in figure 1, have superior magnetic and mechanical properties to any previous NW-based sensors. For this reason, we are now using them as MFM transducers to investigate a potentially spin-polarized

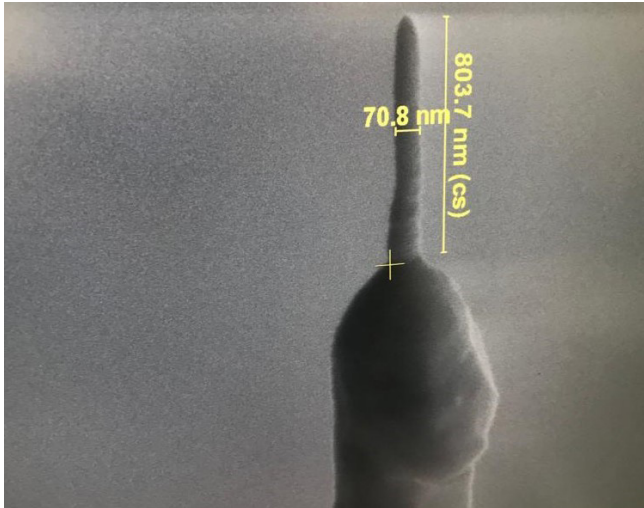


Fig. 1: SEM of the tip of a 15- $\mu\text{m}$ -long GaAs NW with a magnetic tip made from Co deposited via FEBID by the De Teresa Group from University of Zaragoza.

electron state in monolayer  $\text{MoS}_2$ . This work is a collaboration with the Warburton Group here in Basel, who has found evidence of this state in optical measurements [6]. Their measurements support a first-order magnetic phase transition in a gated sample of  $\text{MoS}_2$ . The phase boundary separates a ferromagnetic phase at low electron density and a paramagnetic phase at high electron density. The magnetic order is thereby controlled via the voltage applied to the gate electrode of the device. We now seek to use our extremely sensitive scanning magnetic probe, to find direct evidence of this magnetic state.

In collaboration with the Warburton Group, we have produced a gated monolayer  $\text{MoS}_2$  sample, which can be approached using our NW MFM probe. This involved a complicated process designed to place the sample within a few tens of  $\mu\text{m}$  from the chip edge (see Fig. 2). The sample was then characterized optically and was confirmed to show the same optical signatures of spin polarization. Then, the sample was loaded into our custom-built scanning NW microscope, which is capable of running at temperatures down to 4.2 K and in magnetic fields up to 8 T. The sample was mounted together with already tested and calibrated NW MFM probes made by our collaborators at the University of Zaragoza. The experiments on  $\text{MoS}_2$  are currently on-going.

Although conventional MFM is already applied to a wide array of samples for its ability to work at various temperatures, some experiments remain out of reach because of limitations in magnetic field sensitivity. The extreme sensitivity to subtle magnetic field patterns offered by NW MFM bring experiments like the one on  $\text{MoS}_2$  back within the realm of possibility. We hope that these measurements in  $\text{MoS}_2$  will

serve to open a door to a large number of 2D magnets and other 2D materials with unexplored nanometer-scale magnetic contrast.

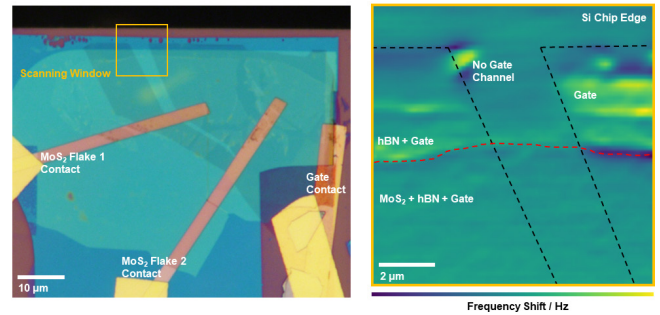


Fig. 2:  $\text{MoS}_2$  Sample. Right: The sample is fabricated near the edge of an undoped Si chip. Left: Frequency shift signal from NW MFM of the scanning window shown on the right. Topographic features, down to single layers appear due to electrostatic interactions between the sample and NW tip.

## References

- [1] N. Rossi, F. R. Braakman, D. Cadeddu, Denis Vasyukov, G. Tütüncüoğlu, A. Fontcuberta i Morral, M. Poggio, Vectorial scanning force microscopy using a nanowire sensor, *Nat. Nanotechnol.* 12, 150 (2017)
- [2] N. Rossi, B. Gross, F. Dirnberger, D. Bougeard, M. Poggio, Magnetic Force Sensing Using a Self-Assembled Nanowire, *Nano Lett.* 19, 930 (2019)
- [3] E. Marchiori, L. Ceccarelli, N. Rossi, L. Lorenzelli, C. L. Degen, M. Poggio, Nanoscale magnetic field imaging for 2D materials, *Nat. Rev. Phys.* 4, 49 (2022)
- [4] H. Mattiat, N. Rossi, B. Gross, J. P. Navarro, C. Magén, R. Badea, J. Berezovsky, J. M. De Teresa, M. Poggio, Nanowire Magnetic Force Sensors Fabricated by Focused-Electron-Beam-Induced Deposition, *Phys. Rev. Appl.* 13, 044043 (2020)
- [5] A. Avsar, A. Ciarrocchi, M. Pizzochero, D. Unuchek, O. V. Yazyev, A. Kis, Defect Induced, Layer-Modulated Magnetism in Ultrathin Metallic  $\text{PtSe}_2$ , *Nat. Nanotechnol.* 14, 674 (2019)
- [6] J. G. Roch, G. Froehlicher, N. Leisgang, P. Makk, K. Watanabe, T. Taniguchi, R. J. Warburton, Spin-polarized electrons in monolayer  $\text{MoS}_2$ , *Nat. Nanotechnol.* 14, 432 (2019)

# Screening for heteromeric nm-sized self-assembled molecular containers

Project P1906: Machine learning assisted design of heteromeric self-assembled molecular capsules

Project Leader: K. Tiefenbacher and A. von Lilienfeld

Collaborator: I. Martyn (SNI PhD Student)

## Introduction

Self-assembled supramolecular capsules have exhibited promising behavior as catalysts, due to their ability to mimic the binding site of an enzyme. These molecular containers can encapsulate guests within their rigid internal cavity and stabilize reactive intermediates with non-covalent interactions, providing a lower energy pathway for reactions such as terpene cyclization[1]. However, most known hydrogen-bonded capsules, such as the resorcinarene hexamer, are homomeric (assembled from only one building block). Homomeric capsules are limited in their ability to impose specific conformations on the encapsulated guest, due to the high symmetry of the internal cavity (depicted in Fig. 1)[2]. The resulting lack of product selectivity limits the scope of the catalyzed reactions. The aim of this project is to discover novel heteromeric capsules with an asymmetric cavity, which will allow for design principles of heteromeric capsules to be developed, to inform future synthetic strategies.

As there are no general synthetic routes to follow, the approach taken towards the discovery of novel heteromeric assemblies consists of a broad screening of a library of building blocks. This library contains a range of building blocks derived from resorcinarene, in addition to building blocks of literature-known assemblies and organic molecules with hydrogen bonding motifs.

## Screening

Screening of heteromeric assemblies is conducted by  $^1\text{H}$  NMR. New, broadened, shifted, or missing peaks are all potentially indicative of heteromeric self-assembly. Further analysis of these assemblies is conducted by 2D NMR, DOSY, and other techniques as relevant. In order to quantify the experimental results, combinations of building blocks are graded from 0-4 (see Table 1).

Table 1: Scale of screening results

Screening experiment result	Definition
0	Solubility issue of one or more components.
1	Superposition of individual spectra; no interaction.
2	Encapsulation of one or more building blocks by a homomeric assembly.
3	Some interaction between building blocks; no single defined heteromeric assembly.
4	Defined heteromeric assembly.

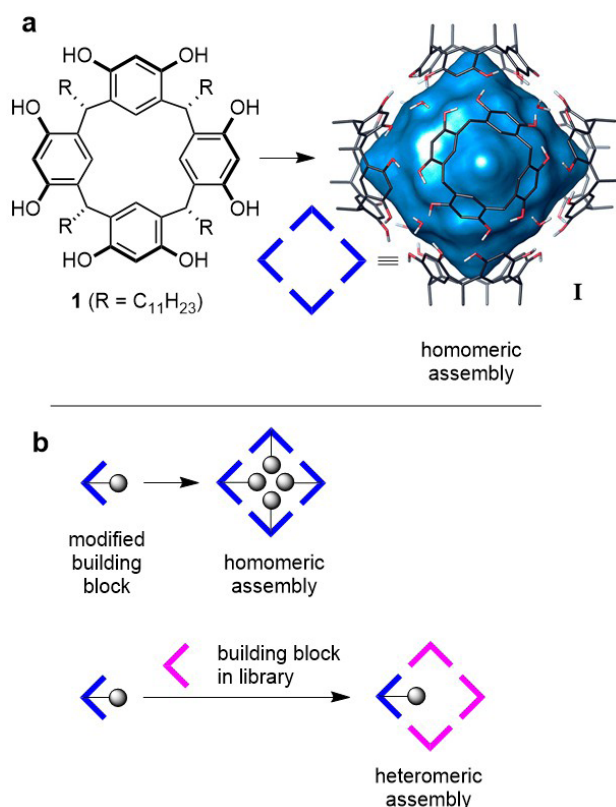


Fig. 1: a) Homomeric assembly of the resorcinarene capsule; b) Homomeric and heteromeric assembly of resorcinarene-based building blocks. The capsule remains symmetric even in the homomeric assembly of modified building blocks; symmetry is only reduced in the heteromeric assembly.

## Results

The synthesis of the library of building blocks is nearing completion, with the library currently consisting of 43 building blocks (Fig. 2).

The results of the binary screening are visualized in figure 3. One clear example of a binary heteromeric assembly was discovered by  $^1\text{H}$  NMR. The assembly was found to consist of one resorcinarene derivative building block and another building block of similar size, in a 2:1 ratio. DOSY NMR analysis yielded a value similar to that of the hexameric resorcinarene capsule.

In many cases, resorcinarene-based building blocks encapsulated smaller building blocks as a guest, rather than form a heteromeric assembly. This indicates that not only are factors such as the matching of hydrogen bonding motifs important in the formation of heteromeric assemblies [3], but that size complementarity may also play an important role

in determining which building blocks will form heteromeric assemblies.

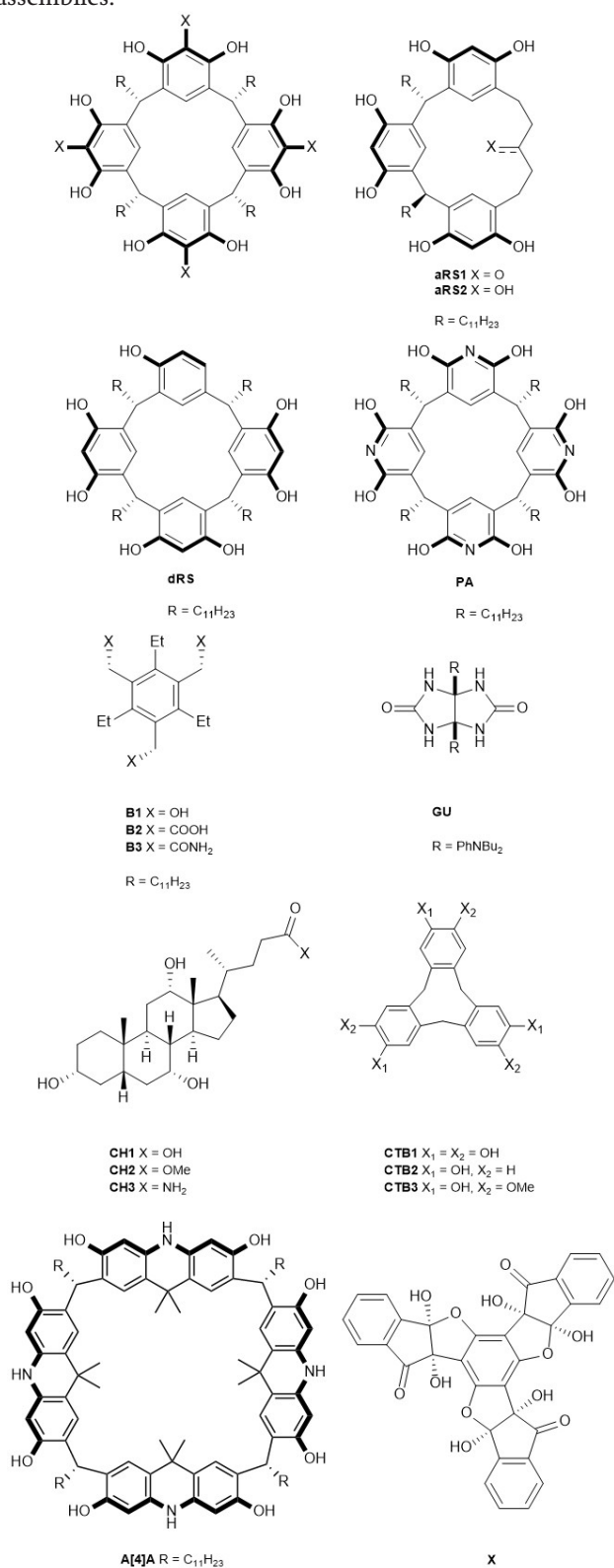


Fig. 2: Examples of building blocks from the heteromeric assembly screening library.

### Conclusion and Further Work

The novel assembly is still undergoing characterization by means of guest uptake experiments and X-ray crystallography. The latter method poses a challenge due to the difficulty of crystallizing the complete assembly, especially considering the differing solubilities of the building blocks.

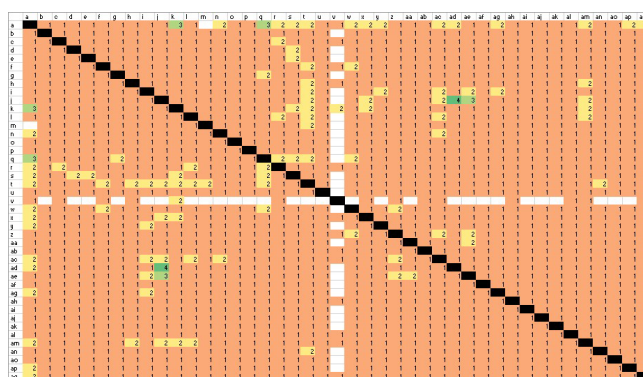


Fig. 3: Results of binary combinations of building blocks.

In conclusion, although a promising novel heteromeric assembly has been discovered, the screening process did not yield a large number of new heteromeric assemblies. This hinders the development of a machine learning model, as a small training dataset would result in a poorly performing model.

One solution to this lack of high-quality data would be to make use of STK (Supramolecular Toolkit), a Python library which constructs supramolecular structures from molecular building blocks [4]. This software makes use of an evolutionary algorithm for the discovery of new supramolecular assemblies with user-defined properties. Challenges associated with this approach include the design of a topology graph to represent the shape of the resulting assembly, and the definition of a fitness function to evaluate the real-world feasibility of the machine-generated solutions.

### References

- [1] Q. Zhang, L. Catti, K. Tiefenbacher, Catalysis inside the Hexameric Resorcinarene Capsule, *Acc. Chem. Res.*, 51, 2107-2114 (2018)
- [2] Q. Zhang, J. Rinkel, B. Goldfuss, J. Dickschat, K. Tiefenbacher, Sesquiterpene cyclizations catalysed inside the resorcinarene capsule and application in the short synthesis of isolongifolene and isolongifolenone, *Nat. Catal.*, 1, 609-615 (2018)
- [3] A. Wu, L. Isaacs, Self-Sorting: The Exception or the Rule?, *J. Am. Chem. Soc.*, 125, 4831-4835 (2003)
- [4] L. Turcani, A. Tarzia, F. Szczypiński, K. Jelfs, stk: An extendable Python framework for automated molecular and supramolecular structure assembly and discovery, *J. Chem. Phys.*, 154, 214102-13 (2021)

# Coherent feedback cooling of a nano-mechanical membrane with atomic spins

Project P1907: Spin-opto-nanomechanics

Project Leader: P. Treutlein and P. Maletinsky

Collaborators: G.-L. Schmid (SNI PhD Student), C.T. Ngai, M. Ernzer, M. Bosch, T. Karg

We use a spin-mechanical hybrid system to study the intriguing concept of coherent feedback [1]. In coherent feedback a quantum system is controlled through its interaction with another one, in such a way that quantum coherence is preserved. In contrast to measurement-based feedback, coherent feedback does not rely on measurements, thus avoiding the quantum backaction inherent to them. Coherent feedback can outperform measurement-based feedback in certain tasks such as cooling of an oscillator. Here, we employ optical coherent feedback to remotely cool a nanomechanical membrane by two orders of magnitude in temperature using atomic spins as a controller.

## Setup

Our hybrid system consists of a mechanical oscillator and a collective atomic spin coupled by a laser light over a distance of one meter in a looped geometry (Fig. 1). The mechanical oscillator is placed in a single-sided optical cavity which enhances the optomechanical coupling to external fields. The cavity is driven by an auxiliary laser beam that is red-detuned from the cavity resonance, providing some initial cavity optomechanical cooling of the membrane. In presence of this auxiliary laser beam and the coupling laser the membrane is cooled to  $\bar{n}_{m,bath} = 2.0 \times 10^4$  phonons and its linewidth is broadened to  $\gamma_m = 2\pi \times 262$  Hz. The collective spin is realized with an ensemble of  $1.3 \times 10^7$  ultracold  $^{87}\text{Rb}$  atoms confined in an optical dipole trap. The atoms are optically pumped into the hyperfine ground state  $|F=2, m_F=-2\rangle$  with respect to a static magnetic field. The Larmor frequency  $\Omega_s$  is tuned into resonance with the membrane frequency  $\Omega_m = 2\pi \times 1.957$  MHz. A coupling laser interacts first with the spin, then with the membrane and once again with the spin as sketched in figure 1 and detailed in [2]. Tracing out the light field and neglecting the propagation delay, the resonant part of the effective spin-membrane interaction is described by a beam splitter Hamiltonian  $H_{BS} = \hbar g(b_s^\dagger b_m + b_m^\dagger b_s)$ , where  $b_m$  ( $b_s$ ) is the annihilation operator of the membrane (spin) oscillator and  $g$  is the effective spin-membrane coupling [3].

## Continuous Cooling

Strong coupling of spin and membrane [2] is manifested by the hybridization of the membrane and the spin modes, which leads to a normal mode splitting as shown in figure 2b). In figure 2a we show the time evolution of the membrane occupation number after switching on the coupling beam. For  $2g > \gamma_s$ , state swaps between membrane in a room temperature environment and ground state cooled spin are observed. These state swaps decrease the phonon number of the membrane due to the damping that occurs in the spin system, whose initial occupation is much smaller and whose damping rate is larger than that of the membrane. The oscillations dephase after approximately 1 ms and a steady state with a membrane occupation of  $\bar{n}_{m,ss} \approx 2.3 \times 10^3$  pho-

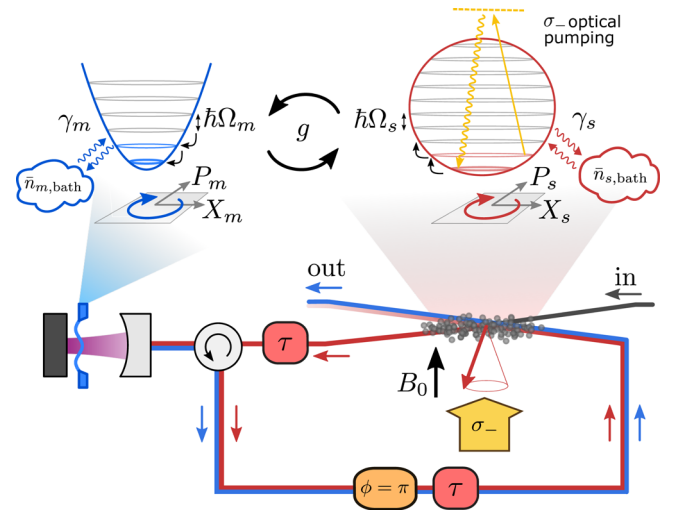


Fig. 1: Sketch of the light-mediated spin-membrane coupling. Light interacts first with the spin, then with the membrane, and then again with the spin. On the way back from the membrane to the spin, a  $\pi$ -phase is imprinted on the light, rendering the spin-membrane interaction effectively Hamiltonian for zero delay  $\tau=0$ . The systems can be approximated by harmonic oscillators of frequencies  $\Omega_m$  and  $\Omega_s$  with damping rates  $\gamma_m$  and  $\gamma_s$  coupling them to a bath with  $\bar{n}_{m,bath}$  and  $\bar{n}_{s,bath}$  phonons, respectively. The oscillators are coupled at a rate  $g$ . The spin damping rate can be increased by applying a  $\sigma$ -polarized pumping laser.

nons is reached, corresponding to a temperature decrease by two orders of magnitude compared to the initial state. In this process the membrane is predominantly cooled via its coupling to the cold and damped spin, reaching a temperature one order of magnitude lower than in the presence of the optomechanical cooling beams alone. Increasing the spin damping rate  $\gamma_s$  first enhances the membrane cooling, until the overdamped regime  $\gamma_s \gg 2g$  is reached where the membrane couples incoherently to a quasi-continuum of cold spin fluctuations. The membrane decay is then governed by Fermi's golden rule, with the occupation number decreasing at the sympathetic cooling rate  $\gamma_{sym} \approx 4g^2/\gamma_s$ , i.e., the cooling becomes less effective as  $\gamma_s$  is increased further. In this weak-coupling regime, the modes decouple and the membrane spectrum shows a single Lorentzian peak, broadened by the interaction with the spin (Fig. 2b).

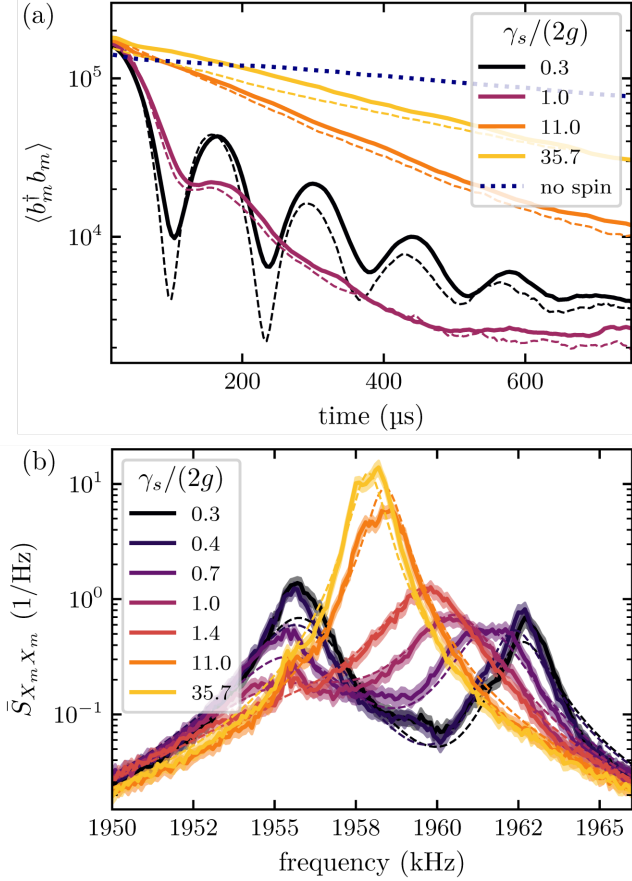


Fig. 2: a) Time traces of the membrane occupation number after turning on the coupling to the atoms. The different traces show measurements with different spin damping rates  $\gamma_s$ . The dashed lines correspond to the simulation. The dotted line shows the membrane dynamics without atoms but with the coupling beam turned on. b) Power spectral density of the membrane displacement. The dashed lines show a global fit to the data.

### Stroboscopic Cooling

We can combine strong coupling and strong spin damping in a stroboscopic fashion to cool the membrane much faster than in the continuous cooling case discussed above. In figure 3, we show a comparison between stroboscopic and continuous cooling, where time traces for (a) the membrane occupation number and (b) the spin occupation number are shown. In the stroboscopic sequence we perform a coherent  $\pi$ -pulse to swap membrane and spin states. Afterwards, we apply an optical pumping pulse of  $10 \mu\text{s}$  which increases the spin damping rate to  $\gamma_s \approx 60 g$ , depleting the spin occupation on a timescale much shorter than the state swap (gray pulses in Fig. 2b). Since the spin is reinitialized close to the ground state, the next coherent state swap does not transfer thermal energy back to the membrane but only cools it further. It takes two to three cycles of a coherent  $\pi$ -pulse followed by a spin pumping pulse to reach the steady state. Using this simple sequence, we can reach the membrane steady state temperature of  $216 \text{ mK}$  ( $\bar{n}_{m,ss} = 2.3 \times 10^3$  phonons) in around  $200 \mu\text{s}$ , approximately a factor of two faster than for continuous cooling. This exemplarily shows the advantage of a coherent feedback controller, which enables faster cooling than if the membrane is coupled with a similar rate to an incoherent, overdamped system.

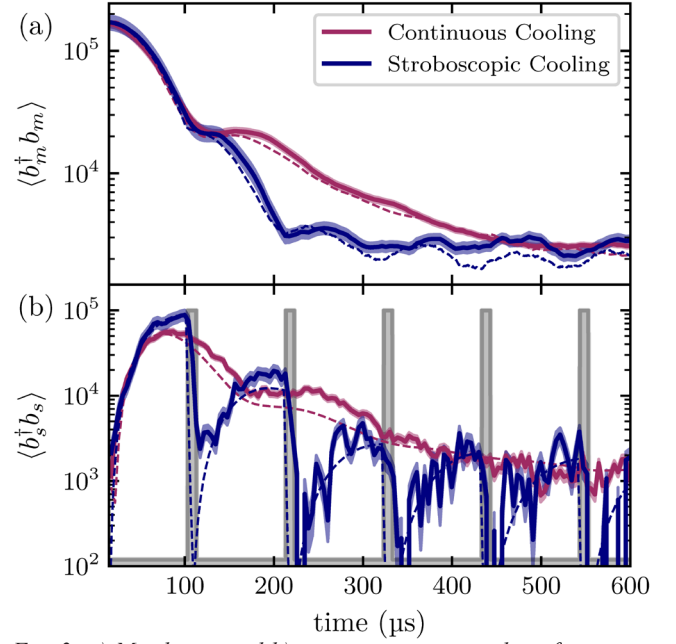


Fig. 3: a) Membrane and b) spin occupation numbers for continuous cooling at  $\gamma_s = 2 g$  and stroboscopic cooling at  $\gamma_s = 0.6 g$ . The gray shaded areas indicate the spin pumping pulses (where  $\gamma_s \approx 60 g$ ).

### Outlook

In our experiment, the cooling rate of the membrane due to its coupling to the spin exceeds the cavity-optomechanical cooling rate by more than one order of magnitude. Applying the same cooling technique to a soft-clamped membrane with a higher quality factor (of around  $50 \times 10^6$  instead of  $1.4 \times 10^6$ ) would allow us to prepare the mechanical oscillator close to its ground state in a  $4 \text{ K}$  environment.

### References

- [1] G.-L. Schmid, C. T. Ngai, M. Ernzer, M. Bosch Aguilera, T. Karg, P. Treutlein, Coherent feedback cooling of a nanomechanical membrane with a spin, Phys. Rev. X 12, 011020 (2022)
- [2] T. M. Karg, B. Gouraud, C. T. Ngai, G.-L. Schmid, K. Hammerer, P. Treutlein, Light-mediated strong coupling between a mechanical oscillator and atomic spins 1 meter apart, Science 369, 174 (2020)
- [3] T. M. Karg, B. Gouraud, P. Treutlein, and K. Hammerer, Remote Hamiltonian interactions mediated by light, Phys. Rev. A 99, 063829 (2019)

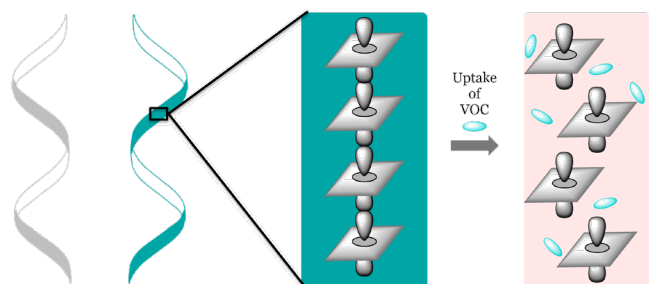
# How to tune molecular stacking towards functional nanowires

Project P1908: Chiral Recognition in Molecular Nanowires from Square-Planar Platinum(II) Complexes

Project Leader: O. Wenger and C. Sparr

Collaborator: A. Huber (SNI PhD Student)

To date, the fundamental functioning principles of chiral recognition of volatile organic compounds (VOCs) with nanostructured materials are somewhat poorly understood, and their applications seem underexplored [1,2]. In this context, we designed new nanostructured “chiral nose”-type materials to selectively sense chiral VOCs. Controlled helical superstructures composed of stacked square planar platinum (II) complexes are of key interest to us (Scheme 1). Interactions of small chiral molecules with the crystal lattice ideally provoke changes in photoluminescence, vapochromism[3], or electrical conductance, thus leading to sensing behavior (Scheme 1).



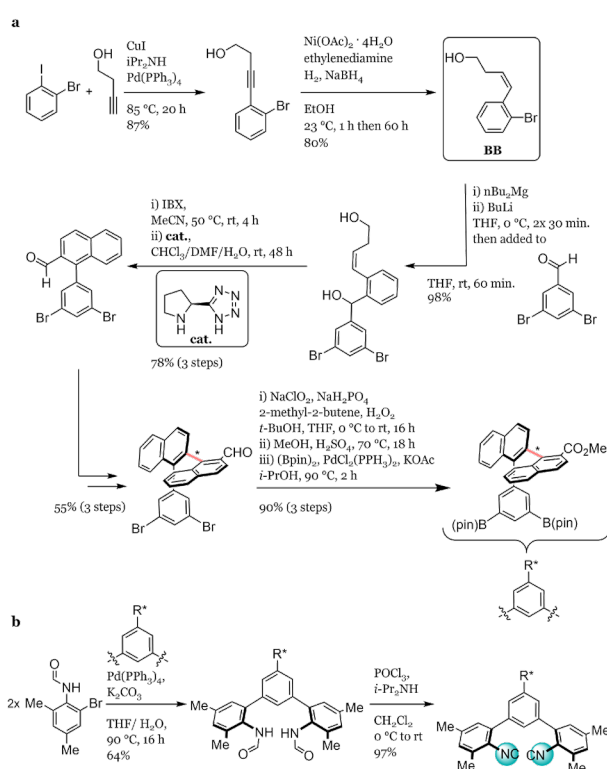
Scheme 1: Helical superstructure from stacked Pt-complexes showing VOC sensing behavior.

Ideally, stereoisomers of specific VOC analytes could interact with the nanowire crystal lattice by intercalation, or through  $\pi$ - $\pi$  interactions directly at the atropisomeric moieties of the complexes. The preference of square planar Pt(II) complexes to form stacked aggregates arises from weak metal-metal interactions between the 5d<sub>z<sup>2</sup></sub> orbitals upon close contact (<3.5 Å)[4].

## Stereogenic Pt(II) isocyanide complexes

In this project, we prepare new chiral Pt(II) complexes by introducing an atropisomeric moiety at the periphery of bi- or tri-dentate isocyanide ligands.

Taking advantage of the Sparr group's expertise on atroposelective oligo-naphthylene synthesis [5,6], the selective formation of (*R<sub>a</sub>*)- or (*S<sub>a</sub>*)- atropisomeric oligo-naphthylenes was achieved by the iterative addition of building blocks to aromatic aldehydes and a subsequent enantioselective arene-forming aldol-condensation (Scheme 2a)[6]. The atropisomeric scaffold was then coupled to isocyanide chelate ligands, which were developed in the Wenger group (Scheme 2b)[7].



Scheme 2: a) Iterative formation of atropisomeric scaffold. b) Synthesis of bidentate isocyanide ligand coupled to the chiral moiety.

The sterically demanding ligand was introduced to perturb the intermolecular stacking in order to induce a helical supramolecular arrangement. On the other hand, the metal-metal interactions stabilize the oligomeric nanowire structures [3,4].

## Anticipating controlled nanowire formation

The isocyanide ligand incorporating a naphthylene backbone was successfully synthesized. We tried to crystallize different Pt(II) complexes, yet so far most of our attempts were unsuccessful (Fig. 1).

Next, we decided to simulate the scaffolds computationally. Various models of stacked Pt complex units were designed. Our recent findings however showed that the spatial distribution of the naphthyl units around the ligand prevented sufficiently short metal-metal distances between adjacent complexes.

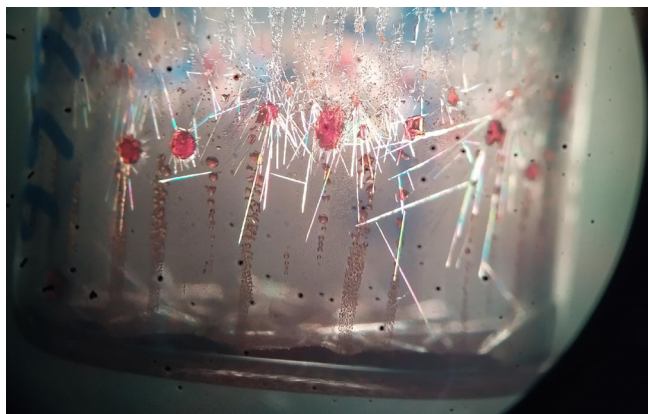


Fig. 1: The devil is in the details – colorless crystals without Pt, while the desired Pt complexes remained in the red droplets.

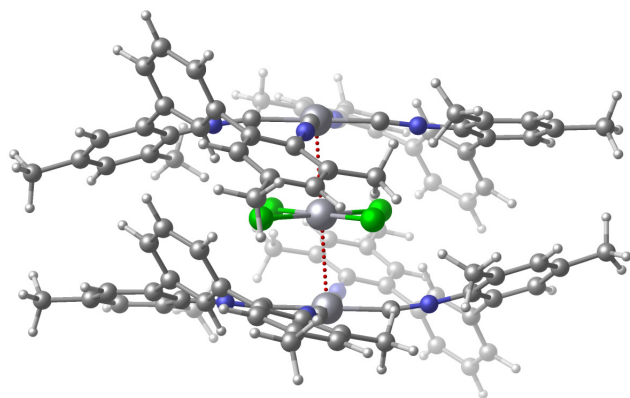


Fig. 2: Illustration of a calculated double salt stacking motif.

Additionally, we increased the scope of our envisaged materials with the formation of double-salt structures (Fig. 2). Electrostatic interactions between cationic and anionic Pt(II) complexes stabilized stacked arrangements, thus incorporating the key atropisomeric elements. At the same time, small ligands at the anionic units would allow for more space around the positive core complexes.

Besides, we started a second project where we investigated interaction-induced stereoselective chromium (III) complex formation. One key goal is to generate circularly polarized luminescence [8,9]. These parallel investigations also help training the photo-physical characterization techniques and analysis.

### Outlook

Guided by computational studies, we will now synthesize new Pt complexes and double salts. Physical characterization will focus on UV-Vis absorbance, photoluminescence, circular dichroism, and circularly polarized luminescence. The complexes and final nanostructures will be studied by X-ray or electron diffraction. Finally, we envisage changes of the aforementioned physical properties upon exposure to chiral VOC analytes. Further investigations and optimization of synthesis, complexations, and crystallizations are ongoing.

### References

- [1] A. Prabodh, D. Bauer, S. Kubik, P. Rebmann, F. G. Klärner, T. Schrader, L. Delarue Bizzini, M. Mayor, F. Biedermann, Chirality Sensing of Terpenes, Steroids, Amino Acids, Peptides and Drugs with Acyclic Cucurbit[n]urils and Molecular Tweezers, *Chem. Commun.* 56, 4652-4655 (2020)
- [2] Z. A. De los Santos, C. Wolf, Optical Terpene and Terpenoid Sensing: Chiral Recognition, Determination of Enantiomeric Composition and Total Concentration Analysis with Late Transition Metal Complexes, *J. Am. Chem. Soc.* 142, 4121-4125 (2020)
- [3] O. S. Wenger, Vapochromism in Organometallic and Coordination Complexes: Chemical Sensors for Volatile Organic Compounds, *Chem. Rev.* 113, 3686-3733 (2013)
- [4] W. B. Connick, R. E. Marsh, W. P. Schaefer, H. B. Gray, Linear-Chain Structures of Platinum(II) Diimine Complexes, *Inorg. Chem.* 36, 913-922 (1997)
- [5] D. Lotter, M. Neuburger, M. Rickhaus, D. Häussinger, C. Sparr, Stereoselective Arene-Forming Aldol Condensation: Synthesis of Configurationally Stable Oligo-1,2-naphthylenes, *Angew. Chem. Int. Ed.* 55, 2920-2923 (2016)
- [6] D. Lotter, A. Castrogiovanni, M. Neuburger, C. Sparr, Catalyst-Controlled Stereodivergent Synthesis of Atropisomeric Multiaxis Systems, *ACS Cent. Sci.* 4, 656-660 (2018)
- [7] L. Büldt, X. Guo, A. Prescimone, O. Wenger, A Molybdenum(o) Isocyanide Analogue of Ru(2,2'-Bipyridine)<sub>3</sub><sup>2+</sup>: A Strong Reductant for Photoredox Catalysis, *Angew. Chem. Int. Ed.* 55, 11247-11250 (2016)
- [8] J.-R. Jiménez, B. Doistau, C. M. Cruz, C. Besnard, J. M. Cuerva, A. G. Campaña, C. Piguet, Chiral Molecular Ruby [Cr(dqp)<sub>2</sub>]<sub>3</sub><sup>+</sup> with Long-Lived Circularly Polarized Luminescence, *J. Am. Chem. Soc.* 141, 13244-13252 (2019)
- [9] J.-R. Jiménez, M. Poncet, B. Doistau, C. Besnard, C. Piguet, Luminescent polypyridyl heteroleptic Cr(III) complexes with high quantum yields and long excited state lifetimes, *Dalton Trans.* 49, 13528-13532 (2020)

# Synthesis of hafnium oxide nanocrystals and their contrast in X-ray phase contrast CT

Project P2001: Imaging cardiovascular macro- and micro-structure using HfO<sub>2</sub> nanocrystals as X-ray tomography

Project Leader: J. De Roo and A. Bonnin

Collaborators: R. Lortzing Martínez (SNI PhD Student)

## Introduction

In 2016, cardiovascular diseases were responsible for 31% of all global deaths (WHO). They alter the cardiac structure and impact the mechanical properties of the heart. To develop personalized treatment, it is essential to analyze the structural organization of the heart. Synchrotron Radiation X-ray Phase Contrast Imaging (SR X-PCI) is a non-destructive tomography technique, providing 3D information: from full heart morphology down to cellular level microstructure [1]. We have recently customized a Perfused Isolated Heart System (PIHS) to study a beating rat heart during its cardiac cycle using SR X-PCI (Fig. 1). While this appears promising to study the heart's dynamic macrostructure, the use of a contrast agent is necessary to enable a high acquisition speed for vasculature visualization. On the other hand, 2D histology (microscopic analysis of tissue) is the conventional technique to clinically assess the microstructure of cardiac tissue. For example, patients with a heart transplant regularly undergo an endo-myocardial biopsy (EMB). The removed cardiac tissue is then analyzed for early signs of transplant rejection. While SR X-PCI measurements can provide 3D virtual histology, it is currently difficult to automatically identify early stages of rejection. Furthermore, for clinical implementation, X-PCI should be compatible with laboratory-source X-rays (having lower sensitivity). Contrast agents would both improve cell differentiation and increase sensitivity. In this project, we aim to develop hafnium oxide ( $Z=72$ ) nanocrystals as novel contrast agents [2].

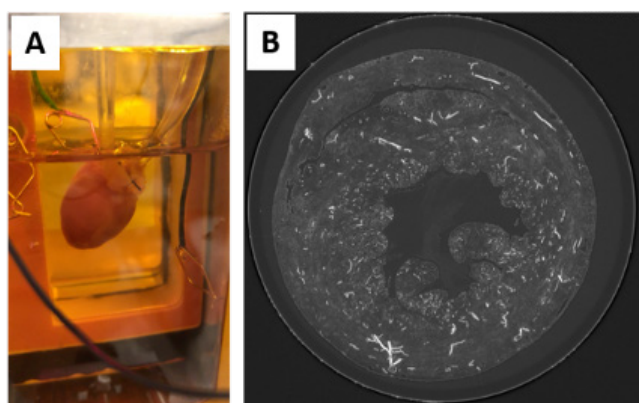


Fig. 1: A) Beating heart in a tomography compatible PIHS. B) Reconstructed slice of a rat heart with indian ink stained vessels (static measurement).

## Nanocrystal synthesis

Hafnium oxide nanocrystals were synthesized according to a microwave assisted process, based on pioneering work of Buha et al.[3] and further developed by us [4, 5]. The tetrahydrofuran complex of hafnium chloride is dissolved in ben-

zylalcohol and heated in 100 mL vessels in a large microwave reactor (MARS model of CEM). After synthesis, the nanocrystals are isolated, purified and stabilized with fatty acids to impart colloidal stability. We achieved multigram scale synthesis, a prerequisite for the large scale application as contrast agent. Figure 2a shows the reaction equation while a transmission electron microscopy image is shown in figure 2b. The nanocrystals are hybrid organic-inorganic objects, as illustrated in figures 2c-d.

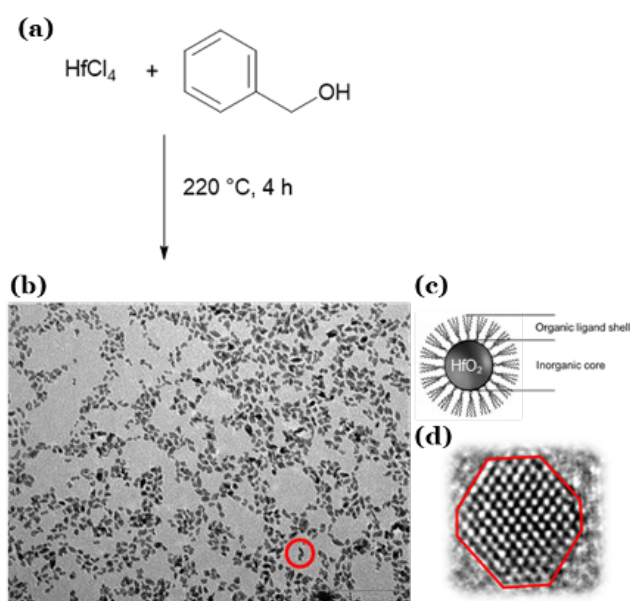


Fig. 2: a) Standard reaction to prepare HfO<sub>2</sub> nanocrystals. b) TEM image of the nanocrystals. c) Representation of a nanocrystal with its ligand shell. d) Example of a HRTEM of a nanocrystal.

## Ligand exchange and stabilization in water

The hafnia nanocrystal stabilized with fatty acids are stable in nonpolar solvents such as hexane, toluene or dichloromethane. However, to impart solubility in aqueous buffer as required for biological contrast agents, we performed a ligand exchange with polar phosphonic acids, see figure 3. The short ethyleneglycol oligomer conveniently provided solubility in water, while the phosphonate binding group provides a strong interaction with the nanocrystal surface [6, 7]. We track the ligand exchange with nuclear magnetic resonance and while the original solution shows the fingerprint of oleic acid ligands, after exchange, the ethyleneglycol moieties are detected (Fig. 3b).

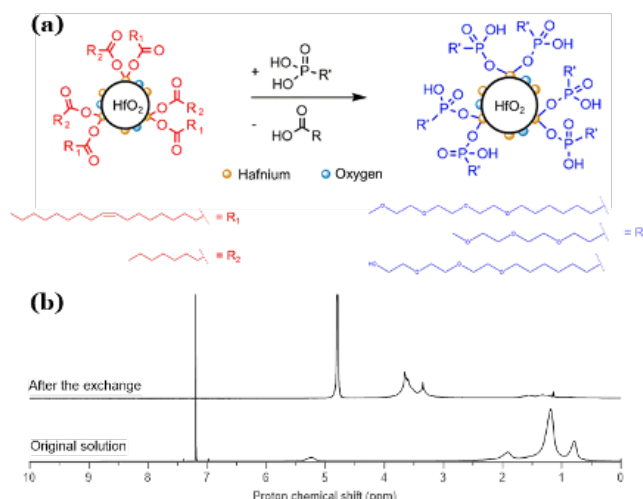


Fig. 3: a) Ligand exchange of carboxylic acids for phosphonic acids. b) Example of NMR spectra of that ligand exchange.

### Preliminary data on CT contrast

Aqueous solution of hafnia nanocrystals with different loading were prepared and compared with other types of contrast agents; iodine based or indian ink. The contrast-to-noise ratio (CNR) was determined at the synchrotron in PSI (TOMCAT beamline) at 20 keV. It is clear from figure 4 that hafnia nanocrystals are superior contrast agents and hold promise for further applications in medical computed tomography. Hafnium oxide is nontoxic and hafnia nanocrystals are currently developed as an enhancer for radiotherapy and thus one of the few nanocrystals that made it to clinical translation [8].

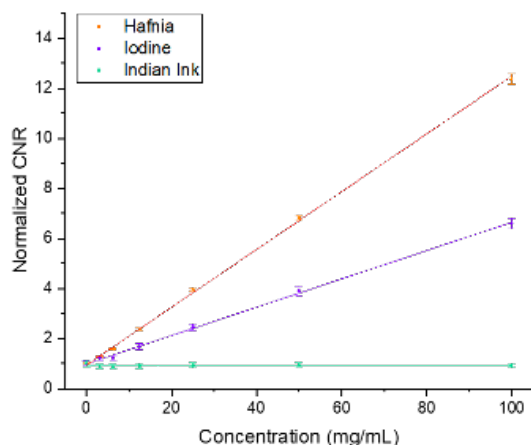


Fig. 4: Comparison of contrast-to-noise ratio (normalized to 1 at 0 mg/mL concentration) at 20 keV for hafnia nanocrystals, iodine and Indian ink. Linear fits are also included.

### Conclusion and outlook

We managed to scale up the nanocrystals synthesis from 80 mg per batch to several grams per batch. We successfully transferred the hafnia nanocrystals to water and have proven their superior contrast to noise ratio in comparison with other contrast agents. We will further implement these contrast agents in vitro in the coming year.

### References

- [1] H. Dejea, P. Garcia-Canadilla, A. C. Cook, E. Guasch, M. Zamora, F. Crispi, M. Stampanoni, B. Bijmens, A. Bonnin, Comprehensive Analysis of Animal Models of Cardiovascular Disease using Multiscale X-Ray Phase Contrast Tomography. *Scientific Reports* 9 (1), 6996 (2019)
- [2] P. F. FitzGerald, R. E. Colborn, P. M. Edic, J. W. Lambert, A. S. Torres, P. J. Bonitatibus, B. M. Yeh, CT Image Contrast of High-Z Elements: Phantom Imaging Studies and Clinical Implications. *Radiology*, 278 (3), 723-733 (2016)
- [3] J. Buha, D. Arcon, M. Niederberger, I. Djerdj, Solvothermal and surfactant-free synthesis of crystalline Nb<sub>2</sub>O<sub>5</sub>, Ta<sub>2</sub>O<sub>5</sub>, HfO<sub>2</sub>, and Co-doped HfO<sub>2</sub> nanoparticles. *Phys. Chem. Chem. Phys.* 12 (47), 15537-15543 (2010)
- [4] J. De Roo, F. Van den Broeck, K. De Keukeleere, J. C. Martins, I. Van Driessche, Z. Hens, Unravelling the Surface Chemistry of Metal Oxide Nanocrystals, the Role of Acids and Bases. *J. Am. Chem. Soc.* 136 (27), 9650-9657 (2014)
- [5] J. De Roo, I. Van Driessche, J. C. Martins, Z. Hens, Colloidal metal oxide nanocrystal catalysis by sustained chemically driven ligand displacement. *Nat. Mater.* 15 (5), 517-521 (2016)
- [6] L. Deblock, R. Pokratath, K. De Buysser, J. De Roo, Mapping out the aqueous surface chemistry of metal oxide nanocrystals; carboxylate, phosphonate and catecholate ligands, *JACS Au* (2022)
- [7] R. R. Knauf, J. C. Lennox, J. L. Dempsey, Quantifying Ligand Exchange Reactions at CdSe Nanocrystal Surfaces. *Chem Mater* 28 (13), 4762-4770 (2016)
- [8] Y. Min, J. M. Caster, M. J. Eblan, A. Z. Wang, Clinical Translation of Nanomedicine. *Chem Rev* 115 (19), 11147-90 (2015)

# A death-dealing nanomachine

Project P2002: A death-dealing nanomachine

Project Leader: R. H. Y. Lim and M. Basler

Collaborators: M. Bruderlin (SNI PhD Student), P. Cedro (MSc Nanoscience student)

## Introduction

The type 6 secretion system (T6SS) in *Pseudomonas aeruginosa* (PA) is a highly complex protein machinery that is used as a self-defense mechanism in interbacterial competition [1]. Its harpoon-like structure is well resolved and examined [2]. However, the mechanism behind its activation and the signals that allow PA to sense neighboring cells and target them is largely unknown. In this project, we investigate the reaction of PA to mechanical stress using atomic force microscopy (AFM) along with live-cell fluorescence microscopy (FM). Additionally, we are developing an AFM-based method to assess and understand the mechanobiological properties of the T6SS spike that facilitate membrane puncture.

## T6SS is pressure sensitive in *P. aeruginosa*

In the first part of the project, we developed a method to exert localized pressure on PA cells with constant force. To achieve this goal, we developed protocols to optimize both our sample as well as the AFM/FM set-up. This includes (1) knocking out the flagellum protein *FliC* in all examined PA strains, and (2) increasing the overall activity of the T6SS by adding  $\Delta retS$  to our PA strain, which leads to higher expression of the T6SS components. To visualize the cells in FM we labelled the T6SS sheath protein *VipA* with neongreen fluorescence tag.

Initial pressure experiments were performed using a stiff tipless wedged AFM cantilever with a spring constant of 58 N/m. As shown in figure 1, compressing the cells leads to an increase in firing events. This indicates that PA is capable of sensing mechanical force and reacts to it by assembling the T6SS.

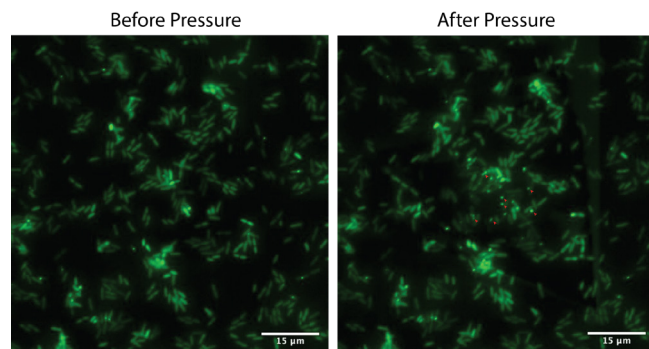


Fig. 1: Pressure response test of *Pseudomonas aeruginosa*  $\Delta retS$ ,  $\Delta FliC$ , *VipA*-neogreen. Fluorescence images show T6SS activation before and after (red arrows) engaging the cells with a wedged cantilever using 4.0 V of applied force. Scale bar, 15  $\mu$ m.

Subsequently, the AFM experiment was further fine-tuned to study how force impacts on individual cells. Instead of

tipless cantilevers, HMX-10 cantilevers (Bruker) exposing tips with nominal radii of 20-50 nm per tip were used in AFM force mapping mode. This allowed for more precise application of specific forces onto individual cells instead of pressuring biofilms of PA cells at the same time.

A summary of both wedged and tip-based experiments is shown in figure 2. Our results suggest that the number of T6SS firings per cell correlates with an increase in applied force, reaching an eightfold increase in firing rate in the low nN range. Indeed, force mapping indicated that indentation by an approaching AFM tip suitably mimics the attack of a neighboring cell. This was evident given that each PA cell exhibited a 10s delay after contact by the AFM tip to fire off a T6SS response. This time delay was previously seen in investigations of the dueling phenotype of *pseudomonas aeruginosa* [3].

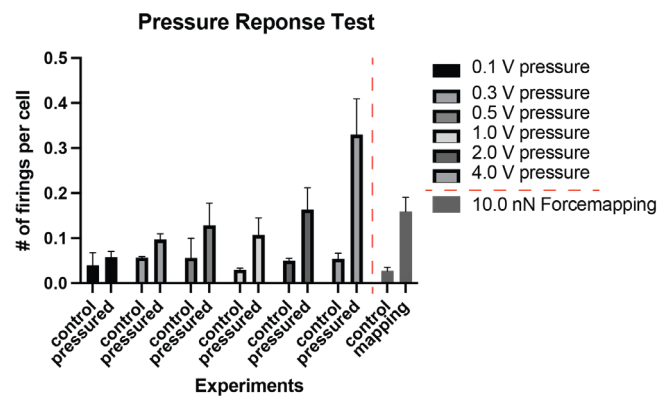


Fig. 2: Number of firing events per cell as a function of the applied pressure. All experiments were done in triplicate and the errors displayed correspond to the standard deviation of the experiments. The results of the force mapping experiments are separated from the wedged cantilever experiments by the red dotted line.

## Modification of the AFM cantilever for physiological conditions.

To further improve on our set-up, we decided to modify the AFM cantilever used for the force mapping experiments. As shown in figure 3, this involved using focused ion beam (FIB) metal deposition to create a high aspect ratio Pt spike on top of a flattened tip. This Pt spike mimics the thin long sheath of a T6SS and should allow us to penetrate the cell wall of *pseudomonas* in future experiments. Additionally, we cloned, expressed, and purified a mutated version of the *VgrG* protein that constitutes the T6SS spike. By mutating the base of this protein with additional cysteine residues, we will attempt to attach it to the produced platinum spike. In

future, this will allow us to use AFM as a means of mimicking a controlled T6SS attack while quantifying the mechanical properties of the T6SS spike during membrane puncture. Furthermore, we will be able to investigate if and how the presence of effector proteins might additionally influence these processes.

Thus far, we have verified that the expressed spike protein folds properly outside of the cell and is not impaired by the cysteine mutations. Indeed, negative stain electron microscopy reveals that the VgrGs self-assemble into trimeric “spikes” (figure 3B). Moreover, EM and also other spectroscopic means verify that trimer formation proceeds without forming larger inviable aggregates. It is noteworthy that the presence of cysteines at the base of each trimer might facilitate the formation of disulphide bonds that link neighboring VgrG pairs in a back-to-back orientation. This is a good first indication that the introduced mutations are accessible in vitro and present as viable functional groups to link them to Pt in future experiments.

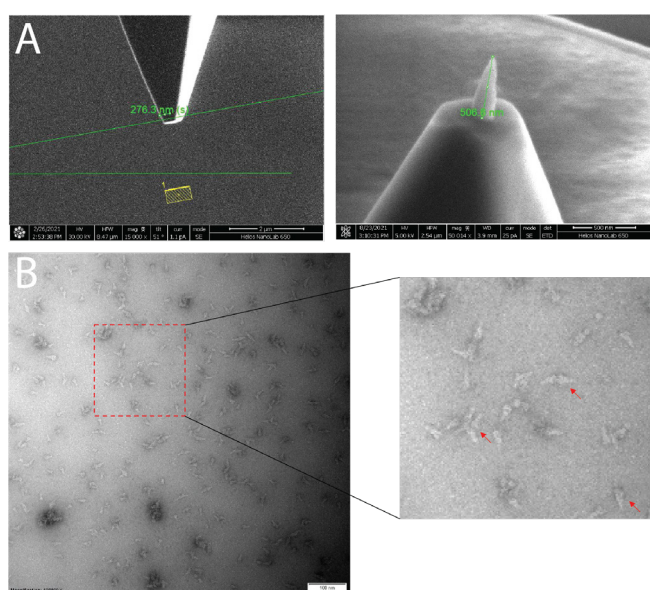


*Fig. 3: A) Scanning electron microscopy (SEM) images of a modified AFM tip. The base cantilever was an MLCT triangular tipped cantilever with a spring constant of 0.5 N/m. Its tip was cut at an angle of 10 degrees to account for the tilt of the cantilever holder. Pt spike was grown using FIB deposition and grown to a length of 524 nm. B) Negative stain EM images displaying VgrG spike protein correctly formed as trimers. Highlighting the possible formation of cysteine disulfide bonds between two spike complexes at the bases of the proteins.*

### Conclusion and Outlook

Our results show that PA responds to physical force by T6SS assembly and provide a strong basis to understand the underlying mechanisms behind bacterial mechano-sensing cascades. Additionally, mimicking bacterial attack by use of the VgrG spike protein provides a minimal system to investigate whether the examined signaling cascade is purely reliant on physical stress or if the stress response of pseudomonas depends on other biochemical triggers as well.

The next steps in this project will be to test if certain mutations within the T6SS can lead to different phenotypic bacterial responses. This could help to identify the exact proteins that are involved in bacterial mechano-sensing.

### References

- [1] J. Wang, M. Brodmann, M. Basler, Assembly and Subcellular Localization of Bacterial Type VI Secretion Systems. *Annual Review of Microbiology* 73, 621–638 (2019)
- [2] M. M. Shneider, S. A. Buth, B. T. Ho, M. Basler, J. J. Mekalanos, P. G. Leiman, PAAR-repeat proteins sharpen and diversify the type VI secretion system spike, *Nature* 500, 350–+ (2013)
- [3] W. P. J. Smith, M. Brodmann, D. Unterweger, Y. Davit, L. E. Comstock, M. Basler, K. R. Foster, The evolution of tit-for-tat in bacteria via the type VI secretion system, *Nat Commun* 11, 5395 (2020)

# Towards all-optical single-spin scanning magnetometry

Project P2003: Nanoscale quantum sensing of complex spin systems in extreme environments

Project Leader: P. Maletinsky and M. Poggio

Collaborators: J. Zuber (SNI PhD Student), M. Li, J. Happacher, M. Grimau, B. Shields

## Introduction

This project aims at further advancing the field of quantum sensing by pushing the functionality and performance of a promising alternative to the nitrogen vacancy (NV) center in single spin magnetometry: the negatively charged silicon vacancy (SiV) center in diamond. While the NV center is widely established as a versatile magnetometer in the temperature range from 4 K - 300 K [1,2], ultra-low temperatures and strong magnetic fields have proved to be largely inaccessible due to the intrinsic properties of the NV defect. This regime however is home to exotic physics such as topologically non-trivial spin textures known as Skyrmions, which have attracted considerable recent attention in the field of nano-magnetism. In addition to its exceptional optical properties, the SiV is inherently less susceptible to its charge environment [3] and all-optical coherent control has been demonstrated down to 40 mK [4], presenting it as a viable candidate for applications unsuitable for the NV center. The goal of this project is, therefore, to establish the SiV center as a novel quantum sensor in our reliable scanning probe geometry.

## Key experimental results

### 1. Towards coherent single silicon vacancy centers in diamond

Last year we have successfully implemented shallow (~50 nm from the diamond surface) SiV centers into diamond nanopillars all while retaining the excellent optical coherence the defect exhibits in bulk diamond [5].

Our conventional approach to creating SiV centers in diamond micropillars consists of preparing a pristine diamond bulk sample, which is subsequently implanted with Si ions. In addition to introducing Si into the diamond lattice, this process also generates lattice vacancies. During a high-temperature (>1200°C) vacuum anneal the vacancies become mobile and may combine with Si ad-atoms to form a stable defect complex – the SiV center. Upon confirmation that implantation and anneal have been successful (i.e. that SiV emission can be detected) we fabricate parabolic diamond nanopillars by electron lithography and reactive ion etching. Such parabolic pillars enhance light-extraction efficiencies by at least one order of magnitude over the bulk, and we employ the resulting cylinders as scanning probes for nanoscale magnetometry [6].

To assess the optical coherence of the SiV centers in the pillars, we employ a resonant 737 nm laser, sweeping across one of the optical transitions and collecting the phonon side band (PSB) emission.

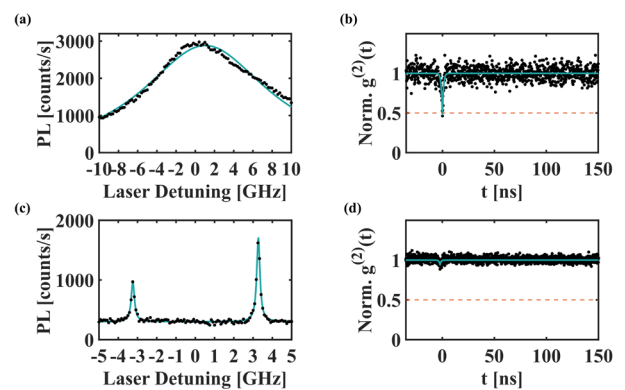


Fig. 1: a) Photoluminescence excitation (PLE) spectrum of a pillar containing SiV- before after fabrication. A Gaussian fit (in mint) reveals a line width of 16 GHz. b) Second order correlation function  $g^{(2)}$  after fabrication (fit in mint). The dotted orange line denotes the single emitter regime, indicating a single SiV in this pillar. c) PLE spectrum of a pillar after the second anneal. Gaussian fits (in mint) reveal line widths of 172 MHz and 197 MHz, close to the lifetime limit of 100 MHz. The two lines indicate there are at least two separate SiVs in present in this pillar. d) Second order correlation function  $g^{(2)}$  after a second high-temperature vacuum anneal (fit in mint), indicating a significant increase in the number of emitters per pillar.

Examples of such resulting “Photoluminescence excitation (PLE) spectrum” obtained this way are depicted in figure 1a and 1c. It has been shown that a second high-temperature anneal of the diamond sample increases the quality of emission, and inspired by the notion that annealing diminishes damage introduced to the diamond lattice [7], we measured PLE spectra before and after the second annealing step, in addition to second order correlation function  $g^{(2)}$  measurements. The result of these experiments was striking: Before the second annealing step, we observe broad emission of the order of several GHz line widths in PLE, whereas after the annealing step, SiVs in pillars exhibit close to lifetime limited (100 MHz) line widths with the narrowest being 172 MHz (Fig. 1c). These are the first near-surface SiV centers with such narrow line widths which have been reported in diamond nanostructures and these results constitute a significant step towards the goal of this PhD project.

Unfortunately, the second annealing step introduces a complication:  $g^{(2)}$  measurements reveal that the second anneal increases the number of emitters in a single pillar. Before the second annealing step, we operate in the single emitter regime as indicated in figure 1b, after the anneal, the number of emitters increases significantly as indicated by the almost non-existent dip in the  $g^{(2)}$  function in figure 1d.

To counteract the increased yield in SiV centers, we plan on further reducing the Si implantation dose in future runs. We estimate that a dose of  $1 \times 10^{10}$  ions/cm<sup>2</sup> will result in one SiV per pillar (of around 300 nm diameter) on average.

Once we have established single shallow coherent SiVs in our diamond nanopillars we will investigate all-optical coherent control of the defect center's spin states, paving the way towards all-optical single spin magnetometry.

## 2. Charge state control of silicon vacancy centers in diamond nanopillars

Hydrogen-terminated surfaces result in a band-bending within the diamond, which typically leads to de-ionization (from negative to neutral or positive) of color centers [7]. While this charge conversion is undesired in many cases, recent results [7] showed that it can be highly beneficial for SiV centers. Remarkably, the resulting neutral SiV centers (SiV<sup>0</sup>) have recently been shown to exhibit excellent coherence properties and could therefore be very well suited for quantum sensing [8]. A key difficulty there, however, is the required charge state control to favor SiV<sup>0</sup> over the normally prevalent SiV<sup>-</sup> state.

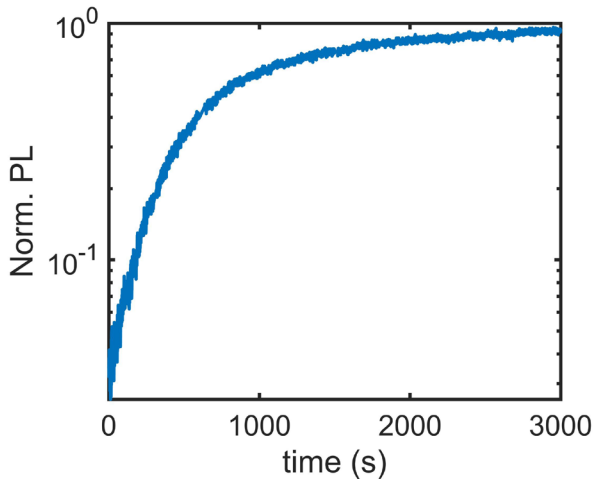


Fig. 2: Controlled, all-optical charge-state conversion of an individual SiV center. The data shows the photoluminescence intensity in the spectral window of SiV<sup>-</sup> for a single SiV center over time. The center is initially in charge state of SiV<sup>0</sup> (leading to no detected PL signal) and gradually transitions to SiV<sup>-</sup> during our process,

Building upon previous work in our group, we are exploring ways to deterministically stabilize the SiV<sup>0</sup> charge state in diamond nanopillars. Indeed, hydrogen terminating the diamond leads to complete disappearance of SiV<sup>-</sup> emission in the sample and SiV<sup>0</sup> could also not be detected, but there is indication of a third charge state that appears in a freshly hydrogen terminated sample, possibly SiV<sup>+</sup>. We found a way to revert this charge-state in an all-optical way on the level of individual and thereby gradually return to SiV<sup>-</sup> emission over time. We currently explore the parameter space of this process to controllably stabilize individual SiV<sup>0</sup> in nanopillars for quantum sensing.

When subjecting a single SiV to our charge-conversion procedure, while monitoring the zero-phonon-line intensity with an APD as seen in figure 2, we observe an exponential increase in luminescence. This is assigned to a controlled transition from SiV<sup>0</sup> to SiV<sup>-</sup> which happens over a slow (and therefore controllable) timescale of several minutes. As a next step, we will expose an array of pillars with various charge-conversion parameters to find the optimal conversion conditions to stabilize SiV<sup>0</sup>. This will pave the way to-

wards deterministic charge state control of SiV centers in diamond nanopillars for nanoscale quantum sensing.

## Summary

Project P2003 has reached significant milestones in the last year including the coherent optical emission from SiV centers in diamond nanopillars. Upon reducing the number of emitters per pillar and establishing coherent optical control of the defect centers' spin, this will ultimately enable all-optical single spin magnetometry in ultra-low temperatures and tesla-range magnetic fields.

## References

- [1] L. Thiel, Z. Wang, M. A. Tschudin, D. Rohner, I. Gutiérrez-Lezama, N. Ubrig, M. Gibertini, E. Giannini, A. F. Morpurgo, P. Maletinsky, Probing magnetism in 2D materials at the nanoscale with single-spin microscopy. *Science*, 364(6444), 973-976 (2019)
- [2] N. Hedrich, K. Wagner, O. V. Pylypovskiy, B. J. Shields, T. Kosub, D. D. Sheka, D. Makaraov, P. Maletinsky, Nanoscale mechanics of antiferromagnetic domain walls, *Nature Physics*, 17(5), 574-577 (2021)
- [3] L. J. Rogers et al. Electronic structure of the negatively charged silicon-vacancy center in diamond, *Phys. Rev. B*, 89(23), 235101 (2014)
- [4] J. N. Becker, B. Pingault, D. Groß, M. Gündoğan, N. Kukharchyk, M. Markham, A. Edmonds, M. Atatüre, P. Bushev, C. Becher, All-optical control of the silicon-vacancy spin in diamond at millikelvin temperatures, *Phys. Rev. Lett.*, 120(5), 053603 (2018)
- [5] R. E. Evans, A. Sipahigil, D. D. Sukachev, A. S. Zibrov, M. D. Lukin, Narrow-linewidth homogeneous optical emitters in diamond nanostructures via silicon ion implantation, *Phys. Rev. Appl.* 5(4), 044010 (2016)
- [6] N. Hedrich, D. Rohner, M. Batzer, P. Maletinsky, B. J. Shields, Parabolic diamond scanning probes for single-spin magnetic field imaging, *Phys. Rev. Appl.*, 14(6), 064007 (2020)
- [7] M. V. Hauf, B. Grotz, B. Naydenov, M. Dankerl, S. Pezzagna, J. Meijer, F. Jelezko, J. Wrachtrup, M. Stutzmann, F. Reinhard, A. J. Garrido, Chemical control of the charge state of nitrogen-vacancy centers in diamond. *Phys. Rev. B*, 83(8), 081304 (2011)
- [8] B. C. Rose, D. Huang, Z. H. Zhang, P. Stevenson, A. M. Tyryshkin, S. Sangtawesin, S. Srinivasan, L. Loudin, M. L. Markaw, N. P. De Leon, Observation of an environmentally insensitive solid-state spin defect in diamond. *Science*, 361(6397), 60-63 (2018)

# Surface preparation of multiferroic GeTe

Project P2004: Local manipulation of spin domains in a multiferroic Rashba semiconductor

Project Leader: M. Muntwiler and T. Jung

Collaborators: M. Heinrich (SNI PhD Student)

## Introduction

Multiferroics are materials exhibiting multiple ferroic orders such as ferromagnetism, ferroelectricity and ferroelasticity. Often, the orders are coupled whereby, for example, the spin polarization responds to an external electric field (magnetolectric coupling), or an electric polarization is induced by applied strain (piezoelectric effect) [1]. The magnetolectric coupling offers new possibilities for future information technology devices such as spin field-effect transistors (FETs) where a multiferroic material could be used to flip the spins of a spin-polarized current via an applied electric field at a gate electrode circumventing the need for energy consuming high magnetic fields [2]. The realization of such devices on the micro- and nanometer scale depends immensely on a thorough understanding of the atomic and electronic surface structure of these materials.

## Project goals

This project aims at studying multiferroic effects in GeTe and  $\text{Ge}_{1-x}\text{Mn}_x\text{Te}$  on the nanometer scale by scanning probe techniques. Pristine GeTe is a well-known ferroelectric semiconductor with a built-in electric polarization and a strong Rashba splitting of the electronic bands. Upon doping with Mn, the material becomes ferromagnetic. Previous studies show that the ferroelectric and ferromagnetic polarizations are coupled, and that the susceptibility to external fields may be localized at the surface of ultrathin films [3].

Therefore we study the surface structure using complementary synchrotron based photoelectron spectroscopy and diffraction techniques (ARPES, XPD) as well as scanning tunneling techniques (STM, STS) at the PEARL beamline of the Paul Scherrer Institut [4]. To probe the multiferroic behaviour in STM, the sample shall be polarized locally by an applied electric field and consequently read-out by probing the spin-resolved local density of states (LDOS) via spin-resolved scanning tunneling microscopy and spectroscopy (SP-STM, SP-STs).

## Results

The project started in July 2021. In a first step, particular attention was given to the preparation of clean GeTe and GeMnTe surfaces. Samples were prepared by a project partner in Linz, Austria [5], and were sent to us with a protective selenium capping layer. The removal of this capping layer by annealing the sample and the cleanliness of the sample afterwards were investigated. XPS spectra before (red) and after (blue) this decapping process are depicted in figure 1 showing that the Se peaks disappeared while Te and Ge peaks appear. Figure 2 (a) shows the low energy electron diffraction (LEED) picture of a decapped GeTe sample on InP(111) clearly depicting the expected hexagonal surface symmetry while (b) depicts an STM image taken on the same sample. The inset illustrates the observed hexagonal surface structure.

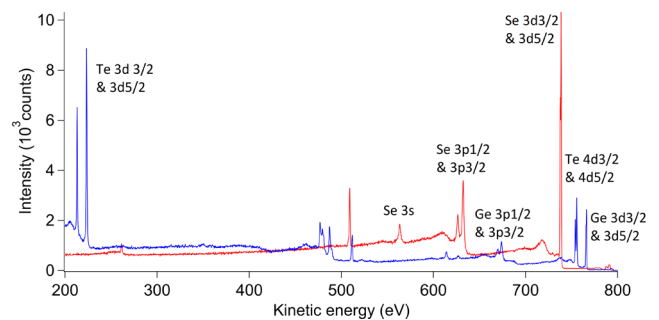


Fig. 1: Survey XPS spectra of a GeTe sample before (red) decapping the protective Se layer and after (blue) the decapping process. It is clearly visible that the Se peaks disappear while Te and Ge peaks appear meaning that the decapping process was successful.

The decapping study showed though that a systematic and repeatable removal of the capping layer leading to a clean sample surface is hard to achieve as the evaporation temperatures of the capping layer and the GeTe film are not clearly distinct. STM and STS are particularly sensitive to remainders of the capping layer or surface defects induced by excessive annealing. Good quality STM pictures like those in figure 2 were obtained in few locations on the sample. Hence we conclude that uncapped samples brought via vacuum suitcase or the direct preparation on site, if possible, should be favored in the future.

## Outlook

In the next steps of this project, the possibility of a direct preparation of samples in our lab will be tested to avoid regular time-consuming trips to Austria and having a quick and direct access to clean and well prepared samples. This task involves finding the right parameters in a multi evaporation source setup for a stoichiometric growth of GeTe and GeMnTe.

Also, the surface atomic and domain structure as well as the surface electronic structure of GeTe and GeMnTe samples will be further probed via STM and STS. Our STM will then undergo an upgrade, including a magnet, to be able to perform spin-resolved STM and STS in the future. The preparation of adequate magnetic tips will be an important prerequisite to perform such measurements.

At the synchrotron light source photoelectron diffraction measurements and corresponding simulations are in progress and shall bring a complementary understanding of the underlying atomic surface structure. Angular resolved photoemission spectroscopy measurements will give insight into the band structure of our samples.

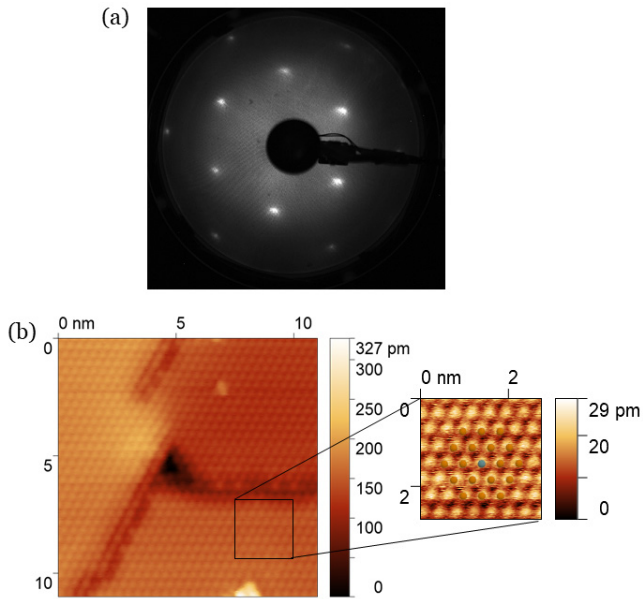


Fig. 2: a) Low energy electron diffraction picture at 87 eV of a decapped GeTe sample showing a hexagonal surface symmetry. b) STM (-1 V, 20 pA) taken on the same sample with an inset demonstrating the expected hexagonal surface structure.

## References

- [1] N. Spaldin, S. Cheong, R. Ramesh, Multiferroics: Past, present, and future, *Physics Today* 63, 38-43 (2010)
- [2] S. Datta, B. Das, Electronic analog of the electro-optic modulator, *Appl. Phys. Lett.* 56, 665-667 (1990)
- [3] J. Krempaský et al., Operando Imaging of All-Electric Spin Texture Manipulation in Ferroelectric and Multiferroic Rashba Semiconductors, *Phys. Rev. X* 8, 021067 (2018)
- [4] M. Muntwiler et al., Surface science at the PEARL beamline of the Swiss Light Source, *J. Synchrotron Rad.* 24, 354 (2017)
- [5] M. Hassan, G. Springholz, R.T. Lechner, H. Groiss, R. Kirchschrager, G. Bauer, Molecular beam epitaxy of single phase GeMnTe with high ferromagnetic transition temperature, *J. Cryst. Growth* 323(1), 363-367 (2011)

# Harnessing polymer compartments with bacterial toxins

Project P2005: Transmembrane protein-mediated loading of synthetic compartments

Project Leader: C. Palivan and R. A. Kammerer

Collaborators: P. Jaško (SNI PhD Student)

Compartmentalization, a prerequisite for the spatiotemporal control of biochemical pathways in cells, is an emerging concept in designing new materials for medical and technological applications. Synthetic nano- and micro-compartments (NCs, MCs) with their chemical versatility and superior stability provide the basis for developing catalytic compartments, artificial organelles, or cell mimics that are furnished with specific biomolecules to drive desired reactions or deliver therapeutic payloads [1][2]. However, a higher compartment loading efficiency and better permeability of the synthetic membrane remain hurdles that need to be overcome to increase the efficacy of in situ reactions. Tools that already exist in living organisms, such as pore-forming toxins that can translocate protein cargo, provide inspiration to tackle these hurdles [3]. Transmembrane proteins have evolved to function within the lipidic bilayers of living cells. Little is known how this class of proteins behaves within artificial membranes made of polymers, in particular, whether they retain their native function in biomedical and industrial applications of such biohybrid systems [4]. In this interdisciplinary project, we set out to develop next-generation functional artificial compartments comprising specific pore-forming transmembrane proteins. Besides using these biohybrid model membranes to explore the structural and functional features of the pore-forming proteins, we plan to engineer the system such that protein cargo can translocate to the compartment interior or that specific molecular flow across the membrane can take place.

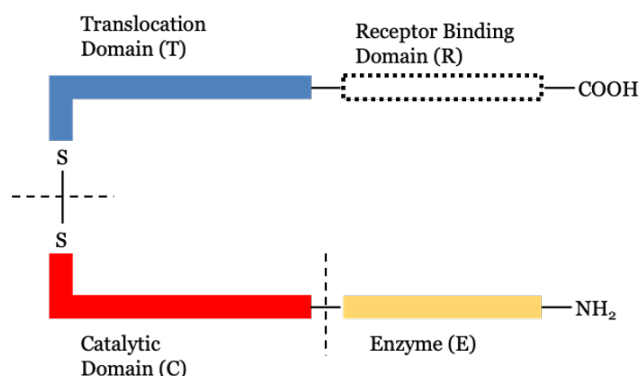


Fig. 1: Schematic representation of the architecture common to the toxins. Our recombinant toxins are devoid of the receptor-binding domain (R). An additional enzyme (E) can be fused to the catalytic domain or directly to the translocation domain.

For membrane insertion, we selected a set of bacterial AB toxins (referred to as toxin X and Y) with a similar three-do-

main architecture (Fig. 1; Fig. 2A): a catalytic domain (C), translocation domain (T), and receptor-binding domain (R), the latter being absent in our constructs. Once a toxin variant successfully inserted into an artificial membrane (Fig. 2B), we will examine if the catalytic domain is shuttled across the synthetic membrane under specific conditions. Finally, the ability of the C-domain to piggyback extra cargo to the compartment interior will be explored by fusing an enzyme at the N-terminus of the C-domain. The second scenario assumes direct fusion of a cargo to the T-domain. The reducing environment inside the compartment will release the enzymes (Fig. 2C). To monitor the interaction of recombinant toxin variants with the synthetic membrane by means of fluorescence-based methods, we produced a set of recombinant GFP fusion T-domains.

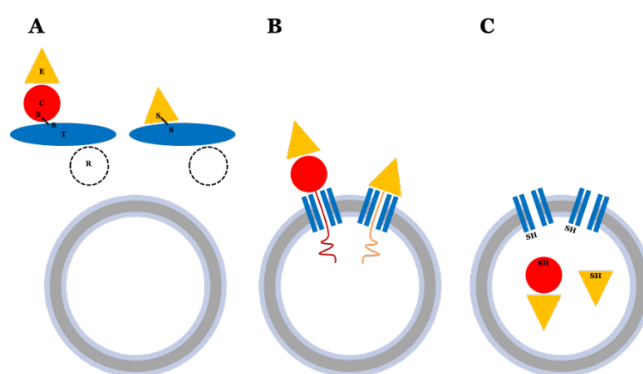


Fig. 2: Concept flow scheme.

Constructs were designed based on the translocation domain sequences encoding wild-type variants of toxins X and Y with and without GFP as a fusion partner, which were initially cloned into an adapted pET22b vector. This vector comprises His<sub>6</sub>-tag and Strep-tag II sequences for the purification of recombinant proteins and restriction sites for further engineering. Recombinant proteins were expressed in BL21 (DE3) E. coli strain and affinity purified using His<sub>6</sub>-tag and/or Strep-tag II. Expression conditions were analyzed by SDS-PAGE analysis followed by immunoblotting as well as SDS-PAGE in-gel fluorescence for GFP fusion constructs.

For the protein purification bacteria pellets were resuspended in Tris buffer (20 mM Tris-HCl pH 7.4, 400 mM NaCl) with 2x cComplete™ EDTA-free protease inhibitor cocktail and lysed by sonication and clarified via centrifugation to separate soluble and insoluble fractions. For the toxin X variants overnight incubation at 4°C with a detergent was carried out. For these samples, detergent was present in all following buffers. His<sub>6</sub>-tag purification was performed using a Ni-NTA (nitrilotriacetic acid, Qiagen) (Fig. 3) affinity col-

umn in a buffer containing 20 mM Tris-HCl pH 7.4, 400 mM NaCl, and 20 mM imidazole. The protein was eluted in the same buffer with 400 mM imidazole. For Strep-tag II purification, the Strep-Tactin® affinity column was used in a buffer composed of 20 mM Tris-HCl pH 7.4, 400 mM NaCl. Elution was carried out in the same buffer with 2.5 mM d-Desthiobiotin. The eluted fractions were pooled, desalted, and purified by Superdex-200 size-exclusion chromatography (SEC; GE Healthcare, Germany) (Fig. 4). Each protein was concentrated to ~1 mg/ml using Amicon Ultra centrifugal filters (Millipore) and stored at -80°C until used for further studies. We are currently using toxin variants to establish conditions for the functional insertion of these proteins into nano- and micrometer-sized vesicles and planar membranes assembled from amphiphilic block copolymers.

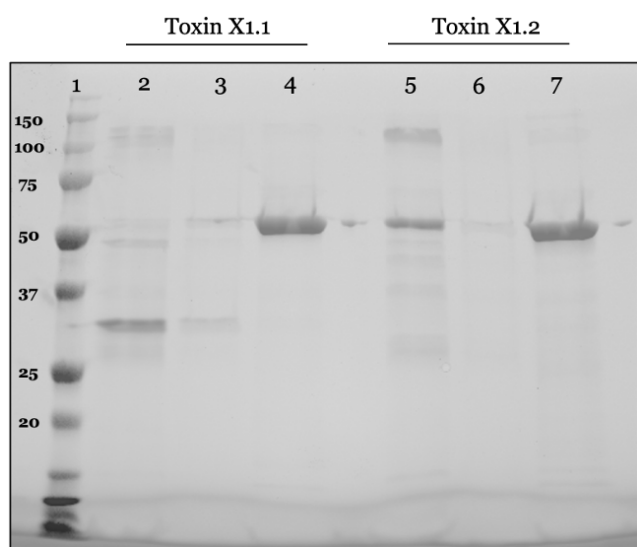


Fig. 3: SDS-PAGE analysis of Toxin X1.1 and X1.2 purification by Ni-NTA affinity chromatography. Lane 1 – molecular weight marker; lanes 2 and 5, flow-through; lanes 3 and 6, wash; lanes 4 and 7, elution.

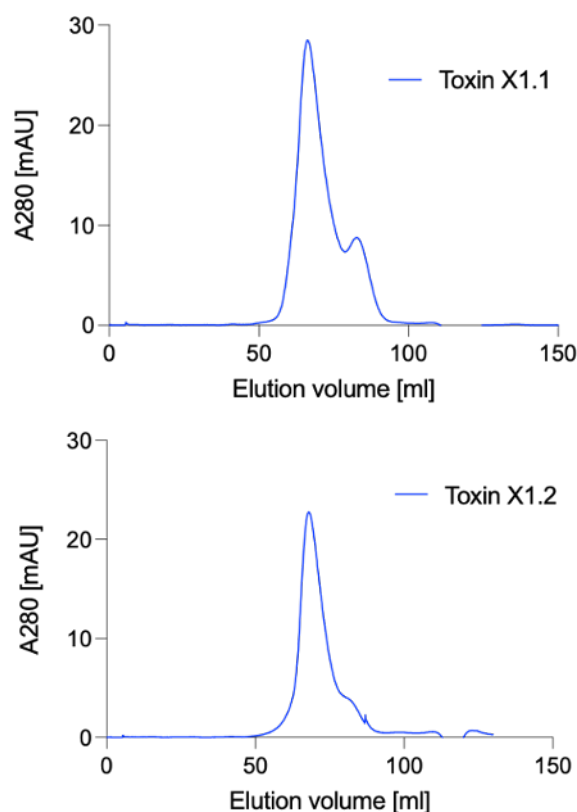


Fig. 4: Size exclusion chromatography of Ni-NTA affinity chromatography purified toxins. Top panel, elution profile of the toxin variant X1.1. Bottom panel, elution profile of the toxin variant X1.2.

## References

- [1] E. C. Dos Santos, A. Belluati, D. Necula, D. Scherrer, C. E. Meyer, R. P. Wehr, E. Lörtscher, C. G. Palivan, W. Meier. Combinatorial Strategy for Studying Biochemical Pathways in Double Emulsion Templated Cell-Sized Compartments. *Adv Mater.* 32, 48 (2020)
- [2] V. Maffei, A. Belluati, I. Craciun, D. Wu, S. Novak, C. A. Schoenenberger, C. G. Palivan. Clustering of catalytic nanocompartments for enhancing an extracellular non-native cascade reaction, *Chem Sci.* 12, 37 (2021)
- [3] R. A. Kammerer, R. M. Benoit, Botulinum neurotoxins: new questions arising from structural biology, *Trends Biochem. Sci.* 39, 11 (2014)
- [4] U. Chawla, Y. Jiang, W. Zheng, L. Kuang, S. M. Perera, M. C. Pitman, M. F. Brown, H. Liang. A Usual G-Protein-Coupled Receptor in Unusual Membranes, *Angew. Chem. Int. Ed. Engl.* 55, 2 (2016)

# Synthesis and surface chemistry studies of zirconium oxo clusters

Project P2006: RESTRAIN – Reticular chemistry at interfaces as a form of nanotechnology

Project Leader: P. Shahgaldian and J. De Roo

Collaborators: A. Roshan (SNI PhD Student)

## Introduction

Reticular chemistry is defined as the chemistry of linking discrete chemical entities by coordination bonds to yield extended crystalline materials [1]. Produced by reticular chemistry, metal-organic frameworks (MOFs) – organic-inorganic materials consisting of a regular array of metal clusters and rigid polytopic organic linkers - display unprecedented physicochemical properties (e.g., porosity, gas adsorption)[2]. The choice of secondary building units (SBUs) and organic linkers is crucial in MOF design since these constituents have a substantial impact on these properties [3]. While MOFs are developed for applications in catalysis, gas storage and separation, their implementation is somewhat limited by their relatively small size, typically in the micrometer range. RESTRAIN aims at addressing this challenge by applying a rational design approach based on the use of atomically precise nanocluster-based SBUs in MOFs' template-based production.

## Synthesis of secondary building units

RESTRAIN aims at using metal oxo clusters, the smallest conceivable nanocrystals, as SBUs. To that end, we produced well-defined zirconium oxo clusters, particularly  $Zr_6O_8$  core ( $Zr_6(\mu_3-O)_4(\mu_3-OH)_4$ ) displaying high thermal stability expected to positively impact the properties of the corresponding MOFs (Fig. 1).

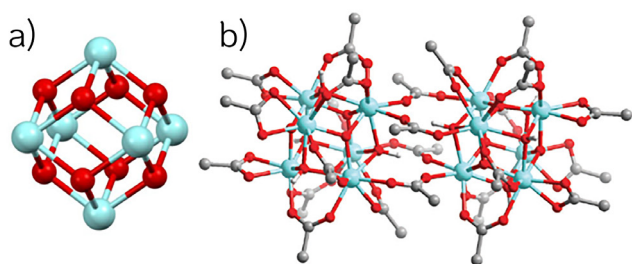


Fig. 1: a)  $Zr_6O_8$  core b)  $[Zr_6(O)_4(OH)_4(CH_3COO)_{12}]_2$

Clusters capped with different carboxylates are conveniently synthesized from zirconium propoxide solution (70% in propanol) and respective carboxylic acids under inert conditions with a yield ranging from 50-90% (Fig. 2). Most often, excess carboxylates, solvents or byproducts co-crystallize with the clusters (e.g.  $[Zr_6(O)_4(OH)_4(CH_3COO)_{12}]_2 \cdot 6CH_3COOH \cdot 3.5DCM$ ). All the clusters were fully characterized with nuclear magnetic resonance (NMR). Carboxylic acids bearing an  $\alpha$ -branched-chain yielded a monomer octaeder while linear acids yielded a dimer. The long aliphatic chains of acids make the corresponding clusters soluble in nonpolar solvents.



Fig. 2: Synthetic scheme of the zirconium oxo clusters from zirconium propoxide and carboxylic acids.

## Surface chemistry studies of clusters

The opportunity to modify the surface chemistry of the oxo clusters produced with phosphonic acids with varying chain length (i.e., hexyl, oleyl and hexyldecyl) has been investigated. We demonstrated that the ligand shell of zirconium octaeters can be partially or fully replaced applying appropriate synthetic conditions. Interestingly, non-carboxylate ligand shells can be developed around these smallest conceivable nanocrystals. The effect of aliphatic chain length, steric hindrance effects and multiple coordinating functionalities on ligands were studied by means of NMR spectroscopy.

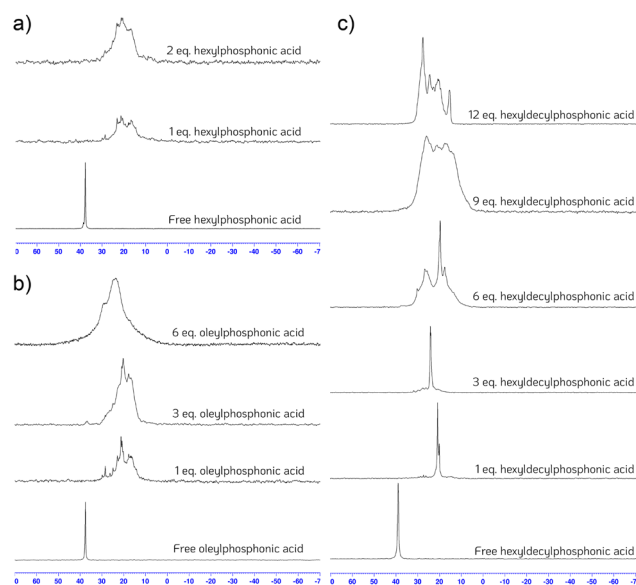


Fig. 3:  $^{31}P$  NMR spectra of the titration studies of  $[Zr_6(O)_4(OH)_4(CH_3COO)_{12}]_2$  with a) hexylphosphonic acid b) oleylphosphonic acid, and c) hexyldecylphosphonic acid.

The addition of one equivalent hexylphosphonic acid to the  $Zr_{12}$  acetate cluster gelled out the entire solution, probably owing to the shorter length of the aliphatic chains and presence of multiple hydroxyl groups, which can crosslink the clusters. On the other hand, no gelation yet multiple bind-

ing modes were observed upon titrating with hexyldecylphosphonic acids. Our results indicate that steric hindrance, chain length, and coordinating functionalities must be considered while capping the clusters. This set of results is expected to be of importance for the further application of the produced clusters in the design of MOFs.

### Synthesis of amphiphilic organic linkers

Besides the design of oxo clusters, we also focused on the synthesis of organic building blocks that can be used to produce MOFs. Those molecules can be linked by metals such as copper and possible oxo-clusters. The first calixarenes we focused on, owing to a highly symmetric and rigid macrocyclic, are based on the 4-membered ring macrocycle as depicted in figure 4 (5 and 8).

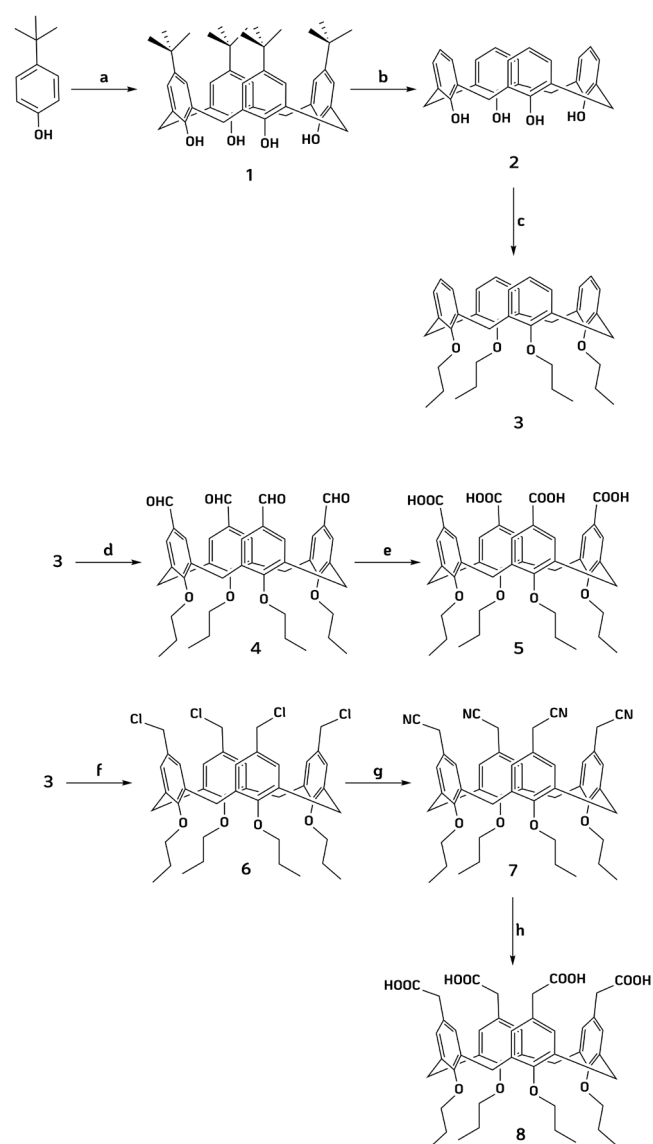


Fig. 4: Synthetic route of the amphiphilic calix[4]arenes 5 and 8 from 4-tert-butylphenol. a) NaOH, formaldehyde, diphenylether, toluene, 260°C, 4h. b) AlCl<sub>3</sub>, phenol, toluene, rt, 3h. c) iodopropane, NaH, DMF, rt, overnight. d) Hexamethylenetetramine, trifluoroacetic acid, 120°C, 4h. e) Sulfamic acid, sodium chlorite, H<sub>3</sub>PO<sub>4</sub>, water, chloroform/acetone, 100°C, overnight. f) paraformaldehyde, acetic acid, HCl, H<sub>3</sub>PO<sub>4</sub>, dioxane, 80°C, 18 h. g) NaCN, DMSO, 80°C, 3h. h) KOH, ethanol, water.

The amphiphiles 5 and 8 can form crystalline metal-organic coordination networks in the presence of metal ions such

as Cu<sup>2+</sup> and Ni<sup>2+</sup>, which encouraged us to combine them with zirconium oxo clusters [4,5]. Calix[4]arenes were produced through a rigorous multistep synthesis starting from 4-tert-butylphenol. Base-catalyzed condensation of 4-tert-butylphenol and formaldehyde triggers the cyclization to form 1, followed by retro-Friedel-Craft dealkylation yielding 2. Later, the lower rim was protected with iodopropane to give 3. Upper-rim formylation of 3 yielded 4, and further oxidation to 5 resulted in our first amphiphilic macrocycle [6]. Chloromethylation, nitrile substitution and subsequent base hydrolysis of 3 yielded the second amphiphilic calix[4]arene 8[7]. The final molecules and intermediates were well-characterized with NMR, ESI-MS and IR spectroscopy.

### Conclusion and outlook

We have successfully synthesized inorganic oxo clusters and carboxylate-bearing calix[4]arenes. Also, surface chemistry studies are being extrapolated to DFT calculations to understand the theoretical aspects in detail. Work in underway to study the self-assembly of the produced molecular entities.

### References

- [1] O. M. Yaghi, M. J. Kalmutzki, C. S. Diercks, Introduction to Reticular Chemistry : Metal-Organic Frameworks and Covalent Organic Frameworks, Wiley-VCH, Weinheim (2019)
- [2] A. E. Baumann, D. A. Burns, B. Liu, V. S. Thoi, Metal-organic framework functionalization and design strategies for advanced electrochemical energy storage devices. Commun. Chem. 2, 1-14 (2019)
- [3] Y. Bai, J. Dou, L.-H. Xie, W. Rutledge, J.-R. Li, H.-C. Zhou, Zr-based metal-organic frameworks: design, synthesis, structure, and applications. Chem. Soc. Rev. 45, 2327–2367 (2016)
- [4] M. Moradi, L. G. Tulli, J. Nowakowski, M. Baljovic, T. A. Jung, P. Shahgaldian, Two-Dimensional calix[4]arene-based metal-Organic coordination networks of tunable crystallinity. Angew. Chem. Int. Ed. 129, 14587–14591 (2017)
- [5] M. Moradi, N. L. Lengweiler, C. E. Housecroft, L. G. Tulli, H. Stahlberg, T. A. Jung, P. Shahgaldian, Coordination-driven monolayer-to-bilayer transition in two-dimensional metal-organic networks. J. Phys. Chem. B 125, 4204–4211 (2021)
- [6] F. Sansone, S. Barbosa, A. Casnati, M. Fabbi, A. Pochini, F. Uguzzoli, R. Ungaro, Synthesis and structure of chiral cone calix[4]arenes functionalized at the upper Rim with L-Alanine units. Eur. J. Org. Chem. 897-905 (1998)
- [7] S. K. Sharma, S. Kanamathareddy, C. D. Gutsche, Upper rim substitution of calixarenes: carboxylic acids. Synthesis 1997, 1268–1272 (1997)

# Manipulation of small particles by acoustic radiation pressure

Project P2007: Development of nanoscale acoustic tweezers for mechanobiology application

Project Leader: S. Tsujino and R. H. Y. Lim

Collaborators: S. Jia (SNI PhD Student)

## Introduction

We are developing an ultrasound tool kit for manipulating small particles with the aim of application for cellular mechanobiology. Here we describe the current development of the acoustic tweezers (ATZs) based on the acoustic radiation pressure which acts on the difference of acoustic impedance between particles and fluid [1]. This different modality of small microparticle manipulation than optical tweezers can work from large objects, for chemical and biochemical analysis and protein crystallography [2,3], to submicron scale objects such as including the intracellular organelle by increasing the ultrasound frequency.

## Manipulation of cells and polystyrene (PS) particles by ATZs

To establish the principle and characterization methods, we applied ultrasound transducers with the frequency of 2-8 MHz for manipulation of cells and polystyrene particles via standing wave ultrasound (see Fig. 1). The cells and particles are spatially localized at the node of the acoustic standing wave horizontally and vertically. By displacing the standing wave via the movement of the transducer, an efficient positional manipulation of the objects, so far down to 20 microns, are conducted as shown in figure 2 and 3.

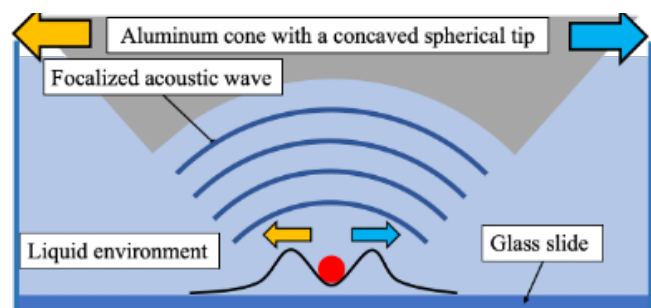


Fig. 1: Schematic of the mechanism of particle manipulation by ATZ.

As shown by figure 2a-c, a cluster of HEK<sub>293</sub>T cells, suspended in DMEM buffer, can be moved from the left to the right and then back to where it was initially located. Although these cells were transfected with the red fluorescence protein mCherryCAS, no fluorescence was seen, which necessitates the improvement on the lighting for the microscope. Similarly, a red fluorescent spherical PS particle of 90  $\mu\text{m}$  in diameter, suspended in water, can be manipulated by an ATZ as well, as shown by figure 2d-f.

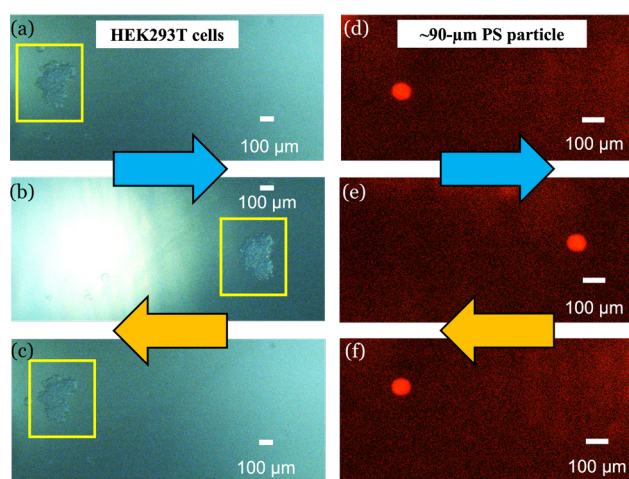


Fig. 2: Manipulation of (a-c) HEK<sub>293</sub>T cells and (d-f) a 90- $\mu\text{m}$ -diameter PS particle, respectively

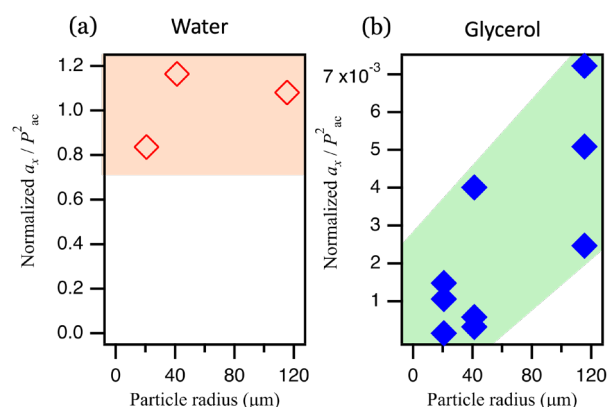


Fig. 3: Normalized  $a_x / P_{ac}^2$  of different sized particles manipulated in water and glycerol, respectively.

Subsequently, to establish a proof of principle, we used ATZs to manipulate PS particles of 20  $\mu\text{m}$ , 45  $\mu\text{m}$ , and 100  $\mu\text{m}$  in radius in water and glycerol, respectively. To compare the particle size dependence of acceleration, we plot the normalized  $a_x / P_{ac}^2$  versus the particle radius in figure 3a and b, where the particle acceleration in x direction,  $a_x$ , is divided by the square of the acoustic pressure,  $P_{ac}^2$ , to exclude the difference in acoustic energy density, and the quantity  $a_x / P_{ac}^2$  is then normalized with regard to its average in water. It is obvious that a larger particle radius in glycerol leads to a higher acceleration, which can be attributed to a correspondingly smaller damping constant,  $\gamma = 6\pi\eta R / m = 9\eta / (2R^2 \rho)$ ,

originating from the Stokes drag force, where  $\eta$ ,  $R$ ,  $m$ , and  $\rho$  are the dynamic viscosity of the medium, the radius, mass and mass density of the particle, respectively. Nevertheless, such dependence, unseen in water (Fig. 3a), is perhaps obscured by the suspected friction that comes into play when the particles are sliding on the glass rather floating in water.

### Lithography-defined acoustically driven rotors

We also investigated ultrasound-actuated rotors fabricated by lithography. Their shape follows from the recent experiment on the application of polymer thin films for protein crystallography experiments [4]. In figure 4, we show pictures of two rotors. These are fabricated from a negative photoresist mr-DWL 40 (Micro Resist Technology, GmbH) using a direct laser writing tool (Heidelberg Instruments DWL66+). Despite the few residues left on the legs of the 400- $\mu\text{m}$  rotor, these rotors have smooth surfaces and sharply defined edges. We have found that these rotors turn at high speed despite their apparent symmetry in the same ATZ experiment setup up to  $\sim 10$  rotation per second (rps). We found that their rotation efficiency is highly dependent on the wavelength of the ultrasound: the maximum rotation was observed when the half wavelength matches the disk diameter (Fig. 4). We note that although asymmetric structure will more efficiently couple with the acoustic radiation pressure, it will at the same time increase the friction, which can result in a smaller rotation speed and the positional instability.

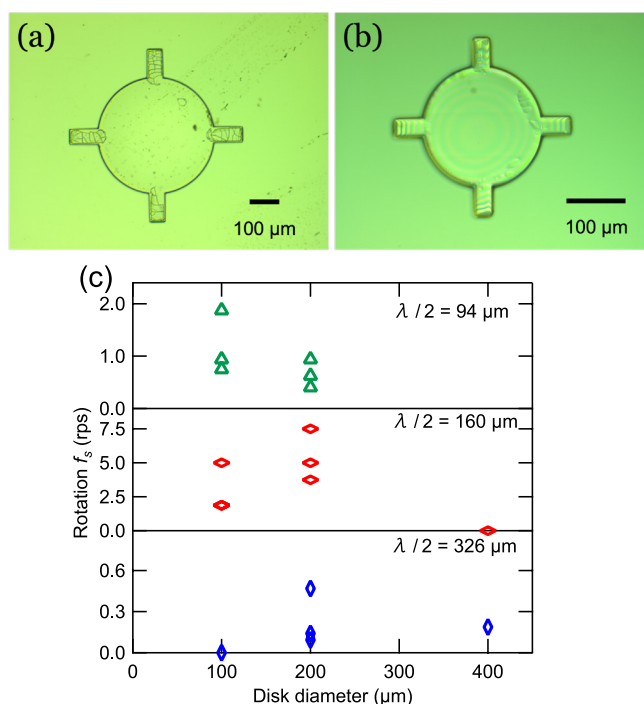


Fig. 4: a) and b) Fabricated acoustic rotors with the diameter of 400  $\mu\text{m}$  and 200  $\mu\text{m}$ ; c) size-dependent rotation characteristic of acoustic rotors at three ultrasound frequencies.

We plan to extend this investigation to 10 - 100 times smaller scale together with the acoustic wavelength of ATZ, to assist the mechanobiology investigation.

On the side, we have extended the acoustic rotation of disks in airborne acoustic levitator. In the case of the 4 mm-diameter-disk rotors levitated in air with the 40 kHz ultrasound, the levitation and rotation has been intensively studied as the sample holder for X-ray protein crystallography [4], wherein the mechanism of rotation, the precise roles of the disk size and the short blades have been elusive. The result shown in figure 5 demonstrates the size dependent enhancement of the acoustic pressure and the rotation control for different sizes.

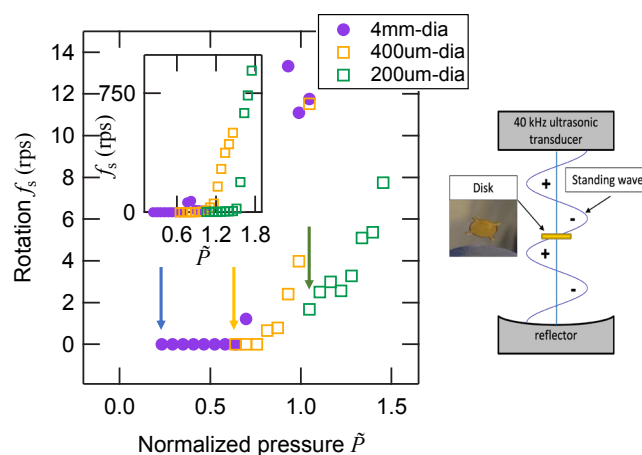


Fig. 5: Airborne rotation rate versus acoustic radiation pressure normalized by 1.35 kPa which is the minimum acoustic radiation pressure to levitate a small water droplet (the insets show these three disks being levitated)

### Summary

In this first year of the project, we have demonstrated the manipulation of small particles and cells by acoustic radiation pressure in fluid. An efficient acoustic tweezing was shown even in a fluid with orders of magnitude higher viscosity than water, suggesting the effectiveness of the method even in an intracellular fluid environment. The ATZ manipulation was also used for the rotation control of lithography-defined rotors, that was found to be largely dependent on the acoustic wavelength. The extension of the investigation of these rotors in different sizes confirmed the previous conclusion on the acoustic-radiation-pressure origin of the disk rotation [4] and the importance of the short blades around the disk structure.

### References

- [1] A. Ozcelik, J. Rufo, F. Guo, Y. Gu, P. Li, J. Lata, T. J. Huang, Acoustic tweezers for the life sciences, Nat Methods 15, 1021 (2018)
- [2] S. Tsujino, T. Tomizaki, Ultrasonic acoustic levitation for fast frame rate X-ray protein crystallography at room temperature, Sci Rep 6, 25558 (2016)
- [3] S. Tsujino, A. Shinoda, T. Tomizaki, On-demand droplet loading of ultrasonic acoustic levitator and its application for protein crystallography experiments, Appl. Phys. Lett. 114, 213702 (2019)
- [4] M. Kepa, T. Tomizaki, Y. Sato, D. Ozerov, H. Sekiguchi, N. Yasuda, K. Aoyama, P. Skopintsev, J. Standfuss, R. Cheng, M. Henning, S. Tsujino, Acoustic levitation and rotation of thin films and their application for protein crystallography (in preparation, 2021)

# Integrating a nanowire quantum dot on a scanning probe tip

Project P2008: Scanning nanowire quantum dot

Project Leader: D. Zumbühl and M. Poggio

Collaborators: L. Forrer (SNI PhD Student)

## Introduction

We are developing a new kind of scanning probe microscope, which employs gated quantum dots (QDs) embedded in semiconductor nanowires (NWs), integrated on the tip of standard force microscopy cantilevers. These sensors will be sensitive scanning probes of charge and electronic density [1]. The sensors will be used to characterize the spatial profile of charge noise, quantum dots, and electric fields [2] in spin qubit devices, aiding the design of coherent quantum computation processors. This is particularly relevant here in the Department of Physics of the University of Basel, where the NCCR SPIN, aimed at producing scalable spin qubits in Si was established in the summer of 2020.

Our scanning probe method builds on previously developed scanning single-electron transistors (SETs) made from metallic islands [1] or scanning QDs defined in carbon nanotubes (CNTs) [2]. Research efforts using such devices have been extremely fruitful, due to the high sensitivity to electric field. Indeed, QD-based sensors are the preferred sensors of charge in applications in quantum computation with spins in QDs, where they are incorporated on the same substrate as the sample of interest. Such charge sensors make use of sharp spikes in the electrical conductance of the QDs (Coulomb peaks) and are capable of detecting a small fraction of an electronic charge at micron distance. Until now, however, both scanning SETs and scanning QDs in CNTs have been relatively cumbersome to use, extremely delicate, and limited in their design. These drawbacks are a result of the specialized processes involved in their fabrication.

Our approach addresses this shortcoming by using standard AFM cantilevers as the scanning probe combined with NWs as the QD hosts. By developing a scheme for patterning leads, gates, and contacts directly to the cantilever tip, we will have maximum flexibility for the design of our sensors. AFM levers allow easy tip-sample distance control, topographic contrast. NW QDs possess many qualities that make them suitable for use in scanning probes: they are small (~10-50 nm), need few gates because of the natural 1D confinement, and can due to the low-dimensional geometry of the NW be easily brought closer than 100 nm to a sample. Importantly, their strong confinement and tunable nature endows NW QDs with a higher sensitivity to electric fields and nearby charges than their SET counterparts. Moreover, NW crystals can be grown with an exceptional control over material composition. The specific NW material composition can pass on useful properties to the embedded probe QDs, such as a strong spin-orbit interaction, which may offer interesting new modalities of sensing.

So far, we have developed and optimized techniques for patterning scanning probe cantilevers with the suitable electrical contacts and gates. Furthermore, we have developed methods for transferring individual NWs to the apex of such prepatterned cantilevers, completing the probe. We are now

in the process of optimizing electrical contact to the NWs, which are placed on the cantilever, as well as constructing a suitable low-temperature scanning probe setup.

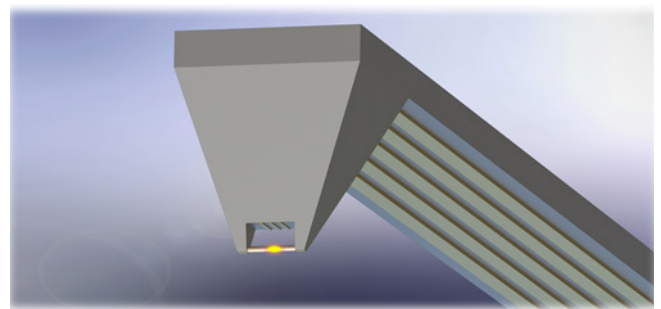


*Fig. 1: A schematic representation of a cantilever with a gate-controlled NW QD at its tip. Such a scanning probe would represent a new and highly sensitive tool for measuring tiny electric fields with nanometer-scale resolution, all on the familiar platform of an atomic force microscopy cantilever.*

## Goals

The main goals of this project are to: 1) Fabricate scanning probe cantilevers hosting a NW with embedded gated QDs (T); 2) Image the electronic density of nanoscale samples with unprecedented sensitivity (F); 3) Implement high-bandwidth scanning probe imaging using microwave reflectometry techniques (T); 4) Image and study the dynamics of charge fluctuators in semiconducting devices (F).

As indicated, the project will yield advances of technological (T) and of a more fundamental (F) nature. Whereas the necessary technological advances will include proof-of-principle experiments, with the fundamental advances we expect to move past this demonstration stage and gain new physical insights of nanoscale devices and novel materials. It is here that the project will have its major impact. The proposed scanning NW QD will allow fast, high-resolution imaging with minimal invasiveness and under a large variability of environmental conditions of novel nanoscale physical phenomena, including highly correlated electronic states, Majorana fermions, and phase transitions in 2D materials.

## Results

In the first year, we have developed fabrication techniques for patterning electrical contacts and gates on commercially available cantilevers through two methods: 1) focused ion beam (FIB) lithography and 2) specialized electron beam lithography (EBL).

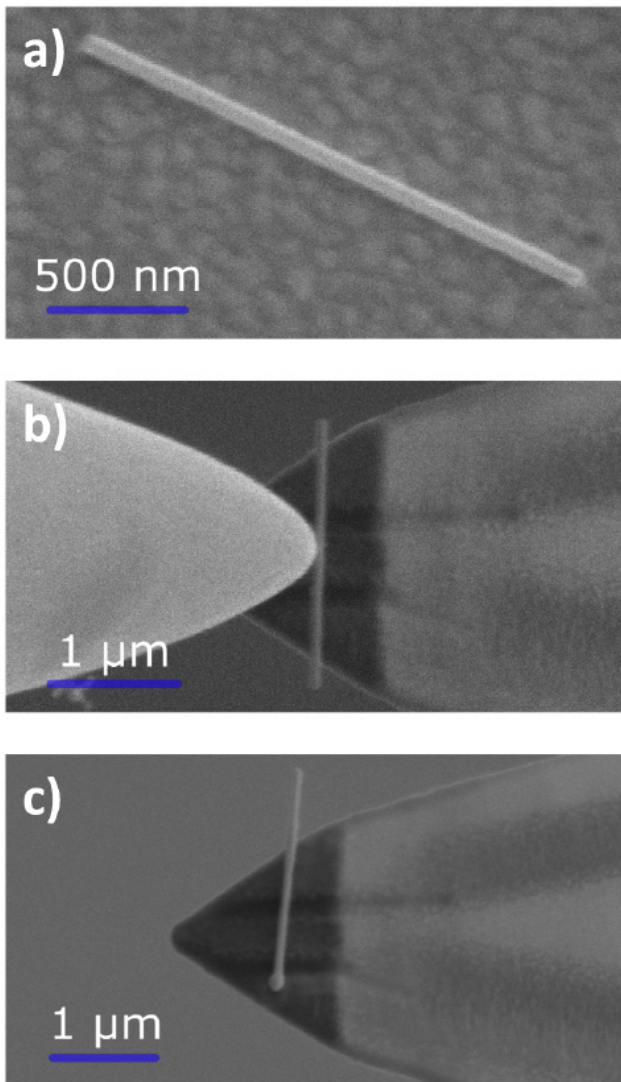


Fig. 2: a) InAs/InP NW on gold surface, b) NW on tungsten nanomanipulator probe, c) NW transferred onto cantilever; suspended by contact over a single gate.

Method 1 involves FIB milling and focused-ion-beam-induced deposition (FIBID) of Pt to bring these electrodes from the bond pads on the main cantilever body to the apex of the cantilever tip. We have reduced gate-to-gate leakage through the deposition of an insulating layer underneath the gates. Furthermore, we have reduced leakage caused by implanted Ga<sup>+</sup> ions through suitable reactive ion etching. We now reach negligible values of gate leakage at low temperature operating conditions. Moreover, we have optimized the placing and fixing of individual NWs onto the prepatterned cantilever tip, where the NW is suspended over a set of gates and contacted from both sides. We have tested this process with Ge/Si core/shell NWs, as well as InAs/InP NWs featuring in-built tunnel barriers. Figure 2 shows such a transfer process, performed with a nanomanipulator probe inside the FIB apparatus.

Method 2 involves EBL to pattern the cantilever. We have developed a method to cover a high-aspect-ratio sample – in our case the tip of a cantilever – with PMMA. Using this specialized EBL, we are able to carry out patterning, evaporation, and lift-off at the cantilever apex, resulting in structures with sizes down to 150 nm. This method gives us the opportunity to fabricate gates on the tip of our lever and contact NWs by evaporation of metal as done on conventional planar substrates [3,4].

## Outlook

We are currently optimizing the production of Ohmic contacts to the NWs on cantilever, by reducing carbon content in the Pt contacts, as well as testing various methods of etching the NWs surface oxide prior to metallization. Optionally, other metal sources than Pt will be purchased and installed in the FIB, in order to optimize Ohmic contacting. In addition, we are optimizing the developed EBL process and we are working on contacting a InAs/InP NW on the tip of a cantilever. Finally, we have nearly completed the construction of a custom-built 1 K setup used for transport characterization of the devices, as well as a 4 K setup used to perform the initial scanning probe measurements. We anticipate the first application of our scanning probe in the coming year.

Once the on-tip NW QDs are functioning as scanning probes for electric field, we intend to measure and optimize new fully-depleted Si-on-insulator (FD-SOI) spin qubit devices to minimize charge noise due to defects at the surface and in oxides. We expect that nanometer-scale spatial maps of the sources of charge noise will be crucial in the mitigation of such noise sources, which lead to spin decoherence in electron-spin qubit devices.

## References

- [1] M. J. Yoo, T. A. Fulton, H. F. Hess, R. L. Willett, L. N. Dunkleberger, R. J. Chichester, L. N. Pfeiffer, and K. W. West, Scanning Single-Electron Transistor Microscopy: Imaging Individual Charges. *Science* 276, 579 (1997)
- [2] L. Ella, A. Rozen, J. Birkbeck, M. Ben-Shalom, D. Perello, J. Zultak, T. Taniguchi, K. Watanabe, A. K. Geim, S. Ilani, and J. A. Sulpizio, Simultaneous voltage and current density imaging of flowing electrons in two dimensions, *Nat. Nanotechnol.* 14, 480 (2019)
- [3] F. S. Thomas, A. Baumgartner, L. Gubser, C. Jünger, G. Fülöp, M. Nilsson, F. Rossi, V. Zannier, L. Sorba, C. Schönenberger, Highly symmetric and tunable tunnel couplings in InAs/InP nanowire heterostructure quantum dots, *Nanotechnology.* 31 (2020)
- [4] F. N. M. Froning, M. Rehmann, J. Ridderbos, M. Brauns, F. A. Zwanenburg, A. Li, E. P. A. M. Bakkers, D. M. Zumbühl, F. R. Braakman, Single, double, and triple quantum dots in Ge/Si nanowires, *APL.* 113 (2018)

# Hybrid Van der Waals heterostructures for organic electronics

Project P2009: Hybrid Van der Waals heterostructures for vertical permeable-base organic transistors

Project Leader: M. Calame and H.-J. Hug

Collaborators: J. Oswald (Associate SNI PhD Student), D. Beretta (Empa)

## Introduction and state-of-the-art

The mechanical and electrical properties of organic thin films and 2D materials, such as graphene, enables the realization of flexible electronics operating at low-voltage and high frequency. In this project, we study the structural and electrical properties of vertical hetero-structures made of graphene and organic thin films. In such architecture, the charge transport occurs in very short vertical channels allowing for the realization of fast switching devices, e.g. vertical organic transistors and light emitting diodes [1-3].

## Fabrication and material characterization

We fabricate graphene/organic interfaces by optical lithography. (i) Metallic bottom electrodes are patterned on a Si/SiO<sub>2</sub> substrate. (ii) A thin film of organic semiconductor (e.g. C<sub>60</sub>) is deposited by thermal evaporation. (iii) CVD (Chemical Vapor Deposition) graphene is grown on a copper foil, wet transferred on the organic film (Fig. 1a), and subsequently structured by photolithography and reactive ion etching. The morphology and chemical composition of the devices are then investigated by atomic force microscopy (Fig. 1c) and Raman spectroscopy (Fig. 1b), respectively.

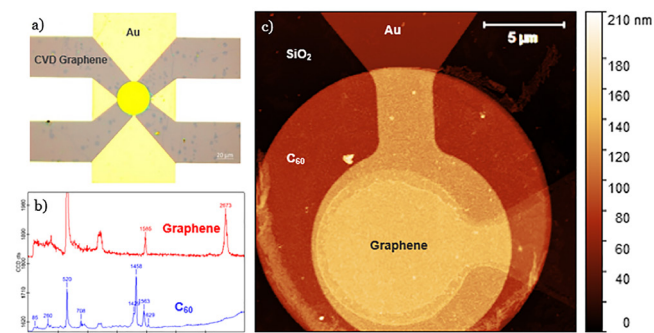


Fig. 1: a) Optical microscope picture of CVD graphene transferred on the organic semiconductor C<sub>60</sub>. b) Raman spectra of the CVD graphene and C<sub>60</sub>. c) Atomic force microscope image of the stack.

## Measurement setup

The electrical characterizations are carried out in the setup shown in figure 2, which include four probes and an annealing stage. A Keithley 236 source-measure unit and an Agilent 4294a impedance analyzer are used for the electrical measurements.

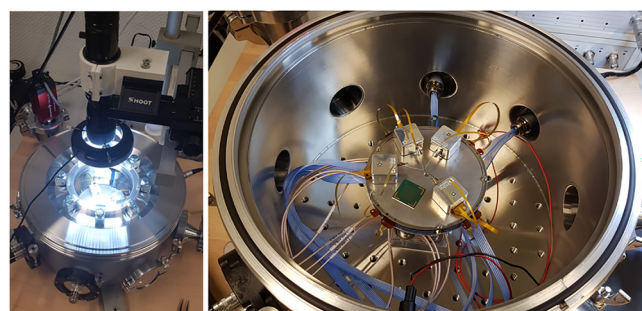


Fig. 2: The measurement setup used for the electrical characterization of the devices. The devices are measured under high vacuum ( $p < 10^{-5}$  mbar).

## Electrical characterization

Au/C<sub>60</sub>/Graphene junctions were characterized as shown in the inset of figure 3a. Electrical measurements at several different temperatures are shown. The IV traces were fit with a double Schottky barrier model. [4] Using this model, we were able to extract the potential barriers and ideality factors for both interfaces (i.e. Au/C<sub>60</sub> and C<sub>60</sub>/Graphene). The potential barriers at room temperature are roughly 0.7 eV and 0.8 eV for C<sub>60</sub>/Graphene (circles in Fig. 3b) and C<sub>60</sub>/Au (squares in Fig. 3b), respectively. We observe a linear increase of the potential barriers with the temperature.

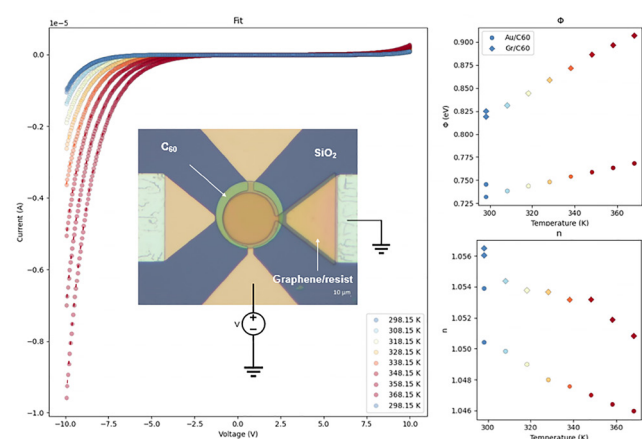


Fig. 3: a) IV characteristic of the Au/C<sub>60</sub>/Graphene at different temperatures. The solid lines represent the measurements while the dashed lines are the double Schottky barrier model fit. [4]. b) Potential barrier at the interfaces extracted with the Double Schottky barrier model. [4]. c) Ideality factors extracted with the Double Schottky barrier model.

## Conclusions and outlook

This preliminary study on the Au/C<sub>60</sub>/Graphene junction showed us the importance of achieving a low carrier injection barrier at the emitter electrode in order to develop high frequency devices. We will investigate the fabrication of quasi-Ohmic contact by introducing a doped layer between the emitter and the organic semiconductor. For the graphene/C<sub>60</sub> interface, we observed a relatively high Schottky barrier at the graphene/C<sub>60</sub> interface. We expect that the resulting high interface resistance can be beneficial for the operation of vertical transistors as the base current is thus reduced.

## References

- [1] B. Lüssem, A. Günther, A. Fischer, D. Kasemann, K. Leo, Vertical organic transistors. *J. Phys. Condens. Matter* 27, 443003 (2015)
- [2] E. Guo, S. Xing, F. Dollinger, R. Hübner, S. J. Wang, Z. Wu, K. Leo, H. Kleemann, Integrated complementary inverters and ring oscillators based on vertical-channel dual-base organic thin-film transistors. *Nat Electron* 4, 588–594 (2021)
- [3] Z. Wu, Y. Liu, E. Guo, G. Darbandy, S. J. Wang, R. Hübner, A. Kloes, H. Kleemann, K. Leo, Efficient and low-voltage vertical organic permeable base light-emitting transistors. *Nat. Mater.* 20, 1007–1014 (2021)
- [4] A. Grillo, A. Di Bartolomeo, A Current–Voltage Model for Double Schottky Barrier Devices. *Adv. Electron. Mater.* 7, 2000979 (2021)

# Mechanoresponsive liposomes: formulation and process development

Project A15.01: ForMeL (FHNW Muttentz, ANAXAM, Acthera Therapeutics AG, Basel)

Project Leader: O. Germershaus

Collaborators: V. Flück, D. Ali, A. Zumbühl, P.-A. Monnard, Y. Schmid, C. Grünzweig, C. S. T. Chang, M. Dürrenberger, S. Erpel

## Background

The release of drugs in response to rheological changes of the immediate environment may be achieved using mechanoresponsive liposomes. This strategy allows for new options in bioresponsive drug release and provides a potential novel treatment modality for several diseases. As an example, mechanoresponsive liposomes could release anticoagulants in response to higher shear rates at sites of atherosclerotic narrowing. Instead of systemic anticoagulant treatment, the drug is locally released only at the site of action, reducing side effects while allowing for higher local drug concentration.

The Nano Argovia project ForMeL, contributes to the translation of mechanoresponsivity in drug release from academic research to industrial product development. Within the project, scalable manufacturing methods for mechanoresponsive liposomes were developed and long-term product stability was assessed. Furthermore, different formulation and stabilization approaches were established to initiate drug product development.

## Manufacturing process and long-term stability

Several different manufacturing methods for the preparation of mechanoresponsive liposomes were established in the first phase of the project. Thin-layer hydration and ethanol injection were investigated in more detail. Thin-layer hydration represented a well-established preparation procedure at lab-scale, while ethanol injection is suited for large-scale manufacturing. It was shown in the first phase of this project, that after optimization of ethanol injection procedure, quality of liposome preparation was comparable to thin-layer hydration. Liposomes produced by thin-layer hydration showed hydrodynamic radii of 130 nm with polydispersity indices of 0.08. Liposomes produced using optimized ethanol injection had hydrodynamic radii of 200 nm with polydispersity indices of 0.08.

The long-term stability of liquid liposome formulations prepared by thin-layer hydration (Fig. 1) and by ethanol injection (Fig. 2) was assessed over up to 52 weeks at 5°C and 25°C. Both formulations were stable with regards to hydrodynamic radii and polydispersity indices at 5°C and showed a constant increase of particle size as well as polydispersity index at 25°C. Only minor differences between samples prepared by thin-layer hydration and ethanol injection were observed. Liposomes prepared by ethanol injection showed lower increase of the polydispersity index, but both samples showed monomodal size distributions with low polydispersity index throughout the study.

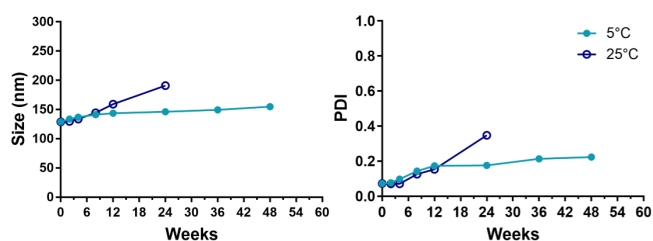


Fig. 1: Long-term storage of liposomes prepared by thin-layer hydration.

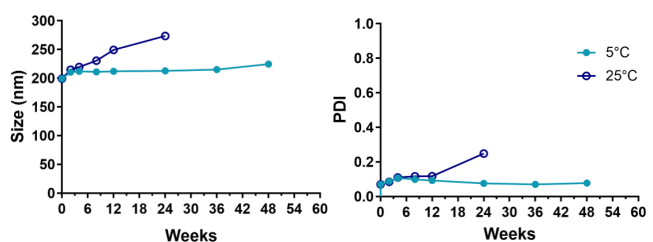


Fig. 2: Long-term storage of liposomes prepared by ethanol injection.

## Effect of formulation pH

The effect of formulation pH on liposome size and polydispersity index was evaluated over 4 weeks (Fig. 3). Overall, liposome formulations showed no pH-dependent instability with regards to the investigated quality parameters. A minor increase of hydrodynamic diameter was observed during storage, the polydispersity index remained virtually unchanged.

## Long-term stability of optimized liposome composition and preparation sequence

The lipid composition of liposomes and the preparation sequence was modified to further improve drug load and long-term stability. As described above, the different samples were stored at 5°C and 25°C for up to 26 weeks.

The optimization of liposome composition resulted in further improved stability. Samples prepared by thin-layer hydration showed almost no change of particle size during storage at either temperature. The polydispersity index remained significantly below 0.2 at both temperatures.

The modification of the preparation sequence in conjunction with optimized liposome composition resulted in further improvement of long-term stability. Virtually no change of either hydrodynamic diameter or polydispersity was observed over 26 weeks at both 5°C and 25°C.

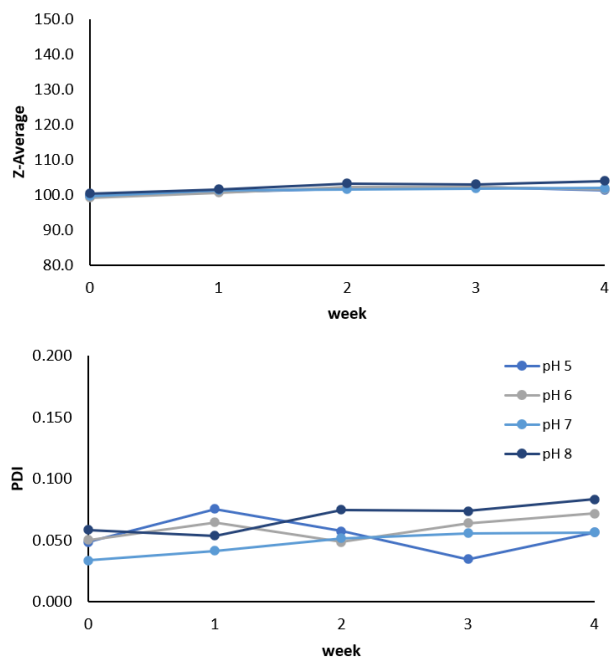


Fig. 3: Effect of formulation pH on critical liposome characteristics.

#### Development of lyophilization process and formulation

Development of a lyophilized formulation of mechanoreponsive liposomes was started as a backup in case of insufficient stability of either liposomes or encapsulated drug in a liquid formulation. However, lyophilization of liposomes prepared by ethanol injection proved to be challenging due to ethanol concentration of up to 10% (Fig. 4).

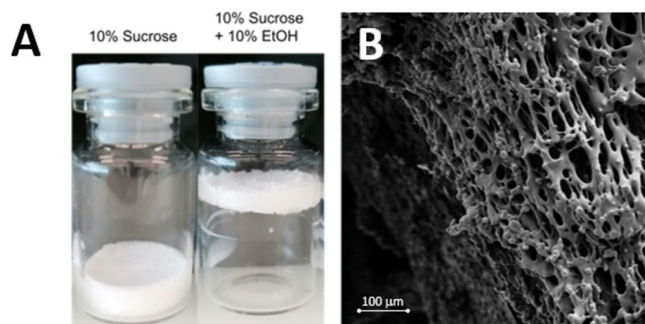


Fig. 4: Effect of presence of 10% ethanol during lyophilization. A: Typical appearance of the product cake after lyophilization with 10% sucrose and with 10% sucrose and 10% ethanol. B: Electron micrograph of lyophilized product.

A reduction of ethanol concentration was achieved by extended evaporation during ethanol injection and through introduction of an evaporation phase prior to primary drying during lyophilization.

Formulation development was focused on selection of suitable lyo- and cryoprotectants. A formulation containing 10% sucrose was found to protect liposomes during lyophilization and was used as initial formulation.

Lyophilization from formulations containing ethanol resulted in a shift of the particle size distribution to larger particles or aggregates (Fig. 5A). Due to significant challenges related to lyophilization of ethanol containing formulations, tert-butanol was selected as an alternative solvent and ethanol injection procedure was optimized for use of tert-butanol. Lyophilization of formulations containing tert-butanol

resulted in proper lyophilized product cakes and an improved cake structure. However, a shift to larger particle sizes was observed also for tert-butanol as a solvent (Fig. 5B).

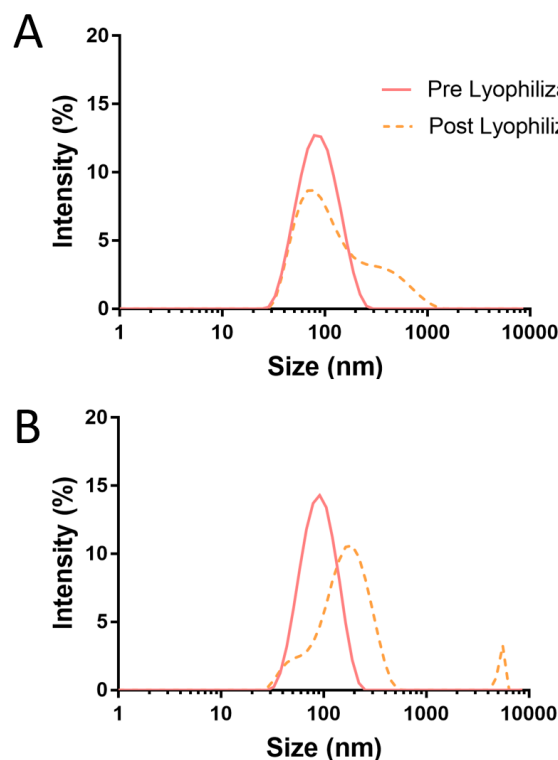


Fig. 5: Size distribution of liposome formulations prior to and after lyophilization. A: formulation containing ethanol, B: formulation containing tert-butanol.

#### Summary

Ethanol injection was successfully established as a scalable manufacturing process for mechanoreponsive liposomes. Using this process, either scale-up to a larger batch volume can be considered or the process can be scaled out, i.e. several smaller batches may be produced in parallel.

Liquid liposome formulations showed high stability with regards to physicochemical characteristics of liposomes and hence are promising as potential clinical formulations (depending on drug stability).

Lyophilization process and formulation development was initiated, and key challenges associated with ethanol content of the formulation have been successfully addressed.

Further development of the lyophilization process and formulation composition as well as studies focusing on scale-out of ethanol injection are ongoing.

# Post-treatment of wear-resistant implant coatings

Project A15.08: Promucola (FHNW MuttENZ, ANAXAM, Orchid Orthopedics Switzerland GmbH, Baden-Dättwil)

Project Leader: M. de Wild

Collaborators: R. Burger, A. Carmona, N. P. M. Casati, C. S. T. Chang, C. Grünzweig, M. Olbinado, A. Salito, F. Schuler, M. de Wild

## Summary of the project progress

The aim of this project is to develop a suitable post-treatment for Advanced Plasma Sprayed (APS) ceramic coatings on articulating titanium implants. With this wear-resistant Protective multi-component layer Orchid Orthopaedics Switzerland GmbH wants to replace CoCr-systems and offer non-allergic [1], long life orthopedic implants. The novel  $\text{Al}_2\text{O}_3\text{-TiO}_2$  ceramic powder mixture is used to create a thick, layered coating [2]. During the APS-process, the molten droplets impact the titanium substrate and rapidly solidify by a high cooling rate. Due to thermal quenching, different phases like  $\alpha\text{-Al}_2\text{O}_3$ ,  $\text{TiO}_2$ , aluminum titanate  $\text{Al}_2\text{TiO}_5$  and  $\text{Al}_6\text{Ti}_2\text{O}_{13}$  with distinct properties emerge in a stratified microstructure with micro-cracks and micropores [3]. In this project, the tribological, microstructural and crystallographic properties of the protective coating were investigated as a function of the following three post-treatments: Electro-chemical anodization, heat treatment in air and in an oxygen atmosphere.

A  $\varnothing 25$  mm sample and its preparation by low-speed diamond cutting, followed by metallographic preparation using ion-milling, is shown in figure 1. A zoned microstructure with dark, Al-rich and brighter, Ti-rich, areas can be observed in figure 2.

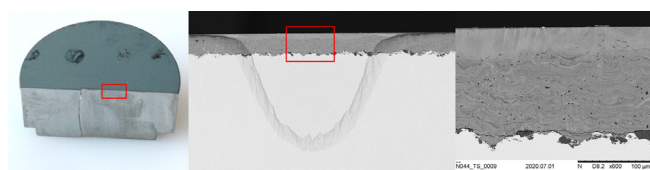


Fig. 1: Sample preparation for cross-sectional investigations of the APS coatings.

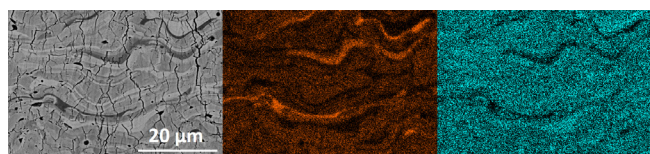


Fig. 2: BSE image and EDX mapping of cross-section after scratch test at  $F_N = 36$  N. Al- and Ti-channel indicate the mixed elemental composition.

Ball-on-disk experiments on a Bruker Tribolab system according to ASTM G99 [4] using  $\varnothing 10$  mm sapphire balls, normal forces  $F_N$  of 1 N, 3 N and 5 N during 12'500 cycles, revealed that thermal post-treatments reduce the wear rate and can be explained by the increased hardness [5]. A similar trend was observed in scratch experiments carried out on the same tribosystem using a diamond tip with a tip radius

of 200  $\mu\text{m}$ , a speed of 0.073 mm/sec and a progressive normal force  $F_N$  from 4 N to 60 N. None of the scratch-tested samples showed delamination (adhesion failure) despite the contact pressure significantly exceeded the applicable physiological condition. The width of the created scratch increased with  $F_N$  and was influenced by the post-treatment: At 60 N the widths were 166  $\mu\text{m}$  on as-deposited, 143  $\mu\text{m}$  on polished, 138  $\mu\text{m}$  on anodized, 131  $\mu\text{m}$  on oxygen- and 124  $\mu\text{m}$  on air-treated coatings (Fig. 3).

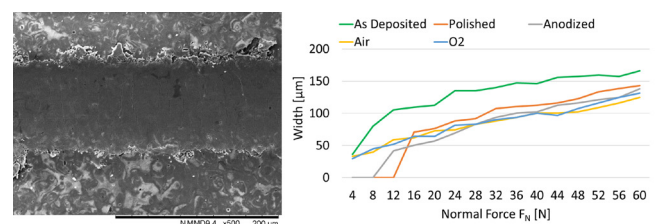


Fig. 3: Left: Scratch mark at position  $F_N = 44$  N on an air-treated  $\text{Al}_2\text{O}_3\text{-TiO}_2$  coating. Right: Course of the progressive scratch width, determined by SEM analysis.

To simulate the abrasive effect of bone or bone-cement particles [6] on the coating in a load situation, 3-body-wear experiments were performed: A  $\varnothing 3.2$  mm cylindrical medical HDPE counter body was pressed on the sample at 10 N for 12'000 cycles in a stable aqueous dispersion of non-spherical hydroxyapatite particles with a d50 value of 2.77  $\mu\text{m}$  in a concentration of 0.02 g/ml. While CoCr samples showed wear tracks of 0.2-0.4  $\mu\text{m}$  depth, no defects were found on coated samples heat-treated in oxygen (Fig. 4).

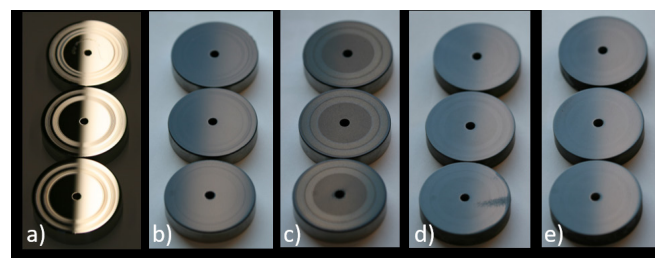


Fig. 4:  $\varnothing 40$  mm samples after the 3-body wear test. a) CoCr sample. b) Polished, c) anodized, d) annealed in air and e) in  $\text{O}_2$  coated specimens.

Similarly, the coefficient of friction (COF) was influenced by the post-treatment (Fig. 5), indicating that the properly treated coating is superior to a CoCr substrate.

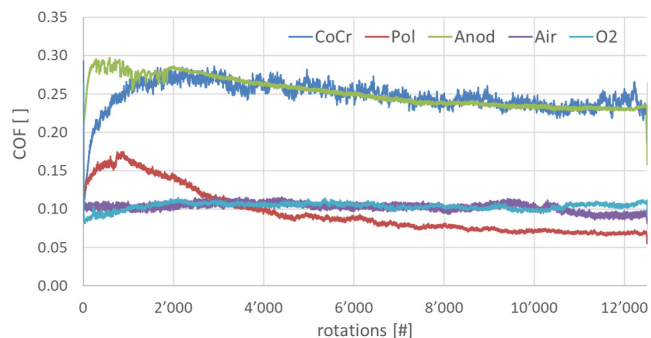


Fig. 5: Averaged COF measurements in 3-body-wear test ( $n=6$ ) after different post-treatments.

Synchrotron X-ray micro-computed tomography (SXR $\mu$ CT) of the coatings were performed at the TOMCAT beamline of the Swiss Light Source (SLS) at the Paul Scherrer Institute (PSI). The goal was to study the microstructures of the coatings. Porosity analyses were performed on the tomography data of the coatings. The sizes of the pores in all coatings ranged from  $1 \mu\text{m}^3$  to  $4'000 \mu\text{m}^3$ . The total pore volume fraction for the polished  $\text{Al}_2\text{O}_3$  sample was 4.2%. This value decreased to 1.8% after annealing. The most dominant pore size (volume) was  $10\text{--}50 \mu\text{m}^3$ . The total pore volume fraction for the polished  $\text{TiO}_2$  sample was 0.34%, which is significantly smaller than in  $\text{Al}_2\text{O}_3$ . The total pore volume fraction did not change after annealing. The total pore volume fraction for the polished  $\text{Al}_2\text{O}_3\text{-TiO}_2$  sample was 0.35% (Fig. 6), which is similar to that of  $\text{TiO}_2$ . In contrast with the  $\text{Al}_2\text{O}_3$  and  $\text{TiO}_2$  coatings, the total pore volume fraction of the  $\text{Al}_2\text{O}_3\text{-TiO}_2$  sample increased after annealing.

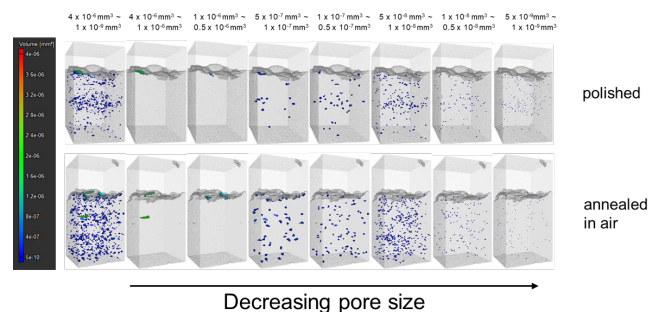


Fig. 6: 3D-porosity analysis by SXR $\mu$ CT: Spatial arrangement of total porosity (left) and size-dependent pores (to the right) of polished (top row) and heat-treated  $\text{Al}_2\text{O}_3\text{-TiO}_2$ -coating (bottom row).

Diffraction measurements were performed at the MS beamline of SLS at PSI to identify the phases present in the coatings. From the diffraction patterns obtained (Fig. 7), it can be concluded that the coating processes are very consistent, and the number of phases present in each sample are very similar. The phases present and their fractions through the thickness of the coatings are the same for the  $\text{Al}_2\text{O}_3$  and  $\text{TiO}_2$  coatings. In the  $\text{Al}_2\text{O}_3\text{-TiO}_2$  coatings, there is a difference between the phases present on the surface to the bulk of the coating. For the  $\text{Al}_2\text{O}_3$  coatings, 3 phases can be identified, main phases present are cubic  $\text{Al}_2\text{O}_3$  and  $\gamma$ -Alumina with a minor fraction of Corundum. For the  $\text{TiO}_2$  coatings, the diffraction patterns are far more complicated which indicates more metastable phases are present. In the  $\text{Al}_2\text{O}_3\text{-TiO}_2$  coatings, we tentatively identified the presence of Aluminium-Titanate phase  $\text{Al}_{2+X}\text{Ti}_{1-X}\text{O}_{5-0.5X}$ . After anodizing, the diffraction

patterns do not change for all 3 types of coatings, that means anodizing does not alter the phases present in the coatings. For the  $\text{Al}_2\text{O}_3$  coatings, the diffraction patterns before and after heat treatments are very similar. Phase transformation happens during heat treatments in the  $\text{TiO}_2$  and  $\text{Al}_2\text{O}_3\text{-TiO}_2$  coatings. The Aluminium Titanate phase is not present anymore.

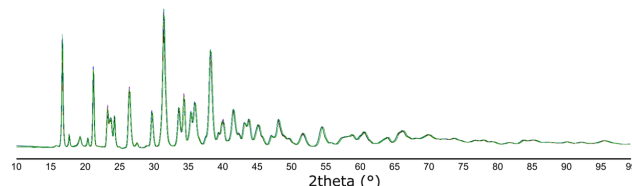


Fig. 7: Overlapped XRD powder patterns of as deposited and polished  $\text{Al}_2\text{O}_3\text{-TiO}_2$  coatings.

The results of the systematic characterization of the ceramic coating in terms of microstructure, crystallography and tribology has confirmed that the developed  $\text{Al}_2\text{O}_3\text{-TiO}_2$  coating can be used potentially as anti-wear coating for medical devices. Thanks to the obtained results of the Promucola project, Orchid Orthopaedics Switzerland GmbH was able to prepare and submit in 2021 a master file to the US Federal Drug Administration (US FDA) related to the  $\text{Al}_2\text{O}_3\text{-TiO}_2$  ceramic anti-wear coating.

## References

- [1] D. Guenther, P. Thomas, D. Kendoff, M. Omar, T. Gehrke, C. Haasper, Allergic reactions in arthroplasty: myth or serious problem?, *Int Orthop*. 40:239–44 (2016)
- [2] N. Vogt, K. Wozniak, A. Salito, M. de Wild, Biocompatible wear-resistant VPS coatings, *Current Directions in Biomedical Engineering* 2(1): 31–34 (2016)
- [3] A. Richter, et al., Emergence and impact of  $\text{Al}_2\text{TiO}_5$  in  $\text{Al}_2\text{O}_3\text{-TiO}_2$  APS coatings, *IOP Conf. Ser. Mater. Sci. Eng.* 480 012007 (2019)
- [4] ASTM G99-17, Standard Test Method for Wear Testing with a Pin-on-Disk Apparatus, (2017)
- [5] R. Burger, A. Carmona, N. P. M. Casati, C. S. T. Chang, M. de Wild, C. Grünzweig, M. Olbinado, A. Salito, and F. Schuler, Post-treatment of wear-resistant implant coatings, Annual Report 2020, Supplement, Swiss NanoScience Institute, University of Basel, Nano Argovia Project A15.08 Promucola, 82-83 (2020)
- [6] E. Ingham, T. R. Green, M. H. Stone, R. Kowalski, N. Watkins, and J. Fisher, Production of TNF- $\alpha$  and bone resorbing activity by macrophages in response to different types of bone cement particles, *Biomaterials* 21: 1005-1013 (2000)

# Antibacterial titanium nanostructures by helium plasma irradiation

Project A15.11: TiSpikes (University of Basel, Dept. of Physics and Klinik für Oral Health & Medicine, FHNW Muttentz, Institut Straumann AG, Basel)

Project Leader: L. Marot

Collaborators: F. Sanchez, R. Steiner, R. Antunes, M. Kisiel, E. Meyer, K. Mukaddam, S. Köhl, M. Astasov-Frauenhoffer, I. Hauser-Gerspach, J. Köser, R. Wagner, J. Hofstetter

## Introduction

The development of biomaterials that hinder or prevent bacterial colonization and growth is an important challenge in biomaterial research. The inhibition of initial bacterial colonization reduces the chance of biofilm formation and might avoid most implant-related infections. Therefore, the observation that nano-pillar surfaces on gecko skin exerted bactericidal effects on certain adherent bacteria by an assumed physicochemical mechanism drew much attention. In contrast to the majority of studies conducted on antibacterial materials, the proposed project aims at directly nanostructuring a material that is widely used in medical applications such as orthopedic and dental implants, namely titanium and titanium alloys.

Within this project, a unique nanostructuring method developed at the University of Basel will allow geometrical parameters of the nanostructures to be tuned in order to obtain surfaces exhibiting optimum bactericidal effects (low bacteria attachment and/or survival). Such a physical bactericidal method may become an attractive approach to tackle multi-antibiotic resistant bacteria and could solve an escalating medical issue that poses a threat to global public health. Nanostructuring of the implant surface will also be optimized towards improved soft tissue cell adhesion which is expected to reduce bacterial invasion in the space between implant and tissue leading to peri-implantitis. Considering the objective of industrialization, dental implants and abutments will be tested in vivo for pre-clinical evaluation by our industrial partner.

## Nanocone formation on titanium and titanium alloy surfaces

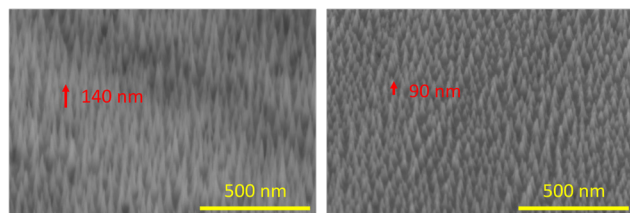


Fig. 1: Tilted top views ( $52^\circ$ ) SEM images of nanocones formed on titanium and Roxolid® surfaces.

Surface structuration of titanium and Roxolid® (TiZr) by helium (He) bombardment was achieved using an eH1000 ion gun (Kaufman). For the same production conditions (e.g. surface temperature, He ion energy), both surfaces exhibited spikes imaged in figure 1 through scanning electron microscopy (SEM). The density and surface topology were analyzed by atomic force microscopy.

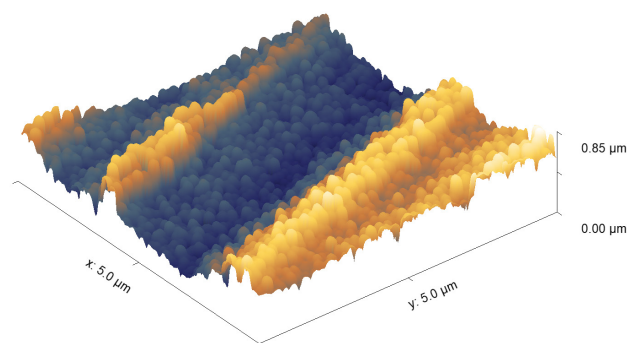


Fig. 2: 3D representation of the surface topology of structured titanium discs with spikes of 340 nm.

## Nanostructuring of the titanium surface

The eH1000 ion source induced tungsten (W) and iron contamination, which affects the spikes' growth rate. Systematic surface chemical analyses using X-ray photoelectron spectroscopy (XPS) were carried out. Modification of the source was performed and successfully suppressed the iron contamination. Unbalanced magnetron sputtering (UBM) technique was used as a source of He ions to structure titanium discs and contaminant-free spikes were produced. Using a pulsed DC-generator, the flux of He ions measured by the use of a retarding field-energy analyzer (RFEA) was measured to be ten times lower (from  $2.04 \times 10^{24} \text{ m}^{-2}\text{s}^{-1}$  to  $10 \times 10^{24} \text{ m}^{-2}\text{s}^{-1}$ ) compared to the eH1000 ion source. In order to increase the ion flux, a new high-power impulse magnetron sputtering generator (HiPIMS) was tested. However, the production of 12 homogeneously structured samples was not achieved due to the ion spatial distribution. Modulation of the magnetron field lines and/or confining the beam (Fig. 2) did not completely suppress the inhomogeneities.



Fig. 3: Confined He ion beam produced by a HiPIMS excited UBM sputtering technique.

## Titanium coated structured surfaces

Further experiments were performed using the Kaufman ion source and XPS confirmed the systematic presence of few atomic percent of tungsten on the surface of the structured titanium discs. The obtention of contaminant-free structured surfaces was achieved by the addition of a titanium coating after the irradiation. The required coating thickness was in-

investigated using XPS chemical analyses and various coating temperatures were tested. When coated, topology changes can be observed, as presented in figure 4.

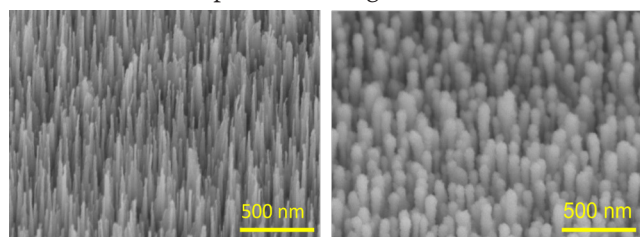


Fig. 4: Tilted top view (52°) SEM images of Ti spikes of 540 nm heights. From the left to right, uncoated and coated titanium structured surfaces.

#### Analysis of antibacterial efficacy and contact angle measurements

Analysis of the antibacterial efficacy was carried out on Ti nanostructured and coated samples with peak heights from 250 nm to 500 nm. For most cases, the bactericidal properties of such surfaces were confirmed by reducing the *E. coli* and *P. gingivalis* population of about 90% compared to control discs (Fig. 5). However, 500 nm coated peaks did not affect the vitality of *E. coli* (Fig. 7). The coatings performed did affect the peak shapes thus, the antibacterial effect was not present any longer.

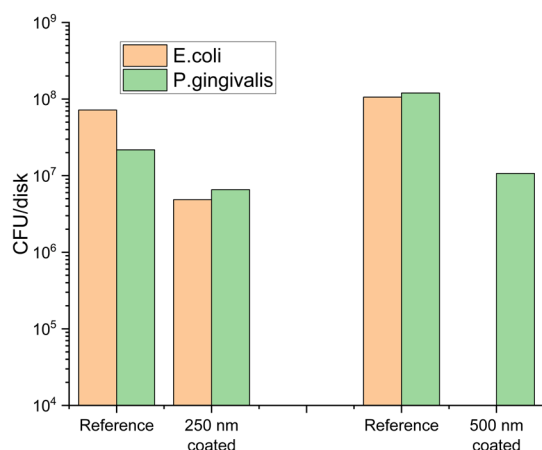


Fig. 5: Colony-forming unit (CFU) of *P. gingivalis* and *E. coli* deposited on pristine reference samples compared to structured discs.

All the bactericidal tests and water contact angle (WCA) measurements performed during the project are reported in figure 6. In the absence of contaminants, the sample surfaces are observed to be hydrophilic. Contaminated structured samples exhibit hydrophobic surfaces. A link between surface wettability and bactericidal effect cannot be established.

Date	Production technique	Contaminants	Peak heights (nm)	WCA (°)		Bacteria reduction (%)	
				Native	Post MetOH	<i>E. Coli</i>	<i>P. Gingivalis</i>
Pristine M-surfaces				74	56	0	0
2019	eH1000	Fe, W	225	123	85	70	96
2019	eH1000	Fe, W	475	123	85	77	99.9
2021	eH1000	None	250	26	12	93	91
2021	eH1000	None	540	26	12	-	90
2017	UMS	None	500	26	12	-	25
2017	UMS	None	1000	26	12	-	38

Fig. 6: Titanium structured characteristics and their associated water contact angle measurements and bactericidal effects.

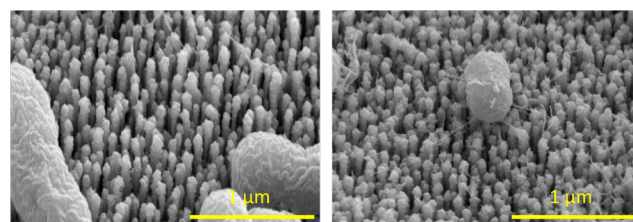


Fig. 7: SEM tilted view images of structured titanium discs on which a bactericidal test using *E. coli* has been performed.

Afterward, simulated body fluid (SBF) was deposited on top of new structured samples. Around 60% of the tungsten (W) on the discs' surface was released into the SBF. Bactericidal tests performed on SBF evidenced a 5-log reduction in the presence of W, affecting mainly *P. gingivalis*. After pre-extracting the W in SBF, the structured discs exhibited a strongly reduced antibacterial effect.

#### Summary and outlook

Ti and Ti alloy surfaces were nanostructured at the University of Basel by He ion exposure. XPS analysis demonstrates contaminants with antimicrobial efficacy present on the surface of the structured samples after He ion irradiation using the Kaufman ion source. The Fe contamination was successfully suppressed. After structuring, titanium coatings were performed and XPS chemical analysis confirmed the absence of tungsten on the surface of the structured discs. Coating structured discs of 250 nm and 500 nm were produced and subject to antibacterial and surface wettability tests. The amount of tungsten on the surface was observed to be reduced after SBF exposure.

Further investigation on the kinetics of the tungsten release in SBF is ongoing since it could enhance the antibacterial effect of the implant in the very important first days after implantation. Additional structured titanium discs will be produced and antibacterial efficacy of *E. coli* and *P. gingivalis* will be tested. Considering the objective of industrialization, more complex surfaces of commercially available dental implants and abutments will be nanostructured in a next step. If successful, these experimental samples will undergo mechanical and potential pre-clinical testing.

# An achromatic X-ray lens

Project A16.01: ACHROMATIX (Paul Scherrer Institut, University of Basel, Biomaterials Science Center , XRnanotech GmbH, Villigen)

Project Leader: J. Vila Comamala

Collaborators: G. Schulz, G. Rodgers, M.-C. Zdora, U. T. Sanli, A. Kubec, F. Döring, B. Müller, C. David

## Introduction

Refractive and diffractive X-ray optics are key components for X-ray analysis and imaging methods with numerous scientific applications in biology, energy science and materials science. Nevertheless, refractive and diffractive lenses suffer from severe chromatic aberration, only focusing X-rays from a narrow energy range to the same position. This hinders the development of full-field transmission

X-ray microscopy using laboratory X-ray tube sources, since broad-bandwidth radiation cannot be used with chromatic optics. On the other hand, the use of a monochromator dramatically cuts down the photon flux to inoperable X-ray intensities. To overcome the limitations of the chromatic aberration, we have started the development of an achromatic X-ray element by combining a refractive and a diffractive lens [1-3], as shown in figure 1a, and with the specific aim of its implementation for laboratory transmission X-ray microscopy. During the first year of the project, we have analyzed and simulated how the chromatic aberrations of the two individual optical elements can be canceled when the right design parameters are chosen. We have developed a fabrication method based on two-photon polymerization 3D printing to realize X-ray refractive lenses. For the fabrication of the X-ray diffractive elements, we have applied state-of-art electron beam lithography and electroplating deposition available at the cleanroom facilities of the Paul Scherrer Institute. Following these steps, we have successfully assembled the first X-ray achromat and demonstrated achromatic X-ray focusing at a synchrotron [4]. The achromatic element was characterized by scanning transmission X-ray microscopy and ptychography demonstrating the achromatic behavior for an X-ray energy range from 5.8 to 7.2 keV. In addition, we have started developing a laboratory X-ray setup exploiting the benefits of the achromat with the vision to make X-ray microscopy accessible to a wider user community. As a first feasibility demonstration of a laboratory-based setup, an image of the microfocus X-ray source spot has been obtained with the achromatic X-ray lens.

## Nanofabrication methods

The primary goal of the first year of the project has been the fabrication of a refractive and a diffractive lens suitable for a proof-of-principle experiment of an X-ray achromat working at an energy of 6.2 keV. The refractive lens was made of polymer resist and it was fabricated by two-photon polymerization 3D printing. It consisted of a stack of four individual paraboloids with an apex radius of 5.3  $\mu\text{m}$ , a diameter of 100  $\mu\text{m}$ , and a height of 235  $\mu\text{m}$  each, as shown in figure 1b.

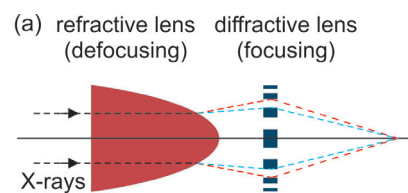


Fig. 1: a) Achromat X-ray focusing can be realized by the combination of a refractive and diffractive lens. b) Refractive X-ray lens fabricated by two-photon polymerization 3D printing. c) Diffractive X-ray lens fabricated by electron-beam lithography and nickel electroplating.

The diffractive optical element was produced by state-of-the-art electron beam lithography and nickel electrodeposition. It has a diameter of 100  $\mu\text{m}$  and ring structures down to a few hundreds of nanometers, as shown in figure 2c. Both refractive and diffractive lens were fabricated in separated very thin silicon nitride membrane supports to ensure enough transmission of the X-ray beam.

### Synchrotron and laboratory X-ray experiments

During the first year of the project, two beamtime proposals at synchrotron facilities for the development of the X-ray achromat were accepted. The experiments were carried out at the cSAXS beamline of the Swiss Light Source (PSI, Switzerland) and at the P06 beamline of PETRA III (DESY, Hamburg).

The two optical elements were aligned in the synchrotron X-ray beam. The combined optical element was characterized by scanning transmission X-ray microscopy (STXM) and ptychographic measurements while varying the X-ray energy from 5.5 to 8.0 keV.

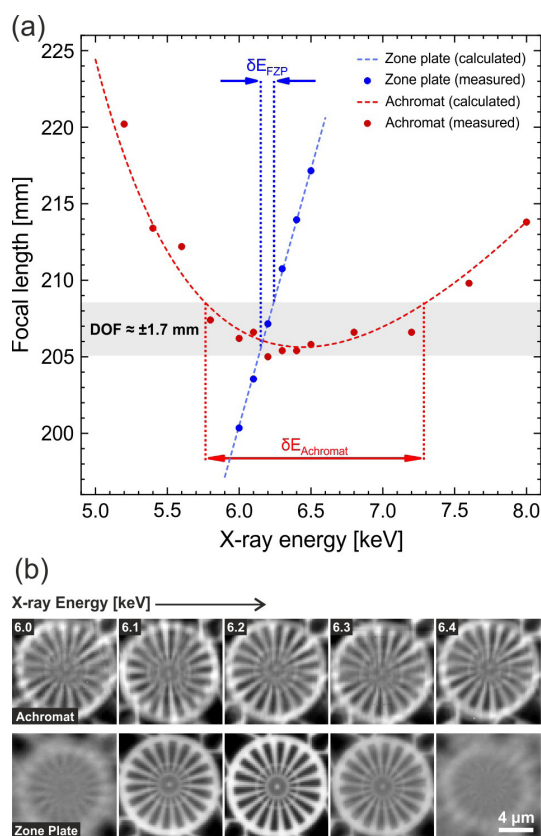


Fig. 2: a) Focal length as function of the X-ray energy following the expected achromatic behavior. The focal length was determined by ptychographic measurements. b) Comparison of the images obtained at different X-ray energies using the X-ray achromat and an ordinary X-ray zone plate. The images obtained by the achromat stayed sharp while the images obtained by the zone plate clearly became blurred when changing the X-ray energy.

During the synchrotron experiments, the focal length of the achromat displayed the expected parabolic behavior as a function of the X-ray energy, as shown in figure 2a. In comparison, the focal length of an X-ray Fresnel zone plate follows a linear energy dependency, causing a pronounced defocusing even for small changes of the X-ray energy. The X-ray achromat delivered a focal spot of 500 nm. Figure 2b shows STXM images of the test pattern acquired at different X-ray energies without adjusting the separation between

the lens and the test pattern. The images obtained by the X-ray achromat stay sharp with the energy change while the images obtained by the zone plate became quickly blurred. In addition, the achromatic X-ray lens was used to obtain an image of a microfocus X-ray source spot on an X-ray detector using a 1:1 magnification. The focal length of the achromat was designed to be 325 mm for a central X-ray energy of 8.0 keV. Such measurement would be impossible to realize with a diffractive or a refractive X-ray lens as an optical element, as the strong chromatic aberration would lead to a very blurred image due to the wide range of photon energies emitted by the X-ray tube. The imaged size of the X-ray source was about 10  $\mu\text{m}$ , as expected from the specifications of the X-ray tube manufacturer.

### Outlook

During the second year of the project, three more beamtime proposals have already been accepted to further develop the concept of the X-ray achromat, with particular emphasis to obtaining higher spatial resolutions, down to 100 nm, and to developing the scientific applications that can take advantage of the X-ray achromat.

Also during the second year of the project, we will explore the development of the micro and nanotechnology processes to produce the refractive and diffractive lenses in a single silicon nitride support. Such advancement will simplify the use of the X-ray achromat at the X-ray experimental setups and pave the way for a future commercialization of such X-ray optical element by the industrial partner of the project.

In parallel, we will work for the implementation of a laboratory full-field transmission X-ray microscope based on the X-ray achromat with special attention to the applications of X-ray nanoimaging for biomedical and materials science.

### References

- [1] Y. Wang, W. Yun and C. Jacobsen, Achromatic Fresnel optics for wideband extreme-ultraviolet and X-ray imaging, *Nature* 424, 50 (2003)
- [2] G. K. Skinner, Design and imaging performance of achromatic diffractive–refractive x-ray and gamma-ray Fresnel lenses, *Appl. Opt.* 43, 4845 (2004)
- [3] H. N. Chapman and S. Bajt, High-resolution achromatic X-ray optical systems for broad-band imaging and for focusing attosecond pulses, *Proc. R. Soc. A* 477, 20210334 (2021)
- [4] A. Kubeck et al., An achromatic X-ray lens, *Nat. Commun.* 13, 1305 (2022)

# Detectors to look inside cells

Project A16.04: HPDET-EM (University of Basel, Biozentrum, Paul Scherrer Institut, Dectris Ltd., Baden-Dättwil)

Project Leader: T. Maier

Collaborators: A. Alamoudi, M. Chami, M. Steinmetz, M. Meffert, C. Schulze-Briese

## The resolution revolution in electron microscopy

Electron microscopy has a long history of usage to visualize stained and dried or cryo-preserved biological materials. Despite obtaining atomic resolution for radiation hard non-biological samples, the resolution for visualizing cryo-preserved biomolecules remained at around 8 Å, even when combining information from hundred thousands of particles in single particle analysis. This resolution was insufficient for deriving atomistic structural models and detailed mechanistic insights.

The combination of several technological advances then led to a true “resolution revolution” in biological cryo electron microscopy [1]. Faster and more sensitive direct electron detectors allowed recording movies at sub-second frame duration instead of still images. These movies revealed strong motions of the vitrified water layer during electron exposure, which could be tracked and corrected computationally. Advanced algorithms for Bayesian refinement of particle orientations provided higher resolution from noisy data. As a result, in the past several years, cryo electron microscopic single particle analysis has become an efficient and favored method for high-resolution structure determination for medium-sized or larger proteins and protein- or protein-nucleic acid complexes. Typical resolutions for non-symmetric biological macromolecules are around 2.5–3.5 Å, fully sufficient for deriving and refining atomic models of proteins, while record resolutions for symmetric assemblies are approaching true atomic resolution at around 1 Å.

## Electron Tomography opens a window into cells

Obtaining very high resolution in single particle analysis cryo electron microscopy requires many identical particles embedded in random orientations in a very thin layer of vitrified aqueous solution. Data are collected by taking individual projection images (or time-resolved movies) of different sample areas each containing multiple individual particles by horizontally scanning a flat sample. Three-dimensional information is reconstructed by back-projection from many individual particles.

Visualizing cellular structures in situ requires a different approach for two reasons: (1) cells and subcellular regions are non-regular and non-repetitive objects. Thus, combining information from different areas is not feasible and all information for three-dimensional reconstruction has to be collected for each sample volume. (2) Most cells are too thick for direct imaging by transmission electron microscopy. Cells are typically in the micrometer size range, where limited transmission and secondary scattering of electrons degrades images quality.

The preferred approach for high-resolution visualization of biomolecules in their cellular environment is cryo electron tomography of thin sections of cells [2]. Thin sections can be generated by cutting or with more control and thinner

layers by cutting lamellae using dual beam microscopy for focused ion beam milling. Data collection is carried out by taking series of images for a single location of a vitrified thin section or lamella at different tilt angles (Fig. 1).

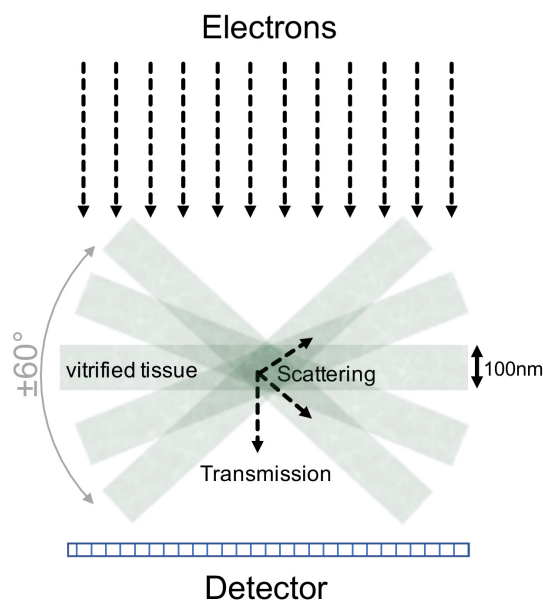


Fig. 1: Biological cryo electron tomography data are acquired by tilt-series imaging of thin sections of vitrified cells or tissue.

Tomographic tilt-series data collection poses problems not encountered in single-particle data collection. Radiation damage limits the total dose that a single location of the sample tolerates. First, for collecting entire tilt series this dose must be distributed over many images, with less electrons per area for each individual image. Second, the tilting of the sample causes substantial variations in sample thickness and the need for correcting errors in alignment across the tilt series. Third, a large sample volume has to be imaged in a single tilt series to obtain sufficient information for interpreting the biological context. Fourth, high-energy electrons accelerated at above 200 kV are required to image lamellae of typical thickness. Due to all this additional challenges, detector performance is particularly critical for biological cryo electron tomography.

## Novel detectors for electron tomography

Cryo electron microscopy single particle analysis was revolutionized by replacing radiation sensitive film or charge-coupled device (CCD) cameras with direct electron detectors. The detector technology currently used for biological electron microscopy studies are commercially available direct

electron detectors based on CMOS monolithic active pixel sensor (MAPS) technology. MAPS sensors detect energy partial energy loss of electrons passing through the sensor. They are characterized by small pixels with large numbers of small pixels, up to 24MPixels, and medium to high read-out and tolerated dose-rates, suited for measurements at high electron energy between 200 kV and 300 kV. Faster detectors with improved detected quantum efficiency would offer potential for improving data quality.

Dectris has developed hybrid-pixel detectors [3], where a semiconductor pixelated sensor layer is connected via bump-bonds to a layer of application-specific-integrated circuits (ASIC) (Fig. 2). Incoming electrons are absorbed and deposit their entire energy in the sensor layer, and the resulting electrical signal is transduced via the bump bonds to the ASIC. Hybrid -pixel detectors are a leading solution already for X-ray detection in biological X-ray crystallography; however, adaptations are required for their efficient use in electron microscopy and in biological cryo electron tomography in particular.

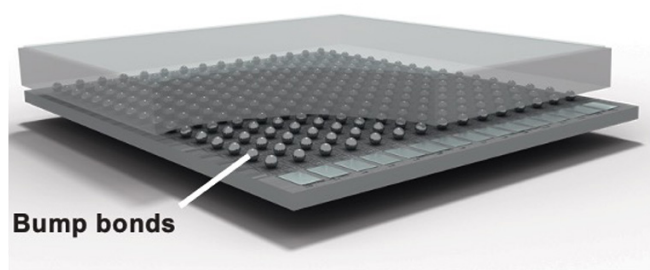


Fig. 2: Principal design of hybrid-pixel detectors. The semiconductor sensor layer on top is connected via bump-bonds to a lower ASIC layer.

This project aims at testing a detector prototype and at developing tools and strategies for applying this detector to cryo electron tomography of biological samples. The detector prototype builds upon the established bump-bond technology for hybrid-pixel detectors, but has been specifically adapted for the challenges of cryo electron tomography. Key steps in this project are to develop samples for efficient detector testing, to mount and connect the detector to a 200 kV electron microscope and to establish software control for successful data collection, to determine principal detector characteristics, to collect data on biological test samples and to evaluate these data by tomographic reconstruction. A particular emphasis is on analyzing the effects of a modular detector design with inter-module gaps (Fig. 3) and to develop adapted data collection strategies.

The HPDET-EM project unfortunately was delayed by a combination of factors. The Covid-19 pandemics created a situation of uncertainty for recruitment and led to substantial delays in linked processes and projects, by delayed deliveries and access restrictions to the University of Basel EM facilities. We have already developed test samples for data collection. The detector and related read-out electronics and computer have been installed on the Talos F200C microscope of the BioEM lab of University of Basel. Instrument control was successfully established, but more time is required to overcome additional challenges in detector read-out.

The project has been extended by another year, and we remain fully determined to achieve all aims. Recent investments and recruitments at University of Basel provide a highly supportive environment for the future development of cryo electron tomography beyond this specific project.



Fig. 3: Prototype dual-module Dectris detector for future applications in cryo electron tomography of biological specimens.

#### References

- [1] W. Kühlbrandt, The Resolution Revolution, *Science* 343, 1443 (2014)
- [2] M. Turk and W. Baumeister, The promise and the challenges of cryo-electron tomography, *FEBS Letters* 594, 3243 (2020)
- [3] A. Förster, S. Brandstetter and C. Schulze-Briese, Transforming X-ray detection with hybrid photon counting detectors, *Philos. Trans. R. Soc. A* 377, 20180241 (2019)

# Peptide-hydrogel-patch for lesion coverage on oral mucosa

Project A16.05: Hydrogel-Patch (FHNW MuttENZ, University of Basel, Universitäres Zentrum für Zahnmedizin Basel, credentis AG – vVardis, Windisch)

Project Leader: L. Kind

Collaborators: M. Bornstein, F. Schlottig, O. Germershaus, M. Hug

Unspecific ulcer in oral mucosa can drastically impair patients' normal oral function and cause pain during eating, chewing, and talking. The of nonspecific ulceration remain unclear and are likely due to a combination of factors which contributes to the outbreak. Therefore, the primary focus is on symptoms treatment, which in most of the cases consists in a topical therapy to provide the patient with initial relief before further (e.g. systemic) therapies are determined.

In this project, the promising self-assembling synthetic peptide P11-4 was used to develop a hydrogel patch to cover ulcerative lesions in oral mucosa. This hydrogel can be stabilized through biocompatible crosslinking with e.g. transglutaminase and is able to adhere to soft tissue. Since the application of this peptide has already been established in other areas of oral medicine (guided enamel regeneration [1], desensitization [3], periodontal treatment [4] and periimplantitis treatment), it turned out that the potential of P11 peptides family can go further. Therefore, this project focus on the union of attained experience and knowledge, for a newly designed biocompatible crosslinked hydrogel patch with drug-loading potential. This hydrogel patch will be explored for its topical use on oral mucosa and may overcome most of the limitations accompanied by hydrogel matrices derived from naturally occurring molecules or from other synthetic materials [5].

## Material and Methods

Within the first year, significant progress has been made with regards to establishing suitable crosslinking conditions (ratio of peptide to crosslinker) and investigating the crosslinker influence on stability and stiffness of P11-4 hydrogels. The development of a preparation protocol for uniform stable crosslinked P11-4 hydrogel was a crucial first step, leading to reproducible hydrogel quality and to comparable results in the characterization of the different hydrogel. An optimal peptide concentration of 20 mg/ml was recorded for the protocol and the crosslinking-agent concentrations were within: chitosan (0.15 %); chitosan and genipin (1.5% & 0.5%, 1:1); transglutaminase (TG) (80 and 200 U/g) and riboflavin (0.8%). P11-4 (negative control) and Glutaraldehyde (GA) (positive control) were used as reference samples. The analytical methods were established including swelling ratio, differential scanning calorimetry (DSC), viscometry, nanoindentation, Fourier-transformed infrared spectroscopy (FTIR) and the imaging methods like scanning electron microscopy (SEM) and transmission electron microscopy (TEM).

## Results and Discussion

The swelling ratio was calculated by weighting crosslinked hydrogels in comparison to non-crosslinked hydrogel references. Crosslinking is expected to reduce the swelling capacity of the hydrogels. The diagram (Fig. 1) shows that

crosslinked hydrogels have a reduced swelling capacity, confirming successful crosslinking.

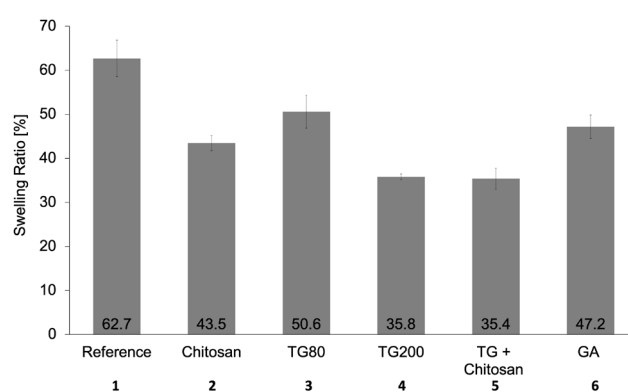


Fig. 1: Crosslinking performed after self-assembly. Data represent mean  $\pm$  SD,  $n = 3$ . (1) P11-4, (2) P11-4 + chitosan (0.15%), (3) + transglutaminase (TG) (80 U/g), (4) + TG (200 U/g), (5) + [TG (200 U/g):chitosan (0.15%) (1:1)], (6) + glutaraldehyde (GA) (2.5%).

In nanoindentation, the stiffness is analyzed by measuring the applied indentation force and indentation distance of the tip (Fig. 2). Through crosslinking of the hydrogel, it is assumed that the three-dimensional network is stabilized and is thus expected to exhibit increased stiffness.

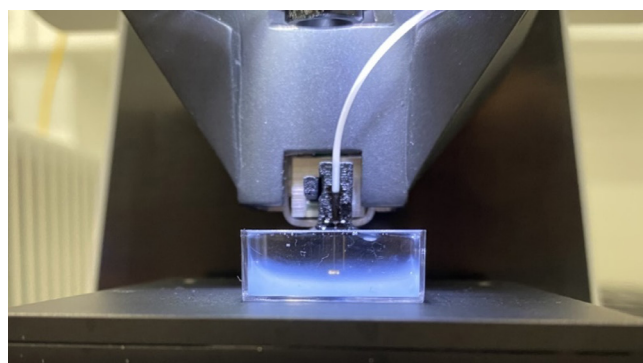


Fig. 2: Image of crosslinked P11-4 hydrogel measured with Nanoindenter (Optics11 Life) in wet-state.

In figure 3, the results show an increased hardness of crosslinked samples, but with a high standard deviation. This can be explained by the presence of inhomogeneities on the hydrogel surface stiffness, thus suggesting that further work need to be carried out to optimize the sample preparation. Figure 1 and 3 showed promising results in samples of P11-4 and chitosan, but also higher concentrated TG-samples pro-

duced very promising results in comparison with the positive (GA) and negative (P11-4 w/o crosslinking) control. The self-assembled  $\beta$ -sheet structure of P11-4 was present in all sample compositions (confirmed by FTIR).

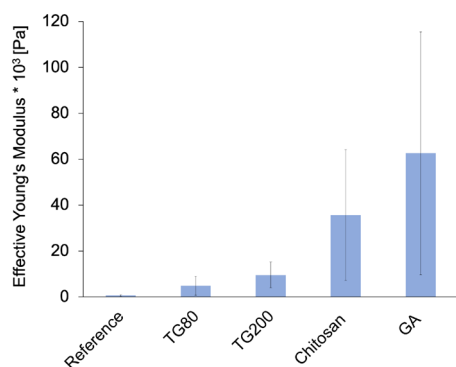


Fig. 3: Nanoindentation measurements of reference P11-4 hydrogel (not crosslinked) and crosslinked P11-4 hydrogels. Data represent mean  $\pm$  standard deviation,  $n = 6$  points per sample.

Furthermore one can say that there is still potential to expand and optimize the methods of measuring stiffness. Potential crosslinker systems were selected for further testing (transglutaminase, chitosan and alginate).

In addition to the sample preparation, combination and analysis mentioned here, adhesion on mucosal tissue is an essential property of hydrogels intended for oral application. Several tests are described in literature to examine the adhesion behavior of adhesives on adherent materials, where probe pull, lab shear or peeling tests are only a few to name. It has been shown that a constructed wash-off test [6] to screen mucoadhesion on pig mucosa, was a well feasible method. In general, porcine mucosa samples were glued onto microscope slides and the hydrogel samples were placed onto the mucosa. Microscope slides with the samples were then attached to a disintegration tester, permitting a constant and slow up- and down movement in saline medium at 37°C.

The above described set up was adapted accordingly to the properties of the P11-4 hydrogels. Therefore, to mimic the oral mucosa, pig tongues were cut into approx. 1.5 x 1.5 cm<sup>2</sup> pieces and mounted on microscope slides. To improve traceability and visibility, the colorless hydrogel was stained blue using Brilliant Black before it was applied on top of the pig tongue. To improve the stability, hydrogels were treated with three different crosslinkers: glutaraldehyde, chitosan and transglutaminase. Figure 4 depicts several aspects of the test.

So far the test set up is readily established, and first adhesion tests were performed with preliminary results showing that P11-4/chitosan and P11-4/GA crosslinked hydrogels exhibit a reduced adhesion in comparison to untreated and TA treated hydrogels. The tests were performed for a duration of 1 hour and in this time frame, P11-4/GA and P11-4/chitosan samples detached within a few seconds, whereas in untreated samples approx. 75% of the hydrogel was still intact and adhered up to 20 min. Most promising results were obtained with TA samples, which were almost unchanged attached after 1 hour. Further washing tests will be performed to confirm the findings and further evaluate the ability of P11-4/TA to adhere on mucosal surface.

In the frame of this project the biocompatibility study with human gingival fibroblast (HGF-1) cells over seven days showed a comparable metabolic activity for non-crosslinked P11-4 hydrogel and P11-4 crosslinked with either chitosan or TG. In contrast, P11-4 crosslinked with GA appeared to be

cytotoxic to HGF-1 cells. These experiments will be repeated with human periodontal ligament fibroblasts (HPdLF-1).

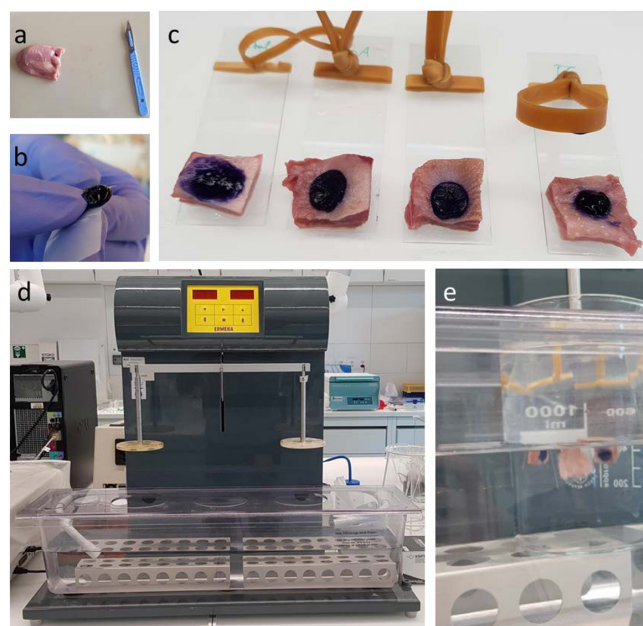


Fig. 4: a) pig tongue. b) blue stained hydrogel sample. c) hydrogel samples with different crosslinkers applied to pig tongue pieces. d) disintegration tester. e) samples attached to disintegration tester being constantly moved in saline solution.

## References

- [1] L. Kind, S. Stevanovic, S. Wuttig, S. Wimberger, J. Hofer, B. Müller. U. Pieves, Biomimetic Remineralization of Carious Lesions by Self-Assembling Peptide, *J. Dent. Res.* 96, 790 (2017)
- [2] M. Schlee, F. Rathe, C. Bommer, F. Bröseler, L. Kind, Self-assembling peptide matrix for treatment of dentin hypersensitivity: A randomized controlled clinical trial, *J. Periodontol.* 89, 653 (2018)
- [3] S. Saha, X. B. Yang, N. Wijayathunga, S. Harris, G. A. Feichtinger, R. P. W. Davies, J. Kirkham, A biomimetic self-assembling peptide promotes bone regeneration in vivo: A rat cranial defect study, *Bone* 127, 602 (2019)
- [4] F. Koch, A. Wolff, S. Mathes, U. Pieves, S. Saxer, B. Kreikemeyer, K. Peters, Amino acid composition of nanofibrillar self-assembling peptide hydrogels affects responses of periodontal tissue cells in vitro, *Int. J. Nanomedicine* 13, 6717 (2018)
- [5] E. Caló and V.V. Khutoryanskiy, Biomedical applications of hydrogels: A review of patents and commercial products, *European Polymer Journal* 65, 252 (2015)
- [6] C. M. Lehr, J. A. Bouwstra, E. H. Schacht, H. E. Junginger, In vitro evaluation of mucoadhesive properties of chitosan and some other natural polymers, *Int. J. Pharmaceutics* 78, 43 (1992)

# Acoustic signal to control laser ablation processes

Project A16.06: LanakPro (FHNW Windisch, FHNW Muttenz, Orvinum AG, Magden)  
 Project Leader: A. Stumpp  
 Collaborators: C. Furrer, M. Hoebel, F. Dieterle, B. Lüscher, M. Ehrat

## Introduction

To achieve structures or layers in the micro- and nanometer range, it is essential to monitor and automatically control the laser process (see Fig. 1). Laser ablation experiments are carried out in this project with a JenLas.D2fs,  $\lambda=513$  nm,  $\tau < 400$  fs, PRF = 100 kHz, the IntelliSCAN de14 scanning system with VarioScan 20i and 115 mm F-Theta optics.

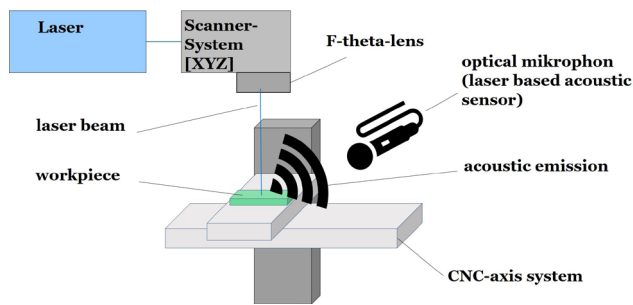


Fig. 1: General setup of a laser system with acoustic monitoring.

The decisive parameters for precision ablation are, on the one hand, the constant parameters such as the absorption and ablation threshold of the material, the wavelength and pulse duration of the laser. On the other hand, the variable parameters such as the focal position or the fluence. Especially in precision machining in the  $\mu\text{m}$  and sub- $\mu\text{m}$  range, a defined fluence ( $F$ ), i.e., energy input per area ( $W_0$ ), is of great importance (Fig. 2). For this purpose, the optimum focal position ( $Z_0$ ) must be identified and continuously tracked and adjusted within 25% of the Rayleigh length during laser material processing.

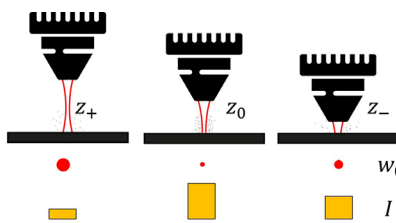


Fig. 2: Influence of focal distance and size on the energy input.

## Acoustic monitoring

Acoustic monitoring can detect important process events [2], such as the ablation of a thin film on a substrate or the breakthrough timing of a micro hole on a closed body [3]. In this project, acoustic signatures are recorded without contact, analyzed, and used specifically for pulsed laser ablation

processes. The appropriate acoustic sensor system with high resolution capability for data acquisition and data analysis, must be able to detect the ablation thresholds of the materials. The threshold fluence for glass (microscope slide) is  $0.54$  J/cm<sup>2</sup>, for metal (1.2083)  $0.08$  J/cm<sup>2</sup>. Figure 3 shows the sensitivity comparison of different sensor systems at optimum ablation ( $3.56$  J/cm<sup>2</sup>) using glass as an example. The differences of the acoustic signatures in focus are clearly visible. The blue plot represents the optical microphone with signal-to-noise-ratio (SNR) up to 26 dB at 400 kHz, the red plot shows the spectrum recorded with a free field microphone and SNR of appr. 8 dB at the same point. The green plot corresponds to the spectral response taken with an accelerometer, where at 400 kHz no peak appears. The most sensitive optical microphone [1] can detect signatures up to 300 kHz even at the ablation threshold ( $0.54$  J/cm<sup>2</sup>).

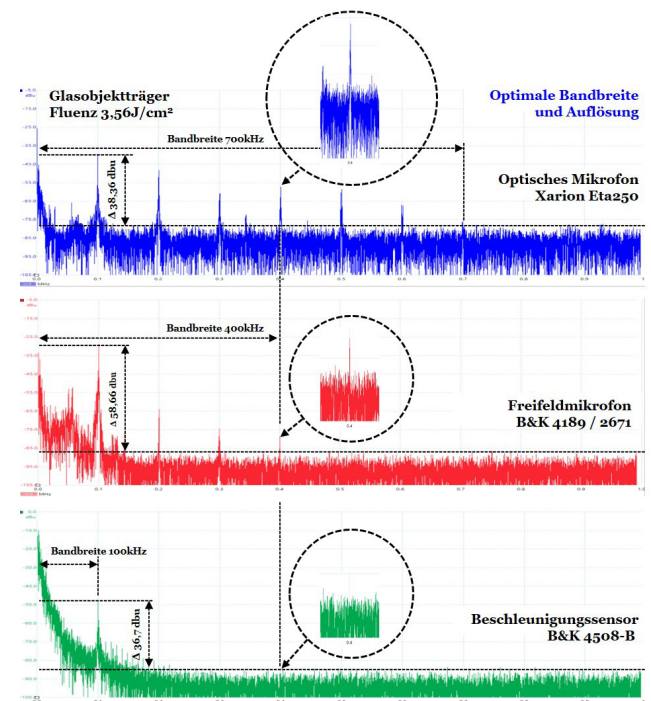


Fig. 3: Sensitivity comparison of three sensor systems – optical microphone, free field microphone and accelerometer.

## Method for determining the focus position

For layer-by-layer 3D ablation in the nm range, the fluence per layer must be controlled and readjusted if necessary. The line pattern in figure 4 shows the correlation between the focus position in the Z-direction, at a height difference per

line of 20  $\mu\text{m}$ , and the corresponding acoustic signature. The left image shows the acoustic signature in the focused situation, with the 0 line on the glass surface. The other images show the defocused acoustic signature with 0.2 mm above or in the material. The Rayleigh length of the F-Theta optics is  $\approx z_r = 0.3$  mm.

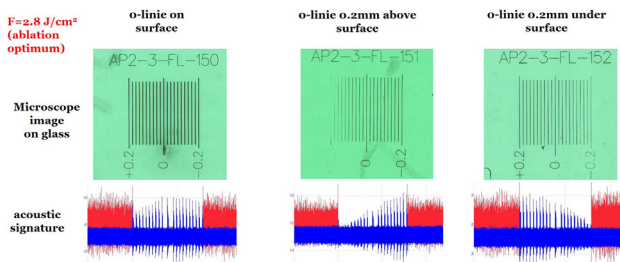


Fig. 4: Acoustic signature change depending on focal position

### Acoustic focal monitoring & control

As a proof of concept, a laser ablation system was equipped with an additional data acquisition and analysis system. As shown in figure 5, the whole concept consisted of three main parts. A laser process was started and ablating a layer of different lines as mentioned before in figure 4. Data acquisition recorded the acoustic emissions with an optical micro-phone at a sampling rate of 3.9 MS/s. These analog signals were digitized, converted to millivolts, and passed to a data queue. As next data analysis chunked these data from queue in matching data pieces for the following Fast Fourier Transform (FFT). Every 0.5 ms a new FFT was calculated, with a bandwidth of 1.95 MHz and a spectral resolution of appr. 512 Hz. Frequencies were added to specifically weighted frequency bins and normalized. The resulting 177 frequency bins were then separated to single lines with assistance of trigger signals. When laser process finished the current layer, all data points were added up and normalized for each line and frequency bin including a background noise correction. Those sums were passed to a trained machine learning model (ML) to predict the focal position. With a target-performance comparison the resulting difference value was passed to the laser process to correct the focal position for the next ablation layer.

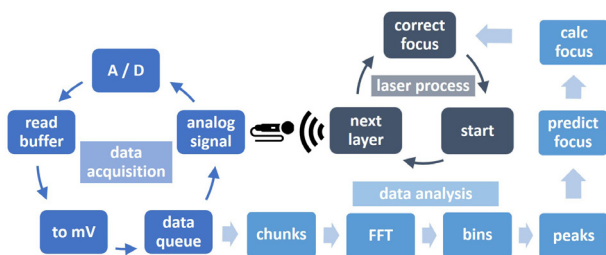


Fig. 5: Scheme of the proof of concept consisting of three main parts: laser ablation, data acquisition of acoustic emissions and data analysis with calculation of focal point correction.

Ablation experiments of lines were performed by systematically varying the focus from -0.2 mm to +0.2 mm (21 levels in total, see Fig. 4). These experiments were repeated 5 times at the same line locations and reproduced in 10 experiments (new lines). Based on the acoustic patterns, different machine learning algorithms were trained and predicted the shift of focus to correct the focus (10-fold cross-validations). Among different algorithms applied the Random Forest models performed best in reproduced experiments, also using different surface material. Using glass surfaces, more than 96% of the predictions of the laser shift were in between +/- 0.25 of the

Rayleigh length of the laser system as demonstrated in figure 6. Overall, the results demonstrate that a prediction of a shift of laser focus and thus a required correction of the focus when ablating material is possible using acoustic signatures and Random Forest models.

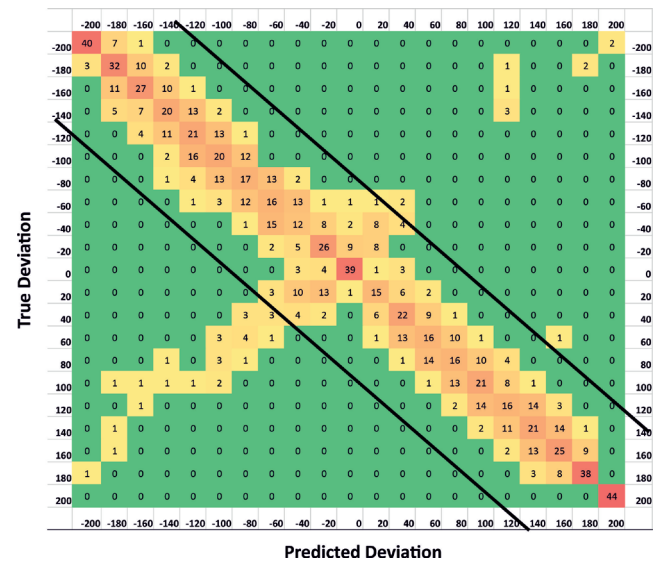


Fig. 6: Predicted offset of the laser focus with Random Forest algorithm versus the true offset in experiments with 21 lines using a 10-fold cross-validation. The black lines represent +/- 0.25 of the Rayleigh length.

### Summary

To control and perform laser ablation of glass, metal, or multi-layered materials within a narrow and well-defined process window we applied a high-resolution optical microphone able to detect signals in the 300 kHz range at the ablation threshold. Based on FFT of the acoustic signals, frequency binning and data normalization for each line the focal position was determined by a trained machine learning model, followed by the focus adjustment for the subsequent line. Using glass surfaces, more than 96% of the predictions of the laser deviations from the ideal focus were in between +/- of 0.25 of the Rayleigh length. In a real-world application the principle of focal prediction and direct adjustment in the laser process was successfully demonstrated. Further development is planned to optimize the algorithm and expand the application scope.

### References

- [1] B. Fischer, W. Rohringer, N. Panzer, S. Hecker, Acoustic Process Control for Laser Material Processing, Laser Tech. J. 5 (2017)
- [2] P. Weber, Steigerung der Prozesswiederholbarkeit mittels Analyse akustischer Emissionen bei der Mikrolaserablation mit UV-Pikosekundenlasern, Dissertation, KIT, Karlsruhe (2014)
- [3] C. Furrer, Laserprozessoptimierung mit Akustik- und Beschleunigungssensor, Master-Thesis, FHNW, Windisch (2020)

# Microstructured degradable hydrogel-based periodontal LIGament RE-COnstitution device

Project A16.07: LIGARECO (FHNW Muttentz, University of Basel, Klinik für Oral Health & Medicine , Novonexile AG, Füllinsdorf)

Project Leader: J. Köser

Collaborators: K. Mukaddam, S. Köhl, S. Tugulu

## Introduction

Peri-implant infections of osseointegrated implants represent a topic of major concern in contemporary dentistry. The mechanical relatively weak adhesion of soft tissue at the coronal part of the implant has been proposed as a potential risk factor for peri-implant infections [1]. Micro- and nanostructured implant collars have been tested as potential candidates to improve soft tissue adhesion. Despite encouraging preclinical results, none of the presented approaches has so far yielded a mechanically robust soft tissue organization comparable to the one around natural teeth with its characteristic arrangement of radially oriented collagenous periodontal ligament fibers.

Within the presented project, we aim to develop a regenerative device that mediates and guides the formation of radially oriented periodontal ligament bundles around the collar of dental implants. Radial channels within the device target fiber-producing periodontal ligament cells to orient them and guide collagen fiber production in a perpendicular and mechanically stable orientation around the implant surface. This arrangement may significantly improve the soft tissue strength and sealing around dental implants and render it comparable to healthy gingival tissues around natural teeth. The regenerative device is designed for placement as part of dental implant treatment (Fig.1). While scientists ultimately aim to develop reconstituted periodontal ligaments for the bone-dental implant interaction [2], our approach aims to improve conventionally and commercially available osseointegrated dental implants by an improved ligament reinforced soft tissue attachment.

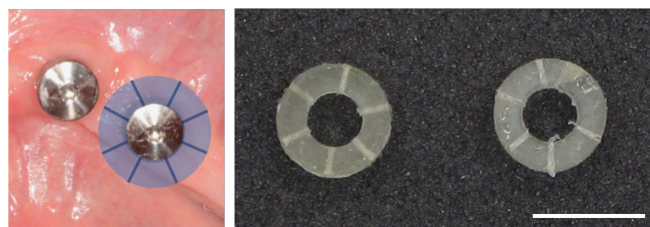


Fig. 1: a) Scheme of the location of the proposed device, which is placed around the upper part of the implant before wound closing, and b) sample devices prepared during the project. Scale bar 8 mm.

Cell alignment in microchannels has been investigated worldwide for basic research and specific tissue engineering approaches like, e.g., neuronal lesion repair, tissue vascularization, or tendon regeneration. Cell colonization of such microchannels in cell culture conditions is supported by using a cell adhesive biomaterial or coating the channel walls with adhesion molecules.

Within the presented project, we use an in-situ cross-linkable and biodegradable PEG-hydrogel for device fabrication. Multi-functional PEG precursors are combined and formulated to provide specific viscosities and polymerization kinetics that allow the fabrication of form-stable, patterned hydrogel templates with biological functionalities and degradation times that are specifically adjusted to the requirements of the targeted biological indication.

## Hydrogel biofunctionalization

Bioinert materials like the PEG-hydrogel employed in this project are intrinsically non-adhesive and need to be functionalized with cell type-specific ligands to allow cell adhesion. In a first approach, integrin-specific RGD ligands were copolymerized with the PEG-precursors to result in RGD-functionalized hydrogels.

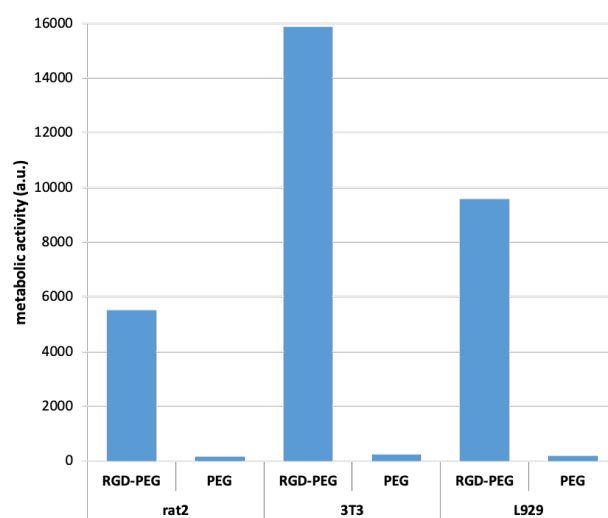


Fig. 2: Effect of PEG-hydrogel modification with RGD-peptides on fibroblast adhesion. Results from metabolic assays to quantify adhering cells of three different fibroblast lines, rat2, 3T3 and L929, on RGD-functionalized vs. unmodified PEG-hydrogels.

Fibroblast adhesion was analyzed by comparing the number of adhering cells on native and RGD-functionalized PEG hydrogel surfaces (Fig. 2).

## Cell colonization of hydrogel microchannels

Typical periodontal ligament fibers have dimensions in the range of 0.2 to 0.4 mm. Hydrogel-channels with these dimensions could be successfully manufactured as part of the first working prototypes.

Immortalized rat2 fibroblast cells were seeded on the channeled hydrogels and, following 1-2 weeks of growth, were found colonizing the channel structures.

During the reported project period, the influence of channel dimensions on cell colonization and orientation was systematically investigated by varying the channel diameters between 200 and 600  $\mu\text{m}$ . Further, the influence of structuration of the channel walls was investigated by comparing smooth and micro-grooved channel walls. The experiments demonstrated that the microchannels in the PEG-hydrogel were successfully colonized by cells independent of the channel diameters. However, the micro-structuration of the channel walls significantly affected the cell orientation. As evidenced by the microscopic comparison of cells adhering in unstructured, smooth channels and channels exhibiting a micro-structuration of the inner channel walls, the latter considerably enhanced fibroblast cell orientation (Fig. 3).

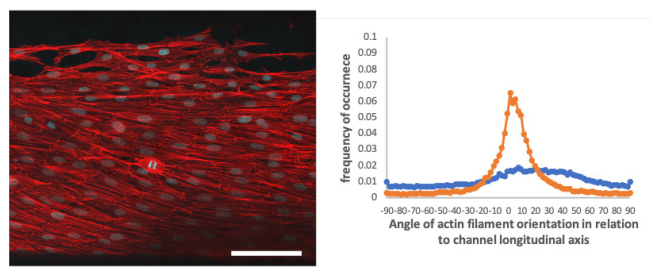


Fig. 3: Cell invasion of hydrogel channels and orientation of cells assessed by fluorescence microscopy. Fibroblasts are seeded onto channeled hydrogel samples and cell invasion and orientation are analyzed after 7 days by phalloidin rhodamine staining of the actin cytoskeleton. a) Rat-2 fibroblasts colonizing a microstructured channel, and b) directionality evaluation of actin filaments of cells growing in 0.4 mm channels (orange line, microstructured side-walls, blue, reference channel). Scale bar: 100  $\mu\text{m}$ .

#### Periodontal ligament cell colonization of microchannels

The mechanical strength of periodontal ligament fibers has been attributed to longitudinally oriented collagen bundles secreted by a specific form of fibroblasts, the periodontal ligament cells. These cells can be obtained from patient samples and cultured in vitro for a limited number of passages. In culture, periodontal ligament cells exhibit an elongated morphology. As part of our microchannel cell colonization assays, we could show that in contrast to rat2 fibroblasts, these cells aligned along the channel axis, even in the absence of microstructures on the channel walls (Fig. 4).

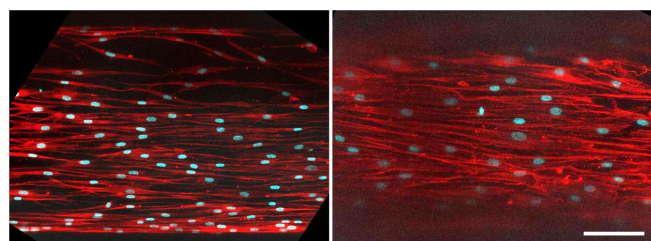


Fig. 4: Orientation of primary periodontal ligament cells in 0.4 mm channels with (a) and without (b) additional microstructuration. Cells were seeded onto channeled hydrogel samples. Cell invasion and orientation were analyzed by fluorescence microscopy after 7 days by phalloidin rhodamine staining of the actin cytoskeleton and DNA counter staining. Scale bar: 100  $\mu\text{m}$ .

In all our assays, immortalized fibroblasts or primary periodontal ligament cells formed monolayers on the channel sidewalls, resulting in a central lumen in the microchannels.

This lumen can be considered essential for transporting nutrients and factors from the surroundings to the cells. In contrast to this observation, in vivo the periodontal ligament is composed of a continuous assembly of different cell types and fiber-forming extracellular matrix proteins. Currently, ongoing experiments investigate if the observed lumen persists in devices with reduced channel diameters. These experiments will also specifically investigate how ongoing cell proliferation and matrix deposition within the confined channel dimensions will influence the alignment of cells within the channel. These experiments ultimately aim to investigate and understand if the channel diameter influences ligament fiber formation and identify the final device's optimal channel geometry and dimensions.

The next project phase shall also address potential alternative microchannel fabrication methodologies and optimized biofunctionalization strategies to enhance cell invasion of the periodontal ligament reconstituting device.

#### References

- [1] I. Atsuta, Y. Ayukawa, R. Kondo, W. Oshiro, Y. Matsuu-  
ra, A. Furuhashi, Y. Tsukiyama, K. Koyano, Soft tissue  
sealing around dental implants based on histological  
interpretation. *J. Prosthodont. Res.* 60, 3–11 (2016)
- [2] M. Gulati, V. Anand, V. Govila, N. Jain, P. Rastogi, R.  
Bahuguna, B. Anand, Periodontio-integrated implants:  
A revolutionary concept. *Dent Res J (Isfahan)* 11, 154–  
162 (2014)

# Nanocompass: Nanoscale magnetometer with nanotesla resolution

Project A16.10: Nanocompass (FHNW Muttentz, FHNW Windisch, Camille Bauer Metrawatt AG, Wohlen)

Project Leader: J. Pascal

Collaborators: H. Nicolas, A. Inderbitzin, J-B. Kammerer, R. Sousa, S. Gorenflo, M. Ulrich

## Introduction

Magnetic memories MRAMs are often based on structures called magnetic tunnel junctions (MTJs) and are using spin transfer torque (STT) to change the orientation of the magnetization of a soft ferromagnetic layer by applying a strong voltage across the junction. This leads to a change of resistance allowing the MRAM to be set in two different resistive states. However, the energy required to flip the magnetization of the layer from one state to the other is not only related to the voltage applied to the junction but also to the external magnetic field. Using this property, this work investigates a new application of an MTJ, which consists of using it as a magnetic sensor.

## Magnetic Tunnel Junctions (MTJs)

Tunnel magnetoresistance effect (TMR) can be observed in MTJ made of multiple layers, including two layers of conductive ferromagnetic materials (pinned layer, PL, and free layer, FL) separated by a non-magnetic material, called the barrier. MTJs are usually manufactured with the shape of a pillar (Fig. 1) and called perpendicular MTJs or P-MTJs, with the two contacts of the junction at the top and bottom of the structure. The FL and the PL (usually FeCoB) are surrounded by several layers of different materials and thicknesses that will create a spin polarized current [1].

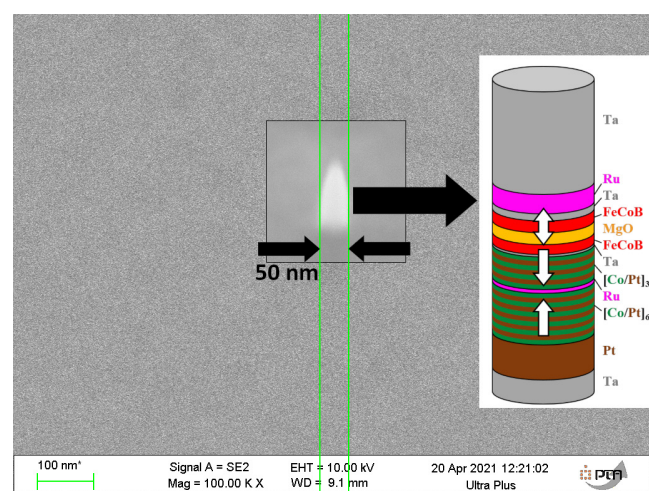


Fig. 1: SEM image of a 50nm-MTJ (left) and standard MTJ stack pillar [1] (right).

The diameter of these junctions is usually a few dozens of nanometers, and the barrier, often MgO, is usually a few dozens of angstroms, to a few nanometers thick to ensure the spin orientation conservation principle, which cannot apply to thicker barriers (Fig. 2).

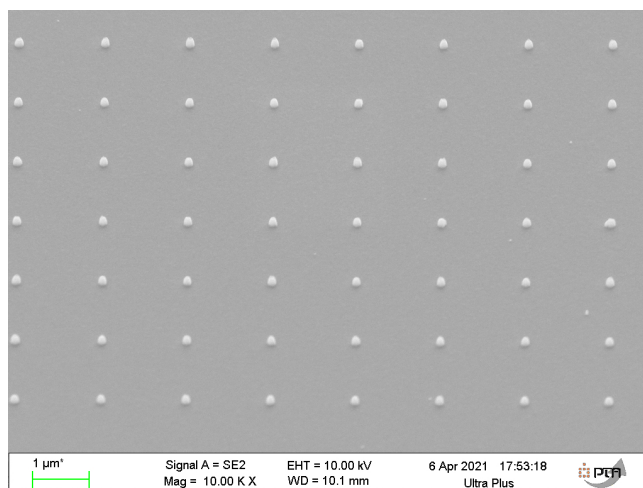


Fig. 2: SEM image of 56 samples of 100nm-MTJs on a single wafer.

## MTJ-based Magnetic Sensors

A repeated reversal of the magnetization of the MTJFL leads to a hysteresis cycle of the junction resistance. This cycle is not only dependent of the spin polarized current but also depends on the external magnetic field. This principle of operation is inspired from the macroscopic fluxgate sensor technology [2] and is applied here to a nanoscale spintronic device. To extract the value of the magnetic field from the hysteresis curve a signal processing scheme is required. A Matlab-Simulink model of the sensor including a physical model of the MTJ associated to a model of the analog and mixed signal processing has been developed to support the hardware implementation of the sensor as described in the next section. A further step for improving the sensor is an independent MTJ emulator as a hardware model to develop a pure digital solution of the sensor control and signal processing unit. The interfaces are designed very flexible, so that both the real junctions as the emulator can be applied for testing [2].

## Experimental Results

Two large pads are available for each of the MTJ on a wafer and are used to contact with a probe. In the first experimental setup, the wafer is placed underneath large electromagnets (Fig. 3) that generate an external magnetic field. Short voltage pulses of 100 nanoseconds and increasing intensity were applied on MTJ having a diameter of 100 nm.

For each pulse, a resistance measurement was performed to check if the layers are in the parallel P or antiparallel AP configuration. The threshold voltage where the magnetization of the free layer is reversed was then saved. Each of the measurement included a full hysteresis cycle, with one APP

and one PAP reversal. The reversal events were estimated through data processing on a computer. In this manner, the reversal events have been recorded for different values of the external magnetic field applied with the electromagnets. Finally, we could demonstrate that the reversal events are dependent of the external magnetic field and the characteristics of the proposed sensor, obtained experimentally, is depicted in figure 4.

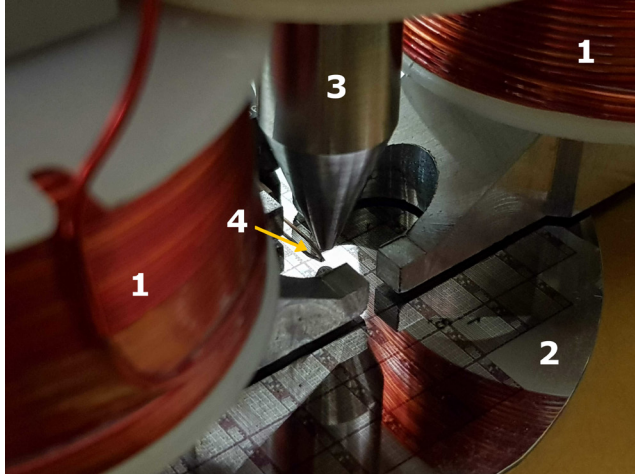


Fig. 3: Experimental setup (1. Electromagnets, 2. Wafer under test, 3. Iron core of electromagnets, 4. Probe).

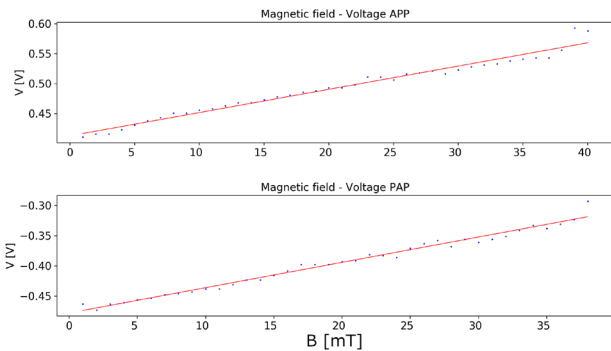


Fig. 4: Evolution of APP and PAP switching voltages as a function of the applied external magnetic field.

### Discussion

The sensor characteristics exhibits a large dynamic range of 40 mT, which outperforms the commercially available magneto resistive sensors (MR). The observed sensitivity is 4 mV/mT. However, because of the stochasticity of the phenomena involved in the flipping of the magnetization of the MTJ-FL we observe a higher noise level than for instance in conventional MR sensors. Alternative MTJ pillar arrangements as well as advanced signal processing needs to be investigated to reduce the sensor noise level. Besides, a better controlled test environment has been developed implementing Helmholtz coils (Fig. 5) and a dedicated control and signal processing electronics (Fig. 6) to characterize more precisely the sensor performances.

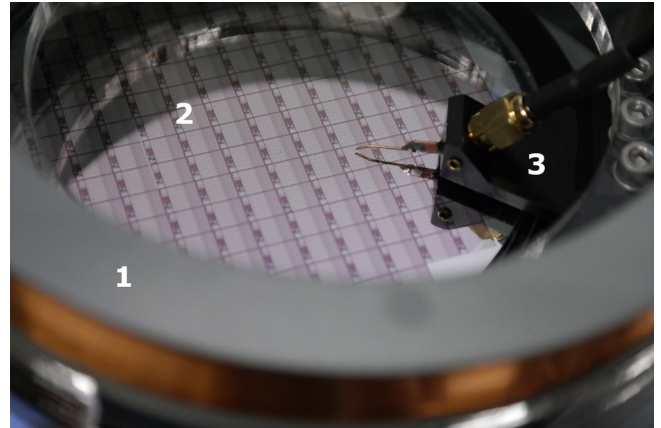


Fig. 5: Improved experimental setup (1. Helmholtz coil, 2. Wafer, 3. Probe).



Fig. 6: Control and signal processing electronics.

### Conclusion

MTJ-based magnetic sensors will have significant advantages over existing magnetic sensors. Unlike commercially available Hall sensors or MR sensors which have micrometer dimensions, the proposed MTJ based magnetic sensor has a diameter of less than 100 nm. Its applications range from the medical field and physics experiments to industrial products. An optimization of the MTJ stacks combined with an improved signal processing and dedicated test setup shall lead to a lower sensor noise level.

### References

- [1] N. Perrissin Fabert. Ultimate scalability of STTMRAM: storage layer with perpendicular shape anisotropy. PhD thesis, University Grenoble Alpes (2018)
- [2] Ripka, Pavel. Magnetic sensors and magnetometers. Artech house (2021)

# Blue laser diode pumped Ti:Sapphire sub-100 fs laser amplifier for nanomachining

Project A16.11: NanoLase (FHNW Windisch, Paul Scherrer Institut, TLD Photonics AG, Wettingen)

Project Leader: B. Resan

Collaborators: D. Hug, F. Friebe, A. Trisorio, A. Dax, R. Carreto, S. von Wolff

## Introduction

The workhorse for most of demanding laser applications are femtosecond lasers based on Titanium doped Sapphire (Ti:Sa) gain medium. The main drawback up to now is the absence of direct diode pumping scheme enforcing the use of Q-switched, nanosecond solid-state laser (e.g Nd:YAG) as pump laser source. This leads to very inefficient optical pumping and a large purchasing and maintenance cost for such systems, the later prohibiting the spread of Ti:Sa lasers in wider industrial applications. In this project, we aim to develop a high average power, 100- $\mu$ J energy level, sub-100fs Ti:Sa laser amplifier, based first, on recently available high power blue diodes at 450 nm, and second, on a novel Single Crystal Fiber (SCF) geometry. The SCF geometry will increase couple of times the laser average power, due to superior cooling capability. The direct diode pumping will increase wall-plug efficiency by  $\sim 10$  times (wall-plug efficiency  $\sim 5\%$  versus typical  $\sim 0.5\%$ ). It will also make the laser much more compact and reliable. In addition, we will design a wavelength conversion stage (second harmonic generation - SHG) to obtain blue fs pulse at 400 nm. We will perform first material processing tests with this novel laser with blue beam suitable for metal nanomachining and IR for polymers. Couple of times shorter pulses, compared to currently commercially available, and high power blue lasers, should enable us to make a breakthrough in laser materials processing and move from micro to nanomachining, with high throughput.

## Experimental setup

For the diode pumped amplifier, the Ti:Sa crystal is pumped from two sides as depicted in figure 1. On the left side, three laser diodes, each with 6 W optical output power @ 450 nm, are mounted at different heights. They are combined and focused onto the crystal with a diameter of 100  $\mu$ m at  $1/e^2$ . From the other side, a fiber coupled diode with 20 W optical output power is also focused into the crystal with a diameter of 100  $\mu$ m at  $1/e^2$ , yielding a total pump power of 38 W. The different divergences of the two diode types prevent back-focusing on the opposite diode and thus potential subsequent damage. A directly blue diode pumped laser oscillator delivering  $>200$  mW average power, 70 fs pulses @ 80 MHz and 800 nm is used as seed laser. The pulses to be amplified are coupled in, focused and coupled out again via curved dichroic mirrors. The pumped setup is shown in figure 1 and a picture of the amplifier in operation is shown in figure 2.

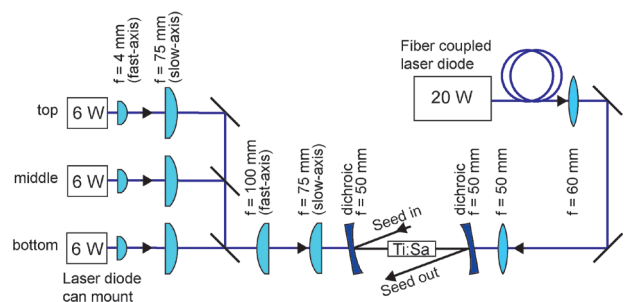


Fig. 1: Ti:Sa amplifier setup.

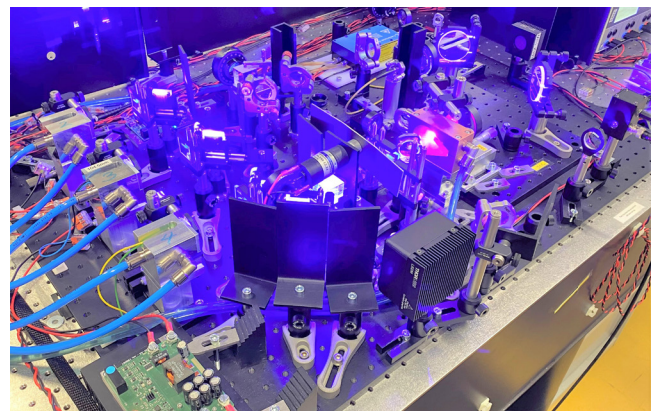


Fig. 2: Ti:Sa amplifier pumped by blue diodes at 450 nm.

## Thermal simulations

High pump intensities  $>500$  kW/cm<sup>2</sup> inside the Ti:Sa crystal are needed for population inversion. The absorbed pump light creates sharp temperature gradients as shown in figure 3. The temperature gradients inside the Ti:Sa crystal lead to strong thermal lensing effects, affecting the amplified beam as simulations show in figure 4.

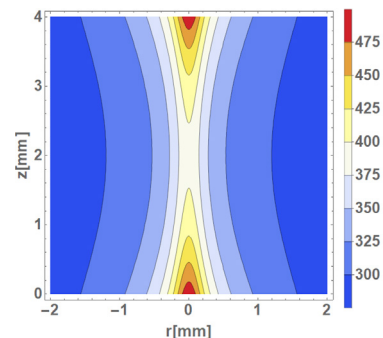


Fig. 3: Simulation of temperature profile through Ti:Sa crystal (cross section) in [°C] done by PSI.

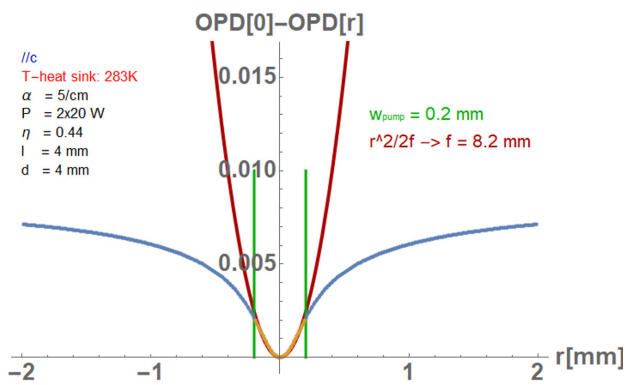


Fig. 4: Simulation of thermal lens done by PSI.

Therefore it is fundamental to cool the Ti:Sa crystal sufficiently, uniformly and symmetrically.

### Optimized crystal cooling

A new crystal holder cooling design, based on a copper module with high thermal conductivity (Fig. 5), selective laser melted 3D print inserts and micro-graphite-foil (Fig. 6) was optimized with several thermal FEM simulations to generate a symmetric temperature profile inside the Ti:Sa crystal (Fig. 7).

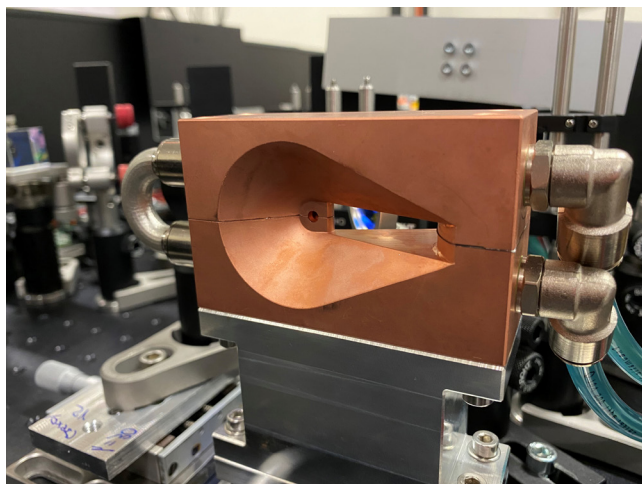


Fig. 5: Optimized housing of Ti:Sa crystal.

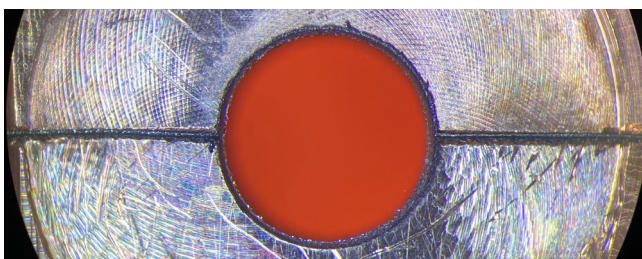
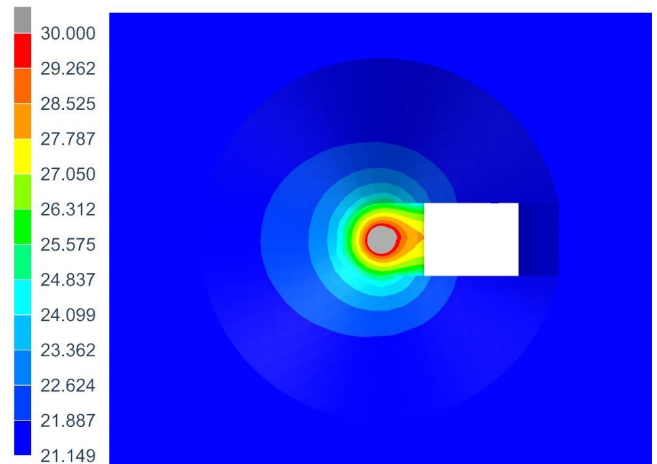


Fig. 6: Micro-Graphite-Foil for optimized thermal conductivity between Ti:Sa crystal and cooling housing



[°C]

Fig. 7: Simulation of temperature distribution in crystal holder when cooled at room temperature [°C].

### Small signal gain measurements

Optimizing the pump focus spot size and position inside the crystal, cooled at 20°C, as well as the overlapping of pump and signal beam, a small signal gain of 5% was measured only using 18 W of pump power from one side as shown in figure 8.

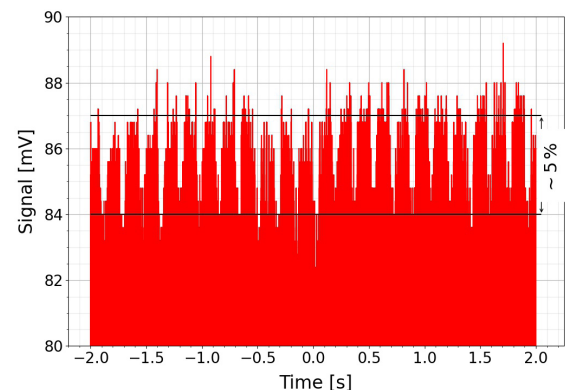


Fig. 8: Measured small signal gain when pumped with only 18 W of CW light from left side diodes.

By modulating the 6 W diodes with a TTL signal at 1.5 kHz and 20% duty cycle we reached 17 W peak power from each diode, which should increase the small signal gain. Modulation of the pump diodes also decreased the overall thermal load of the Ti:Sa crystal and therefore lowers the thermal lensing effect. Pumping from both sides will generate the small signal gain of > 10%, which will enable us to build up a regenerative amplifier to be used for the first nanomachining applications.

### References

- [1] A. Rohrbacher, O. E. Olarte, V. Villamaina, P. Loza-Alvarez, B. Resan, Multiphoton imaging with blue-diode-pumped SESAM-modelocked Ti:sapphire oscillator generating 5 nJ 82 fs pulses, *Opt. Express* 25, 10677 (2017)
- [2] S. Backus, M. Kirchner, R. Lemons, D. Schmidt, C. Durfee, M. Murnane, H. Kapteyn, Direct diode pumped Ti:sapphire ultrafast regenerative amplifier system, *Opt. Express* 25, 3666 (2017)

# Combinatorial nanoparticle design for therapeutic drug delivery across the blood brain barrier

Project A16.12: NANOthruBBB (FHNW Muttenz, University of Basel, Pharmaceutical Technology, Perseo Pharma AG, Muttenz)

Project Leader: P. Shahgaldian

Collaborators: C. Wu, N. Santacroce, L. Suter-Dick, N. J. Roos, J. Huwyler, E. Laprevotte, Y. Dudal

## Introduction

The blood brain barrier (BBB), a complex cellular filter protecting the brain from outside unwanted intrusions, represents a major hurdle for the delivery of therapeutic biomacromolecules. As a consequence, benefits of biological drugs (i.e., biologics), achieved in a large number of diseases (e.g., cancer, autoimmune diseases), do not significantly impact pathologies where the therapeutic target is in the brain [1]. To overcome this hurdle, a variety of nanoparticulate drug carriers have been designed and several targeting moieties have been shown to favor their transport through the BBB [2]. It is remarkable, however, that no systematic study allowed defining the optimal nanoparticles (NPs) parameters to design such carriers. This represents the foremost objective of NANO-thru-BBB.

In NANO-thru-BBB, the project partners aim at establishing a combinatorial surface modification method allowing to produce a large number of NP systems with varying surface properties (i.e. charge, polarity, chemistry, targeting ligands). The NPs produced are currently tested for their ability to cross the BBB both in vitro and in vivo models. The large set of data acquired, analyzed using modern data analysis methods, shall allow establishing a set of rules to predict the optimal surface properties of nanoparticulate systems to efficiently cross the BBB. This strategy will be applied to nanomedicines for the treatment of lysosomal storage diseases (LSDs) developed by Perseo Pharma aiming at delivering stable and active enzymes, through the BBB, to the brain. LSDs arise from inherited lysosomal dysfunctions caused by deficient lysosomal enzymes and/or membrane proteins. Enzyme replacement therapies (ERTs) are currently frontline treatments of LSDs. ERTs, however, fall short when it comes to deliver therapeutic lysosomal enzymes through the BBB. Consequently, more than two-thirds of LSD patients treated with ERT suffer from progressive and severe central nervous system dysfunctions [3].

In order to build a library of surface-modified nanoparticles (NPs), we developed a combinatorial surface modification method. The chemical strategy developed allows, for the first time, the production of NPs displaying a large combination of chemical functionalities at their surface. The NPs produced are currently tested for their ability to cross the BBB both in vitro and in vivo.

## Development of ligands to be used for combinatorial surface modification

In order to construct the targeted NPs library, we developed a combinatorial surface modification that allows a fully stoichiometric reaction of soluble ligands at the surface of organosilica. The core NPs are synthesized using methods available at Perseo. They consist of a silica core on which the selected model protein (i.e. albumin) is immobilized and further protected in an organosilica shield [4]. This shield is

further modified in order to provide anchoring residues for subsequent surface functionalization (Fig. 1).

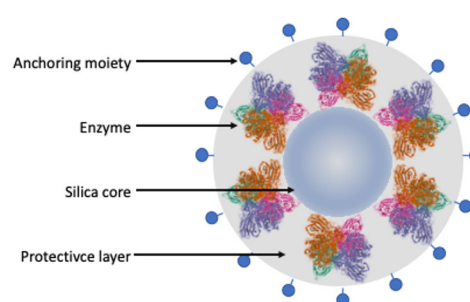


Fig. 1: Nanoparticle design. The enzyme is immobilized at the surface of a silica nanoparticle and further protected in an organosilica layer of controlled thickness and chemical composition. This layer is, in turn, modified in order to introduce chemical moieties allowing further combinatorial modification.

We then designed and produced a series of novel ligands that can be attached to the surface of the NPs. Besides simple ligands bearing carboxy-, hydroxyl- and amino-functions, we selected additional complex ligands including transferrin receptor-targeting peptide (T7 peptide) and a cell-penetrating peptide (HIV TAT peptide) (Fig. 2). In order to check the stoichiometry of the surface coupling reaction, we used a reporter molecule that emits fluorescence only when attached to the surface of the SNPs. Our results confirmed the full stoichiometry of the reaction. Next, we produced a first series of 30 different types of NPs and tested their ability to cross the BBB using an in vitro model.

## In vitro screening of BBB transport properties of modified NPs

In order to build an in vitro BBB model, human brain endothelial cells (hCMEC/D3) were cultured onto semipermeable membranes in transwell inserts (Fig. 1). At day 7 hCMEC/D3 cells reach highest transepithelial electrical resistance (TEER) value and express typical BBB tight junction proteins ZO-1 and Claudin-5, as demonstrated by means of immunofluorescence microscopy (Fig. 3). This study allowed confirming that cell-cell contacts are formed and a functional barrier is established. Preliminary experiments show that specifically modified NPs have the ability to efficiently cross the BBB.

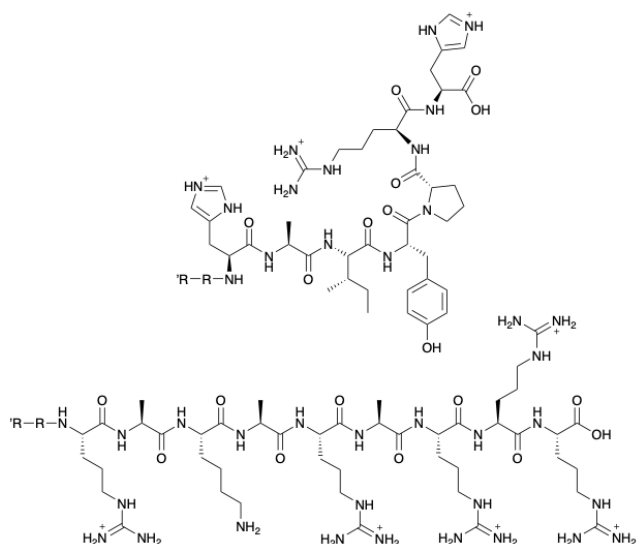


Fig. 2: Example of peptide ligands produced for building the SNPs library [R': surface reactive function; R'': linker].

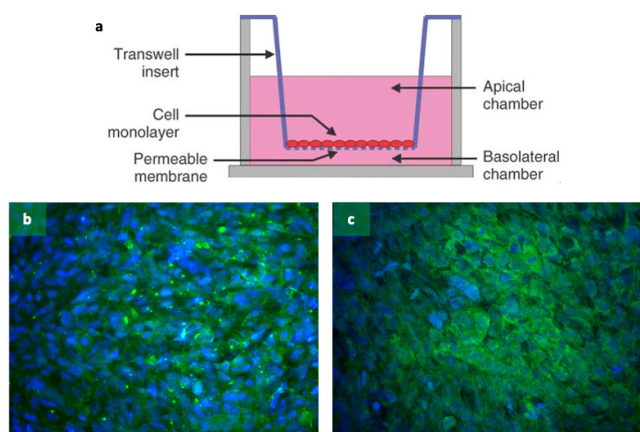


Fig. 3: Schematic representation of the transwell system used to produce a BBB in vitro model a) and immunofluorescence staining showing expression of tight junction proteins zonula occludens 1 (ZO-1, b) and Claudin-5 c). The images show a dense monolayer of cell where tight junctions proteins are expressed.

Preliminary experiments have also been carried out with the selected in vivo model, i.e. transgenic zebrafish (*Danio rerio*) expressing green fluorescent proteins. Our results show that SNPs labeled with a fluorescent dye (Cy5.5) can be visualized when circulating in the living embryo.

### Conclusion and outlook

The partners of Nano-thru-BBB, during the first phase of the project, have developed the first method allowing a combinatorial modification of silica-based nanoparticles. The stoichiometric nature of the reaction has been confirmed by fluorescent spectroscopy. This method has been applied to produce a first set of SNPs, displaying different chemical moieties at their surface. Initial tests carried out in vitro confirmed the importance of the surface modification on the capacity of the SNPs to enter the brain endothelial cells and to cross the BBB. Additionally, our results confirmed that the SNPs did not affect significantly cell viability up to 100  $\mu\text{g}/\text{mL}$ . Preliminary experiments carried out on a zebrafish model have confirmed the possibility to track fluorescently labeled SNPs in the fish embryo. Work is underway to test a larger number of SNPs from the established library and to test their capacity to cross the BBB both in vitro and in vivo.

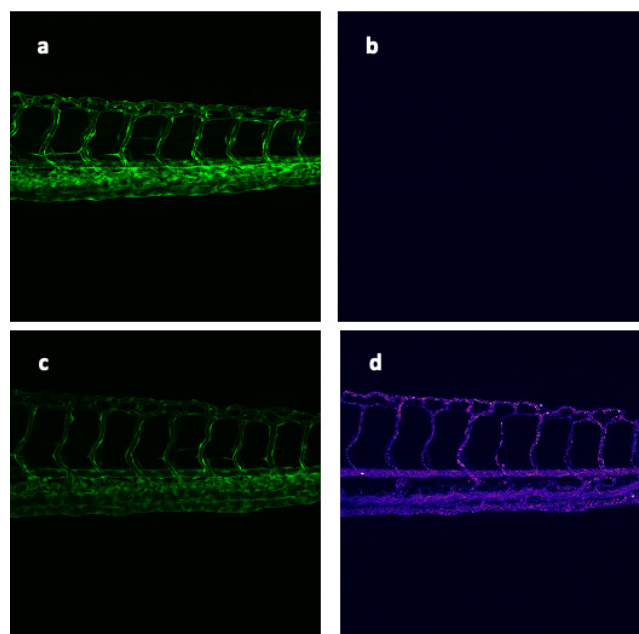


Fig. 4: Fluorescence imaging of fluorescently labeled SNPs in zebrafish embryo. Fluorescence micrographs acquired at wavelengths of  $\lambda = 485 \text{ nm}$  (a, c) and  $683 \text{ nm}$  (c, d) before injection (a, b) and 15 min after injection of NPs labeled with Cy5.5 (c, d). The micrograph d shows circulating NPs imaged in the living fish embryo blood vessels. Longer durations after injection suggest reduced interactions of the SNPs with macrophages.

### References

- [1] A. Villabona-Rueda, C. Erice, C. A. Pardo, M. F. Stins, The evolving concept of the blood brain barrier (BBB): from a single static barrier to a heterogeneous and dynamic relay center. *Front. Cell. Neurosci.* 13, 405 (2019)
- [2] S. Ding, A. I. Khan, X. Cai, Y. Song, Z. Lyu, D. Du, P. Dutta, Y. Lin, Overcoming blood–brain barrier transport: advances in nanoparticle-based drug delivery strategies. *Mater. Today* 37, 112–125 (2020)
- [3] F. M. Platt, A. d'Azzo, B. L. Davidson, E. F. Neufeld, C. J. Tiffit, Lysosomal storage diseases. *Nat. Rev. Dis. Primers* 4, 27 (2018)
- [4] M. R. Correro, N. Moridi, H. Schützinger, S. Sykora, E. M. Amman, E. H. Peters, P. F.-X. Corvini, P. Shahgaldian, Enzyme shielding in an enzyme-thin and soft organosilica layer, *Angew. Chem. Int. Ed.* 55, 6285 (2016)

# PEPS: Printed Electrochemical Protein Sensor

Project A16.13: PEPS (CSEM Muttentz, CSEM Landquart, FHNW Muttentz, MOMM Diagnostics GmbH, Basel)

Project Leader: M. Zinggeler

Collaborators: S. Generelli, D. Gygax, D. Meinel, M. Wipf

## Introduction

In the PEPS project, we are developing an electrochemical sensor platform for the analysis of low concentrated protein biomarkers at the point-of-care (POC). Such digital devices could revolutionize the diagnosis and monitoring of various diseases, making testing as convenient and effective as monitoring diabetes with a glucose meter. However, successful industrial applications of such sensors have not yet been achieved, mainly because of problems with surface fouling, low POC compatibility and/or expensive sensor fabrication [1, 2]. To address these limitations, we are studying the development of novel nanomaterial-polymer composite electrodes (Fig. 1). Such electrodes combine high conductivity and strong antifouling properties, which render them ideally suited for measurements in complex body fluids. The sensors will be printed on flexible foils using highly scalable processes and read-out on simple electronic devices which are compatible with standard consumer electronics. The goal of the project is to realize demonstrator platforms for the analysis of two highly relevant biomarkers (placental growth factor PlGF and the cytokine CXCL10) which could enable POC applications for the diagnosis of preeclampsia or early kidney transplant rejection.

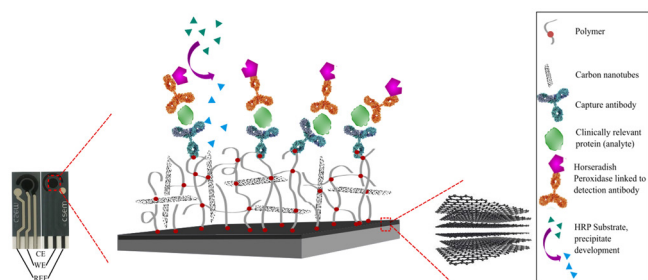


Fig. 1: Photograph (left) of miniaturized 3-electrode system on foil (CE: Counter electrode, WE: Working electrode, REF: Reference electrode) and schematic depiction (right) of the WE functionalization and protein assay strategy.

We report our progress regarding nanocomposite electrode fabrication and characterization, protein assay development on a standard lateral flow assay (LFA) format and present the first results of electrochemical protein assays performed on our “eWell” demonstrator platform.

## Nanocomposite electrodes

Functional inks were prepared by blending photoreactive copolymer solutions with conductive carbon nanotubes (CNTs). The mixtures were homogenized by sonication and printed onto the WE of printed, miniaturized 3-electrode systems on foil, followed by drying and UV-crosslinking. The prepared

electrodes were characterized by measuring cyclic voltammetry with different scan rates in ferricyanide solutions. The electrochemically active surface area (EASA) was calculated using the Randles-Ševčík equation. The procedure was repeated after incubation with concentrated bovine serum albumin (BSA) solution (40 mg/ml) or undiluted human blood plasma to determine the capability of the electrodes to resist surface-fouling. The ink composition and printing parameters were optimized to maximize EASA and retain strong anti-fouling properties. Optimized parameters led to an EASA increase by almost factor 2 compared to uncoated (blank) electrodes (calculated EASA values at 0 minutes, see Fig. 2 and 3). Further, the EASA remained stable even after an incubation of 1 hour in both fouling solutions, while non-modified electrodes lost almost 70% after being exposed to the BSA solution for only 10 minutes (Fig. 2 and 3).

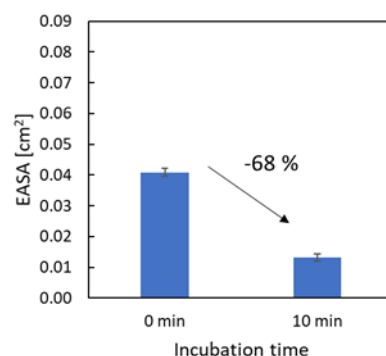


Fig. 2: Measured EASA for blank screen-printed carbon electrodes as a function of incubation time in concentrated BSA solution. Mean values and standard deviations are shown ( $n = 3$ ).

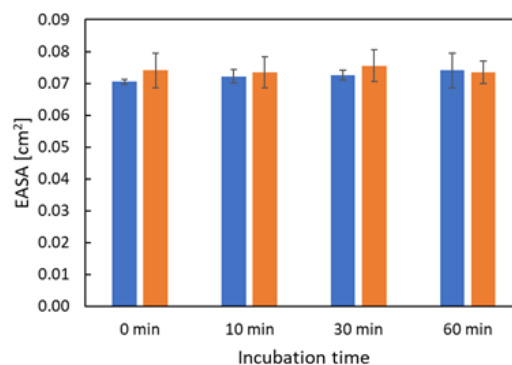


Fig. 3: Measured EASA for PEPS nanocomposite electrodes as a function of incubation time in concentrated BSA solution (blue) and undiluted human blood serum (orange). Mean values and standard deviations are shown ( $n = 3$ ).

### Protein assay

Commercial affinity reagents against PIGF were selected based on a characterization study involving a combination of biolayer interferometry (BLI), flow-induced dispersion analysis (FIDA) and surface plasmon resonance (SPR) spectroscopy. Two amplification methods were studied for the oxidation of 3,3',5,5'-tetramethylbenzidine (TMB) in the presence of hydrogen peroxide. These were gold nanoparticles (AuNPs) attached to several horseradish peroxidase (HRP) enzymes (AuNP-HRP) and a platinum nanoparticle system (PtNP). Both methods showed high catalytic activity and can be combined with the affinity reagents previously identified for use in LFAs. The signal was detectable optically as well as electrochemically. An LFA device for the detection of PIGF in human serum was developed and tested using spiked human serum samples. The running buffer was optimized to reduce interferences from nonspecific binding. With the AuNP-HRP based device, a limit of detection (LOD) of 10 pg/ml was achieved for the detection of PIGF in spiked human serum samples (Fig. 4). Time to result was 30 minutes, involving 4 liquid handling steps.

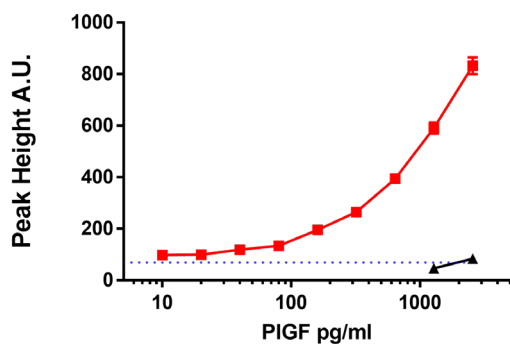


Fig. 4: Optical ELLFA standard curve of PIGF spiked into human serum samples using a AuNP-HRP based amplification system. The red line represents the LF test line (TL) peak intensity after amplification with TMB and the black line represents TL intensity before signal amplification.  $N = 2$  for both data groups. Some error bars are obscured under the data point symbol.

### eWell platform

The developed electrodes were integrated into a standard 96-well plate format to study protein assays with electrochemical read-out (Fig. 5). An electrochemical binding assay for the detection of CXCL10 was successfully demonstrated (Fig. 6). With this first non-optimized assay an LOD of 1.9 ng/ml and a dynamic range covering the complete ng-ml range was achieved. We are currently studying the transfer of the high-sensitivity PIGF assay to our PEPS platform and their integration into a POC device.

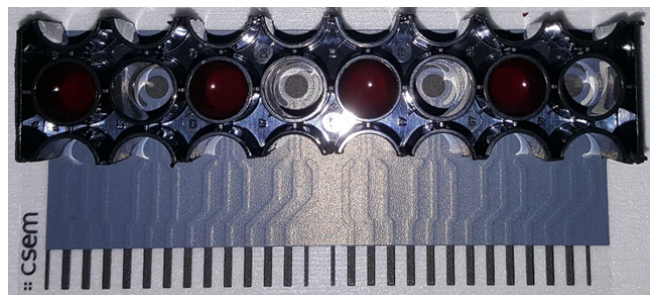


Fig. 5: Image of the PEPS eWell platform.

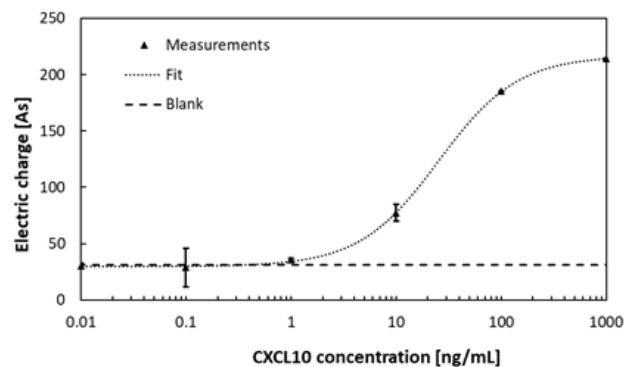


Fig. 6: Results from a sandwich-immunoassay with electrochemical read-out for the detection of CXCL10. Mean values and standard deviations are shown in the graph ( $n = 3$ ).

### References

- [1] J. Sabaté Del Río, O. Henry, P. Jolly, D. Ingber, An antifouling coating that enables affinity-based electrochemical biosensing in complex biological fluids, *Nat Nanotechnol.* 14, 1143-1149 (2019)
- [2] U. Zupančič, P. Jolley, P. Estrela, D. Moschou, D. Ingber, Graphene Enabled Low-Noise Surface Chemistry for Multiplexed Sepsis Biomarker Detection in Whole Blood, *Adv. Funct. Mater.* 31, 2010638 (2021)

# Publications

Aderneuer T, Stefani O, Fernández O, Cajochen C, Ferrini R, Circadian tuning with metameric white light: Visual and non-visual aspects. *Light. Res. Technol.* 53(6), 543-554(2021). <https://doi.org/10.1177/1477153520976934>

Aderneuer T, Fernández O, and Ferrini R, Two-Photon Gray-scale Lithography for Free-Form Micro-Optical Arrays, *Opt. Express* 29, 39511-39520 (2021) <https://doi.org/10.1364/OE.440251>

Aderneuer T et al., Surface topology and functionality of freeform microlens arrays, *Opt. Express* 29, 5033-5042 (2021) <https://doi.org/10.1364/OE.415453>

Antunes R, Steiner R, Muñiz CR, Soni K, Marot L and Meyer E, Plasma-Assisted Catalysis of Ammonia Using Tungsten at Low Pressures: A Parametric Study. *ACS Appl. Energy Mater.* 4, 4385-4394 (2021). <https://doi.org/10.1021/acsaem.0c03217>

Antunes R, Marot L, Romero-Muñiz C, Steiner R and Meyer E, The role of tungsten chemical state and boron on ammonia formation using N<sub>2</sub>-H<sub>2</sub> radiofrequency discharges. *Nucl. Fusion* 61, 126046 (2021). <https://iopscience.iop.org/article/10.1088/1741-4326/ac33c6/pdf>

Arand K, Bieler E, Dürrenberger M and Kassemeyer H-H, Developmental pattern of grapevine (*Vitis vinifera* L.) berry cuticular wax: Differentiation between epicuticular crystals and underlying wax. *PLoS ONE* 16(2): e0246693. <https://doi.org/10.1371/journal.pone.0246693>

Baljozovic M, Liu X, Popova O, Girovsky J, Nowakowski J, et al. Self-Assembly and Magnetic Order of Bi-Molecular 2D Spin Lattices of M(II,III) Phthalocyanines on Au(111). *Magnetochemistry* 7, 119 (2021). <https://doi.org/10.3390/magnetochemistry7080119>

Ben Yaala M, Aumeunier M-H, Steiner R, Schönenberger M, Martin C, Le Bohec M, Talatizi C, Marot L and Meyer E, Bi-directional reflectance measurement of tungsten samples to assess reflection model in WEST tokamak. *Rev. Sci. Instrum.* 92, 093501 (2021). <https://doi.org/10.1063/5.0046140>

Braun O, Overbeck J, El Abbassi M, Käser S, Furrer R, et al., Optimized graphene electrodes for contacting graphene nanoribbons. *Carbon*, 184, pp 331-339 (2021). <https://doi.org/10.1016/j.carbon.2021.08.001>

Camenzind LC, Svab S, Stano P, Yu L, Zimmerman JD, Gosard AC, Loss D and Zumbühl DM, Isotropic and Anisotropic g-Factor Corrections in GaAs Quantum Dots. *Phys. Rev. Lett.* 127, 5, p.057701 (2021). <https://doi.org/10.1103/PhysRevLett.127.057701>

Di Leone S, Vallapurackal J, Yorulmaz Avsar S, Kyropolou M, Ward TR, Palivan CG and Meier W, Expanding the Potential of the Solvent-Assisted Method to Create Bio-Interfaces from Amphiphilic Block Copolymers. *Biomacromolecules* 22 (7), 3005-3016 (2021). <https://doi.org/10.1021/acs.biomac.1c00424>

Driencourt L, Gallinet B, Housecroft CE, Fricke S and Constable EC, Modeling Enhanced Performances by Optical Nanostructures in Water-Splitting Photoelectrodes. *J. Phys. Chem. C* 125, 7010-7021 (2021), <https://doi.org/10.1021/acs.jpcc.0c11342>

Driencourt L, Gallinet B, Housecroft CE, Fricke S and Constable EC, High refractive index dielectric nanoparticles for optically-enhanced activity of water-splitting photoanodes. *Chem. Photo. Chem.* e202100248 (2021), <https://doi.org/10.1002/cptc.202100248>

El Abbassi M, Overbeck J, Braun O, Calame M, van der Zant HSJ and Perrin ML, Benchmark and application of unsupervised classification approaches for univariate data. *Commun. Phys.* 4, 50 (2021). <https://doi.org/10.1038/s42005-021-00549-9>

Froning FNM, Camenzind LC, van der Molen OAH, Li A, Bakkers EPAM, Zumbühl DM and Braakman FR, Ultrafast hole spin qubit with gate-tunable spin-orbit switch functionality. *Nat. Nanotechnol.* 16, p.308-312 (2021). <https://doi.org/10.1038/s41565-020-00828-6>

Fülöp B, Márffy A, Tovari E, Kedves M, Zihlmann S et al., New method of transport measurements on van der Waals heterostructures under pressure, *J. Appl. Phys.* 130, 064303 (2021). <https://doi.org/10.1063/5.0058583>

Fülöp B, Márffy A, Zihlmann S, Gmitra M, Tóvári E et al. Boosting proximity spin orbit coupling in graphene(SSe<sub>2</sub> heterostructures via hydrostatic pressure, *npj 2D Mater. Appl.* 5, 82 (2021). <https://doi.org/10.1038/s41699-021-00262-9>

Gross B, Philipp S, Josten E, Leliaert J, Wetterskog E, Bergström L, and Poggio M, Magnetic anisotropy of individual maghemite mesocrystals, *Phys. Rev. B* 103, 014402 (2021) <https://doi.org/10.1103/PhysRevB.103.014402>

Hedrich N, Wagner K, Pylypovskiy OV, Shields BJ, Kosub T, et al., Nanoscale mechanics of antiferromagnetic domain walls, *Nat. Phys.*, 17, 574-577, <https://doi.org/10.1038/s41567-020-01157-0>

Hinaut A, Scherb S, Freund S, Liu Z, Glatzel T and Meyer E, Influence of electrospray deposition on C<sub>60</sub> molecular assemblies. *Beilstein J. Nanotechnol.* 12, 552-558 (2021). <https://doi.org/10.3762/bjnano.12.45>

Hoogenboom BW, Hough LE, Lemke EA, Lim RYH, Onck PR and Zilman A, Physics of the nuclear pore complex: Theory, modeling and experiment. *Phys. Rep.* 921, pp 1-53 (2021). <https://doi.org/10.1016/j.physrep.2021.03.003>

Huber F, Lang HP, Lang D, Wüthrich D, Hinić V, Gerber C, Egli A and Meyer E, Rapid and Ultrasensitive Detection of Mutations and Genes Relevant to Antimicrobial Resistance in Bacteria. *Global Challenges*, 5, 2000066 (2021). <https://doi.org/10.1002/gch2.202000066>

- Jahnke K, Ritzmann N, Fichtler J, Nitschke A, et al. Proton gradients from light-harvesting *E. coli* control DNA assemblies for synthetic cells, *Nat. Commun.* 12, 3967 (2021). <https://doi.org/10.1038/s41467-021-24103-x>
- Kalita J, Kapinos LE, Lim RYH. On the asymmetric partitioning of nucleocytoplasmic transport - recent insights and open questions. *J. Cell. Sci.* 1, 134(7), jcs240382 (2021). <https://doi.org/10.1242/jcs.240382>
- Khatab M, Sahi VP, Baltenweck R, Maia-Grondard A, Hugueney P, Bieler E, Dürrenberger M, Riemann M, Nick P, Ancestral chemotypes of cultivated grapevine with resistance to Botryosphaeriaceae-related dieback allocate metabolism towards bioactive stilbenes, *New Phytol.* 229(2), 1133-1146 (2021). <https://doi.org/10.1111/nph.16919>
- Kochetkova T, Peruzzi C, Braun O, Overbeck J, Maurya AK, Neels A, Calame M, Michler J, Zysset P, Schwiedrzik J, Combining polarized Raman spectroscopy and micropillar compression to study microscale structure-property relationships in mineralized tissues. *Acta Biomaterialia*, 119 390-404 (2021). <https://doi.org/10.1016/j.actbio.2020.10.034>
- Konov A, Endres M, Abulizi G, Qu K, Yan J, Mandrus DG, Watanabe K, Taniguchi T, Schönenberger C, Superconductivity in type-II Weyl-semimetal WTe<sub>2</sub> induced by a normal metal contact, *J. Appl. Phys.* 129, 113903 (2021). <https://doi.org/10.1063/5.0021350>
- Krywko-Cendrowska A, Marot L, Mathys D, and Boulmedais F, Ion-Imprinted Nanofilms Based on Tannic Acid and Silver Nanoparticles for Sensing of Al(III). *ACS Appl. Nano Mater.* 4, 5372-5382 (2021). <https://doi.org/10.1021/acsanm.1c00716>
- Liu Z, Hinaut A, Peeters S, Scherb S, Meyer E, Righi MC and Glatzel T, Reconstruction of a 2D layer of KBr on Ir(111) and electromechanical alteration by graphene. *Beilstein J. Nanotechnol.* 12, 432-439 (2021). <https://doi.org/10.3762/bjnano.12.35>
- Lüder L, Gubicza A, Stiefel M, Overbeck J, Beretta D, Sadehpour A, Neels A, Nirmalraj PN, Rossi RM, Toncelli C, and Calame M, Conductive Hybrid Cu-HHTP-TCNQ Metal-Organic Frameworks for Chemiresistive Sensing. *Adv. Electron. Mater.*, 2100871 (2021). <https://doi.org/10.1002/aelm.202100871>
- Mergenthaler M, Nersisyan A, Patterson A, Esposito M, Baumgartner A, Schönenberger C, Briggs GAD, Laird EA, Leek PJ, Circuit quantum electrodynamics with carbon-nanotube-based superconducting quantum circuit, *Phys. Rev. Applied* 15, 064050 (2021). <https://doi.org/10.1103/PhysRevApplied.15.064050>
- Mergenthaler M, Schupp FJ, Nersisyan A, Ares N, Baumgartner A, Schönenberger C, Briggs GAD, Leek PJ, Laird EA, Radio-frequency characterization of a supercurrent transistor made of a carbon nanotube, *Mater. Quantum. Technol.* 1 035003 (2021). <https://doi.org/10.1088/2633-4356/ac1d57>
- Miklík D, Fatemeh Mousavi S, Burešová Z, Middleton A, Matsushita Y, et al., Pyrazinacenes Exhibit On-Surface Oxidation-State-Dependent Conformational and Self-Assembly Behaviours. *Commun. Chem.* 4 (1), 29 (2021). <https://doi.org/10.1038/s42004-021-00470-w>
- Moradi M, Lengweiler NL, Housecroft CE, Tulli LG, Stahlberg H, Jung TA, Shahgaldian P, Coordination-Driven Monolayer-to-Bilayer Transition in Two-Dimensional Metal-Organic Networks, *J. Phys. Chem. B* 2021, 125. <https://doi.org/10.1021/acs.jpcc.1c01058>
- Mortelmans T, Kazazis D, Padeste C, Berger P, Li X, Ekinici Y, A nanofluidic device for rapid and multiplexed SARS-CoV-2 serological antibody detection. *Research Square* (2021). <https://doi.org/10.21203/rs.3.rs-537056/v1>
- Neumann S, Wenger OS and Kerzig C, Controlling Spin-Correlated Radical Pairs with Donor-Acceptor Dyads: A New Concept to Generate Reduced Metal Complexes for More Efficient Photocatalysis. *Chem. Eur. J.* 27, 4115 - 4123 (2021). <https://doi.org/10.1002/chem.202004638>
- Pawlak R, Liu X, Ninova S, D'Astolfo P, Drechsel C, et al., On-Surface Synthesis of Nitrogen-Doped Kagome Graphene, *Angew. Chem. Int.* 60, 8370-8375 (2021). <https://doi.org/10.1002/ange.202016469>
- Philipp S, Gross B, Reginka M, Merkel M, Claus MM, Sulzger M, Ehresmann A, and Poggio M, Magnetic hysteresis of individual Janus particles with hemispherical exchange-biased caps, *Appl. Phys. Lett.* 119, 222406 (2021) <https://doi.org/10.1063/5.0076116>
- Ramezani M, Sampaio CI, Watanabe K, Taniguchi T, Schönenberger C, Baumgartner A, Superconducting contacts to a monolayer semiconductor, *Nano Letters*, 21, 5614 (2021). <https://doi.org/10.1021/acs.nanolett.1c00615>
- Ritzmann N, Manioglu S, Hiller S, Müller DJ, Monitoring the antibiotic darobactin modulating the  $\beta$ -barrel assembly factor BamA, *Structure* 30, 1 (2021) <https://doi.org/10.1016/j.str.2021.11.004>
- Schreiner V, Detampel P, Jirkof P, Puchkov M and Huwyler J, Buprenorphine loaded PLGA microparticles: Characterization of a sustained-release formulation. *J. Drug Deliv. Sci. Technol.*, Volume 63, June 2021, 102558 <https://doi.org/10.1016/j.jddst.2021.102558>
- Sharma D, Lim RYH, Pfohl T and Ekinici Y, Surface-modified elastomeric nanofluidic devices for single nanoparticle trapping. *Microsyst. Nanoeng.* 7, 46 (2021). <https://doi.org/10.1038/s41378-021-00273-y>
- Sharma D, Lim RYH, Pfohl T and Ekinici Y, Optimization of Nanofluidic Devices for Geometry-Induced Electrostatic Trapping. *Part. Part. Syst. Charact.* 38, 2000275 (2021). <https://doi.org/10.1002/ppsc.202000275>
- Soni K, Steiner R, Antunes R, Moser L, Shigin P, Reichle R, Marot L and Meyer E, Study of wall re-deposition on DC-grounded ITER-relevant mirrors with RF plasma in a first mirror unit. *Nucl. Fusion* 61, 126017 (2021). <https://doi.org/10.1088/1741-4326/ac2b74>
- Soni K, Moser L, an Donkó Z, Hartmann P, Korolov I, Antunes R, Juhász Z, Steiner R, Marot L and Meyer E, Experimental and numerical characterization of a radio-frequency plasma source with a DC-grounded electrode configuration using a quarter-wavelength filter. *Plasma Phys. Control. Fusion* 63, 045005 (2021). <https://doi.org/10.1088/1361-6587/abdbd1>

Sun K, Sagisaka K, Peng L, Watanabe H, Xu F, Pawlak R, Meyer E, Okuda Y, Orita A, Kawai S, Head-to-Tail Oligomerization by Silylene-Tethered Sonogashira Coupling on Ag(111). *Angew. Chem. Int. 60*, 19598–19603 (2021). <https://doi.org/10.1002/ange.202102882>

Szmyt W, Guerra-Nuñez C, Dransfeld C, Utke I, Solving the inverse Knudsen problem: Gas diffusion in random fibrous media. *J. Membr. Sci., J. Membr. Sci.*, Volume 620, 2021, 118728, <https://doi.org/10.1016/j.memsci.2020.118728>

Tarvirdipour S, Skowicki M, Mihali V, Schoenenberger C-A, Palivan CG, Peptide-Assisted Nucleic Acid Delivery Systems on the Rise, *Int. J. Mol. Sci.* 22(16), 9092(2021), <https://doi.org/10.3390/ijms22169092>

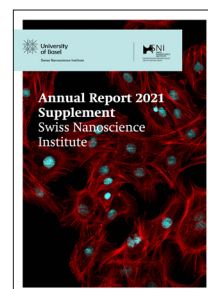
Thomas FS, Nilsson M, Ciaccia C, Jünger C, Rossi F, Zannier V, Sorba L, Baumgartner A, Schönenberger C, Spectroscopy of the local density-of-states in nanowires using integrated quantum dots, *Phys. Rev. B* 104, 115415 (2021). <https://doi.org/10.1103/PhysRevB.104.115415>

Umar M, Swinkels MY, De Luca M, Fasolato C, Moser L, Ga-dea G, Marot L, Glatzel T, Zardo I, Morphological and stoichiometric optimization of Cu<sub>2</sub>O thin films by deposition conditions and post-growth annealing, *Thin Solid Films* 732 138763 (2021). <https://doi.org/10.1016/j.tsf.2021.138763>

Wang L, Baumgartner A, Makk P, Zihlmann S, Varghese BS, Indolese DI, Watanabe K, Taniguchi T, Schönenberger C, Global strain-induced scalar potential in graphene devices, *Comm. Phys.* 4, 147 (2021).

Wehr R, dos Santos EC, Muthwill MS, Chimisso V, Gaitzsch J, Meier W, Fully amorphous atactic and isotactic block copolymers and their self-assembly into nano- and microscopic vesicles. *Polym. Chem.* 12, 5377-5389 (2021). <https://doi.org/10.1039/D1PY00952D>

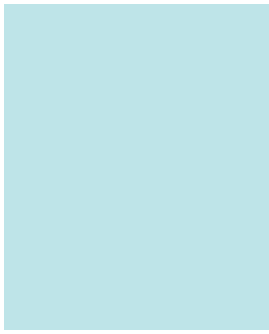
Weißinger L, Arand K, Bieler E, Kassemeyer H-H, Breuer M, Müller C, Physical and Chemical Traits of Grape Varieties Influence *Drosophila suzukii* Preferences and Performance. *Front. Plant Sci.* 12, 664636 (2021). <https://doi.org/10.3389/fpls.2021.664636>



**Cover image:**

The image shows heart cells (red) and their nuclei (turquoise). (Image: F. Züger, FHNW and University of Basel)

© Swiss Nanoscience Institute, March 2022



**Educating  
Talents**  
since 1460.

University of Basel  
Petersplatz 1  
P.O. Box 2148  
4001 Basel  
Switzerland

[www.unibas.ch](http://www.unibas.ch)

Swiss Nanoscience Institute  
University of Basel  
Klingelbergstrasse 82  
4056 Basel  
Switzerland

[www.nanoscience.ch](http://www.nanoscience.ch)